DISSERTATION

submitted to the

Combined Faculties for the Natural Sciences and for Mathematics

of the Ruperto-Carola University of Heidelberg, Germany

for the degree of

Doctor of Natural Sciences

put forward by

Dipl.-Phys. Patrick Thomas Philipp Klenk

born in Ulm

Oral Examination on December 12th 2012

Developing Ground-Penetrating Radar
for Quantitative Soil Hydrology

Referees: Prof. Dr. Kurt Roth

                         Prof. Dr. Jan van der Kruk

Abstracts - English - German - Chinese

Abstract

Ground-Penetrating Radar (GPR) is a non-invasive electromagnetic geophysical method, which is sensitive to variations of subsurface dielectric properties. With this, GPR has become a versatile tool in various fields of geophysics and the soil science. In particular the determination of field-scale soil water content has drawn considerable research interest over the past decade. However, the quantifiability of achieved results remains often contested. In this thesis, three approaches for a quantitative use of GPR in soil hydrology are presented. First, a new calibration approach is developed for quantifying near-surface soil water contents with GPR and its applicability is demonstrated in field applications. Second, the ability of GPR methods for monitoring soil water dynamics is tested in well-controlled field experiments featuring imbibition into and drainage from a known subsurface structure. Finally, GPR applications are demonstrated in the broader context of developing monitoring schemes at a set of representative sites in a highly structured watershed.

Kurzfassung

Das Boden- oder Georadar (GPR) ist eine elektromagnetische Meßmethode in der Geophysik, mit dessen Hilfe Veränderungen der dielektrischen Eigenschaften des Untergrunds nicht-invasiv bestimmt werden können. Daher findet GPR vielfache Anwendung in verschiedenen Bereichen der Geophysik und der Bodenwissenschaften. Insbesondere seine Verwendung zur Bestimmung von Bodenwassergehalten auf der Feldskala wurde im Laufe des letzten Jahrzehnts intensiv untersucht. Die Quantifizierbarkeit der erreichten Ergebnisse ist dennoch oft schwierig. In dieser Arbeit werden daher drei Ansätze präsentiert, quantitative Ergebnisse mit GPR im Umfeld bodenhydrologischer Forschung zu erzielen. Erstens wird ein neuer Kalibrationsansatz entwickelt, um mit GPR gemessene oberflächennahe Bodenwassergehalte zu quantifizieren und dann dessen Anwendbarkeit im Feld demonstriert. Zweitens wird GPR dazu verwandt die Bodenwasserdynamik bei Be- und Entwässerungsexperimenten in und aus einer bekannten Untergrundstruktur zu beobachten. Schließlich werden Anwendungen für Georadar bei der Entwicklung eines Beobachtungssystems in einem hochstrukturierten Wassereinzugsgebiet anhand einer Reihe von repräsentativen Messstellen demonstriert.

摘要

探地雷达在地球物理和土壤科学中有许多应用。特别是在过去的十几年中，它在估计野外小尺度土壤含水量方面引起了众多研究兴趣。但是，其定量化的结果仍有待 商榷。在本论文中，它展示了探地雷达在土壤水文学中三种定量化应用研究。第一， 开发了一种对探地雷达测表层土壤含水量进行校正的新方法，并验证了其野外应用的可行性。第二， 在控制良好并已知土体层状的野外试验中，通过对渗吸和排水过程的监测，测试了探地雷达方法对土壤水动态变化监测的能力。第三， 在一个更大的研究背景下，针对中国新疆乌鲁木齐一个高度结构化的流域进行各种监测方案开发的研究中，在一系列代表性的站点上进一步展示了探地雷达的各种应 用。

Contents

1 Introduction

The challenge is paramount. In 2050, almost 10 billion people may live on this Earth (according to medium projections in *WPP* [2011]), potentially fighting over more than two times this planet's actually available resources (e.g., *Kitzes et al.* [2008]). A planet which by all what we know so far may be unique for quite a distance in the Universe surrounding us. Meanwhile a changing climate is driven by mechanisms which we so far barely begin to grasp. A changing climate which will most probably lead to increasing glacial melt, associated with a non-negligible sea water level rise, escalating extreme weather conditions, intensifying desertification and an ever more unequal distribution of natural water resources (*Solomon et al.* [2007]). Clearly, this list is by no means comprehensive and every year additional consequences of a changing climate are discovered. The change is real and it can be measured, while the extent to which this change has anthropic origins is still a matter of some discussion. It is however out of the question that we humans impact the natural mechanisms governing the functioning of this planet now more than ever throughout all of Earth's history. As proposed by *Crutzen* [2002], we live in the Anthropocene – we are shaping our Earth, with all the positive and negative consequences attached.

Questions of mitigating climate change impacts, plain adaptation or even the sense and sensitivity of active geoengineering have been subject to intensive scientific scrutiny in recent years (e.g., *Keith* [2000]) and increasingly enter the focus of public debate (e.g., *Crutzen* [2006]). For an informed discussion and for well-founded decisions by policy makers on any of these issues, the processes that govern our Earth system have to be profoundly studied and understood. The basic challenge in understanding the Earth system and predicting its future behavior lies in the considerable non-linearities associated with many of the relevant processes. Due to the complex system dynamics, a small change of a condition at one particular location may have severe or even cataclysmic consequences for a different part of the system at some point in the future. We may currently find ourselves in a state of fragile balance of more or less stable overall conditions. As far as we know, the climate has been more favorable for human development over the last ten thousand years than in the past half of a million years (e.g., *Dansgaard et al.* [1993]). Still, indications abound that feedback mechanisms exist which introduce so-called tipping points into the system, points where this fragile stable condition will inevitably spin out of control (e.g., *Lenton et al.* [2008]). In that case most likely new balanced conditions will materialize eventually. This new point of stability might however imply anything from a frozen "Snowball Earth" (*Schrag et al.* [2002]) all the way to the runaway greenhouse conditions currently observed on Venus (e.g., *Fegley Jr.* [2003]).

One concept for investigating these feedback mechanisms and dealing with such tipping points has been introduced in *Rockström et al.* [2009], formulating so-called "planetary boundaries" in an Earth system framework. They defined boundaries for nine distinct aspects of Earth System Sciences, including for instance land use, ocean acidification and climate change. Naturally, the existence of these boundaries and their exact definitions have instantly been a matter of intensive discussion and most likely will have to be adjusted with the increasing understanding of the governing processes. To current knowledge some of these boundaries are claimed to having already been inevitably crossed, like the limits set for climate change and biodiversity loss. For other boundaries we do not seem to be there - yet. One of them is the essence of our life: The global freshwater availability.

The importance of liquid freshwater for life can hardly be overstated. To date, we have not found any form of life which does not for one reason or another have the need for liquid water. This is why we search for water as a signature of life both on this planet and throughout the Universe (e.g., *Gross* [2012]). For example, the Herschel satellite aims at measuring the abundance of water molecules in space (e.g., *Van Dishoeck et al.* [2011]). The Spitzer telescope has recently observed water vapor in the atmosphere of a distant planet (*Beaulieu et al.* [2010]), while ESA's Rosetta spacecraft is currently headed for Comet 67P/Churyumov-Gerasimenko addressing the hypothesis whether most of the water on this Earth could have its origin in comets (*Glassmeier et al.* [2007]). Meanwhile NASA has just sent a new robot vehicle named "Curiosity" to Mars – and (our) Curiosity has landed successfully and recently started its surface operations. One of its main scientific objectives is to address connections of the water which seemingly shaped Mars in a distant past with potential indications for life (*Grotzinger et al.* [2012]).

Despite all these efforts, so far, not much *liquid* water has been confirmed to currently exist elsewhere in the Universe, although strong indications for the existence of some liquid water have been reported recently, for instance on Saturn's moons (*Waite Jr et al.* [2009]). The abundance of liquid water distinguishes our planet, this "pale blue dot" when viewed from space, as Carl Sagan once observed (*Sagan and Druyan* [1997]). Standing at the shores of the ocean, one tends to agree that liquid water seems to be abundant indeed. However, comparing the volume of water to the Earth itself helps putting things into perspective: Water comprises only 1/700 of the Earth's total volume. Shaped into a sphere of its own, it would have a diameter of merely 1400 km. Furthermore, only a staggeringly small amount of less than 3 % of these global water resources is actually fresh water, almost 69 % of which is currently stored away in polar ice caps and glaciers and 30 % in only partly accessible groundwater. The remainder is partly made up of snow and ice, leaving the water in rivers and lakes to account for only 0.3 % of all the freshwater on the Earth and about one per mill for soil water content (figures based on *Henderson and Henderson* [2009]). Or, viewed from a human perspective: Of all the water on Earth, only about 1 % is usable by humans, 99 % of which is ground water.

Exacerbating the challenge, global water resources are unequally distributed. While Northern Middle Europe can be expected to meet its needs at least in the middle term, other regions already now suffer from a severe water shortage, like the Colorado River Basin in the USA or the Jordan River Valley in the Middle East (e.g., *Christensen and Lettenmaier* [2007], *Allan* [2002]). Furthermore, many regions with an acute shortage of water export large parts of this precious resource in form of products manufactured for the world market, mostly agricultural goods. This notion has been formalized under the term "virtual water trade" (see for instance *Hoekstra* [2003a]), where virtual water is defined as the volume of water which is required to produce a commodity or service, which is then traded to other regions and parts of the world (e.g., *Hoekstra* [2003b]). For example, in this sense, a single cup of coffee contains 140 l of virtual water, while 2400 l of water are needed for producing 150 g of hamburger beef (*Hoekstra and Chapagain* [2007]).

Traditionally, assessments of virtual water content in products or services as well as conventional water-resource planning and management have focused mainly on surface and ground water ("blue water"). In recent years, the focus has been widened to include soil water content ("green water") into such considerations, which actually represents two thirds of the real freshwater resource, which is the rainfall over continents (*Falkenmark and Rockström* [2006]). Most of this precipitation never reaches rivers or lakes but is transported back to the atmosphere as vapor flow, with the controlling mechanisms being evaporation from (bare) soils and in this context more importantly transpiration, i.e. the consumptive water use by the vegetation. Hence, for correctly assessing the availability or consumption of water resources, green water has to be included as a second form of water resource. In this sense, transpiration is considered a *productive water* loss, since it actually contributes to plant growth (and thus for example to crop production), while evaporation and deep percolation are termed *non-productive water* losses. Water management and conservation strategies can be adopted accordingly, for instance by aiming at minimizing non-productive water losses. *Falkenmark and Rockström* [2006] argue that such an integrated soil and water management can significantly improve water productivity, "the amount of crop per drop of water".

In any case, whether considering green water as an explicit resource for crop production or including green water into more general water resource management and virtual water assessment schemes, a detailed understanding of the hydrological processes of the near surface is indispensable. This includes in particular accurate knowledge about the spatial distribution and temporal dynamics of *soil water content*, which controls the dynamics in the root zone, the partitioning of precipitation into runoff and infiltration as well as the energy exchange at the boundary between soil and atmosphere. Due to the complex nature of soil properties, these dynamics are highly non-linear. However, as has been shown, e.g., by *Wollschläger et al.* [2009], the properties of soil water content dynamics can in principle be inferred from time series observations of the subsurface water content distribution. This demands methods which can observe the temporal variation of the

spatial distribution of soil water content to a high precision, i.e. with a high reproducibility.

There are various well established methods for observing soil water content dynamics at multiple scales (e.g., *Robinson et al.* [2008]). However, the quantifiability and the representativity of achieved results often remain contested. At the point scale, invasive methods like gravimetric sampling and Time Domain Reflectometry (TDR, e.g., *Robinson et al.* [2003]) remain the accepted standard, offering the highest data quality. However, accurately representing soil water content at larger scales based on point scale methods gets instantly tedious and rapidly plainly impossible, due to its large spatial and temporal variability (*Western et al.* [2002]).

At large scales, remote sensing methods have been more and more established in recent years for monitoring shallow surface moisture contents. The most promising results have been achieved so far with active radar and passive microwave radiometer instruments (e.g., *Wagner et al.* [2008], *Loew et al.* [2006], *Wigneron et al.* [2003]), despite limitations which are typically associated with the vegetation cover and sampling depths of only a few centimeters (e.g., *Walker et al.* [2004]). For example, the active radar instrument ASAR on esa's ENVISAT satellite has shown the ability to retrieve surface soil moisture contents (e.g., *Pathe et al.* [2009], *Van der Velde et al.* [2008], *Loew et al.* [2006]). However, communication with the satellite was lost in spring 2012 and a follow-up mission has not yet been launched. Other recent developments include change detection algorithms for deriving relative soil moisture contents from scatterometer data (e.g., *Bartalis et al.* [2007]) and the evaluation of polarimetric synthetic aperture radar data, which have been demonstrated to show sensitivity also under vegetation cover (*Hajnsek et al.* [2009]). Meanwhile, ESA's currently active Soil Moisture and Ocean Salinity (SMOS) mission features an L-band radiometer which has been specifically designed for observing soil moisture content (*Kerr et al.* [2001]). The instrument provides data at a daily repeat rate, albeit at a very coarse spatial resolution. Although first results have reported significant correlation with surface measurements (e.g., *Albergel et al.* [2011]), SMOS has so far been struggling with severe radio frequency interference issues (*Oliva et al.* [2012]) in many parts of the world. Meanwhile, expectations are on the rise for NASA's upcoming Soil Moisture Active Passive (SMAP) mission, which is currently scheduled for launch in late 2014, featuring both an active and a passive instrument (*Entekhabi et al.* [2010]). At basin to continental scales, the GRACE mission has been employing gravity change detection for determining total water storage since 2002 (e.g., *Tapley et al.* [2004]).

However, despite a variety of novel systems and sophisticated retrieval algorithms, direct in-situ field measurements are currently still indispensable for most state-of-the-art remote sensing methods aimed at retrieving near surface soil moisture in order to provide calibration and validation data. Due to the drawbacks of point measurements formulated above, such in-situ field measurement methods should ideally be directly applicable at similar scales as (at least the high resolution) remote sensing methods. This is one reason

why an often lamented paucity of available measurement methods at these intermediate scales has drawn considerable research interest in recent years (*Robinson et al.* [2008], *Vereecken et al.* [2008]). Promising results have been achieved with wireless sensor networks which have been installed at various experimental catchments, providing water content measurements at high temporal resolution (e.g., *Bogena et al.* [2010], *Cardell-Oliver et al.* [2005]). However, their major drawbacks are the typically high investment costs and the lack of flexibility. Novel instruments like cosmic ray probes have shown sensitivity to soil water content (*Zreda et al.* [2008]), although calibration and representativity issues need further investigation (*Villarreyes Rivera et al.* [2011]).

Throughout the last decade, the potential of GPR as a versatile and efficient tool for mapping soil water content distributions and subsurface structures at scales of several meters to kilometers has been repeatedly demonstrated (e.g., *Huisman et al.* [2003a], *Huisman et al.* [2003b], *Lambot et al.* [2006], *Gerhards et al.* [2008], *Wollschläger et al.* [2010], *Minet et al.* [2010]). Especially under specific conditions leading to dispersive wave propagation, quantitative information about near-surface water contents has been successfully obtained. This includes for example waveguides induced by frozen soils (e.g., *van der Kruk et al.* [2007], *van der Kruk et al.* [2009]) or by precipitation events (*van der Kruk et al.* [2010]). Meanwhile, high-resolution GPR data from cross-borehole measurements have been applied for quantitatively describing flow and transport in the unsaturated zone (e.g., *Winship et al.* [2006]). In recent years, the potential of these high-resolution data for constraining subsurface hydrological models has been demonstrated, mostly in conjunction with additionally using resistivity imaging (e.g., *Binley et al.* [2002], *Deiana et al.* [2008] or *Doetsch et al.* [2010]).

Despite all these considerable advancements, a quantification of the observed GPR response with respect to near-surface soil water content dynamics under more general field conditions has often remained challenging (e.g., *Jacob and Hermance* [2004], *Weihermüller et al.* [2007]). The goal of this dissertation is to alleviate some of these challenges by developing quantitative methods for the investigation of near-surface soil water content dynamics based on *ground-coupled GPR*.

As will be seen in this thesis, quantifying an observed GPR response requires establishing a solid process understanding on several levels. The first is an understanding of the physical interaction of the GPR signal with different subsurface characteristics. Secondly, concepts of soil physics are essential for explaining the highly nonlinear water content dynamics which can be observed by GPR. And finally, we will reach limits where only a deeper understanding of the characteristics of the employed instruments may further reduce observed inconsistencies. Combining these different levels of understanding can lead to establishing GPR as a tool for quantitatively studying near-surface hydrological processes. Admittedly, this is but a small contribution towards addressing the enormous challenges so briskly described in the preceding paragraphs. Nevertheless, also a journey of a thousand miles begins with a single step (Lao-Zi (老子), 5$^{\text{th}}$ century BC).

General Overview

In order to follow the road just outlined towards quantifying surface GPR methods for soil hydrology, this dissertation was originally designed to directly carry out and assess detailed multi-temporal GPR measurements at various representative sites throughout a highly structured watershed in Northwestern China. However, due to limited availability of ancillary data and increasing restrictions with respect to site access in this politically sensitive region, it became obvious after the first year that quantitative results would not be achievable by solely relying on datasets acquired in China. Hence, additional well-controlled experiments have been carried out, foremost on a well-known testsite close to Heidelberg, in order to improve the understanding of the GPR response to water content dynamics in layered media. Furthermore, a novel calibration approach had to be developed which allows for robust determination of near-surface water contents to a similar precision as TDR. To that end, additional datasets had to be incorporated into the analysis as well. This is why this thesis will not follow its historic development. Instead, a more systematic approach is taken. The starting point is an analysis of the precision and accuracy of the employed methods, developing and demonstrating the applicability of the novel calibration approach. Next, the implications of the high-precision experiments will be discussed first, before returning to the more challenging datasets from China. In detail, the separate chapters are structured as follows:

- This chapter introduces the overall context for this work.

- The second chapter includes a few theoretical considerations about electromagnetic wave propagation in soils and a brief introduction to basic concepts of soil physics.

- The third chapter will present a basic overview of current Ground-Penetrating Radar methods for observing the shallow sub-surface and in particular for deriving soil water contents. Other methods for measuring near-surface soil water contents which are relevant for this thesis are briefly introduced and discussed as well. Lastly, the measurement setup used in this work is introduced.

- The fourth chapter gives an introduction to the special characteristics of the respective field sites in Germany and China. Where available, auxiliary data are evaluated.

- The fifth chapter is concerned with a detailed investigation of effects impacting the precision and accuracy of GPR methods, focusing on near-surface soil water content determination. In particular a novel calibration approach for common offset measurements of the direct ground wave signal is developed.

- The sixth chapter shows a field application using the novel calibration approach for deriving near-surface soil water contents at a semi-vegetated desert site in Northwestern China.

- The seventh chapter then turns to evaluating well-defined field-scale experiments with respect to the possibility of deriving quantitative information about subsurface (hydraulic) properties. In particular, a pumping experiment executed at the Heidelberg ASSESS-GPR test site is thoroughly assessed. At the end of this chapter, the reader should have a good overview about the current possibilities of GPR methods under varying but well-defined conditions.

- The eighth chapter will then take a broader view. Here, the focus is on applying the methods introduced in previous chapters for taking a look at relevant processes in a highly dynamic regional watershed in Northwestern China. The applicability of different GPR methods at characteristically distinct measurement sites is discussed. Implications for monitoring hydrological processes under more difficult general field conditions with sparse auxiliary data are presented.

- The last chapter summarizes the major results, discusses the conclusions which can be drawn and gives a brief outlook on the road ahead.

- Lists of figures, tables and acronyms and the acknowledgements can be found in the appendix.

Digital Supplementary Materials

Some of the observed phenomena can be best illustrated in the form of short movies. These are provided with the digital supplementary materials to this dissertation and are linked in the text. An overview of available movies can be found in appendix B.

2 Theoretical Considerations

The largest part of this PhD thesis deals with phenomena involving the emission, propagation, interaction and detection of electromagnetic waves. Hence, some fundamentals of electromagnetic theory will be summarized in this chapter. Furthermore this chapter will briefly discuss the propagation of electromagnetic waves in soils and the dielectric properties of water, providing the theoretical background for observing hydrologic phenomena with electromagnetic geophysical methods. These considerations were adopted from *Klenk* [2009]. More comprehensive treatments can be found for instane in *Daniels et al.* [2004] or *Jol* [2009]. Subsequently, a brief introduction into the concepts of soil physics will provide the basis for later interpreting the hydraulic dynamics which will be observed in chapter 7.

2.1 Propagation of Electromagnetic Waves in Homogeneous Media

In 1873, James Clark Maxwell published his "Treatise on Electricity and Magnetism" *Maxwell* [1873]. Since then, electromagnetic fields in a classical sense have been described using four field vectors, namely:

- the electric field vector $\vec{E}$ [V/m],

- the magnetic field vector $\vec{H}$ [A/m],

- the magnetic induction, or flux density vector $\vec{B}$ [Vs/m²],

- the electric displacement field vector $\vec{D}$ [As/m²].

Those four vectors are related to their sources (the charge density distribution ρ [C/m³] and the electric current density $\vec{j}$ [A/m²]) by the four partial differential equations:

$$\nabla \times \vec{E} = -\frac{\partial \vec{B}}{\partial t} \qquad\qquad \nabla \times \vec{H} = \vec{j} + \frac{\partial \vec{D}}{\partial t}$$
$$\nabla \cdot \vec{B} = 0 \qquad\qquad\qquad \nabla \cdot \vec{D} = \rho \quad . \qquad\qquad (2.1)$$

For solving these Maxwell equations, they have to be supplemented by three additional material equations, which, in the most simple case of linear, homogeneous and isotropic media, read:

$$\vec{D} = \varepsilon \vec{E} \qquad\qquad\qquad \vec{B} = \mu \vec{H} \qquad\qquad\qquad \vec{j} = \sigma \vec{E} \qquad\qquad (2.2)$$

with the dielectric permittivity $\varepsilon\,[\mathrm{F/m}]$, the magnetic permeability $\mu\,[\mathrm{H/m}]$ and the electric conductivity $\sigma\,[\mathrm{S/m}]$, the Maxwell equations can be expressed in terms of the two vectors $\vec{E}$ and $\vec{H}$ (*Telegraph equations*):

$$\Delta\vec{E} = \mu\sigma\frac{\partial\vec{E}}{\partial t} + \mu\varepsilon\frac{\partial^2\vec{E}}{\partial t^2} \tag{2.3}$$

$$\Delta\vec{H} = \mu\sigma\frac{\partial\vec{H}}{\partial t} + \mu\varepsilon\frac{\partial^2\vec{H}}{\partial t^2} \quad . \tag{2.4}$$

If we further assume a time dependency of the form $E(t) = E_0 e^{i\omega t}$, where ω is the angular frequency of the field, we arrive at the following forms:

$$\Delta\vec{E} = i\omega\mu\sigma\vec{E} - \varepsilon\mu\omega^2\vec{E} \tag{2.5}$$

$$\Delta\vec{H} = i\omega\mu\sigma\vec{H} - \varepsilon\mu\omega^2\vec{H} \quad . \tag{2.6}$$

Equations 2.5 and 2.6 constitute the foundation for the propagation of electric and magnetic field vectors in an isotropic, homogeneous medium with physical properties ε, μ and σ. The terms which include $i\omega\sigma$ are associated with the *conduction currents*, while terms with $\varepsilon\mu\omega^2$ are associated with the *displacement currents* (e.g., *Sharma* [1997]). These terms can be grouped together to yield the complex propagation parameter **k**, where

$$k^2 = -i\omega\mu\left(\sigma + i\omega\varepsilon\right) = \mu\varepsilon\omega^2 - i\omega\mu\sigma \quad . \tag{2.7}$$

To facilitate the understanding of electromagnetic wave propagation in homogeneous media, it is instructive to examine the behavior of the propagation parameter with changes in frequency.

For low frequencies ($f < 0.1$ MHz) and high conductivities, the propagation parameter reduces to $k^2 = -i\omega\mu\sigma$, which leads to a highly-damped diffusive character of field propagation in the medium, with conductive currents dominating over displacement currents. This can also be seen from the telegraph equations where in this case the $\frac{\partial}{\partial t^2}$ term can be neglected against the $\frac{\partial}{\partial t}$ term, effectively reducing to a diffusion equation. On the other hand, for high frequencies ($f > 10$ MHz), displacement currents dominate in low conductivity media, which yields a propagation parameter of $k^2 = \mu\varepsilon\omega^2$. In this case we have "classic" electromagnetic wave propagation in the medium, which is again evident from the structure of the telegraph equations, reducing to simple wave equations in this case ($\Delta\vec{E} = -\mu\varepsilon\frac{\partial^2\vec{E}}{\partial t^2}$, and analogue for the magnetic field strength $\vec{H}$).

The transition between the two regimes can be expressed in terms of a transition frequency, defined as (e.g., *Annan* [2005]):

$$\omega_t = \frac{\sigma}{\varepsilon} \quad . \tag{2.8}$$

2.2 Behavior at Boundaries

In general, electromagnetic waves impinging on interfaces between two media with distinct dielectric properties will be partially transmitted and reflected. Incident (I), transmitted (T) and reflected (R) field strengths are related by

$$I = R + T \quad . \tag{2.9}$$

For electromagnetic waves incident on planar boundaries, transmission across and reflection at the interface are governed by the Fresnel coefficients (e.g., *Jackson* [1999]), giving the amplitude ratios of incident, transmitted and reflected waves. For example, assuming non-conductive and non-magnetizing media with dielectric permittivities ε_1 and ε_2, reflection and transmission coefficients for the transversal electric polarized component (TE, where the electric field vector oscillates parallel to the interface) of the incident wave can be expressed through

$$R_{TE} = \frac{\sqrt{\varepsilon_1}\cos\theta_1 - \sqrt{\varepsilon_2}\cos\theta_2}{\sqrt{\varepsilon_1}\cos\theta_1 + \sqrt{\varepsilon_2}\cos\theta_2} \qquad T_{TE} = \frac{2\sqrt{\varepsilon_1}\cos\theta_1}{\sqrt{\varepsilon_1}\cos\theta_1 + \sqrt{\varepsilon_2}\cos\theta_2} \quad , \tag{2.10}$$

where θ_1 and θ_2 are the angles of incidence and refraction, respectively. The travel direction changes, for instance in case the wavefront is refracted, according to Snell's law, which relates the angle of incidence to the angle of refraction depending on the contrast in dielectric permittivity, i.e. the velocity contrast between the adjacent dielectric media:

$$\sqrt{\varepsilon_1}\sin\theta_1 = \sqrt{\varepsilon_2}\sin\theta_2 \tag{2.11}$$

$$\Longleftrightarrow \quad \frac{\sin\theta_1}{v_1} = \frac{\sin\theta_2}{v_2} \quad , \tag{2.12}$$

since we can relate the phase velocity v to permittivities through $v = \omega/k = 1/\sqrt{\varepsilon}$ using relationship 2.7 under the assumptions made above ($\sigma = 0, \mu = 1$).
Therefore, for adjacent media with $\sqrt{\varepsilon_2} > \sqrt{\varepsilon_1}$, there is a maximum angle, beyond which the angle of incidence would have to be assumed imaginary. The existence of this critical angle is the prerequisite for the phenomena of (critical) refraction and wave-guiding which are discussed in more detail in Sections 3.4.1 and 5.5.

Furthermore, we note that there will be no response without a contrast in dielectric permittivity between the materials. Conversely, any small change in permittivity can be expected to lead to partial reflection of the impinging electromagnetic wave. This is the foundation for explaining the generation of reflections from smooth permittivity profiles.

2.3 Dielectric Properties of Natural Media

In order to deal with natural media, the dielectric and magnetic permittivities ε and μ are normally expressed relative to their values in vacuum:

$$\varepsilon = \varepsilon_0 \cdot \varepsilon_r \qquad\qquad\qquad \mu = \mu_0 \cdot \mu_r \quad , \qquad\qquad (2.13)$$

with constants $\varepsilon_0 = 8.8542 \cdot 10^{-12}$ F/m and $\mu_0 = 4\pi \cdot 10^{-7}$ H/m. In general, the relative permittivities ε_r and μ_r are functions of space and frequency as well as other environmental variables, for instance temperature.

In the case of low-loss, non-conductive media, where the propagation parameter reduces to $k = \omega\sqrt{\mu\varepsilon}$, the phase velocity of an electromagnetic wave is then given through

$$v = \frac{w}{k} = \frac{1}{\sqrt{\mu\varepsilon}} = \frac{c_0}{\sqrt{\mu_r \varepsilon_r}} \quad , \qquad\qquad (2.14)$$

where we used the fact that the vacuum speed of light c_0 is given by $1/\sqrt{\mu_0 \varepsilon_0}$.

Furthermore, since most geological media are non-magnetizing, $\mu_r \approx 1$ is usually a good assumption. In this case, the phase velocity is solely determined by the dielectric permittivity of the medium:

$$v = \frac{c_0}{\sqrt{\varepsilon_r}} \quad . \qquad\qquad (2.15)$$

This is why the dielectric permittivity constitutes an important measurement target of all electromagnetic methods used to study soil properties.

2.3.1 Complex dielectric permittivity

Up to this point, we have assumed a single-frequency, continuous wave signal with sinusoidal shape. We will now drop this assumption and look at the behavior of pulsed waveforms since they constitute the main signal used in ground-penetrating radar applications.

Generally, the signal velocity of a pulsed waveform can differ from the phase velocities of its spectral components. This dispersive character is connected to the large number of different polarization mechanisms which contribute to the dielectric response of natural media, leading for instance to absorption processes and to energy dissipation in general when involving friction. Due to the different nature of contributing polarization mechanisms, the dielectric response of the material may vary considerably with frequency. Usually, dielectric response is then expressed through a complex form of the dielectric permittivity $\varepsilon*$, where its imaginary part $\varepsilon''(\omega)$ is associated with energy dissipation and its real part ε' describes energy storage under the application of an alternating field.

When applying an electrical field on fluids with permanent electric dipole moments like
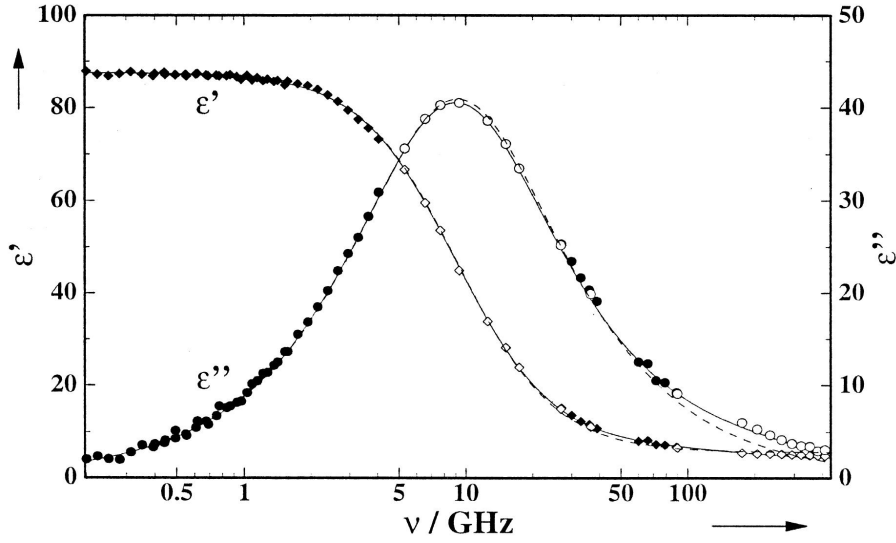
Figure 2.1: Dielectric permittivity of water, real part and imaginary part at a temperature of 0.2 °C, (*as presented in: Buchner et al. [1999]*).

water, these dipole moments will feel a torque, therefore the polarization requires some time to reach an equilibrium state. Their dielectric response can be described by a model labeled after Debye (e.g., *Sihvola* [1999]):

$$\varepsilon\left(\omega\right) = \varepsilon_\infty + \frac{\varepsilon_{st} - \varepsilon_\infty}{1 + i\omega\tau} \quad , \tag{2.16}$$

where ε_{st} and ε_∞ are the static and high frequency limit of the dielectric permittivity in the medium and τ describes the relaxation time. Separating 2.16, its real part will display the relaxation behavior, varying from ε_{st} to ε_∞, while the imaginary part will show Lorentzian shape with its maximum (indicating the highest losses) at the relaxation frequency $\omega = \frac{1}{\tau}$. An impression of the frequency dependency of the dielectric permittivities for water can be received from Figure 2.1, which is modified from the work of *Buchner et al.* [1999]. As can be seen in Figure 2.1, for temperatures around 0°C, the relaxation frequency for water lies around 10 GHz. Furthermore, for frequencies below 1 GHz, losses connected to ε'' remain negligible, while the real part of the dielectric permittivity stays approximately constant. This is why a real and constant dielectric permittivity is usually a reasonable assumption in this frequency range.

However, the real part of the permittivity of water is still a function of temperature. At frequencies below the relaxation frequency, this can for example be taken into account

following *Weast et al.* [1986]:

$$
\begin{aligned}
\varepsilon_{\mathrm{w}}(T) = 78.54 \cdot \big[&1 - 4.579 \cdot 10^{-3} \, (T - 25) \\
&+ 1.19 \cdot 10^{-5} \, (T - 25)^2 - 2.8 \cdot 10^{-8} \, (T - 25)^3 \big] \quad .
\end{aligned}
\tag{2.17}
$$

Calculating the permittivity of water from this equation, the values which can be expected in the field range between $\varepsilon_{\mathrm{w}} = 88.15$ for T = 0 °C and $\varepsilon_{\mathrm{w}} = 73.35$ for T = 40 °C.

2.3.2 Dielectric permittivity of soils

The relative dielectric permittivity of geologic media is usually fairly small (some 5 - 10), whereas water in soils has a permittivity of around 80 - depending on a variety of factors, like temperature or ion concentration. Therefore, the dielectric response of soils is largely determined by the contrast in dielectric permittivity of the solid matrix and the entrenched water, which in connection with relationship 2.15 forms the foundation for successfully measuring soil moisture content with a range of electromagnetic methods.

Extensive data sets on dielectric permittivities of geologic materials and other petrophysical relationships can be found in the literature (e.g., *Davis and Annan* [1989], *Reynolds* [1997], *Sharma* [1997] or *Knight* [2001]). As an overview, an excerpt of some values is provided in Table 2.1.

2.3.3 Petrophysical relationships between water content and dielectric permittivity

Except for water and air, the permittivities reported in Table 2.1 are bulk values, i.e. representing a mixture of different materials. Hence, these numbers constitute only guiding figures as there is a variety of different factors impacting these bulk values. The influence of

Table 2.1: (Bulk) Dielectric permittivities of selected materials

material	ε_r [-]
air	1
water (at 25°C)	78.54
pure ice	3.2
sand (dry)	3 - 6
silt (dry)	5 - 10
clay soil (dry)	2 - 6
granite	5 - 7
limestone	7 - 9

factors like porosity, exact mineral composition or specific layering (anisotropy effects) lead to the comparatively large range of values given in Table 2.1. Hence, the challenge is to find a correct representation for the petrophysical relationship between dielectric permittivities and corresponding water content in soils. Several empirical and semi-empirical models have been described in the literature; for example the relationships developed by *Topp and Davis* [1980] have found widespread use. For a recent comparison of the performance of different petrophysical relationships, refer to *Steelman and Endres* [2011].

Here, a semi-empirical dielectric mixing model is employed for relating dielectric permittivities to soil moisture content, as has been applied, e.g., by *Roth et al.* [1990]. In these models, the bulk permittivity ε_b of a multi-phase system is calculated from the dielectric permittivity of each constituent phase ε_i, weighted by its respective volume fraction θ_i:

$$\varepsilon_b^\alpha = \sum_{i=1}^{n} \theta_i \varepsilon_i^\alpha, \tag{2.18}$$

with α representing a factor which accounts for the orientation of the electric field with respect to the geometry of the medium.
Assuming a typical soil system consisting of the three phases soil, water and air, the volumetric fraction of soil water θ can be expressed as follows:

$$\theta = \frac{\varepsilon_b^\alpha - (1-\phi)\,\varepsilon_s^\alpha - \phi \varepsilon_a^\alpha}{\varepsilon_w^\alpha - \varepsilon_a^\alpha} \quad, \tag{2.19}$$

where ε_s, ε_a and ε_w are the relative dielectric permittivities of the soil matrix, the air phase and free water, respectively, and ϕ denotes soil porosity.
In theory, α can range between -1 and 1, depending on perpendicular or parallel orientation of the electrical field with respect to a layered medium. Assuming isotropic media allows to set $\alpha = 0.5$. Furthermore, when substituting $\varepsilon_a = 1$, 2.19 reduces to the Complex Refractive Index Model (CRIM, e.g., *Birchak et al.* [1974]):

$$\theta = \frac{1}{\sqrt{\varepsilon_w} - 1} \sqrt{\varepsilon_b} - \frac{(1-\phi)\sqrt{\varepsilon_s} + \phi}{\sqrt{\varepsilon_w} - 1} \quad, \tag{2.20}$$

forming a linear relationship as a function of $\sqrt{\varepsilon_b}$. Equation 2.20 will be used throughout this work to calculate volumetric water contents from measured bulk permittivity values ε_b. As can be seen, applying this equation needs auxiliary information on the soil matrix permittivity ε_s, the soil porosity ϕ and the soil temperature T (for calculating the permittivity of the water phase). As will be discussed in Section 5.7, we will in general assume $\varepsilon_s = 5$ for the relative dielectric permittivity of the soil matrix based on available literature values. The soil porosity will be estimated from gravimetric sampling. For completeness, we note that frozen conditions can be incorporated by adding the ice-content as a fourth phase into the formulation in Equation 2.18 (e.g., *Klenk* [2009]).

2.4 A Brisk Introduction to Soil Physics

In this section, several fundamental concepts of soil physics are introduced which will be the foundation for explaining some of the hydraulic processes observed in this thesis, mainly in chapter 7. The aim of this section is not to present a comprehensive theory of soil physics as such, but to briefly outline a macroscopic description of the movement of water in soils based on few effective hydraulic parameters. All considerations largely follow the much more in-depth treatment which can be found in *Roth* [2012].

2.4.1 Porous media

Soil physics aims at describing the movement of water and solutes in the soil. A soil in this context can usually be characterized as a porous medium. Following *Roth* [2012], such a description of a soil as a porous medium assumes (i) a division of the total volume into soil matrix and pore space which is filled by one or more fluids, (ii) the existence of a characteristic length scale l, down to which each volume element consists of both soil matrix and pore space and (iii) the interconnectedness of the pore space for allowing the movement of water and solutes. The volume fraction of the pore space is denoted by the *porosity* ϕ.

2.4.2 Macroscopic state variables

A direct description of the properties of the porous medium is cumbersome and not conducive to the type of problems which will be addressed in the framework of this thesis. However, based on the existence of the characteristic length scale l, we can invoke the existence of a suitable averaging volume, a so-called Representative Elementary Volume (REV), containing all characteristic microscopic heterogeneities of the medium. Suitably averaging the microscopic quantities describing the properties at the pore scale over such a REV, the hydraulic state of the system can be described by two macroscopic state variables, the volumetric fluid content and the potential energy density of the respective phases. Neglecting the potential presence of solutes and assuming a constant temperature T, these state variables are determined by the height z and the pressure p_i in the respective phase i. In the context of this thesis we can restrict all following considerations to two phases, namely air and water. Then, the volumetric fluid contents for air and water, θ_a and θ_w can be defined by:

$$\theta_i = \frac{V_i}{V}, \tag{2.21}$$

with V_i the volume of the respective fluid phase, and V denoting the total volume. The potential energy densities Ψ_a and Ψ_w are defined as the energy which would be needed for moving a unit's volume of this phase from a suitable reference state $\{p_0, z_0\}$ to a certain

location within the porous medium characterized by $\{p_i, z\}$:

$$\Psi_i(x) = p_i - p_0 - \int\limits_{z_0}^{z} \rho_i(z')dz'. \tag{2.22}$$

A suitable $z = z_0$ can for instance represent the position of the water table or the deepest point in the considered profile; p_0 will in our case be assumed to be atmospheric pressure.

2.4.3 Hydraulic dynamics in the vadose zone

The vadose zone is commonly viewed as the unsaturated part of the soil profile above a ground water table. Assuming an arbitrarily mobile airphase, the movement of water can be described by a partial differential equation, the Richards equation, which will be derived in this section based on the conservation of mass and an empirical flux law.
An arbitrarily mobile airphase is a reasonable assumption for profile parts far away from the groundwater table where the air phase can be assumed to be continuous and connected to the atmosphere. In this case, the movement of air will be approximately instantaneous as compared to the movement of water. Hence we can assume $p_a = p_0$ and restrict our considerations to describing the movement of the water phase. This region is usually denoted as the *degenerate multiphase regime*. With these assumptions and further assuming the incompressibility of water under these circumstances (i.e. $\rho_w = $ const), the corresponding *soil water potential Ψ_w* can be written, based on Equation 2.22, as:

$$\Psi_w = p_w - p_0 - \rho g(z - z_0) = p_w - p_a - \rho g(z - z_0) = \Psi_m - \Psi_g, \tag{2.23}$$

with the matric potential

$$\Psi_m = p_w - p_a, \tag{2.24}$$

and the gravitational potential

$$\Psi_g = \rho g(z - z_0). \tag{2.25}$$

From the definition 2.24 the matric potential will be negative for bound water (in the vadose zone) and positive for free water (e.g., in the ground water). At times it might be convenient to express the soil water potential in terms of height. Dividing Equation 2.23 by $\rho_w g$ yields the so-called *hydraulic head h_w*:

$$h_w = h_m - (z - z_0), \tag{2.26}$$

with the *matric head*

$$h_m = \frac{\Psi_m}{\rho_w g} \tag{2.27}$$

describing the negative height above z_0 for the corresponding potential. For $z_0 = 0$ at the position of the water table, and equilibrium conditions (i.e. $h_w = 0$), $h_m = -z$.

The **conservation of mass** for a fluid phase i is given by:

$$\partial_t \left[\theta_i \rho_i\right] + \nabla \cdot \left[\rho_i \vec{j_i}\right] = 0, \tag{2.28}$$

with the macroscopic volume flux $\vec{j_i}$. Assuming again water to be incompressible (i.e. $\rho_w = \mathrm{const}$), the conservation of water can be expressed accordingly:

$$\partial_t \theta_w + \nabla \cdot \vec{j_w} = 0, \tag{2.29}$$

with the water flux $\vec{j_w}$, as long as there is no explicit extraction of water from the considered volume (for example by pumping).
In porous media, a macroscopic volume flux can be described by an empirical macroscopic flux law, Darcy's law:

$$\vec{j_i} = -K_i \nabla \Psi_i, \tag{2.30}$$

stating that a slow, stationary flux of a Newtonian fluid i will be proportional to the forcing by a potential gradient and directed in the negative direction of this gradient. For describing fluid movement in unsaturated porous media, this is supplemented by the Buckingham conjecture assuming that in this case the factor of proportionality K_i will depend on the respective fluid content θ_i. This yields the **Buckingham-Darcy law**, which reads expressed for water flux:

$$\vec{j_w} = -K_w \left(\theta_w\right) \nabla \Psi_w, \tag{2.31}$$

with the *hydraulic conductivity $K_w \left(\theta_w\right)$*. Hence, while the water movement in the ground water can be described by an approximately constant value, the hydraulic conductivity in the unsaturated zone $K_w \left(\theta_w\right)$ will be a strong function of water content.

Now, inserting Equation 2.31 into Equation 2.29 and using the relationship 2.23, this yields the **Richards equation**:

$$\partial_t \theta_w \left(\Psi_m\right) - \nabla \cdot \left[K_w \left(\theta_w \left(\Psi_m\right)\right) \left[\nabla \Psi_m - \rho g\right]\right] = 0, \tag{2.32}$$

which has first been formulated by *Richards* [1931]. We have to reiterate that this equation has just been derived under the explicit assumptions of a degenerate multiphase regime, i.e. it is strictly only applicable for parts of the soil profile with sufficiently small water contents. This has to be kept in mind, especially for comparing numerical simulations and the results of measurements under conditions close to saturation.
Equation 2.32 also acknowledges the strong dependency of the water content θ_w on the

matric potential Ψ_m. Hence, for solving this highly non-linear equation, it needs to be supplemented by constitutive relationships for the *soil water characteristic* $\theta_w(\Psi_m)$ and the *hydraulic conductivity function* $K(\Psi_m)$. These relationships are commonly supplied by different parameterization models which describe these relations for a given soil with a set of effective parameters. As will be shown in the following section, these parameters can in turn be associated with certain hydraulic properties of the studied system.

2.4.4 Parameterizations

The two most widely acknowledged models for these two constitutive relationships have been provided by Mualem-van Genuchten and Mualem-Brooks-Corey. Dropping the explicit subscript w, both models are most conveniently formulated in terms of the hydraulic head h_m and the water saturation Θ:

$$\Theta := \frac{\theta - \theta_r}{\theta_s - \theta_r}, \tag{2.33}$$

with saturated and residual water contents θ_s and θ_r, respectively. The saturated water content is in general not equal to the porosity ϕ of the medium, since depending in the specific conditions even at saturation the medium can retain some entrapped air. The residual water content describes the amount of water which cannot be simply removed from the medium by hydraulic processes, for example by applying a pressure gradient.

Soil water characteristic function

An apt formulation for the soil water characteristic function can be based on considering the porous medium as a bundle of equivalent capillaries. Assuming approximately cylindrical or spherical pores of radius r, the matric head can be related to the capillary pressure as given by the Young-Laplace law:

$$h_m = \frac{p_w - p_a}{\rho_w g} = \frac{-2\sigma_w}{r \rho_w g}, \tag{2.34}$$

with the interfacial energy density of water $\sigma_w = 0.0725 \ \mathrm{N/m^2}$.
Essentially this means that the size of the respective pores determines the strength with which the water is bound in the soil. Conversely, there is a certain maximum pore size for a given matric head in which the water can still be held by capillary forces. When applying a larger pressure gradient, pores of this size will be drained. Hence, in a stationary profile, we will expect a certain region above the water table which will be held at saturation due to capillary forces. The extent of this **Capillary Fringe** is determined by the largest pores in the medium, which can sustain the smallest capillary rise.
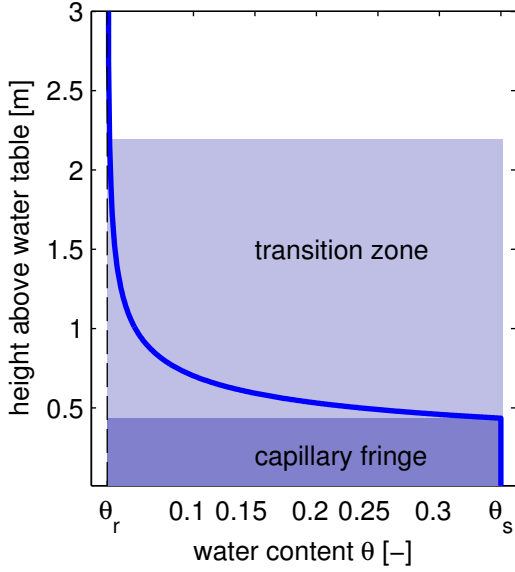
Figure 2.2: Soil water profile above a water table in a homogeneous sand in hydrostatic equilibrium

Hence, the finer the material, the larger the expected height of the capillary fringe. Above the capillary fringe we can expect a gradual decrease of saturation towards the residual water content θ_r. In equilibrium, the shape of this transition zone will depend mainly on the variety of different pore sizes, i.e. the specific pore size distribution. The wider the pore size distribution, the more gradual the transition. For a very narrow pore size distribution all pores will drain for a very narrow range of pressure gradients, leading to a correspondingly rather small transition zone. Based on these considerations, one might envision the soil water characteristic in a form as has been drawn in Figure 2.2. In this diagram, h_m has been directly associated with heights above the water table since $h_m = -z$ for equilibrium conditions as stated above.

There is a multitude of parameterizing models which have been described in the literature. The three most commonly applied models are the Brooks-Corey parameterization (*Brooks* [1966]), the van Genuchten parameterization and a simplified version of the latter (*Van Genuchten* [1980]). Figure 2.2 has in fact been calculated based on the Brooks-Corey parameterization, which is given by:

$$\Theta\left(h_m\right) = \begin{cases} \left[-\frac{h_m}{h_0}\right]^{-\lambda}; & -h_m > h_0 \\ 1; & -h_m < h_0 \end{cases} \tag{2.35}$$

with the *air entry value* $h_0 > 0$ and the shape parameter λ. The more intuitive approach is to consider its inverse function, which is defined for $\Theta < 1$ as:

$$h_m\left(\Theta\right) = -h_0 \Theta^{-\frac{1}{\lambda}}. \tag{2.36}$$

In connection with Equation 2.34, this formulation highlights the association of the air entry value h_0 with the largest available pores as discussed above, and the connection of the parameter λ to the shape of the transition zone above the capillary fringe (and in turn to the specifics of the pore size distribution). In general, h_0 can be viewed as a scaling factor since it has an influence on the shape of the transition zone, as has, e.g., been discussed in *Dagenbach* [2012].

For completeness, the general van Genuchten parameterization is given by:

$$\Theta\left(h_m\right) = \left[1 + \left[-\alpha h_m\right]^n\right]^{-m},\tag{2.37}$$

with shape parameters $\alpha > 0$, $n > 1$ and $m > 0$. The corresponding inverse function can be expressed as:

$$h_m\left(\Theta\right) = -\frac{1}{\alpha}\left[\Theta^{-\frac{1}{m}} - 1\right]^{\frac{1}{n}}.\tag{2.38}$$

Setting $m = 1 - 1/n$ leads to the special case of the simplified van Genuchten parameterization with

$$\Theta\left(h_m\right) = \left[1 + \left[-\alpha h_m\right]^n\right]^{-1+1/n}\tag{2.39}$$

and its inverse formulation

$$h_m\left(\Theta\right) = -\frac{1}{\alpha}\left[\Theta^{\frac{n}{1-n}} - 1\right]^{1/n},\tag{2.40}$$

which has found the most widespread use in literature. The correct choice of a suitable parameterization may depend on the specific application. For example, the van Genuchten formulations have certain advantages for numerical simulations due to their differentiability. However, as has for example been shown by *Dagenbach et al.* [2012], the simplified van Genuchten parameterization is not necessarily suitable for describing the capillary fringe response in a sandy material to a Ground-Penetrating Radar signal. In this case either a Brooks-Corey type model or an equivalently formulated full van Genuchten parameterization has to be used. For more discussion on the different advantages and drawbacks of the different formulations, refer to *Dagenbach* [2012] or *Roth* [2012].

Hydraulic conductivity function

Similarly, the hydraulic conductivity function $K\left(\theta\right)$ will depend strongly on the pore geometry. This can be expressed by the model of *Mualem* [1976], which introduces a few additional parameters:

$$K\left(\Theta\right) = K_s\Theta^\tau\left[\frac{\int_0^\Theta h_m\left(\vartheta\right)^{-1}d\vartheta}{\int_0^1 h_m\left(\vartheta\right)^{-1}d\vartheta}\right]^2.\tag{2.41}$$

Here, K_s is the hydraulic conductivity at saturation, while the term Θ^τ is a measure for the tortuosity of the porous medium. In general, τ is simply treated as an additional fit parameter. Under most conditions a value of $\tau = 0.5$ is usually employed.

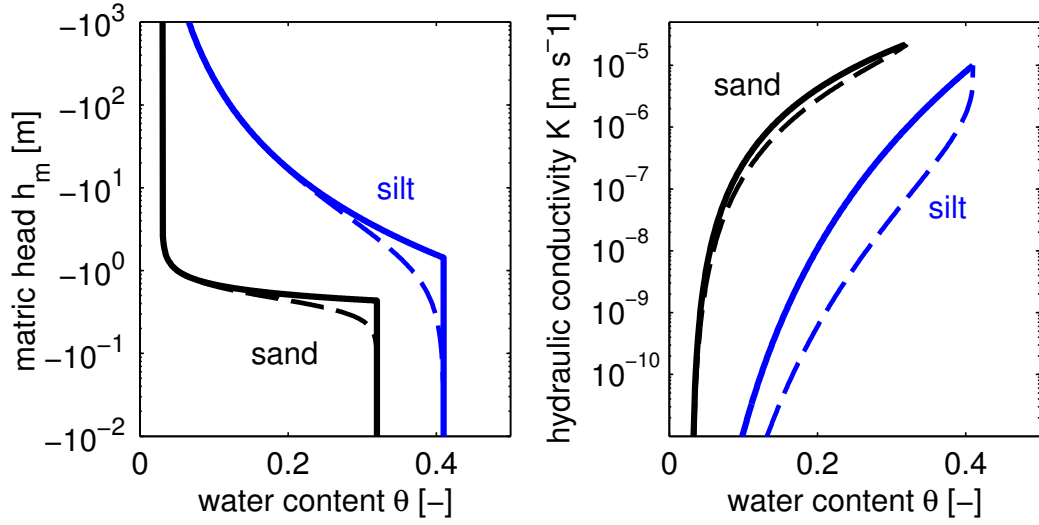Inserting Equation 2.35 into Equation 2.41 yields the Mualem-Brooks-Corey model for

Figure 2.3: Soil water characteristic function $h(\theta)$ (left) and corresponding hydraulic conductivity function $K(\theta)$ (right) plotted for a homogeneous sand and a homogeneous silt. The solid lines have been calculated using the Mualem-Brooks-Corey parametrization, the dashed lines are based on the equivalent simplified Mualem-van Genuchten formulation. The parameters have been taken from *Roth* [2012]. Note the logarithmic scales on the vertical axes.

the hydraulic conductivity function:

$$K\left(\Theta\right) = K_0\Theta^{\tau+2+2/\lambda}. \tag{2.42}$$

Similarly, by inserting Equation 2.40 into Equation 2.41 the corresponding Mualem-van Genuchten model is obtained:

$$K\left(\Theta\right) = K_s\Theta^{\tau}\left[1 - \left[1 - \Theta^{\frac{n}{n-1}}\right]^{1-1/n}\right]^2. \tag{2.43}$$

In fact, the availability of the last analytical expression for $K\left(\Theta\right)$ has been the main reason for the formulation of the simplified van Genuchten parameterization. For the full van Genuchten parameterization (Equation 2.41), the corresponding conductivity relationship can in general only be determined numerically.

Concluding remarks

In summary, these considerations leave us with a set of either six Mualem-Brooks-Corey parameters $\{\theta_s, \theta_r, h_0, \lambda, K_s, \tau\}$ or seven Mualem-van Genuchten parameters $\{\theta_s, \theta_r, \alpha, n, m, K_s, \tau\}$ which also get reduced to six for the simplified formulation. These parameters describe the physical properties of the considered medium and allow the description of soil water

dynamics in the framework of the Richards equation as formulated above.

An overview of both relationships calculated for two different kinds of materials can be found in Figure 2.3. The two most important results for our purposes which can be seen in these diagrams are (i) in a fine-grained silty material, the transition zone can be expected to be much wider than in a comparatively coarse grained sand, and (ii) the corresponding hydraulic conductivity functions may vary over several orders of magnitude with water content, most prominently for low water contents.

3 Materials and Methods

This chapter introduces the measurement methods (Section 3.2), evaluation procedures (Sections 3.3, 3.4 and 3.6) and employed instrument setups (Section 3.5). Of particular interest for this thesis is a brief discussion of Ground-Penetrating Radar methods to (i) measure near-surface soil water contents by evaluating the *direct ground wave signal* (Section 3.3.1), (ii) to evaluate *waveguiding phenomena* (Section 3.4.1) and (iii) to study the GPR response of the *capillary fringe* above a water table (Section 3.4.2). At the end of this chapter, methods employed for ground truth assessment of the GPR derived data are discussed in Section 3.7.

3.1 Ground-Penetrating Radar

As has been mentioned in the introduction to this work, due to its versatile applicability, there is already a rich body of literature concerned with the use of Ground-Penetrating Radar for hydrogeophysical and hydrogeological characterizations. A central aim of most of these studies is the non-invasive retrieval of information about hydrogeologcial subsurface structures and in some cases the variation of dielectric properties associated with dynamic processes.

In general, three main types of measurement principles can be discerned: Borehole GPR (e.g., *Binley et al.* [2002], *Winship et al.* [2006]), off-ground GPR (both ground-based, e.g., *Lambot et al.* [2006], or by employing helicopters, e.g., *Blindow et al.* [2011]) and surface-coupled GPR, which is the focus of this thesis. In the framework of this work, the term "subsurface" comprises no more than the top 2 m below the ground surface.

3.2 Experimental Measurement Setups

There are several standard setups for acquiring surface-coupled GPR data in the field, which will be briefly introduced in this section.

3.2.1 Common offset measurement

In a common offset (CO) measurement, the transmitting antenna T and the receiving antenna R are coupled at a fixed antenna separation a. GPR data are then acquired at this single "common" offset at several locations of the measurement site under investigation. Most commonly, this results in dragging the GPR system in this common offset setup
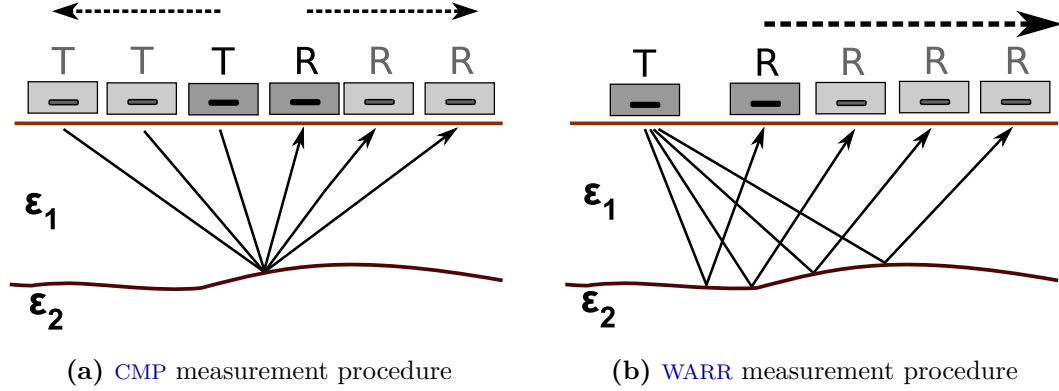
(a) CMP measurement procedure   **(b)** WARR measurement procedure

Figure 3.1: Standard multi-offset measurement setups: The left shows the measurement procedure for a Common Midpoint (CMP) measurement, where both transmitter (T) and receiver (R) are sequentially moved. In comparison, the right diagram illustrates the procedure for a Wide-Angle-Refraction-and-Reflection (WARR) measurement, keeping the transmitter at a fixed position.

along a measurement line while acquiring multiple GPR traces at some fixed spacing dx. This is a fast and efficient method of mapping subsurface characteristics over a larger extent of some $10 \ldots 1000$ m. However, since data is acquired at only one common antenna separation, quantitative evaluation is only possible if the quantity of interest (e.g., the travel time of a certain part of the signal) is determined by only one variable. For example, in order to evaluate the travel time of a signal reflected by a planar subsurface reflector, auxiliary information will already be needed, since it is determined by both the reflector depth d and the bulk permittivity of the soil ε_b (cf. Equation 3.4). This can either be an independent estimation of the soil water content (for example through additional TDR measurements) or the determination of the reflector depth, for instance by a series of borehole measurements.

3.2.2 Multi-offset measurements: CMP and WARR

A non-invasive way to gather more information for quantitative evaluation is to employ multiple offsets for acquiring GPR data. Two standard setups for this type of measurement are the so-called Common-Midpoint (CMP) and Wide-Angle-Refraction-and-Reflection (WARR) measurements; both setups are sketched in Figures 3.1a and 3.1b. In the first case, both the transmitter and the receiver are gradually moved apart while acquiring data at accordingly increasing antenna separations which have the same midpoint - or in terms of a reflector of interest, the same common shotpoint. However, from a practical point of view, this is most often a tedious endeavor. Also, much care has to be taken for consistently repositioning antennas multiple times by some 2-3 cm in the field. More

conveniently, one can keep one of the antenna at a fixed location and move just the second antenna, again acquiring data at gradually increasing antenna separations. In practice this normally allows for acquiring data at a higher spatial resolution, since antennas do not have to be manually triggered at fixed locations. However, if the target of investigation is a reflector, this means that the shot point moves according to the antenna separation. Also, the sampling volumes will not be identical. Hence, with respect to the evaluation of reflected signals, both approaches are only fully equivalent for homogeneous layers over a planar reflecting interface. Essentially, the operator has to determine in the field if a WARR measurement suffices. If the signal of interest is a direct wave this should generally be the case. The largest drawback of both approaches is that they yield information which might be evaluable on a quantitative basis, but which essentially represents only one point in space. Large scale mapping of subsurface characteristics is practically not possible with either of the two approaches.

3.2.3 Multi-common offset measurement

Trying to combine both the advantages of the CO and CMP setups, one can also connect multiple antennas to a multi-common offset setup. In this case on can acquire multi-offset data while moving the resulting antenna train continuously along a measurement profile of interest. The standard setup which will be used in the framework of this thesis consists of a set of two transmitters and receivers, as will be discussed in Section 3.5.

When evaluating the subsurface properties above a continuous reflection, both reflector depth and permittivity can then be simultaneously retrieved by an optimization approach (see *Gerhards et al.* [2008] and Section 3.3.2 for more details). Depending on the amount of offsets available for evaluation, further information can be retrieved as well, e.g., a possible dipping angle of the reflector under investigation. This setup has for instance been successfully employed for mapping the permafrost tables both on the Tibetan Plateau (*Wollschläger et al.* [2010]) and in the Arctic (*Westermann et al.* [2010]). The optimization of such a multi-common offset measurement setup has been recently studied for a system with five different antenna separations by *Pan et al.* [2012].

Having information at more than one antenna separation can also be beneficial for evaluating direct signals, since this should allow for checking the consistency between data acquired at different antenna separations. For the direct ground wave signal, *Klenk et al.* [2011] have shown that there is indeed a considerable offset to be observed for data acquired at two different antenna separations when employing traditional evaluation schemes. Essentially, the implications of the antenna setup have to be taken into account for the ground wave signal. This fact will be discussed in more detail within the framework of this thesis.

3.3 Ray-based Evaluation Methods

One standard method for evaluating GPR data is based on an asymptotic raypath approach. In analogy to ray-based optics, the signal is assumed to consist essentially of a superposition of plane waves. The properties of the medium get reflected in the interaction of the resulting wavelets traveling along different assumed raypaths from the transmitter to the receiver. Most commonly, the travel time of these different wavelets is used for calculating the properties of the medium in between. A sketch of the different wavefronts propagating around a dipole source placed on the air-soil interface can be found in Figure 3.2a. Depending on the specific subsurface conditions, wave propagation can be commonly envisioned to occur along different raypaths as illustrated in Figure 3.2b. For a two layered soil, these different electromagnetic waves are commonly denoted as (numbers refer to respective propagation paths in Figure 3.2b, letters to Figure 3.2a):

Direct air wave (1)/(A) – A spherical interface wave, traveling directly from transmitter to receiver above the air-ground interface.

Direct ground wave (2)/(B) – A spherical interface wave, traveling from transmitting to receiving antenna, but below the air-ground interface, thus sampling the uppermost layer of the soil. The receiver measures the inhomogeneous continuation of this wave into the air (part D in Figure 3.2b).

Reflected wave (3) – At the boundary between the two soil layers, the contrast in dielectric permittivity gives rise to a reflected (plane) wave.

Critically refracted wave at air-ground interface (4) – Since always $\varepsilon_{air} < \varepsilon_1$, a reflected wave incident onto the ground-air interface at an angle greater than the critical angle of total reflection will propagate along the interface to the receiver. This is commonly denoted as the critically refracted wave.

Refracted wave at lower layer boundary (5) – Provided that $\varepsilon_1 > \varepsilon_2$, total reflection can also occur on the lower boundary.

Multiples – Also for $\varepsilon_1 > \varepsilon_2$, multiple reflections can under certain circumstances lead to waveguiding phenomena (see Section 3.4.1).

In the following sections the nature of the ground wave signal and pertinent evaluation procedures for reflections will be discussed in more detail.

3.3.1 The direct ground wave

Signal parts which travel directly from the transmitting to the receiving antenna are denoted as direct waves. In terms of Figure 3.2b, this includes both the direct air and direct ground wave. The latter is one main research objective for this work. Hence, this section will briefly discuss its nature, give an overview of previous work and introduce the basic evaluation procedures.
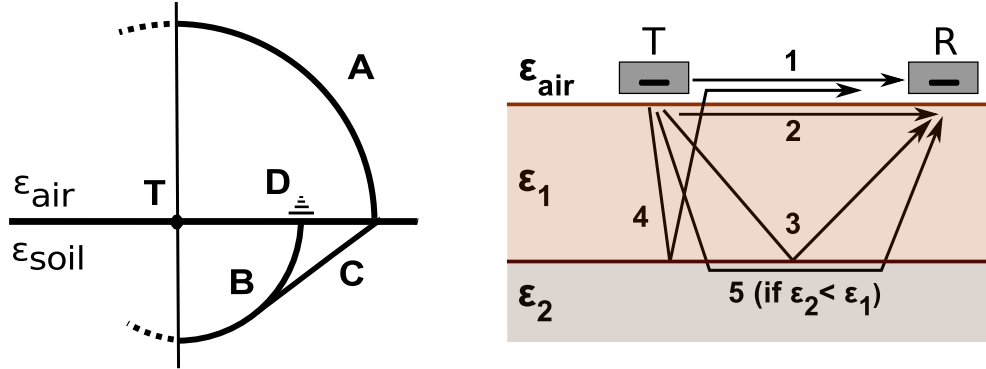
(a) Wave propagation around a dipole source (T) located at the air-soil interface

(b) Assumed propagation paths of electromagnetic waves in a two-layered soil

Figure 3.2: The left figure shows wave fronts propagating around a dipole source (T) located at the air-soil interface: A and B represent spherical wavefronts propagating in the air and the soil; C denotes the lateral or head wave in the soil, D the inhomogeneous continuation of the ground wave in the air (modified from *Huisman et al.* [2003b], after *Annan* [1973]).
The right figure displays typical ray propagation paths of electromagnetic waves in a two-layered soil: 1 and 2 denote the direct air and ground waves, 3 the layer boundary reflection, 4 the critically refracted wave and 5 a refracted wave occurring at the layer boundary due to the assumed permittivity contrast. (modified from *Huisman et al.* [2003b], after *Sperl* [1999])

Current understanding

The part of the GPR signal traveling in the uppermost soil layer directly from the sending to the receiving antenna has commonly been denoted as direct ground wave (e.g., *Grote et al.* [2003], *Huisman et al.* [2003b]). Due to continuity constraints of the wave equations, the front of the ground wave (denoted as "B" in Figure 3.2a) will have an exponentially decreasing, inhomogeneous continuation above the interface ("D" in Figure 3.2a), which will be registered at the receiving antenna as the ground wave signal. Due to interface effects, the corresponding wavelet has a fundamentally different shape as compared, e.g., to reflected signal parts. *Dai and Young* [1997] have shown by analytical modeling of dipole sources placed at the air-soil interface that the wavelets of the direct air and ground wave can be assumed to have the same shape as the applied current, while reflections exhibit the shape of its first derivative. This is an effect which will become important for the considerations about time zero calibration in Section 5.2.2.

Standard ray-based evaluation methods

Traditional evaluation of the direct ground wave signal is usually concerned with defining the ground wave velocity from the slope of the signal in multi-offset (e.g., CMP or WARR) radargrams. Here, a distinct feature of the wavelet, e.g., the first arrival or a central extremum is selected and its travel time determined for different antenna separations. Provided this is possible, we can calculate the ground wave velocity from the slope in such a multi-offset radargram, e.g. as:

$$v = \frac{c_0}{\sqrt{\varepsilon_b}} = \frac{a_{\max} - a_{\min}}{t_{\max} - t_{\min}}, \tag{3.1}$$

with c_0 denoting the free space velocity of light, $a_{\max}$ and $a_{\min}$ the minimum and maximal antenna separations and $t_{\max}$ and $t_{\min}$ the respective measured travel times. Having multiple offsets, the whole procedure can be done by linear regression, which then also can be used for calculating a possible time-zero offset through extrapolation towards a zero antenna offset. Given good identifiability of the ground wave signal at a certain antenna separation, the ground wave velocity can also be directly calculated from a CO dataset acquired at this antenna separation. In such a case, the measured ground wave travel time is given by:

$$t_{\mathrm{gw}} = \frac{a}{v_{\mathrm{gw}}} = \frac{a \cdot \sqrt{\varepsilon_b}}{c_0}. \tag{3.2}$$

Rearranging this equation yields a possibility to determine the bulk dielectric permittivity ε_{b} of the soil between the two antennas as:

$$\varepsilon_b = \left(\frac{c_0 \cdot t}{a} \right)^2. \tag{3.3}$$

These bulk permittivity values can then be converted to water content using a petrophysical relationship as described in Section 5.7. Hence, evaluating the direct ground wave signal in a common offset measurement can yield a fast estimate of soil water content for the near surface at extents up to a few kilometers. However, we have to note that travel times can only be determined with an a-priori unknown time-zero offset when using current GPR systems. This warrants for a time-zero calibration procedure, which will be one of the main subjects to be dealt with in Chapter 5. Several examples of field applications for this measurement method will then be discussed in ensuing Chapters 6 and 8.

3.3.2 Evaluation of reflections

For a reflected signal, the recorded travel time is no longer only a function of the antenna separation and the dielectric permittivity of the soil as in Equation 3.2, but depends on the reflector depth d as well:

$$t_{\mathrm{refl}} = \frac{\sqrt{a^2 + 4d^2}}{c_0} \cdot \sqrt{\varepsilon_b}, \tag{3.4}$$

hence the simple evaluation as described for the direct ground wave signal above is not possible without acquiring additional information. This may for instance include information about the location of the reflecting interface through borehole logging or making assumptions about the water content distribution. For point measurements, the multi-offset nature or CMP or WARR measurement provide sufficient information.
Non-invasive alternatives for covering larger areas are for example employing a multi-common offset setup as described in Section 3.2.3, simultaneously measuring the travel times at several fixed antenna separations while moving along the profile under investigation. In this case the multichannel evaluation procedure developed by *Gerhards et al.* [2008] can be applied, employing a theoretical forward model for calculating travel times $t_{\mathrm{mod}}(x_i, a_k; d, \varepsilon, \alpha)$ from reflector depth d, permittivity ε and dipping angle α as a function of the different antenna separations a_k for every location x_i along a GPR profile. Then, the true parameters are retrieved through inverting the squared differences between these theoretical travel times and the actual field data:

$$\sum_i \sum_k \left[t_{\mathrm{meas}}(x_i, a_k) - t_{\mathrm{mod}}(x_i, a_k; d, \varepsilon, \alpha) \right]^2 \stackrel{!}{=} \min \tag{3.5}$$

Recently, a different approach has been introduced by *Buchner et al.* [2012]. His constructive inversion approach, applied to GPR, aims for the retrieval of subsurface information by representing the latter with a parameterized model in combination with an explicit simulation of the measurement process.

3.4 Other Evaluation Methods Pertinent to This Work

3.4.1 Basic principles of waveguide inversion

There are conditions where the simple picture of wavefronts propagating with a common group velocity cannot correctly describe the observed phenomena. This is for example the case in settings dominated by layering (e.g., soil or ice layers) with a thickness which is on the same order as the dominant wavelength of the GPR signal. In such settings, the recorded signal may be dominated by waveguiding phenomena. As has been shown in recent years (e.g., *van der Kruk* [2006], *van der Kruk et al.* [2007], *Strobbia and Cassiani* [2007] or *van der Kruk et al.* [2010]), the properties of such a dispersed signal (as observed in multi-offset GPR data) can be used to invert for the dielectric permittivity $\varepsilon_{\mathrm{wg}}$ and the thickness d_{wg} of the waveguiding layer(s). The reason is that the phase velocity spectrum of a signal propagating in such a waveguide is essentially determined by both the waveguide's properties, most importantly the dielectric permittivity and its thickness. The governing

equation of modal propagation in such a waveguide has multiple solutions, indicative for multiple modes which in principle can be excited within the waveguide, depending on the bandwith of the employed antenna system. For each mode, the phase velocity spectrum will show a dispersion curve, as the phase velocity will vary with frequency. The exact shape of these dispersion curves is very sensitive to $\varepsilon_{\mathrm{wg}}$ and d_{wg}, hence a deterministic inversion algorithm can be implemented, calculating both parameters. Having more than one dispersion curve available for evaluation enhances the quality of the inversion result. Also, measuring both transverse-electric (TE) and transverse-magnetic (TM) modes and jointly inverting both signals improves the inversion result (*van der Kruk et al.* [2006]). Recently, the concept has been broadened to provide estimates of the uncertainty for the resulting parameters by *Bikowski et al.* [2012]. In the framework of this thesis, waveguide inversion is used in Section 5.5 for a leaky waveguide dataset acquired on a frozen lake for discussing the applicability of a correction to the time base of our measurement system.

3.4.2 Detecting the capillary fringe

Significant permittivity changes in the subsurface do not only occur at layer boundaries. Another candidate for yielding a distinct reflection is the ground water table, where the transition from unsaturated to saturated conditions should be detectable by GPR. There has already been a substantial amount of work reporting on successfully detecting the ground water table with GPR (e.g.,*Roth et al.* [2004], *Doolittle et al.* [2006]). Especially for observing the response of aquifers to pumping tests, monitoring the drawdown in the vicinity of an observation well could yield crucial information for characterizing shallow aquifers. For example, *Endres et al.* [2000] reported having applied GPR during pumping tests for observing the water table dynamics around the pumping well. However, it has also been found that especially under these non-equilibrium conditions the characteristics of the capillary fringe and the associated transition zone seem to notably influence the GPR response. *Bevan et al.* [2003] studied pumping-induced dewatering using GPR and noted that the dynamics of the transition zone above the capillary fringe dynamics might even dominate the GPR response. In that study this lead to an underestimation of the extracted water volume from GPR data. In a smaller setup, *Bano* [2006] investigated the transition zone in a sand tank with GPR. This study found it even difficult to observe a capillary fringe reflection at times, depending on the hydraulic situation. Subsequently, *Gerhards* [2008] concluded from numerical simulations that the observed GPR response should be mainly determined by the shape of the transition zone above the capillary fringe. Hence, a changing shape of this transition zone as induced for example by a varying water table should be observable by GPR as well, if measurements can be conducted with sufficient precision. Since the shape of the capillary fringe is essentially determined by the respective soil material properties, corresponding hydraulic parameters could eventually be retrieved from the observed GPR response. These considerations have been studied numerically by *Dagenbach* [2012] and are the foundation of several high-precision experiments carried out in the framework of this thesis which will be discussed in chapter 7.

3.5 GPR Instrument Setup and Terminology

Unless specified otherwise, the setup used in this work consists of a four channel shielded GPR antenna system. The instruments used for the field experiments are part of the *RIS antenna family* manufactured by *Ingegneria dei Sistemi (IDS), Italy*. Data were acquired using the IDS DAD control unit. The antennas have a bow-tie shape optimized for emitting and receiving a broadband signal with a certain center frequency. Antennas employed for this work are specified at free space center frequencies of 200 or 400 MHz, respectively. Since the focus of this thesis is on studying near surface properties, the higher frequency was preferred for better near surface resolution.

 Each shielded RIS antenna box contains one transmitter (T) and one receiver (R), located close to the bottom of the box, embedded in a foamy material. A sketch of the interior of such an antenna box is provided in Figure 3.3a. Although the outer dimensions are approximately the same for both frequencies, internal antenna separations vary: The 200 MHz antennas have an internal antenna separation a_{int} of 0.19 m, whereas the 400 MHz antennas have an internal separation a_{int} of only 0.14 m. The location of the transmitting antenna feed point with respect to the antenna box has been checked by employing a magnetic field probe and has been found to be compliant with these manufacturer specifications.

In field experiments, the normal measurement setup consists of two of these antenna boxes (A1 and A2) coupled to a four channel setup. In this case (as depicted in Figure 3.3b) the available channels are as follows:

- Front antenna internal channel (T1R1) denoted as **INT1**,

- back antenna internal channel (T2R2), denoted as **INT2**,

- short crossbox channel (T1R2) denoted as **SCBC**, and

- long crossbox channel (T2R1) denoted as **LCBC**.

This setup has several implications for data evaluation. During a WARR measurement, there are two radargrams recorded which can be evaluated: One for each crossbox channel. For CO measurements, one has to distinguish between the different targets of a certain measurement. With respect to the direct ground wave signal, the internal channels are not suitable at all, since their antenna separation is too short to allow for detecting a separate direct ground wave. Hence, in that case each measurement yields again two separate datasets, one for each crossbox channel. With respect to the evaluation of reflection signals, all four channels can in principle be used, for example in the framework of a multichannel evaluation (see Section 3.3.2 above or *Gerhards et al.* [2008] for details). Therefore, with respect to evaluating reflection signals, this setup yields one dataset which can in principle be evaluated for reflector depth, averaged water content and a possible dipping angle of the reflector.
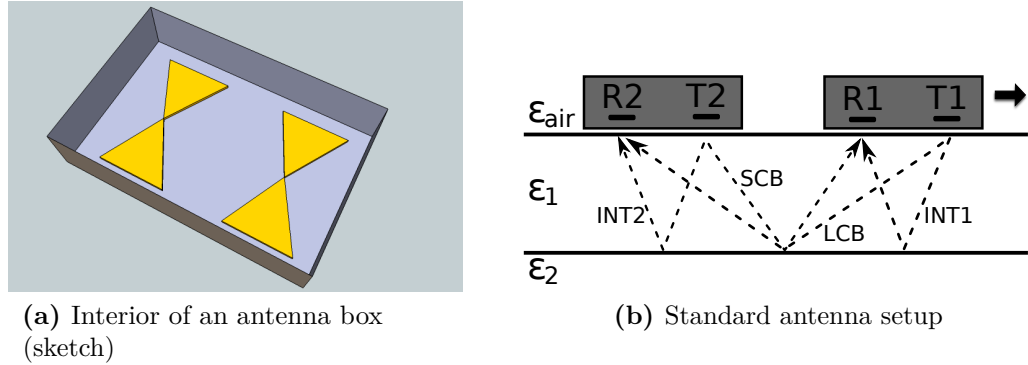
(a) Interior of an antenna box (sketch)

(b) Standard antenna setup

Figure 3.3: The left figure shows a sketch of the interior of one antenna box featuring two bow-tie-shaped antenna. The right pictures our normal antenna setup as a four channel system plotted for the case of mapping reflected signals of a plain reflector.

3.6 Data Processing and other Software Used

The GPR data presented in this work have been evaluated using several different algorithms. Evaluations of ground wave data (see Chapters 5, 6 and 8) and of the high-resolution imbibition and drainage experiments (see Chapter 7) are based on an own toolbox developed in the framework of this thesis using MATLAB (R2010b, The MathWorks, Natick, MA). For the multi-channel analysis discussed in Section 8.3, the "Processing GPR" (pg) package has been employed, which has been in development in our group for the last several years, with most contributions originating from the work of *Gerhards et al.* [2008]. For treating dispersed datasets, the inversion procedure has been adapted from the code described in *van der Kruk et al.* [2007] which was obtained from J.v.d. Kruk *by personal communication.*

In order to minimize the potential for misinterpretation or the introduction of artifacts into the resulting soil water content data, the application of filtering algorithms has been kept to an absolute minimum. Normally, the GPR data were only subjected to a dewow filter as a first processing step, removing low frequency contributions from the spectrum which would otherwise overlay the whole signal. No other filtering or data smoothing has been applied prior to evaluation, unless stated explicitly. For illustrative purposes, peak amplitudes in some radargrams which are shown in this thesis have been cut at a fixed value to emphasize minor features.

For supporting the interpretation of the observed GPR response, dedicated numerical simulations have been carried out, based on two FDTD algorithms: The GPRMax 2D numerical simulator (e.g., *Giannopoulos* [2005]) and MIT Electromagnetic Equation Propagation (MEEP, e.g., *Oskooi et al.* [2010]). Hydraulic simulations of soil water content dynamics were based on two algorithms solving the Richards equation: HYDRUS1D (*Simunek et al.* [2005]) and $\mu\phi$ (MuPhi, introduced by *Ippisch et al.* [2006]), the latter

code was obtained from O. Ippisch *by personal communication.*

3.7 Methods for Ground Truth Assessment

For ground truth assessment of the measured GPR data, soil water content measurements were executed by gravimetric soil sampling (Section 3.7.1) and Time Domain Reflectometry (Section 3.7.2). TDR data can also be employed for determining the electric conductivity (Section 3.7.3).

3.7.1 Gravimetric soil sampling

The conceptually most straight-forward method for determining soil water content is gravimetric sampling. A soil sample is extracted in the field, and the gravimetric water content θ_{grav} can be determined from the difference in weight Δm before and after drying:

$$\theta_{\mathrm{grav}} = \frac{m_{\mathrm{moist}} - m_{\mathrm{dry}}}{m_{\mathrm{dry}}}, \tag{3.6}$$

expressed on a dry weight basis. If the volume and the bulk density of the soil sample ρ_b is known, we can calculate the volumetric soil water content θ_{vol} from the ratio of water volume V_w to the total volume V_t:

$$\theta_{\mathrm{vol}} = \frac{V_w}{V_t} = \frac{\rho_b}{\rho_w} \cdot \theta_{\mathrm{grav}}, \tag{3.7}$$

with the density of water ρ_w. Usual procedure for the drying process is oven-drying the soil sample at 105 °C. Main disadvantages of gravimetric soil sampling is the involved field and laboratory work and its invasiveness. Still, gravimetric soil sampling remains the reference measurement, since moisture content is directly determined without involving the calibration of some indirect measurement quantity.

3.7.2 Time Domain Reflectometry (TDR)

Time Domain Reflectometry is an electromagnetic measurement method relying on the dielectric properties of the soil to determine point scale soil moisture contents. At the same time, it can also be used to determine bulk soil electrical conductivities.

Measuring water content with TDR

As in GPR, the dielectric permittivity of the studied soil is derived by measuring the velocity of a pulsed electromagnetic waveform. In a TDR measurement, the wave velocity in a given medium is determined by measuring its travel time when guided through the medium along metal rods. The signal is partly reflected when entering the medium and
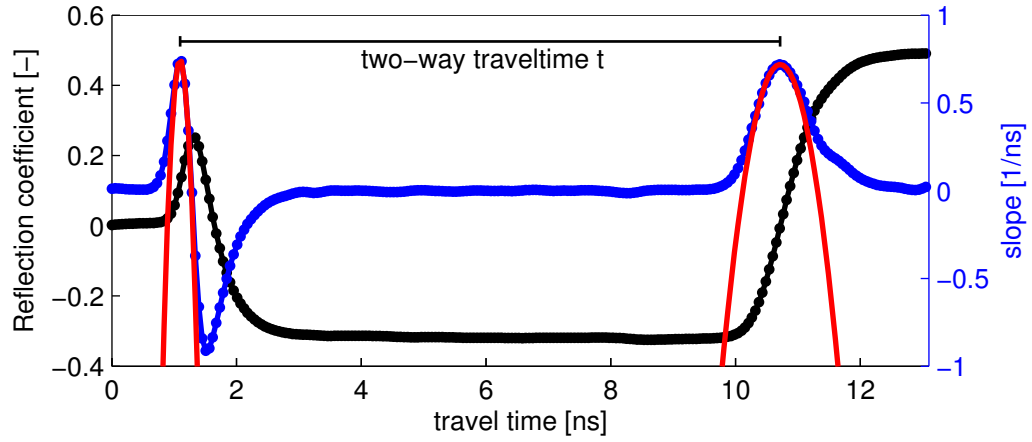
Figure 3.4: Example TDR trace (black) measured with 0.3 m rod length in pure water, its derivative (blue) and the fitted parabolas (red). The two-way travel time is derived from the maxima of the two parabolas.

again at the end of the metal rods, due to the differences in wave impedance. Therefore, its velocity can be calculated from the two-way travel time along metal rods of rodlength l:

$$v = \frac{2l}{t} \quad , \tag{3.8}$$

and in turn the corresponding dielectric permittivity as

$$\varepsilon_r = \frac{c_0 t}{2l} \quad , \tag{3.9}$$

by using Equation 2.15 with c_0 signifying the vacuum speed of light.

In the framework of this thesis, two different instruments have been employed for recording the response of the generated pulse, a Tektronix 1502B cable-tester and a Campell TDR100 Time-Domain Reflectometer. In both cases, the trace is digitally sampled at 255 points and the water content is subsequently automatically calculated. In the current analysis, the time derivative of the measured trace is taken, which results in two distinct peaks representing the signal from the probe head and the soil response. The travel time is then calculated from the maximum values of a second order polynomial fitted to these two peaks. An exemplary evaluation is shown in Figure 3.4.

Eventually, the permittivity is derived by assuming a linear relationship for the travel times between two calibration measurements in air and in water and the associated water content calculated from the CRIM-formula (2.20 in Section 2.3.3). The thus calculated water content constitutes an average over the measurement volume of the TDR probe, which is a function of the surrounding medium and probe geometry (number, length, diameter and distance of the metal rods). The measurement sensitivity has been found to
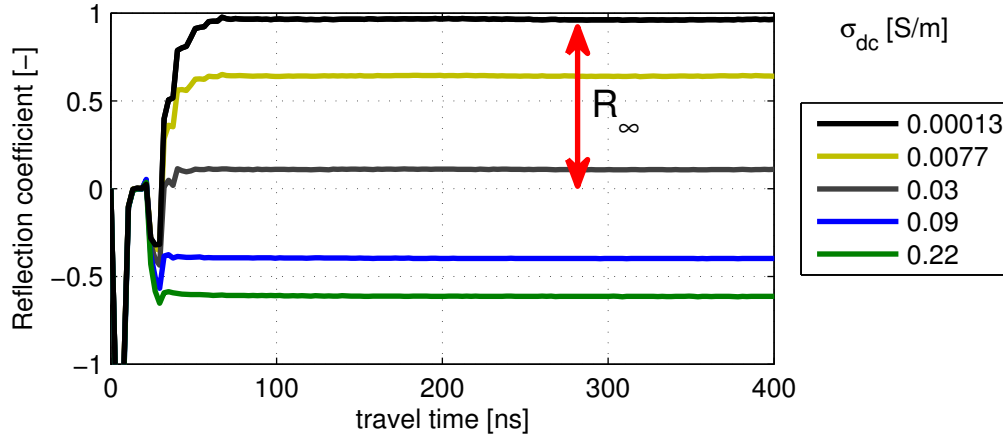
Figure 3.5: Example TDR traces (black) measured with 0.3 m rod length in initially de-ionized water (black). The other traces show the effect of increasing the electrical conductivity step by step by adding KCl on the measured reflection coefficient R_∞.

decline exponentially with perpendicular distance to the rods, resulting in a fairly small measurement volume of some 10^2 cm^3 (e.g., *Robinson et al.* [2003]). Therefore, airgaps along the rods significantly impact the measurement and great care has to be taken when inserting the TDR probes into the soil.

In general, TDR is deemed to be an extremely accurate electromagnetic method for deriving soil water contents, given the rods are inserted airgap-free. A complete error propagation analysis can be found in *Roth et al.* [1990], resulting in an estimated relative error between 1.2% and 16% for two extreme cases of very wet ($\theta = 0.93$) and very dry ($\theta = 0.08$) media.

3.7.3 Measuring electrical conductivity with TDR

Due to the large impact of electrical conductivity on the signal attenuation, TDR measurements can also be used for measuring the direct current electric conductivity σ_{dc} of the soil (e.g., *Robinson et al.* [2003]). The method employed here has been discussed in detail by *Heimovaara et al.* [1995]. In his terms, σ_{dc} can be determined from the amplitude of the reflected TDR signal as follows:

$$\sigma_{dc} = \frac{K}{Z} \frac{1 - R_\infty}{1 + R_\infty}. \tag{3.10}$$

where K is a constant which is determined by the probe geometry, Z is the impedance of the cable (50 Ω), and R_∞ is the reflection coefficient at very long travel times where no further reflections of the signal occur. This is illustrated in Figure 3.5, showing the measured reflection coefficient R_∞ for de-ionized water in black. As can be seen, increasing

the dc-conductivity through the addition of KCl leads to a significant reduction of the reflection coefficient.

The probe geometry constant K can be determined by measuring signals in solutions with known electrical conductivity $\sigma_{dc,T}$ (at T °C). In our case, we derive K from a series of reflection coefficient measurements acquired in initially de-ionized water when sequentially adding increasing amounts of KCl, similar to the series shown in Figure 3.5.

4 Experimental Sites - An Introduction

The experiments for this thesis were mainly carried out at the ASSESS-GPR site close to Heidelberg, Germany, and at multiple sites in the region around Urumqi, Xinjiang, P.R. China. In this chapter, the basic characteristics of these sites are described. Where available, ancillary data are evaluated as a background for considerations in later chapters.

4.1 ASSESS-GPR

In order to facilitate the understanding of hydraulic soil processes and further state-of-the-art GPR measurement and modeling methods, an artificial testbed was built into a former drive-in fodder silo close to Heidelberg in June 2010.

4.1.1 Construction and basic characteristics

Some pictures taken before and during the construction process can be found in Figure 4.3. The testbed is about 20 m long, 4 m wide and approximately 1.9 m deep. Its total surface area has been estimated to 79.94 m^2. The concrete bottom and walls of the structure have been sealed by adding a sturdy polyethylene foil (see picture in Figure 4.3c). A complicated but well-defined quasi-2D architecture was designed as a part of the diploma work of *Antz* [2010]. This design features three distinct kinds of sand with a gravel layer of about 0.1 m thickness at the bottom. A sketch of this subsurface architecture can be found in Figure 4.1. As can be seen in this sketch, there are regions of different complexity with respect to the soil water dynamics and the expected GPR signal evaluation. Ordered by increasing complexity, the following regions can be distinguished:

- a two-layer region (16 m ... 20 m)

- several three-layer regions, in part with swapped layering of the materials (0 m ... 2 m vs. 7 m ... 10 m and 12 m ... 14 m)

- regions with slanted (2 m ... 7 m) and converging reflectors (14 m ... 16 m)

- and, most distinctively, a synclinal structure (10 m ... 12 m)

Since the bottom and the wall of the whole structure have been sealed, precipitation will accumulate at the bottom, leading to a rising water table over time. During normal operations of the test site, the water table is kept at depths between -1.6 and -1 m by
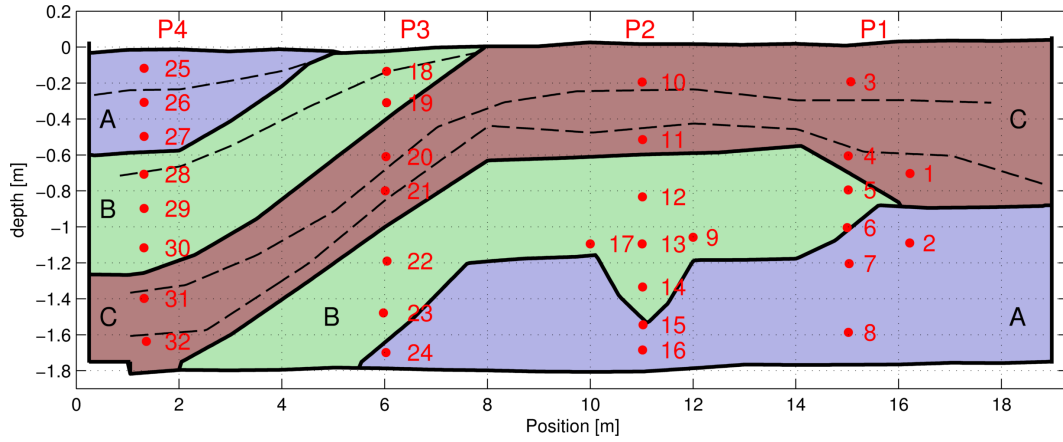
Figure 4.1: Sketch of the structure of the ASSESS-GPR test site. Thick black lines denote layer boundaries between the differently shaded materials, the dashed black lines known compaction interfaces within the same material. TDR sensors are indicated by red dots.

pumping water out of the observation well which is located at approximately 18.4 m. If desired, the pumping well can also be used for artificially raising the water table through imbibition. The high saturated conductivity of the additional gravel layer at the bottom of the structure is to equally distribute imbibition or drainage fluxes along the lower boundary during our experiments.

During the building process, the sand was carefully added layer by layer. To ensure the stability of the boundary layers, the sand was compacted with a vibrating machine after each layer addition. Due to the thickness of the different layers, the sand also had to be compacted several times within the same layer, leading to distinct compaction interfaces. The position of some of these compaction interfaces has been explicitly determined; those interfaces are illustrated by the dashed black lines in Figure 4.1. As will be shown in Chapter 7, the porosity change over these compaction interfaces can give rise to a reflection of the GPR signal, depending on the hydraulic state of the site.
The boundary conditions (e.g. precipitation, air temperatures, water table position) are measured on-site by an automated weather station (see *Antz* [2010] for details). In particular, 32 TDR sensors have been placed in four separate profiles as indicated by the red dots in Figure 4.1.

4.1.2 Exemplary GPR measurement

A typical example of a multi common offset GPR measurement under quasi-equilibrium conditions (acquired at an antenna box separation of 1.3 m after a dry-spell of approximately four weeks) is shown in Figure 4.2. For facilitating the visibility of subsurface structures,

the direct wave has been clipped for the two internal channels (INT1 and INT2). In general, the reflections generated by the subsurface interfaces are clearly distinguishable. Most prominent features include the layer boundary between sands B and C, especially including the reflection signal generated by the synclinal structure at 8...10 m. At travel times between 38 and 50 ns, two continuous reflections can be discerned. The first, fainter reflection is most likely generated by the transition to the gravel layer while the second, more prominent reflection is generated by the concrete bottom. Furthermore, there is a comparatively weak horizontal reflection arriving at travel times around 22 ns. As will be shown in Chapter 7, this reflection is essentially generated by the top of the capillary fringe above the water table.

4.1.3 Previous studies at ASSESS-GPR

Details about the design and the construction process of the ASSESS-GPR site can be found in *Antz* [2010].

The water content measurements recorded by the TDR probes have been the basis for the recent diploma work of *Jaumann* [2012], focusing on the estimation of effective hydraulic parameters for the ASSESS-GPR structure. The current best result of an effective parameter set calculated in a recent inversion based on that work are reported in Table 4.1.

A first GPR related study at the ASSESS-GPR site was carried out by *Kühne* [2010], analyzing the temporal variability of soil water content as measured with multichannel GPR between June and September 2010. Subsequently, this analysis was extended by another time-series measured between December 2010 and April 2011 in the framework of the thesis of *Bogda* [2011], focusing on optimizing the measurement setup for the multichannel analysis. GPR data acquired at the ASSESS-GPR site have been the basis for the novel inversion approach for surface GPR data which has been presented by *Buchner et al.* [2012].

The well-controllable nature of the ASSESS-GPR site provides excellent conditions for studying the GPR response to different hydraulic states of a field site. Such different hydraulic states can be simulated by varying the water table through imbibition and drainage into and from the structure at the observation well. A first description of the GPR response to experiments with fluctuating water tables has been recently provided

Table 4.1: Effective Brooks-Corey Parameters for the three sands used at ASSESS-GPR, based on the results by *Jaumann* [2012].

	h_0	λ	ϕ	K_s	τ
sand A	0.250 ± 0.013	1.46 ± 0.09	0.376 ± 0.001	130 ± 25	0.01 ± 0.2
sand B	0.173 ± 0.013	2.59 ± 0.16	0.315 ± 0.001	23 ± 1	0.001 ± 0.007
sand C	0.182 ± 0.013	5.37 ± 0.33	0.324 ± 0.001	20 ± 1	0.001 ± 0.001

by *Seegers* [2012]. These experiments were also the foundation for the diploma thesis of *Dagenbach* [2012], who performed a detailed numerical analysis of the GPR response to the transition zone above the capillary fringe. Comparing the time-lapse measurements acquired during the experiments to the results of numerical simulations, an appropriate soil hydraulic parametrization has been identified by *Dagenbach et al.* [2012].

In the framework of this dissertation, a comprehensive analysis of these experiments and their implications for GPR studies will be the main topic of Chapter 7.
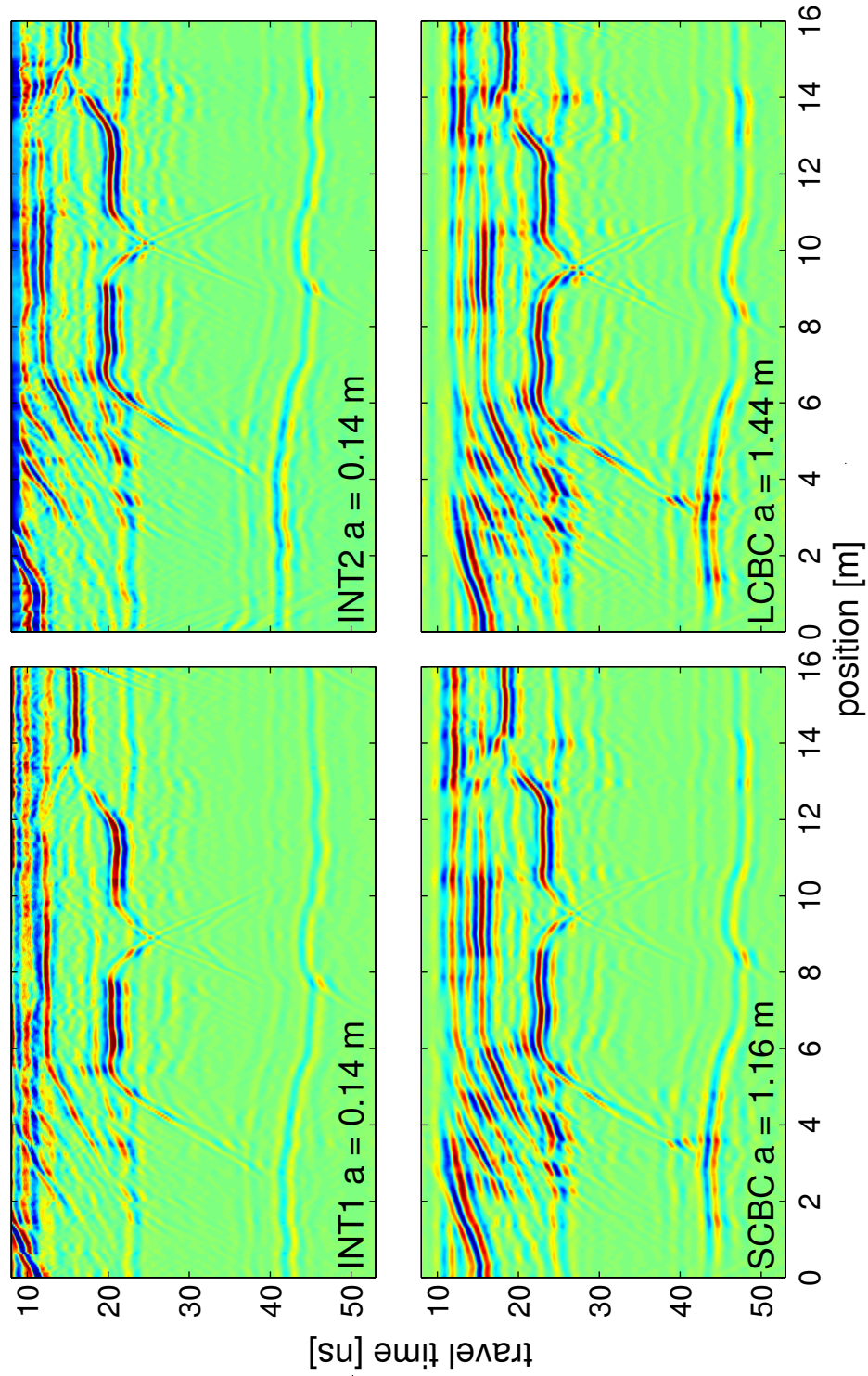
Figure 4.2: Exemplary four channel measurement of the whole ASSESS-GPR site acquired at November 28th 2011 after a long dry spell. Channel designations and the corresponding antenna separations are indicated in each radargram. Channels one and two denote the two internal channels, three and four the long and short crossbox channel, respectively.

(a) ASSESS-GPR site before construction. View towards start of GPR profiles

(b) ASSESS-GPR after smoothing of the ground. View towards end of GPR profiles

(c) ASSESS-GPR after installation of the pond liner

(d) ASSESS-GPR during construction

(e) GPR measurements during imbibition and drainage experiments

(f) GPR measurements during imbibition and drainage experiments

Figure 4.3: Pictures from the ASSESS-GPR site. The top row shows the structure before, the middle row during construction. The bottom row shows the GPR measurement process during the imbibition and drainage experiments discussed in Chapter 7.

4.2 The Urumqi Region, Xinjiang, P.R. China

In the framework of the BMBF-project RECAST Urumqi, two field campaigns were carried out in spring 2010 and 2011, aimed at establishing GPR methods for monitoring soil water contents at several characteristically distinct sites in the Urumqi region.

4.2.1 Introduction and overview

The Urumqi region is situated in Northwestern China on the northern slopes of the Tian Shan mountain range. For a topographic overview, refer to the map which is provided in Figure 4.4. The region is characterized by a strongly continental semi-arid climate with the city of Urumqi being approximately 2400 km from the nearest ocean. The regional geography is dominated by a large vertical gradient with the high mountains of the Tian Shan reaching altitudes of around 5000 m, while the desert area 100 km to the north is located at only about 400 m a.s.l.; in combination with the prevalent climatic conditions this leads to a highly dynamic system with fast seasonal changes. The city of Urumqi is located between the foothills of the mountain range and the ensuing oasis belt which is under intensive agricultural use. The city currently has approximately 3.5 million inhabitants, drawing its water supply partly from groundwater extraction and partly from the Urumqi River. The largest part of the baseflow of the Urumqi River is provided by melt-water of the Urumqi Glacier No. 1, which is located approximately 120 km southwest of the city. This dependence on glacial melt water might have severe implications due to the ambient climatic warming, which amounted to about 0.04 °C per year between 1973 and 2011 and has been increasing over the last decade (*Fuchs* [2012]). Currently, the glacier is melting at an accelerated rate, as has been shown in *Shi et al.* [2007]. The same study predicts, based on climate modeling, that global climate change will effect an increase in precipitation in the area, which will however become more erratic. Also, more precipitation is supposed to fall as rain, changing the run-off characteristics of the Urumqi River. However, based on remote sensing data from the last decades, such an increase in precipitation could not be corroborated so far by *Fuchs* [2012]. For more information about the general geography and climate, refer to *Fricke* [2012].

A schematic overview of the study region can be found in Figure 4.5, portraying the city located along the altitude gradient of the northern slopes of the Tian Shan. The first field campaign in 2010 focused on the area around the desert rim, while the second measurement campaign in spring 2011 has visited several sites along the altitude gradient between the desert and the glacier. For an overview, a few pictures of these sites are provided in Figures 4.8 and 4.9. Furthermore, an introductory movie showcasing the different sites while moving along the altitude gradient from the desert to the glacier can be found in the digital supplementary materials as described in Appendix B. The red rectangles in Figure 4.5 mark the areas where the most promising GPR datasets have been acquired so far and will be discussed in more detail in the following sections. These three areas, the semidesert (A), the foothills of the Tian Shan (B) and the high-mountain grasslands (C)
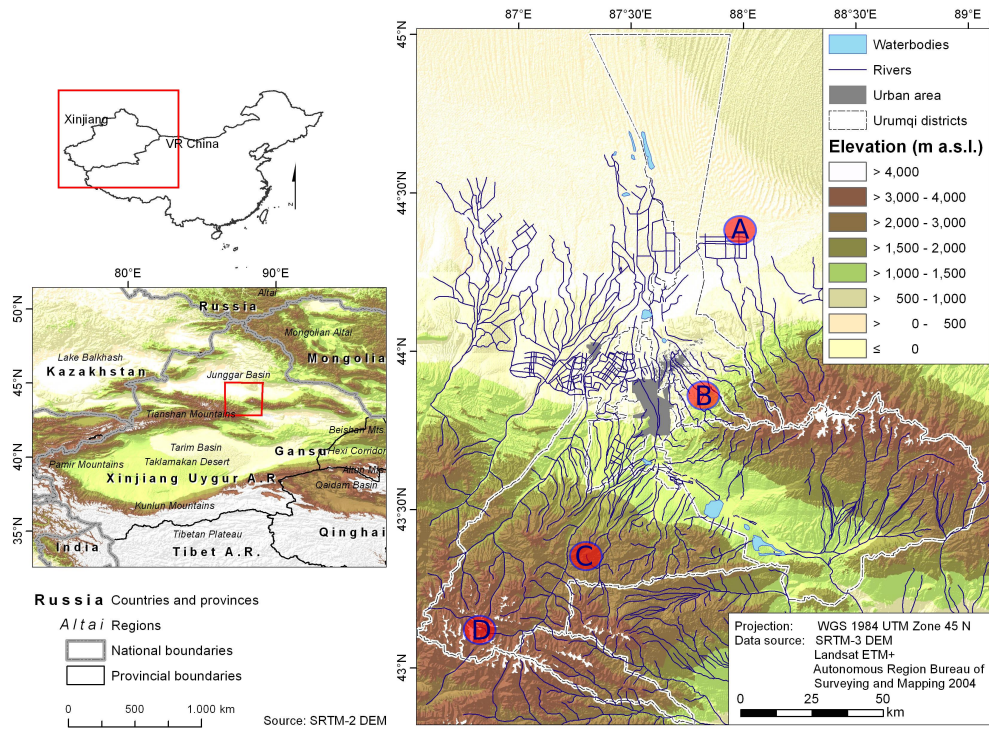
Figure 4.4: Topographic map of the study region, *modified from Fricke [2012]*. The approximate location of the major measurement sites are specifically marked: A - semidesert area, B - mountain foothills, C - high mountain grasslands and D - glacier.

are representative for about 70 % of the study region (*Fricke* [2012]).

4.2.2 Site A: Semi desert area near Fukang

During both field campaigns, measurements could be executed in the semi-arid region around Fukang city, which is located at the onsets of the Gurbantüngüt Desert, approximately 70 km to the northeast of the city center of Urumqi. This area is situated at the foot of the Bogda mountain range, at only about 400 m above sea-level.

The groundwater table is rather shallow and already reaches the surface at some locations. This shallow groundwater table in connection with the strong radiative forcing of a semidesert environment leads to a strongly ascending movement of dissolved salts. At some places, those high salt contents result in large values of electrical conductivity. The area around the desert rim is characterized by long ranges of sparsely vegetated chains of dunes roughly running along a north-south direction. Such semi-vegetated desert areas make up about 30 % of the study region. Dune heights reach some 30 to 50 m, and the interdune spacing ranges between 50 and 100 m. This morphology has distinct implications for the soil water content patterns which will be discussed in Chapters 6 and 8. Two field
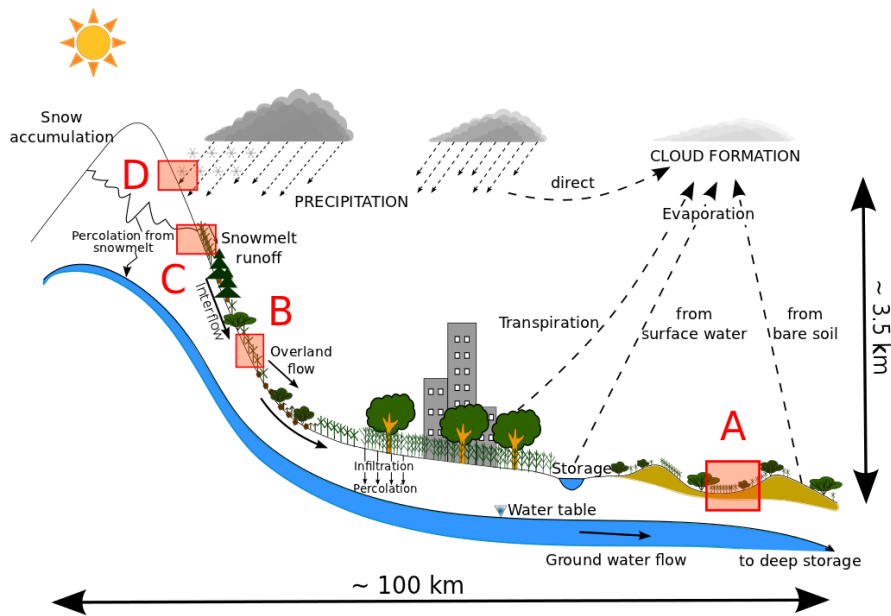
Figure 4.5: Schematic overview of the main hydrological processes of the Urumqi region. The location of the major measurement sites which are discussed in this thesis are indicated by the red rectangles: A - semidesert area, B - mountain foothills, C - high mountain grasslands and D - glacier.

sites have been established and visited both in 2010 and 2011: The first features a 550 m long GPR line, perpendicularly crossing several chains of dunes and is located about five kilometers north of the last agricultural fields along the desert rim. Data from this site will be the main focus of Chapter 6. The second site is located approximately one kilometer closer to the agricultural fields in the south. Here, a 50 m × 50 m 2D-measurement site has been established in a valley between two dune chains, focusing on more closely investigating smaller scale patterns. The corresponding results will be discussed in Chapter 8.

The measurements which will be discussed in this work were taken right after the annual snow melt, in March and April 2010 as well as April 2011. Melting snow represents the most important water input in the semidesert area, with only very little additional precipitation beyond some light rain in spring. For spring 2010, climate data were made available by the XIEG. The rapid change in air temperatures between March and May 2010 is shown in Figure 4.6, indicative for the highly dynamic system: At the beginning of the field campaign (its duration is marked by the light gray shaded area), air temperatures would still fall to around -20 °C at night, while day temperatures would reach more than 30 °C only two months later. As shown in Figure 4.7, these dynamics can also be observed in soil temperatures and soil water contents acquired by the same weather station. At the
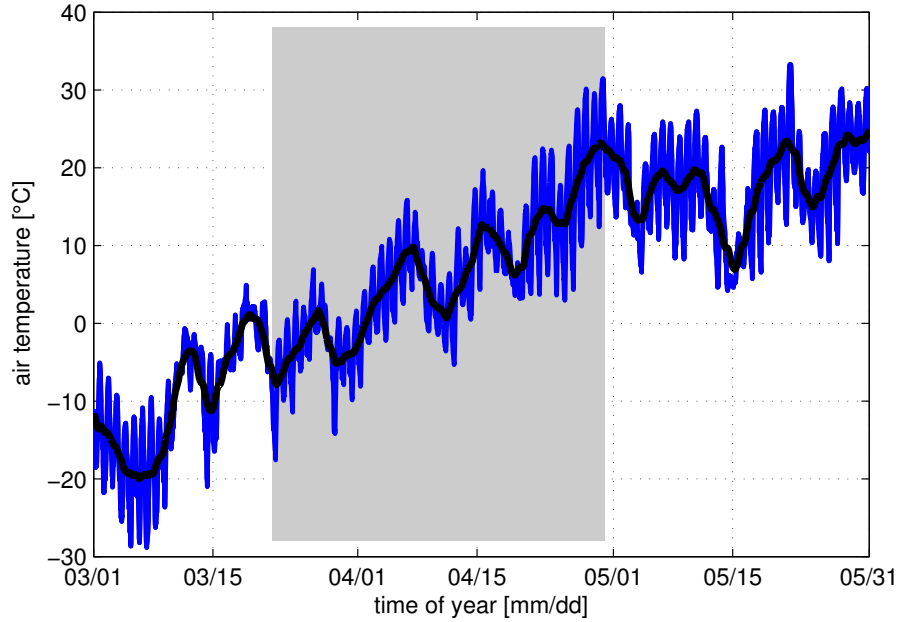
Figure 4.6: Observed air temperature measured at 2 m height in spring 2010 for the Fukang semidesert area. The black line denotes daily averages. The gray box indicates the extent of the 2010 measurement campaign. *Data courtesy of XIEG, CAS, Xinjiang.*

start of the measurement campaign, the soil was still solidly frozen. The ensuing snow melt leads to an increase of water content to about 0.13 $\mathrm{m^3/m^3}$ at the end of March. In the ensuing weeks, two precipitation events lead to a temporary increase in soil moisture by 1-3 % while showing an overall decreasing trend towards around 0.07 % at the end of May.

Other ancillary data include a multitude of TDR measurements of both water content and conductivity which were acquired with probes of five different rod lengths between 0.1 and 0.5 m. Furthermore, soil profiles were dug at characteristic locations for gravimetric sampling and additional ground truth assessment. Two of these soil profiles will be discussed in the context of the 2D-pixel measurement in section 8.1. Soil samples taken for soil texture analysis were classified with respect to the USDA soil classification system. According to this classification, most soil samples acquired from soil profiles in the Fukang semidesert area belong to the loamy fine sand or fine sand fraction.

4.2.3 Site B: Hill-slope site near Shirengou

A second representative site has been chosen in the foothills of the Tian Shan mountains, about 25 km to the east of the city center of Urumqi, which can be seen in the distance
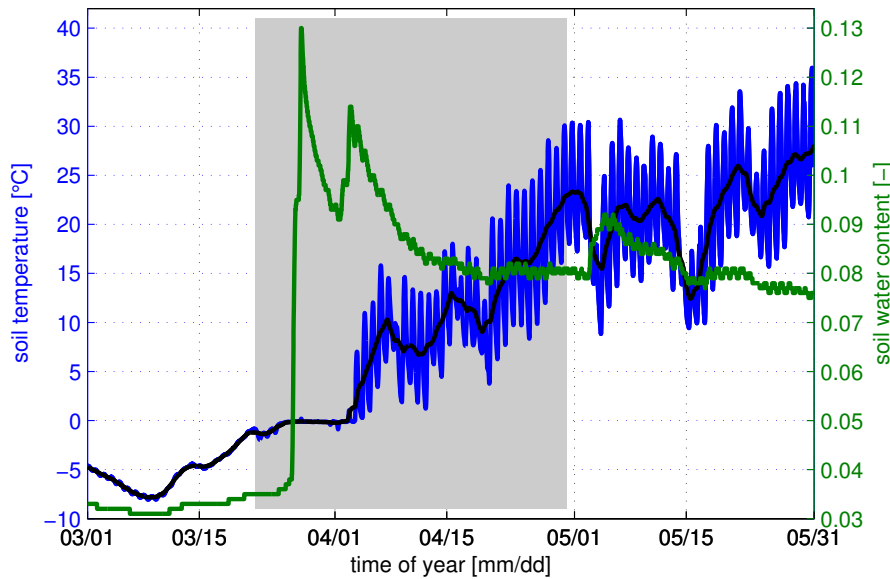
Figure 4.7: Soil water content and soil temperature measured at 10 cm depth in the Fukang semidesert area in spring 2010. The black line denotes daily averaged soil temperatures. The gray box indicates the extent of the 2010 measurement campaign. *Data courtesy of XIEG, CAS, Xinjiang.*

on a clear day. Such hill-slope areas are characteristic for about 23 % of the study region. This particular measurement site lies on a northwards facing hill-slope and covers an area of approximately three square kilometers between a small village and a steep mountain ridge above. The total altitude difference is about 150 meters; prominent ravines dissecting the hill-slope reach a depth of up to ten meters in the lower areas, thus creating steep local slopes. The undulating ground is mainly covered by sparse grass, interspersed with thicker grassy patches and some small shrubs. Two overview pictures can be found in Figures 4.8e (view upslope) and 4.8f (view from above). The entire hill-slope is used for grazing of sheep and goat during the vegetation period. Several soil samples were taken at the start of a 900 m long GPR profile running upslope from the village. The measurement discussed in Chapter 8 has been acquired in early May just after a considerable precipitation input, yielding quite moist overall conditions.

4.2.4 Site C: High mountain grasslands near Houxia

Following the Urumqi River upstream towards Urumqi's Glacier No. 1, a third measurement site has been chosen in the high mountain grasslands around the village of Houxia. Similar high mountain grasslands cover about 17 % of the study region. This site lies at an altitude of approximately 3000 m ASL, which in this case is about 200 m above the tree line. This area is characterized by a thick grass cover leading to a considerable amount of organic

material in the uppermost soil layer. Two overview pictures can be found in Figures 4.9a (view downslope) and 4.9b (view upslope, during a sudden snow shower just two hours later). Despite the short vegetation period, the area is intensively used for grazing cattle in the summer. The specific measurement which is discussed Chapter 8 has been acquired over an area of 50 m × 50 m, gently sloping over a hill ridge. A soil profile dug just outside the measurement area's northeast corner revealed a complex soil structure below with the ground being thawed only to a depth of approximately 0.4 m in late April. Grain size analysis of soil samples taken from several depths of the soil profile show an increasing amount of the fine grained fraction with depth. According to the USDA soil classification, soil samples from the upper part of the profile (samples taken from depths of 12 cm, 24 cm and 33 cm) were classified as silt loam, while the two samples from the lower layer (38 cm and 50 cm) fall into the plain silt class. Both the soil profile and the corresponding GPR measurements will be discussed in Chapter 8.

4.2.5 Other sites considered

Further GPR measurements were conducted at several further sites throughout the Urumqi region, most notably on agricultural lands, as pictured in Figures 4.8c (close to the desert rim) and 4.8d (about 40 km upstream). However, as will be shown in section 8.4, using electromagnetic methods on these field sites is predominantly challenging due to the considerable salinization of the near surface. Especially along the desert rim, this prevents the usage of GPR and TDR methods on lands under agricultural use.

In spring 2011, a measurement could be executed on Urumqi's Glacier No. 1. Two corresponding pictures are provided in Figures 4.9c (showing the two branches of the glacier) and 4.9d (showing an upslope measurement). The GPR data will be briefly discussed in section 8.5. For completeness, Figures 4.9a and 4.9b show the Urumqi River Valley just south of the glacier.

(a) Fukang semidesert

(b) Fukang semidesert

(c) Fukang drip irrigation agriculture

(d) Lucaogou agricultural field

(e) Shirengou hill-slope measurement

(f) Shirengou hill-slope from above

Figure 4.8: Pictures from the Urumqi measurements: Desert rim, agricultural areas and foothills of the Tian Shan
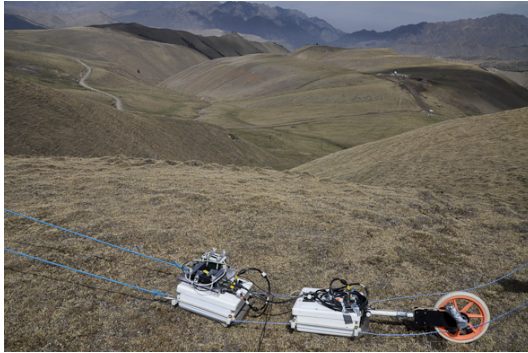
(a) Houxia high mountain grassland

(b) Houxia 2D pixel measurement

(c) Urumqi River upstream area

(d) Urumqi River 5 km from Glacier No.1

(e) Urumqi Glacier No.1 - the two branches

(f) measurement on Urumqi Glacier No.1

Figure 4.9: Pictures from the Urumqi measurements - High mountain area

5 GPR - Precision and Accuracy

Im Gebirge der Wahrheit kletterst du nie umsonst:
Entweder du kommst schon heute
weiter hinauf oder übst deine Kräfte,
um morgen höher steigen zu können.
Friedrich Wilhelm Nietzsche,
Menschliches, Allzumenschliches II, 1. Aph. 358

With respect to a measurement method, accuracy is commonly accepted as the degree to which the true value of a (state) variable of interest can be retrieved, while precision terms the reproducibility of such a measurement. Hence, a certain method could yield a wrong value (low accuracy) to high precision, meaning that repeated measurements will again yield this value with very little variation. On the other hand a (different) method could yield results very close to the true value (high accuracy) but with a large spread, i.e. a low precision. In this sense, this chapter deals with the accuracy and precision of GPR and especially GPR ground wave measurements.

The focus of this chapter will be on using the redundant information our system setup can record with respect to the ground wave signal to understand and to improve the precision and the accuracy of GPR derived soil water contents. Since we do not directly measure water content but the dielectric permittivity as a proxy variable and then employ a petrophysical relationship to calculate the real variable of interest, these considerations should be divided into several parts.
The first part of this chapter deals with *limitations of our instrumentation*. Two issues will be discussed in detail. The first has already been briefly introduced in *Klenk* [2009]: Finding a suitable time zero calibration for common offset measurements. Here, a novel calibration approach will be developed. The second issue concerns apparent time-base non-linearities of our instruments. A corresponding correction will be described for dispersed datasets.
The second part of this chapter then moves to discussing the *influence of distinct site characteristics* on the interpretability of our measurements. Finally, the *impact of auxiliary parameters* required for deriving water contents from the measured permittivities in the framework of the employed petrophysical relationship will be briefly discussed.

5.1 A Rationale for Improving GPR Precision and Accuracy

Highly non-linear small scale soil properties impede reliable large scale estimation and prediction of soil water content dynamics. For example, soil hydraulic conductivity $K(\theta)$ varies over several orders of magnitude with water content. At the same time, it is the key variable for studying soil water dynamics, as $K(\theta)$ links the water flux with the driving force through Darcy's law (see equation 2.31), essentially governing soil water redistribution. In general, directly determining such field-scale hydraulic properties is very difficult. However, as has been shown e.g. by *Wollschläger et al.* [2009], these properties can be inverted if a high-quality time series of the governing state variable, the water content, and corresponding forcing data is available. That study has only dealt with onedimensional soil measurements obtained by Time Domain Reflectometry. However, if GPR could estimate soil water content distributions to similar precision and accuracy as TDR, this would open the door for quantitatively studying 2D soil water dynamics.

5.2 Considerations on Time Zero Calibration for Common Offset Data

Due to instrument limitations, the true starting time of the recorded GPR signal is unknown. For example, the IDS data collection software automatically positions the measured trace in the recording time window for each channel separately; there is no common absolute time zero signal. Hence, for all evaluation methods of common offset GPR data relying on the travel time of a certain part of the signal between transmitting and receiving antenna, a calibration scheme has to be implemented.

5.2.1 Commonly used approaches

An often made assumption is that the time of transmitting the GPR pulse ("true time zero") is independent of the material in the immediate vicinity of the antenna. In that case, a time zero correction can e.g. be carried out by comparing the travel time t_{AW} of the signal measured at a known antenna separation a in air to theoretical expectations (as has e.g. been applied by *Westermann et al.* [2010], *Galagedara et al.* [2003]):

$$t_{\mathrm{off}} = t_{\mathrm{AW}} - \frac{a}{c_0}, \tag{5.1}$$

where c_0 is the speed of light in free space. To reduce the influence of the shielding of the employed antennas, antennas can be turned sideways to truly record the signal through the air, as has also been discussed in *Klenk* [2009]. To assess temporal stability of the signal, it is beneficial as well to record some traces in air at the start and the end of long measurement profiles.

For a ground wave measurement this approach allows to calculate the bulk dielectric permittivity ε_b from the measured ground wave travel time, the antenna separation and

the free space wave velocity at each point of a certain GPR profile:

$$\sqrt{\varepsilon_b} = \frac{c_0 \cdot (t_{\mathrm{GW}} - t_{\mathrm{off}})}{a} = 1 + \frac{c_0}{a} \cdot (t_{\mathrm{GW}} - t_{\mathrm{AW}}). \tag{5.2}$$

A second commonly applied approach for determining the time zero offset for common offset data sets is using the direct air wave fit in a separate WARR or CMP measurement. The rationale here is that without an offset, the extrapolation of the regression line towards zero antenna separation should pass through the origin. Hence, the time zero offset of the instrument is given directly by the travel time axis intercept of this regression fit. Again, for signal quality and interference minimization, a possible approach is to turn the antennas sideways by 90° and carry out a WARR measurement transmitting directly through the air. We call this an AIRWARR measurement.

As it turns out, both approaches for determining the time zero offset cannot account for all effects which need to be considered for estimating the "true" time zero. In the following sections, it will be demonstrated, that the different shapes of the recorded air and ground wavelets as well as ground-coupling induced changes in frequency content and potential near-field effects will have to be considered as well when determining the time zero offset .

5.2.2 Picking the right wavelet feature
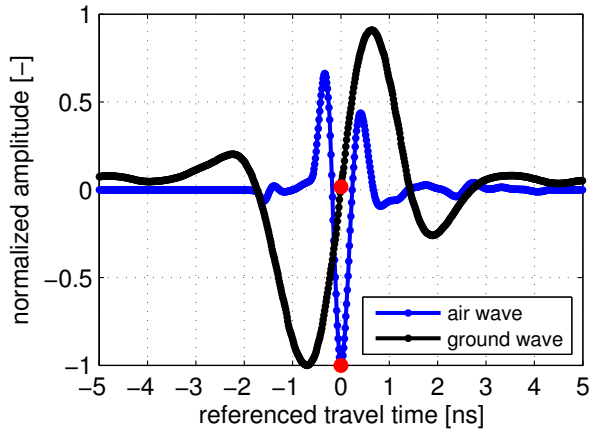
Figure 5.1: Typical shapes of the air wave (blue) and ground wave (black) wavelets as recorded by the SCBC during a common offset measurement. Both wavelets have been shifted to their respective center features which are marked by the red dots. The air wavelet has been measured with antennas turned sideways.

First we take a look at the shape of the recorded wavelets. As can be seen from equation 5.2, determining the bulk permittivity of the soil from a common offset measurement essentially depends on the time difference between the air and the ground wave wavelet. Hence, if the travel times of these wavelets are determined via a picking scheme, it is crucial to pick the same position on both wavelets for preventing a systematic offset. The same is true for the WARR based approach for deriving the time zero offset for a separate CO measurement. Here, the same wavelet feature has to be picked for retrieving the axis intercept as will be used in the common offset ground wave measurement. The resulting challenge is to find corresponding wavelet features. For example, as has been shown by *Dai and Young*

[1997] using an analytical model for dielectric dipoles on multilayered dielectric media,

a pure ground wave signal will have the same shape as the exciting current, whereas reflections for example have the shape of the first derivative. Hence, corresponding features may differ with respect to air wave and ground wave wavelet, and similarly for an air wave and a reflected wavelet.

Comparing experimentally recorded air wave and ground wave wavelets, Figure 5.1 illustrates, that for our antenna systems their basic shapes are indeed different. The air wave wavelet seems to display an approximate axial symmetry with respect to the central minimum, whereas the ground wave wavelet shows point symmetry with respect to the central zero crossing. Furthermore, the frequency content is clearly not the same, which gets reflected in the different extents of the wavelet in the time domain. This is actually to be expected since placing the antenna onto the soil interface increases the dielectric permittivity in the reactive nearfield of the antenna. This changes the dielectric length of the antenna which determines its resonance frequency. In this case the antenna becomes "dielectrically longer". In turn, the radiated wavelets will be characterized by lower dominant frequencies, explaining the differences observed in Figure 5.1 .

As a result, picking corresponding wavelet features is challenging. In previous studies different approaches have been taken. One candidate is picking the first onset of the wavelet. However this "leading edge" is often hard to define, even with a proper thresholding and under many circumstances prone to interferences. As an alternative, *Huisman and Bouten* [2003] proposed the usage of the zero-crossing between the first maximum and minimum wave amplitude. Probably the most well-defined approach for picking corresponding wavelet features in our case is to use the respective center feature for each wavelet, i.e. the central minimum of the air wavelet and the central zero crossing on the ground wave wavelet. Aside from minimizing any possible picking offset, this also minimizes the effect of potentially interfering signals along different raypaths, since such an interference will first impact the marginal features. However, as will be shown in the following section, this picking scheme cannot capture all the occurring offsets, which will have to be separately accounted for.

5.3 GPR Ground Wave Evaluation: A New Approach for Calibration

As described in Section 3.5, there are two channels available for evaluating the ground wave signal when measuring in the normal four channel configuration: The long and the short crossbox channel. Neglecting potential influences of the slightly different averaging volumes of the two channels, evaluating the direct ground wave signal in common offset measurements using equation 5.2 should yield approximately the same result for both cases. Hence, the availability of these two crossbox channel datasets gives the possibility for crosschecking and validating this approach of determining the near-surface soil water contents. One typical example of such a ground wave evaluation for both crossbox channels is shown in Figure 5.2.
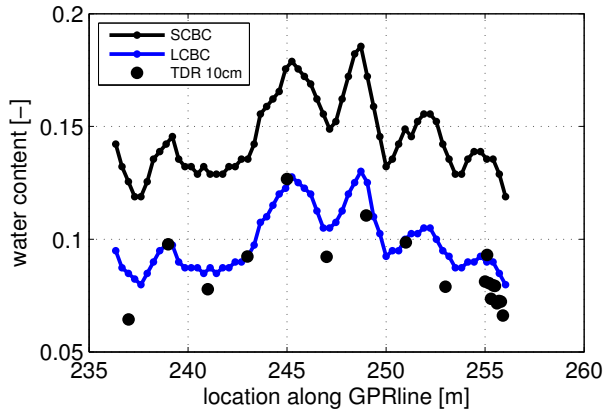
Figure 5.2: Example evaluation illustrating the observed offset between the SCBC (black) and the LCBC (blue) signals, recorded at antenna separations of 0.86 and 1.14 m, respectively. Black dots indicate 10 cm TDR measurements for comparison.

As has already been found in *Klenk et al.* [2011] (see also chapter 6), there is a distinct offset in water content when evaluating both channels in the same measurement and using the calibration scheme described in Section 5.2.1. Applying the same evaluation procedure to the short crossbox channel's signal yields consistently higher absolute water contents, although potential influences of not correctly picking the corresponding portion of the wavelet (as described in Section 5.2.2) have already been taken into account. Furthermore, the retrieved water contents from evaluating the long crossbox channel's signal seems to be more consistent with both

TDR derived water contents (Figure 5.2) and the experience in the field. *Klenk* [2009] and *Lodde* [2009] have shown independently for both IDS and Malå Geoscience manufactured antenna systems, that this effect cannot simply be traced back to either a specific combination of antennas or to a specific manufacturer. Under the conditions investigated in those studies, the same effect could always be associated with the respective SCBC and LCBC channels, independent of the specific setup. Subsequently acquired datasets suggest that this effect depends significantly on the employed antenna separation and only to a lesser extent on the general wetness conditions of the soil.

In this section, this effect will now be systematically investigated. The aim is to implement a calibration procedure, which ensures the compatibility of the results from both crossbox datasets and an agreement with auxiliary field data e.g. from TDR measurements. These considerations will be based on several characteristically different datasets: The first three have been acquired at the Fukang desert site with center frequencies of both 200 and 400 MHz, while the fourth has been subsequently measured at Grenzhof with a center frequency of 400 MHz. Since the extent of the effect seems to depend on the specifically employed antennabox separation, all the now considered datasets feature ground wave measurements of the four channel measurement setup in which the antenna box separation has been varied between 0.5 m and 3.0 m. For details about the different datasets, refer to Table 5.1. Let us now first turn to dataset 3, which was measured at Fukang under comparatively dry sandy soil conditions. TDR data indicate near-surface permittivity values between 6.5 and 7.4, which translates to water content values in the range of 0.1 to 0.12. Twelve GPR profiles were run consecutively along a 50 m measurement line, the ground wave data were averaged over a seemingly homogeneous stretch of approximately

five meters. The resulting GPR derived permittivity values for both crossbox channels are shown in Figure 5.3 (i). The gray marked region in that figure denotes the area where trustworthy data would be expected. Its vertical extend with respect to permittivity is based on the variability observed by multiple onsite TDR measurements acquired vertically with sensor lengths between $0.1 \ldots 0.3$ m. From field experience it is not to be expected to get trustworthy GPR ground wave data at antenna separations below 1 m due to antenna effects and much beyond 2 m due to a rapidly deteriorating signal to noise ratio. As can be clearly observed from Figure 5.3 (i), both channels tend to overestimate the expected true permittivity. This overestimation seems to be based partly on a constant offset affecting both channels, and partly on an additional deviation which depends on the antennabox separation, the latter having a much larger impact on the SCBC. At an antenna separation of about 2 m, the two curves intersect. In this case both channels yield approximately the same permittivity, explaining why the general effect has not been consistently observed in all previously acquired field datasets reported in *Klenk* [2009] and *Lodde* [2009].

Based on these observations, and the considerations about the differing wavelet shapes of the air wave and ground wave wavelets in Section 5.2.2 we can introduce a time-zero correction by adjusting the traditionally determined air wave travel time as follows:

$$t_{\text{AW,corr}} = t_{\text{AW,meas}} + s_1 + s_2 \cdot \left(\frac{a - a_{\text{ref}}}{a_{\text{ref}}} \right), \tag{5.3}$$

with the measured air wave travel time $t_{\text{AW,meas}}$ at a given antenna separation a, s_1 an additional constant offset, s_2 a slope parameter which determines the extent of the correction depending on the difference of the employed antenna separation a for this particular measurement to a reference separation a_{ref}.

Using this equation and focusing on the expected trust region, we can find reasonable agreement between the crossbox channels for all calibration datasets setting $s_{1,\text{SCBC}} = s_{1,\text{LCBC}} = 0.5$, $s_{2,\text{SCBC}} = 1.8$, $s_{2,\text{LCBC}} = 0.1$, and $a_{\text{ref}} = 2.0$. The resulting permittivities are then also compatible with the measured TDR values as shown in Figure 5.3 (ii), where the solid lines denoting the corrected permittivities are reaching the upper limit of the trust region. If we average the difference of permittivities between both cross-box channels

Table 5.1: Overview of the GPR datasets used for establishing the calibration function

profile name	f [MHz]	Location	a_{box} [m]	Δa_{box} [m]	soil conditions
Set 1	200	Fukang	$0.5\ldots 3.2$	0.1	dry sandy, roots
Set 2	200	Fukang	$0.5\ldots 3.2$	0.2	dry sandy
Set 3	400	Fukang	$0.5\ldots 3.2$	0.2	dry sandy, reference set
Set 4	400	Grenzhof	$0.5\ldots 2.8$	0.1	wet loamy, recent rainfall
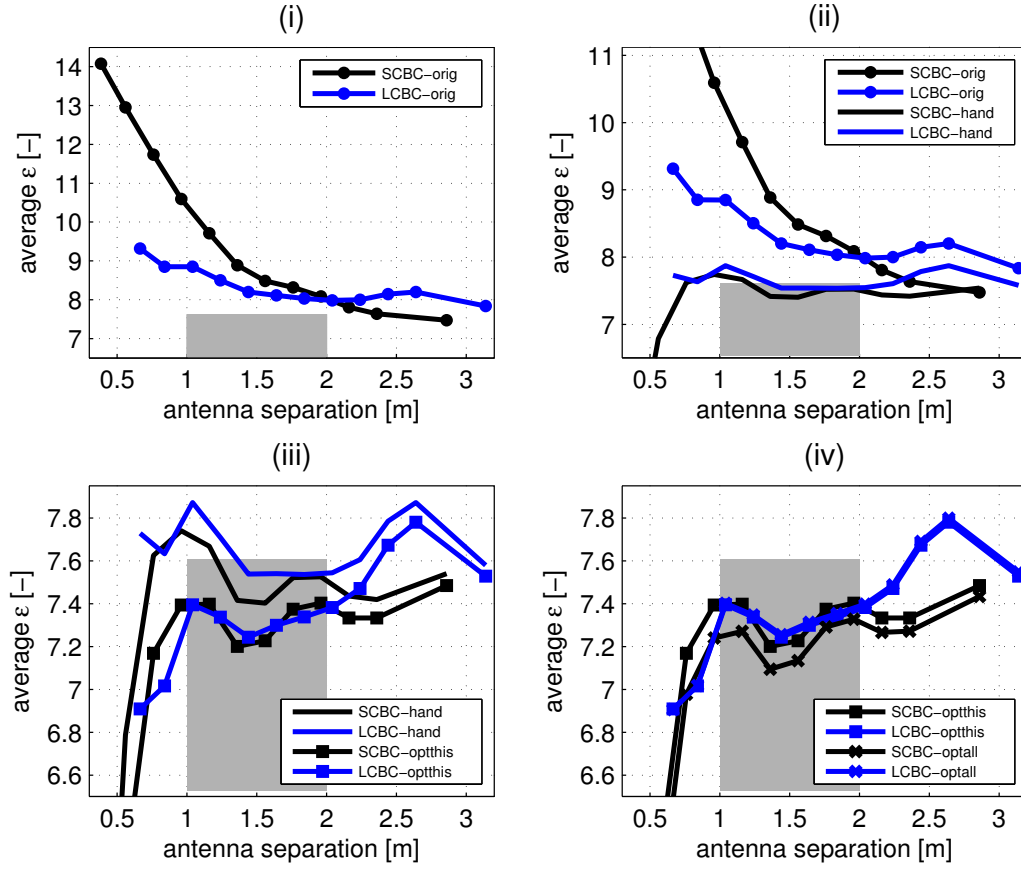
Figure 5.3: Overview for finding a calibration approach for dataset 3 (Fukang, 400 MHz). The four figures show permittivity values for the SCBC (black) and LCBC (blue) as a function of antenna separation, each value is based on a 5 m spatial average. Diagram (i) shows uncorrected permittivity values, (ii) compares original data with hand fit corrected data, (iii) the hand fit results with a specifically optimized correction and (iv) the specifically optimized corrections with a correction equally based on all available datasets. The gray boxes denote the region of expected permittivities based on TDR data. We note that the permittivity axes are scaled between different diagrams for clarity.

for the whole trust region, the difference is below 1 %.

This approach can be objectified by employing an optimization procedure based on equation 5.3. The minimization target is both the difference of a linear fit to the permittivities as derived for both channels within the trust region extent of $1 \ldots 2$ m and the slope of those fits, since both channels should yield the same result and this consistently over the whole trust region. The resulting parameters are quite similar to the hand optimized values with a slightly larger constant offset. Both channels yield now permittivity values around 7.3 as shown by the square-solid lines in Figure 5.3 (iii). The difference in permittivity

between the two channels is smaller than 10^{-4}, averaged over the whole trust region. Hence this approach leads to very well compatible measurement results, both between the two channels and in comparison with TDR data.

Lastly, we can base this optimization approach on jointly minimizing the differences for all the four available datasets, with the result shown in Figure 5.3 (iv). In this case, the globally derived parameters yield very similar results, the average difference between the two channels after applying the correction remains below 0.02. An overview of all three parameter sets and the resulting permittivity values averaged over the whole trust region $\bar{\varepsilon}$ is shown in Table 5.2. A similar approach can be found for all available datasets, with Figure 5.4 showing the results for each data set specific optimization. Again, the trust regions are based on onsite TDR measurements for each specific measurement site, the solid-circled lines show the original data and the solid line the results after having applied the optimized correction. A comparison of all mean permittivity values for the trust region before the application of the correction and the respectively corrected results can be found in Table 5.3.

The site specific optimized parameters yield better results than the globally derived, indicating some sensitivity to site specific properties. However, already with the hand fitted parameters, the achievable deviation from the respective trust region is below 0.02 in water content. If a higher precision is needed, a respective calibration series would have to be run on site. Depending on the signal-to-noise ratio, this might even be possible with running one WARR and one AIRWARR measurement and then calculating permittivity values for all antenna separations in the range of $1\ldots 2$ m.

As a final consistency check, we can synthesize WARR diagrams from all four common offset data sets due to the high resolution of available antenna separations. Calculating the permittivity from a regression fit to the ground wave travel time as a function of antenna separation should not depend on the specific time zero offset as long as this offset does not change with antenna separation (see e.g. Section 3.3.1). Hence, if the effects which were described in this section can be really traced back to an insufficient time zero correction as based on the corresponding air wave travel time for a given antenna separation, then fitting the ground wave travel time directly in such a synthesized WARR radargram should yield more consistent results for both channels than each separate common offset evaluation. This is indeed the case, as can be seen from Figure 5.5, picturing the averaged ground wave

Table 5.2: Optimized model parameters and mean trustregion water contents for dataset 3

type	$s_{1,\text{SCBC}}$	$s_{1,\text{LCBC}}$	$s_{2,\text{SCBC}}$	$s_{2,\text{LCBC}}$	a_{ref}	$\bar{\varepsilon}_{\text{SCBC}}$	$\bar{\varepsilon}_{\text{LCBC}}$
hand fit	0.54 ns	0.54 ns	1.80 ns	0.10 ns	2.10 m	7.55	7.62
optimized this dataset	0.63 ns	0.71 ns	1.96 ns	0.21 ns	2.05 m	7.33	7.33
optimized all datasets	0.67 ns	0.68 ns	2.09 ns	0.16 ns	2.01 m	7.22	7.35
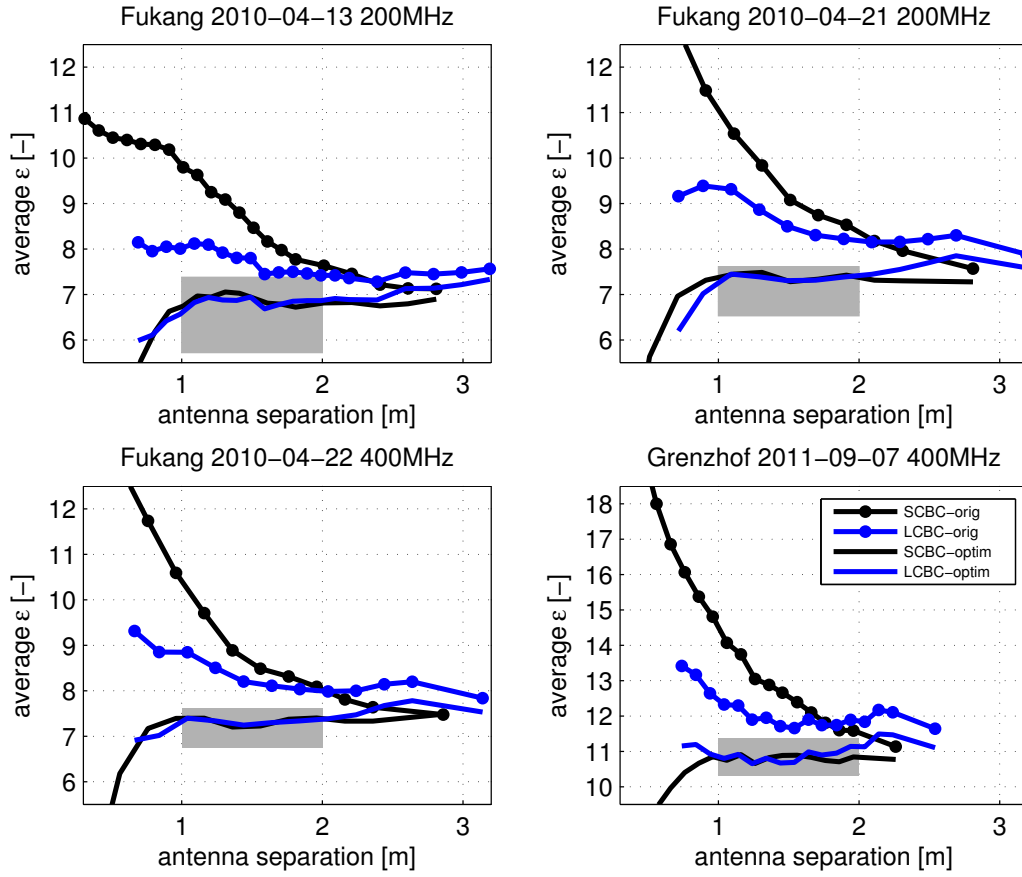
Figure 5.4: Calibration results for all four available datasets. Each figure shows the SCBC (black) and LCBC (blue) derived permittivities before (solid-circled line) and after (solid lines) the application of the site specific optimized calibration of the air travel time as described by equation 5.3. The gray areas denote the respective TDR based regions of expected permittivities.

travel times at each respective antenna separation for all datasets. In order to distinguish the different data sets, corresponding channels have been shifted to the same time zero value for each dataset and the separate datasets have then been additionally shifted by several nanoseconds as indicated in the figure caption. Permittivities calculated from linear regression fits to each of these travel time variations are provided in Table 5.3. The resulting permittivity values are well compatible with the previously calculated optimized common offset GPR values and the TDR data. There are some differences to be observed between the channels, however this can be due to the fact that the instruments might have been restarted during these measurements, which could in fact shift the time zero to some degree independently for both channels for our instrument system.

Summarizing these results, there is a strong indication that the main issue for the common offset measurements is indeed an insufficient time zero calibration if determined by evaluating the corresponding air wave travel times in the fashion described in Section 5.2.1. The considerations in this section suggest that there are at least two additional contributions which cannot be accounted for by the current calibration procedure.

First, the optimization results imply, that there is a constant offset of approximately 0.5-1 ns, which cannot be accounted for by using the original calibration scheme outlined in Section 5.2.1, even if the picking scheme is adapted according to the considerations in Section 5.2.2. Judging from the optimization results for the s_2 parameters shown in Table 5.2, this offset is approximately the same for both channels. Hence, this most likely points to an effect of the ground coupling, e.g. a time difference in the sending of the transmitting pulse when the antennas are put onto the soil as compared to the air measurement or a systematic offset connected to the different frequency contents hampering the picking of corresponding features. Therefore, this additional constant offset is subsequently denoted as $t_{\text{off,coupling}}$.

Secondly, the antenna separation dependent correction factor s_2 is very large for the SCBC while almost no additional antenna separation dependent correction is needed for the LCBC. Hence, this part of the effect depends on the specific system setup and is most likely due to near-field effects and interactions of the emitted wavefield with different parts of the antennas, which can distort the signal when measuring in air. The LCBC is much

Table 5.3: Mean trust region water contents before and after the different corrections for all datasets

data type	set 1	set 2	set 3	set 4
$\bar{\varepsilon}_{\text{SCBC}}$ uncorrected	8.80	9.70	9.01	13.06
$\bar{\varepsilon}_{\text{LCBC}}$ uncorrected	7.68	8.56	8.28	12.01
$\bar{\varepsilon}_{\text{SCBC}}$ handcorrected	7.28	8.06	7.55	11.11
$\bar{\varepsilon}_{\text{LCBC}}$ handcorrected	7.08	7.92	7.62	11.10
$\bar{\varepsilon}_{\text{SCBC}}$ specific optimized	6.855	7.380	7.333	10.816
$\bar{\varepsilon}_{\text{LCBC}}$ specific optimized	6.854	7.380	7.333	10.816
$\bar{\varepsilon}_{\text{SCBC}}$ all sets optimized	6.95	7.71	7.23	10.70
$\bar{\varepsilon}_{\text{LCBC}}$ all sets optimized	6.83	7.65	7.35	10.69
$\varepsilon_{\text{SCBC}}$ synthesized WARR fit	6.4	7.8	6.9	9.6
$\bar{\varepsilon}_{\text{LCBC}}$ synthesized WARR fit	6.6	7.1	7.4	10.2
$\bar{\varepsilon}$ best TDR estimate	5.9-7.2	6.5-7.61	6.5-7.6	10.3-11.3
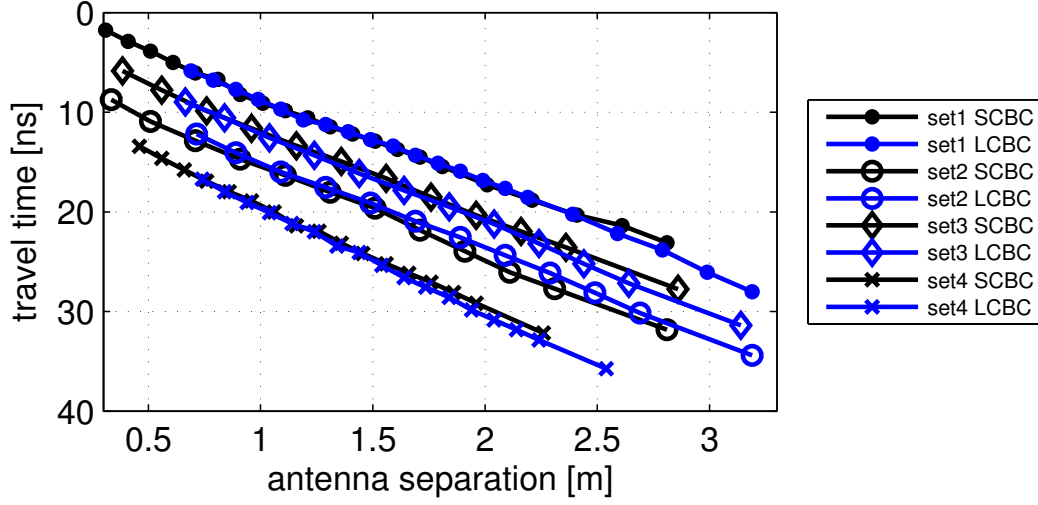
Figure 5.5: Reconstructed WARR radargram, i.e. the ground wave travel times from all four common offset datasets as a function of their respective antenna separation. Black lines indicate SCBC data, blue lines the corresponding LCBC data. The separate sets have been shifted by 3 (set2), 7 (set3) and 9 ns (set4) for clarity.

less affected, most likely due to the more effective antenna shielding. According to our current understanding, we will therefore term this offset the near-field correction factor $t_{\text{off,nearfield}}$. A more comprehensive treatment would probably warrant an explicit modeling of the antenna characteristics for the employed setup, which is beyond the scope of this work.

Hence, the simple relationship in equation 5.1 used for deriving the time zero offset in common offset measurements has to be expanded according to these results:

$$t_{\text{off}} = t_{\text{AW,corr}} - \frac{a}{c_0} \tag{5.4}$$

$$= t_{\text{AW}} - \frac{a}{c_0} + t_{\text{off,coupling}} + t_{\text{off,nearfield}} \tag{5.5}$$

$$= t_{\text{AW}} - \frac{a}{c_0} + s1 + s_2 \cdot \left(\frac{a - a_{\text{ref}}}{a_{\text{ref}}} \right). \tag{5.6}$$

For normal, explorative measurement purposes, each of the parameter sets for s_1, s_2 and a_{ref} discussed above will yield results that are compatible within less than 0.02 in permittivity. For more specific monitoring campaigns, the calibration can be done specifically on site, improving the fit between the two channels to a permittivity difference of less than 10^{-4}.

Even though the averaged deviation of the two channels is extremely small after the

application of this calibration scheme (compare the results for the site specific optimization in Table 5.3), there is still variation in permittivity with antenna separation to be observed over the trust region. Comparing the curves in Figure 5.3 (iv), the variation amounts to about 0.5 in permittivity. Furthermore, permittivity estimates from the reconstructed WARR measurements show some differences between the two channels. This variation is already quite small, in both cases translating into about 0.5 % in water contents. Still, there seems to be a systematic pattern which might to some extent be explained by system or measurement induced noise.

To some extent this remaining variation might also be due to a second effect related to the signal stability of our measurement system which will be studied in the following section. The starting point for these additional considerations are discrepancies between the two crossbox channels which were found for fit results of direct wave signals in multi-offset radar data and cannot be corrected for by the time zero corrections dealt with in this section.

5.4 Signal Stability with Antenna Separation

A second effect can be observed when evaluating the direct waves in WARR or CMP radargrams. Similarly to the issue discussed in the previous section, estimates for both ground wave and air wave velocities are not always consistent for both crossbox channels. This issue can be best illustrated by comparing the deviations found for both crossbox channels between the measured air wave velocity and the vacuum speed of light.
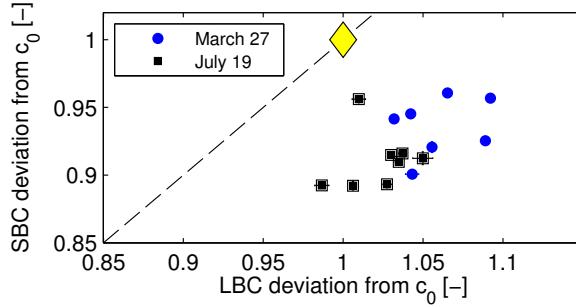
Figure 5.6: Comparison of the WARR-derived air wave velocities from c_0 for both crossbox channels acquired with the normal IDS four-channel setup. Ideally all values should hit the yellow diamond.

Such deviations of the LCBC derived velocities versus the deviations of the corresponding SCBC derived velocities are plotted for two exemplary datasets in Figure 5.6. As can be seen clearly, there is a systematic deviation, both from the intended value and the one-to-one line. LCBC derived velocities tend to be overestimated by up to 10%, whereas SCBC derived values for c_0 tend to be systematically underestimated to a similar extent in the same measurement. There is also a large spread which can be observed between different measurements. Since the WARR approach for estimating direct air wave velocities depends on fitting the slope of a specific feature pick of the air wave in the considered radargram, any deviation in Figure 5.6 can a priori have two reasons: There is an effect either affecting the time or the space axis. Since

WARR measurements are executed with one common measurement wheel, any error in the wheel calibration would affect the space axis for both crossbox channels in the same fashion. This is however not the case, hence an effect impacting the time axis has to be responsible which differently affects both crossbox channels.

For evaluating the velocities leading to Figure 5.6, always the full possible extent of picking the same feature throughout all considered WARR radargrams has been used, which is usually in the range of $1 \ldots 4$ m. More detailed evaluation of the different picks shows that the results seem to depend on the picking extent. Using different parts of the respective picks for fitting the air wave velocities leads to considerable variations in the result shown in Figure 5.6. Hence, for more detailed investigation, we will resort to the simplest possible WARR measurement and discuss the evaluation of several AIRWARR measurements which have been acquired over the past several years.

5.4.1 Wavelet variation in AIRWARR measurements

An AIRWARR measurement is executed just like a normal WARR measurement, with the only difference being that the antennas have been turned sideways by 90°, to ensure that the signal is traveling through the air only. Hence, fitting the velocity of the observed direct signal between corresponding transmitters and receivers should yield a close estimate for c_0. Furthermore the wavelet shape should be stable for all considered antenna separations, since the only change is adding more air between transmitter and receiver while moving the antennas apart. As it turns out, the latter is not the case. In fact, there is quite a considerable variation of the wavelet shape with antenna separation to be observed. If referenced to the first zero crossing, the position of other wavelet features may shift by about 0.4 ns with increasing antenna separation, as can be seen from the explicitly marked wavelets for the two crossbox channels from a nominally 400 MHz AIRWARR measurement in Figure 5.7.

This effect gets reflected in the respective frequency spectrum of the air wave wavelet at each specific antenna separation. Hence we can also consider the resulting change in the center frequency of the air wave wavelet with increasing antenna separation, as pictured in Figure 5.8. This figure shows that the resulting change in center frequency seems to depend only on the specific combination of transmitters and receivers and not on the employed measurement setup. Also, there seems to be some periodicity, especially for the T1R2 combination, excluding a simple dispersive effect.

This effect was investigated in more detail by changing the cables which connect the antennas to the control unit, which does have a significant impact on the result: In the normal setup, the first antenna (the box with T1R1) is connected to the control unit by a short cable of 0.3 m length, since the control unit is normally mounted directly on this antenna. For the second antenna, a 5 m connecting cable is usually used. This setup leads to the results shown in Figure 5.8. Exchanging the short cable connecting the first antenna for a second 5 m cable gives distinctively different results as pictured in
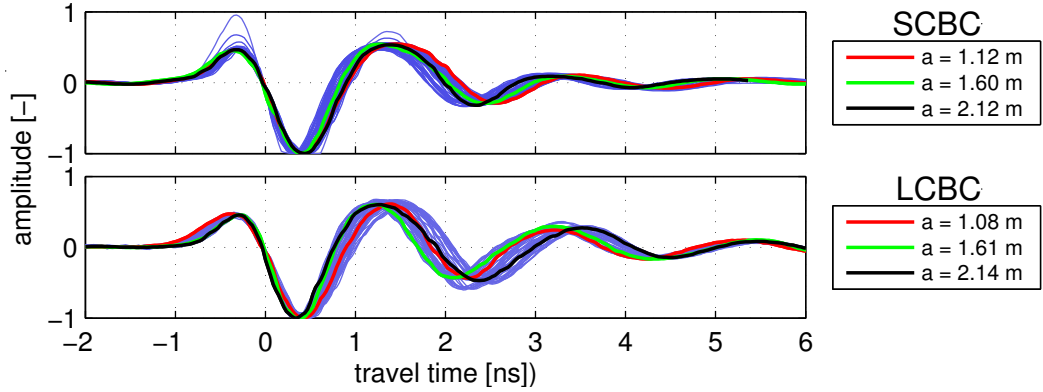
Figure 5.7: All air wave wavelets (light blue) for the two crossbox channels of an exemplary AIRWARR measurement taken with the standard IDS four-channel setup. All wavelets have been referenced to the first zero-crossing. Wavelets acquired at three specific distances have been explicitly marked. A corresponding time-lapse movie can be found in the digital supplementary materials, see Appendix B.

Figure 5.9. Also, exchanging the 5 m cable in the normal setup for an even longer 15 m cable leads to qualitatively the same result as in Figure 5.8, but the periodic variation of the wavelet shape for the T1R2 combination exhibits a much larger periodicity (not shown). Physically exchanging one antenna box for a different antenna also changes the signature variation of the wavelet shape with antenna separation, which then is similar for all different measurement setups as well, as observed in Figures 5.8 and 5.9. This is also true for using the nominally 200 MHz center frequency antennas.

In summary, there seems to be an effect leading to a distinct variation of the recorded wavelet shape which does not depend on the relative positioning of transmitters and receivers but on the length of the employed connecting cables and the antennas in use. This effect is independent of the specific antenna orientation and partly exhibits periodic variation, which excludes simple near-field influences. Hence, this effect is most likely connected to the digital sampling procedure of the signal. Our system employs a multiplexer in the control unit for jointly managing all possible Tx-Rx combinations, with trigger generation and A/D conversion using the same circuit (*IDS, personal communication*). Hence, if the transmission time of signals along the connecting cables is not negligible, the physical time when the signal is sampled will differ for the two setups shown in Figures 5.8 and 5.9, due to the different cable lengths which connect the antennaboxes to the joint control unit. If there is a non-linear variation of the oscillator frequency determining the precise time of signal sampling, the digital representation of the analog signal can get stretched or compressed, depending on its respective arrival time. Such a possible variation of the time base of the measurement has been mentioned before as a possible source of random error (e.g. *Jacob and Hermance* [2005]). However, the high reproduciblity of the

(a) center frequency as a function of antenna separation   **(b)** different setups
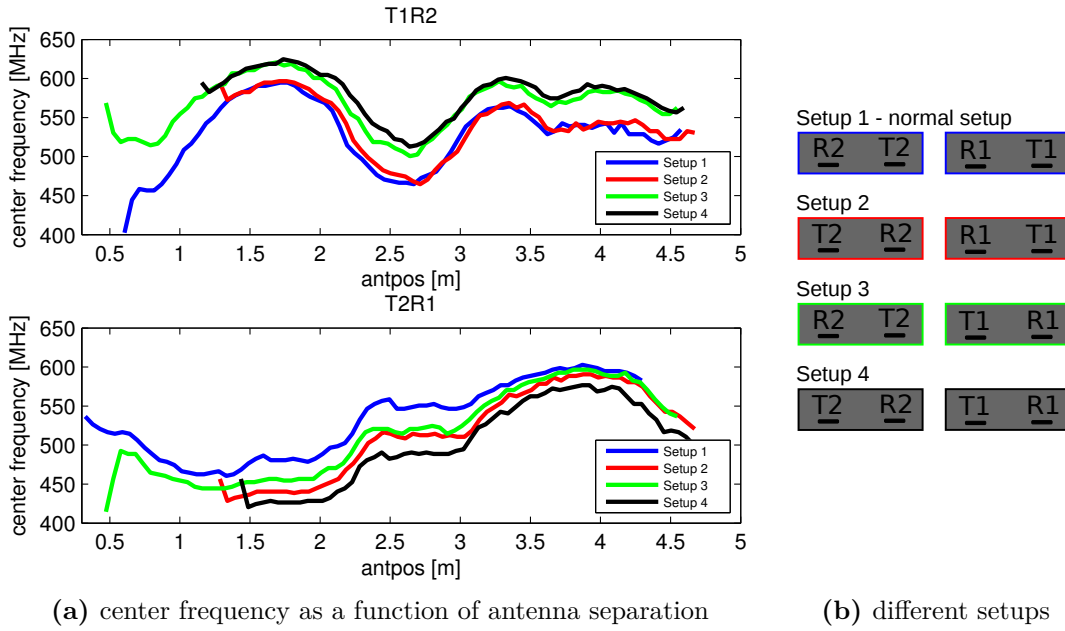
Figure 5.8: Center frequency variation of the air wave wavelet as a function of antenna separation, pictured for both crossbox TR combinations in the four different setups shown to the right. The first antennabox (T1R1) is connected with a short cable (0.3 m), the second (T2R2) with a long cable (5.0 m) to the control unit.

results shown here would imply that there has to be a stable relationship between the time of sampling and the corresponding variation of the oscillator frequency.

5.4.2 Expected consequences

From the considerations in the preceding section, one can expect a variation of the signal wavelet shape depending on the time it is sampled at the receiving antenna. If wavelets recorded in multi-offset measurements are referenced to the first zero crossing, their later features may be shifted by up to 0.4 ns over the whole range of a WARR measurement of some 5 m, judging from Figure 5.7. The non-monotonic nature of this shift makes it hard to quantify the effect, e.g. with respect to a certain travel time delay as a function of recording time. In any case, for WARR-derived velocities, this yields the deviation of up to 10% which was shown in Figure 5.6.

At the same time this might also have an effect on the precision of common offset measurements, as it might distort the relative positions of a picked ground wave feature for different wavelets recorded along a measurement line if the water content along this investigated profile changes significantly. In general, the effect of such a time shift of less than 0.4 ns can be expected to be less than 0.01 $\mathrm{m^3/m^3}$ in water content for a common offset measurement and it will probably not have a significant impact for field applications. However, such an

(a) center frequency as a function of antenna separation   **(b)** employed setups
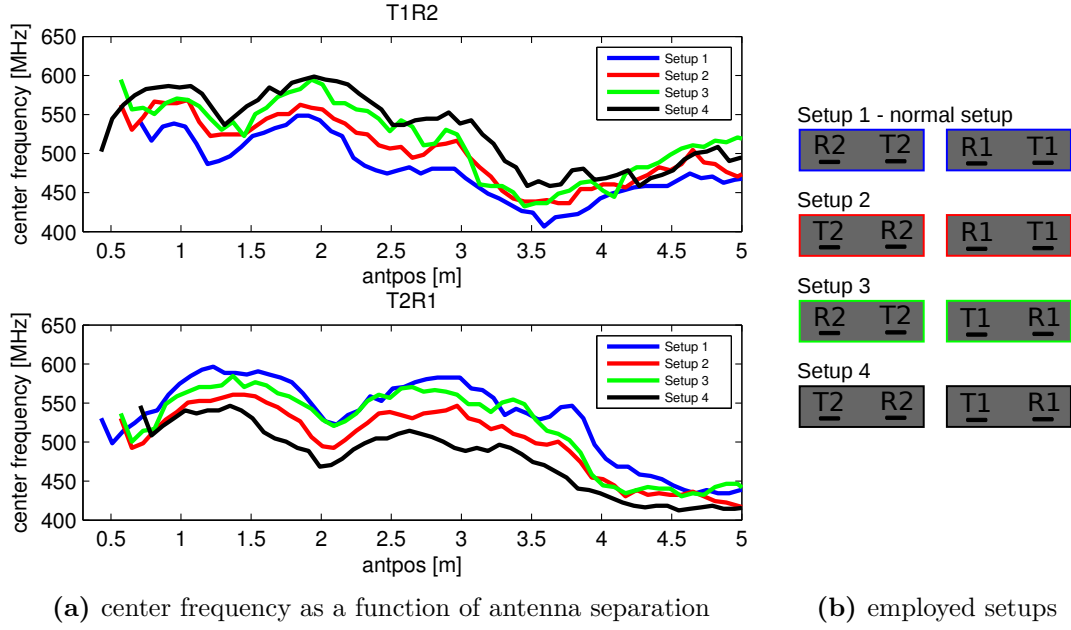
Figure 5.9: Center frequency variation of the air wave wavelet as a function of antenna separation for both channels in all considered setups, if both antennaboxes are connected to the control unit with long cables (5 m).

effect has the right magnitude to account for the higher order structures which are still present in the datasets shown in Figure 5.4 after the ground wave calibration correction has been applied. That figure shows that after the correction, there is still some variation in retrieved water content with an increase in antenna separation. Since total travel time will increase with an increase in antenna separation, the just described effects could lead to such a variation. Furthermore, this effect will also affect all other data like reflected signals, depending on their specific recording time. As such, this effect is a candidate for explaining inconsistencies which can be observed for different channels in high precision measurements (compare the uncertainty discussion (Section 7.3.5 in Chapter 7).

Implementing a direct correction for this effect will be difficult. The straight forward approach for WARR measurements – using the fitted air wave velocity for calculating a dt-correction factor, and then scaling the time axis accordingly – suffers from two major challenges: As has become clear from the discussion in this section, the exact deviation depends on the used range of antenna offsets due to the non-monotonic effect with antenna separation. Hence, any potential correction factor will suffer from a large uncertainty. Secondly, due to the antenna shielding, the signal to noise ratio of the air wave in a ground measurement is usually not very good, hence one might again introduce a larger error than the one which is to be corrected for. Still, as we will see in the following section,

there is potential for successfully employing such a correction under certain conditions.

5.5 A Time Base Correction for Evaluating Dispersive GPR Signals

In February 2012, GPR measurements have been conducted with the standard IDS four-channel setup on a frozen lake close to Heidelberg in order to test the radar equipment under well defined conditions. The thickness of the ice sheet was about 0.17 m. Several multi-offset measurements were carried out at nominal center frequencies of 200 MHz. The radargrams for the two crossbox channels of an exemplary WARR measurement are shown in Figure 5.10, where the TE component of the electrical field has been recorded as usual for our setup. The radargrams have been normalized to the maximum value of each trace. Clearly visible in these radargrams is the shingling effect signifying that the phase velocity of different frequency components of the propagating signal pulse is not equal to the overall group velocity. This effect is indicative for guided wave propagation between the transmitting and receiving antennas. Due to the dielectric contrast and the thickness of the ice layer, the largest part of the wave energy gets trapped inside the ice layer by total reflection at the interfaces, leading to modal propagation within this layer. A movie illustrating this effect as calculated by a corresponding numerical simulation can be found in the digital supplementary materials, as described in Appendix B.

The basic principles of evaluating such a signal have been introduced in Section 3.4.1. Here, first the evaluation process will be briefly described. Next, it will be shown, that the evaluation result will in our case only be reliable if a dt-correction as discussed in the previous section is applied before the evaluation. This will be substantiated through numerical simulation of WARR radargrams for the respective inversion results. Finally, it will be observed, that the LCBC signal cannot be used for such a waveguide inversion processing.

5.5.1 Inversion procedure

The evaluation employed here is based on dispersed signals observed in CMP or WARR radargrams. In the evaluation process (i) unwanted signal contributions are muted by an appropriate windowed filter function, ensuring that only the guided wave signal is used for evaluation, (ii) the phase velocity spectrum is calculated from this part of the radargram and normalized to the maximum power of each frequency, (iii) the maxima for the dispersion curve(s) for the mode(s) propagating in the waveguiding layer are picked by a semi-automated algorithm, and (iv) a combined local and global search algorithm is used for inverting these dispersion curves for the parameters of interest. A detailed description of this whole inversion process can be found in *van der Kruk et al.* [2007].

(a) SCBC WARR radargram   **(b)** LCBC WARR radargram
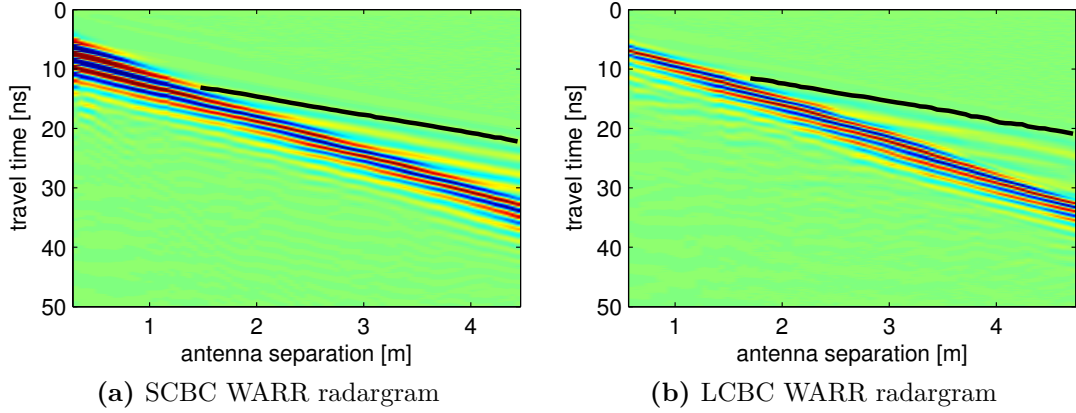
Figure 5.10: WARR Radargrams measured on ice, normalized trace by trace. The black lines show the air wave picks to be used for the dt-correction.

5.5.2 Inversion results for the SCBC data

The objective here is to show, that while using the uncorrected SCBC within such an inversion framework the final result is quite far from acceptable values, applying a dt-correction leads to significant improvement. For this purpose, the SCBC radargram displayed in Figure 5.10a was first inverted without any correction. Then, a dt-correction factor was calculated from the air wave velocity fit to the pick drawn in black in Figure 5.10a, yielding a factor of $dt_{corr} = 1.095$. For the second inversion, the time axis was scaled with this factor. All diagrams showing the different processing steps stem from this second evaluation process, showing the results after the correction.

Before calculating the phase velocity spectrum, the air wave and other unwanted features have been muted out by a windowed filter function; the corresponding preprocessing result is shown in Figure 5.11a. For calculating the phase velocity spectrum of the waveguiding signal in that radargram, a suitable window for evaluation was chosen: In order to exclude antenna proximity effects, only the signal part in the black box has been used for further evaluation. The averaged frequency spectrum for the traces within this window after the muting is shown in Figure 5.11b. Most of the radiated energy is recorded at frequencies between 250 and 800 MHz. This can also be seen in the phase velocity spectrum calculated for the evaluation window shown in Figure 5.11c, where the colorscale represents energy as a function of frequency and phase velocity. The corresponding normalized phase-velocity spectrum which has been normalized for the maximum energy value for each frequency is shown in Figure 5.11d. Due to our measurement setup and the bandwidth of our instrument, we have just the dispersion curve for the TE1 mode available for inversion, which can be seen clearly for frequencies between 400 and 800 MHz. Below 150 MHz, and beyond 800 MHz, the signal seems to get quite noisy, but it has to be kept in mind that due to the limited bandwith of our antenna system, there is very little energy being

(a) preprocessed radargram

(b) average frequency power spectrum

(c) non-normalized phase velocity spectrum

(d) normalized phase velocity spectrum, including the picked (yellow) and the inverted TE1 dispersion curve (black)
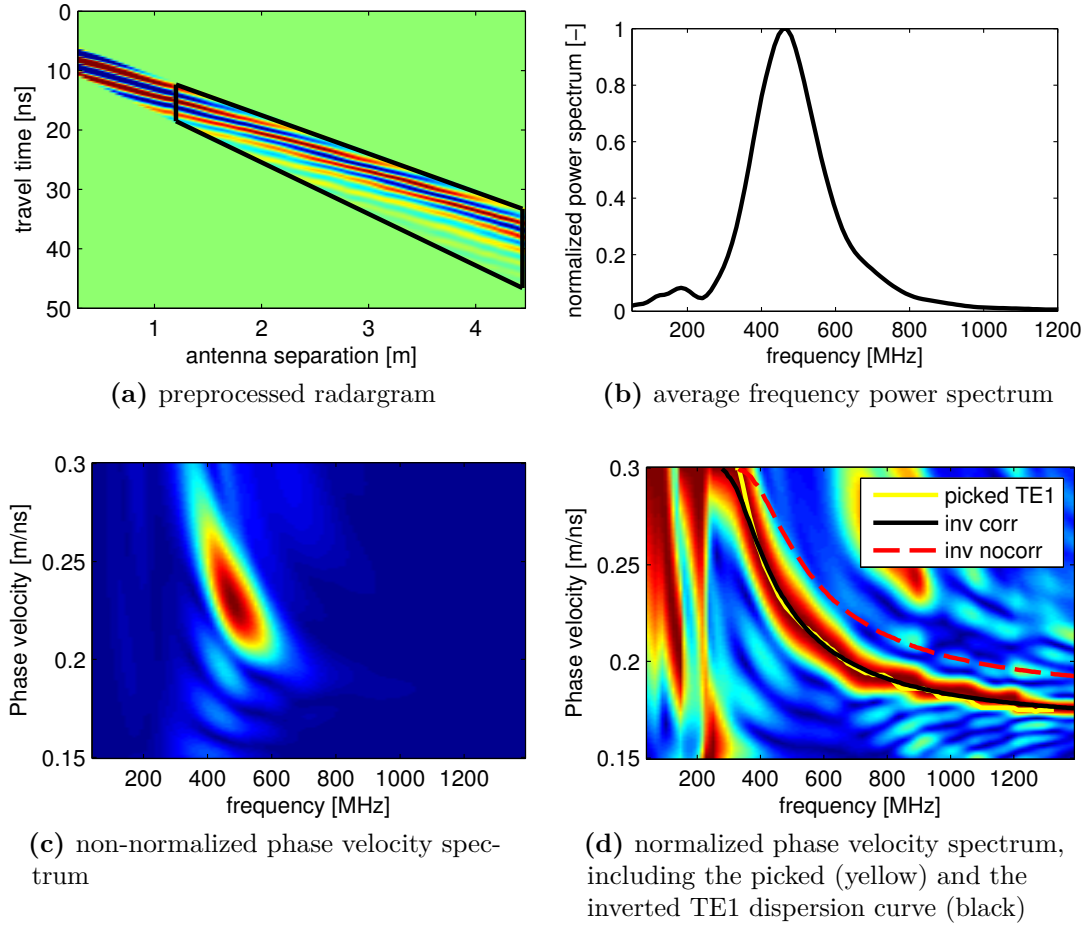
Figure 5.11: Waveguiding Evaluation for the **SCBC** data. Top left shows the preprocessed data after application of the muting filter window. The phase velocity spectrum (as illustrated in the two bottom diagrams) used for the inversion is calculated from the signal part within the black box. Top right shows the average frequency spectrum of this signal part. The colorscale of the bottom left diagram denotes non-normalized power within the corresponding phase velocity spectrum, the bottom right diagram shows the same spectrum after normalization on the maximum power for each frequency. Also pictured are the picked TE1 dispersion curve (yellow) and the inverted curve before (dashed red) and after (solid black) applying the correction.

radiated at these frequencies. For that reason, the dispersion curve as shown by the yellow pick was only used at frequencies below 800 MHz for the inversion process.

The inverted parameters for both inversion runs can be found in Table 5.4. For crosschecking the results, the respective theoretically expected dispersion curves have been calculated and drawn into Figure 5.11d, with the corrected result pictured by the solid black line and

the expectation from the uncorrected inversion pictured by the dashed red line. Clearly, the dispersion curve calculated with the uncorrected inversion result cannot represent the data.

5.5.3 Considerations on uncertainty

In order to test the robustness of these results, the whole process was repeated several times, slightly varying the muting window and the extent of the dispersion curve picked which were used for evaluation. This leads to some variation in the inversion result, but it does not change the qualitative result. For example, the uncorrected $\varepsilon_{\mathrm{wg}}$ varies between 2.7 and 2.8, while the inversion result for the corrected data will always be in the region of 3.2-3.3. Of course, these tests cannot replace a formal treatment of uncertainty in the inversion process, but it can savely be concluded, that the differences of the inversion result cannot be traced back to the choice of input parameters.

As a side remark, a formal treatment of uncertainty would not only have to include the different choices for the input parameters (like muting window size, muting range, antenna separation range used for inversion, etc.) but would also need to account for the fact that the uncertainty of the picked dispersion curve will depend on the energy which is recorded at each given frequency. For example, as can be seen from the non-normalized phase-velocity spectrum in Figure 5.11c, the dispersion curve has to be interpreted with care for frequencies beyond 700 MHz, since there is almost no energy in this region due to the narrow bandwidth of the employed antenna system. This could e.g. be included in the inversion process by weighting the dispersion curve with the averaged power spectrum. A different approach has just been published by *Bikowski et al.* [2012], using a formal Bayesian inversion methodology to explicitly treat the measurement error in the inversion process.

5.5.4 On the waveguide inversion of LCBC data

In principle, the same evaluation procedure can be applied to the LCBC radargram, with the preprocessed result shown in Figure 5.12a. However, already from the average frequency power spectrum in Figure 5.12b, it can be seen that there seems to be an additional contribution around 200 MHz. Altering the evaluation window does not notably change this result. The corresponding phase velocity spectrum is pictured in Figure 5.11c.

Table 5.4: Waveguide Inversion Result SCBC

type	$\varepsilon_{\mathrm{wg}}$ [-]	d_{wg} [m]
uncorrected data	2.75	0.163
dt-corrected data	3.21	0.175

(a) preprocessed data; the phase velocity spectrum is calculated based on the black box

(b) average frequency power spectrum

(c) non-normalized phase velocity spectrum

(d) phase velocity spectrum; for comparison: the SCBC picked (yellow) and the SCBC inverted TE1 dispersion curve (black)
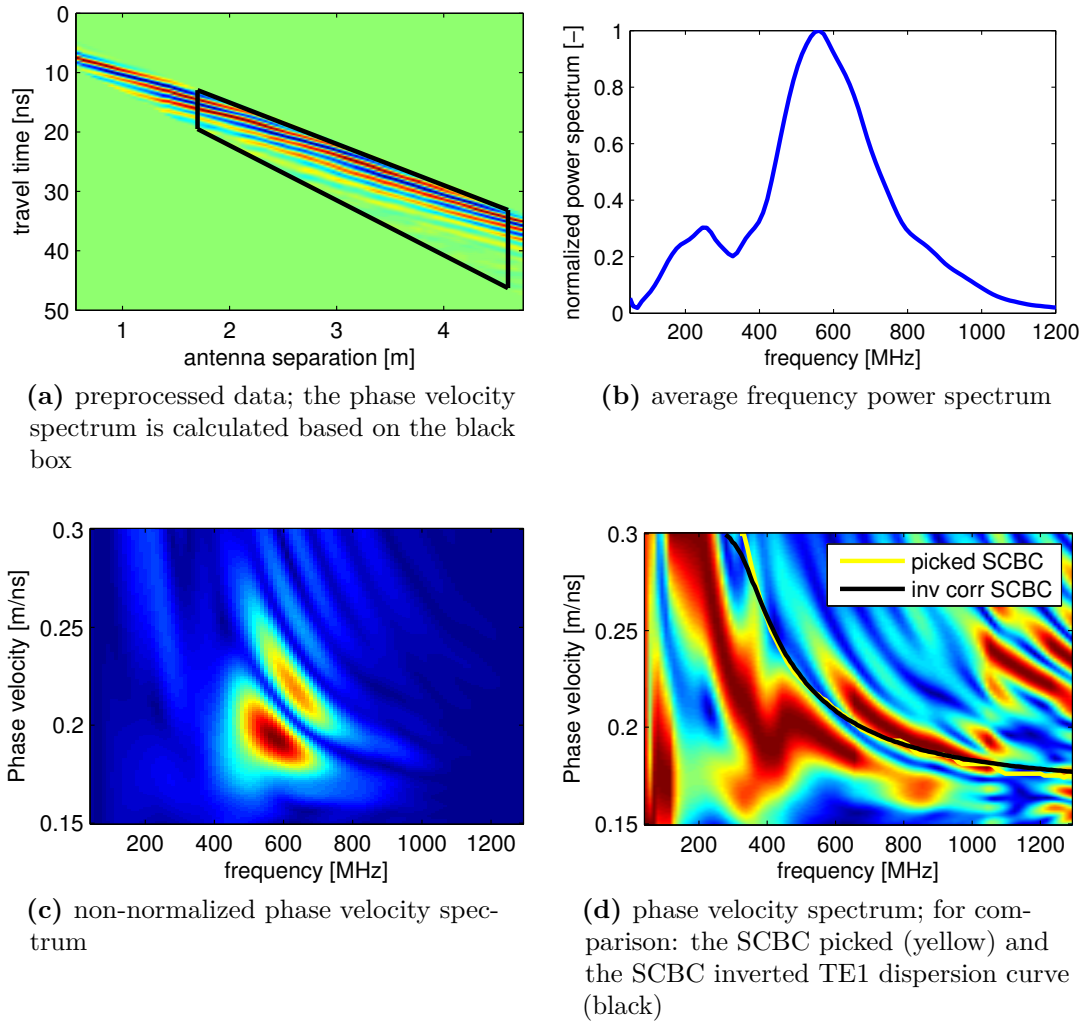
Figure 5.12: Waveguiding Evaluation for the **LCBC** data. The preprocessing procedure is identical to the SCBC data shown in figure 5.11. Since an inversion for this dataset was not possible, the bottom right diagram pictures the picked (yellow) and inverted (black) *SCBC* dispersion curves for comparison.

In contrast to the SCBC data, there are additional contributions to be seen as well. Normalizing the phase velocity spectrum for each frequency (Figure 5.12d), the features seem to be significantly distorted when compared to the SCBC data. For this comparison, also the yellow and black curves denoting the picked and inverted dispersion curve shape from the SCBC radargram have been drawn into Figure 5.12d. Clearly, there does not seem to be a single dispersion curve which can be used for evaluation.

Since the observed features for the LCBC remain similar also for other measurements

taken on the same day, this result is most likely due to the fact that for the LCBC there are always the SCBC-transmitter and receiver located in between. This might have a crucial impact on the propagation of the guided wave in the ice layer beneath, potentially altering the characteristics as seen in this diagram. To investigate this more closely, additional datasets measured with different antenna setups would be needed.

5.5.5 Summary

For our purposes, this section has yielded two notable results. First, for the evaluation of dispersive GPR signals of the SCBC, we can implement a dt-correction based on the direct air wave signal, significantly improving the inversion result. The reason that in this case such a correction works is most likely due to the fact, that the same antenna separation range was used both for deriving the correction and calculating the waveguide properties. Second, dispersive LCBC signals derived from this multi-channel setup seem to be disturbed by the presence of the other channel's transmitter and receiver and thus cannot be used for evaluation.

(a) Δt for air wave and ground wave

(b) Δt for ground wave and a reflection at $d = 0.8$m
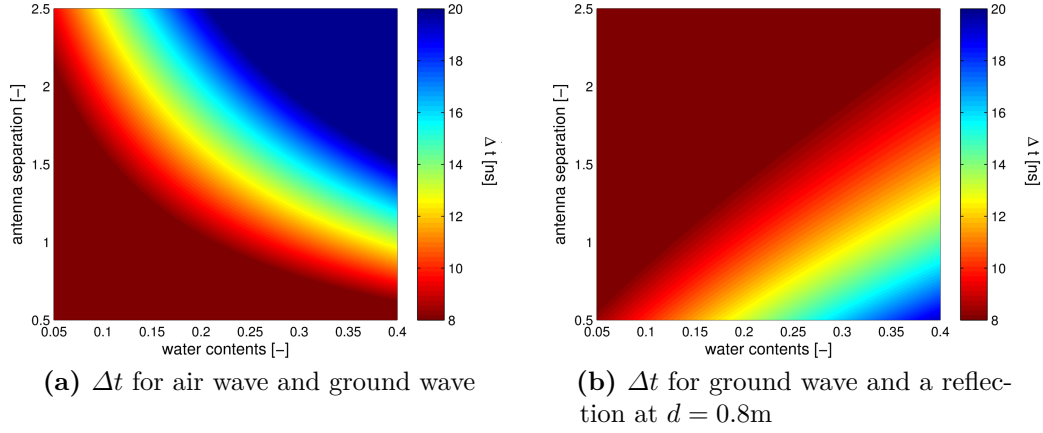
Figure 5.13: Travel time differences Δt between the direct ground wave signal, the direct air wave and a reflection at a depth of $d = 0.8$ m as a function of the wetness condition of the topsoil layer and the employed antenna separation.

5.6 Signal Interference Constraints

The first part of this chapter has dealt with issues which are connected to instrument capabilities or are related to the measurement setup, but seem to be mostly independent of the site characteristics. In this part we now assume an ideal instrument and consider the influence of site characteristics on the ability to reliably estimate near-surface dielectric permittivities. A crucial issue for all common evaluation methods of WARR and CO ground wave data is the possible influence of interferences with other signal parts. Candidates are e.g. an imperfectly shielded air wave signal and also shallow reflections or refractions. As has been seen e.g. from Figure 5.1, the ground wave wavelet of our instruments has a width of about 6-8 ns, which is determined by the bandwidth of the employed antenna system. Hence, in order to ensure that the ground wave wavelet cannot be distorted by any interfering wavelet, one could require a time difference of at least 8 ns between the central features of the different wavelets in question, completely separating them.

5.6.1 Defining an interference-free trust region

To illustrate this requirement we envision a two layered medium, with a layer boundary at 0.8 m. Neglecting the possibility of refracted waves or even waveguiding effects which might occur as well, we would expect in this case at least three different kinds of signals: The direct air wave, the direct ground wave and the reflection from the layer boundary. Now, for a completely undisturbed direct ground wave wavelet, its travel time has to differ by at least 8 ns from the other wavelets. The arrival time difference at the receiving antenna is a function of both the employed antenna separation a and the water content of

(a) Reflector depth at 0.8 m   **(b)** Reflector depth at 1.0 m
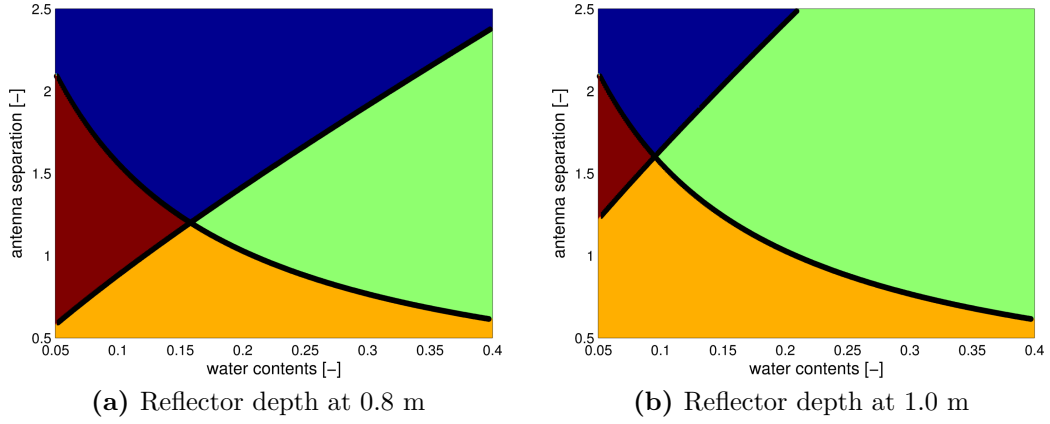
Figure 5.14: Trust regions for the case of two different reflector depths as a function of water content and antenna separation. In the green area, all signals are well separable, blue indicates interference of the reflection signal, orange an interfering air wavelet and dark red the interference of both.

the upper soil layer. This is illustrated by Figure 5.13, showing the travel time difference between air and ground wave as well as ground wave and the reflection from the layer boundary at 0.8 m depth as a function of water content and antenna separation.

As shown in Figure 5.13a, the air wave interferes for small antenna separations and small water contents, since the travel time difference will increase for longer antenna separations or wetter soil conditions. The reflection on the other hand will interfere at longer antenna separations (Figure 5.13b) as the pathway difference between the ground wave and the reflection becomes increasingly negligible.

Combining these two considerations, we can define a trust region of antenna separations under certain wetness conditions, where the existence of a completely undisturbed ground wave signal can be expected. The result is shown in Figure 5.14 for two different reflector depths of 0.8 m and 1.0 m. The green area denotes measurement conditions under which all three signals should be well separable and hence no interferences can occur. The blue region denotes conditions where a reflection from the respective depth will possibly interfere with the ground wave. In the orange region, we could expect the air wave to interfere. For the red region, both interferences from the air wave and the reflection can be expected. These two figures show that especially under dry conditions, the margin for completely interference free measurements is quite small if there is a reflector at less than 1 m depth. For antenna separations between 1...2 m, an effective antenna shielding is mandatory in order to get any interference free ground wave measurements at low water contents.

Furthermore, Figure 5.14 shows that in general there is no single antenna separation
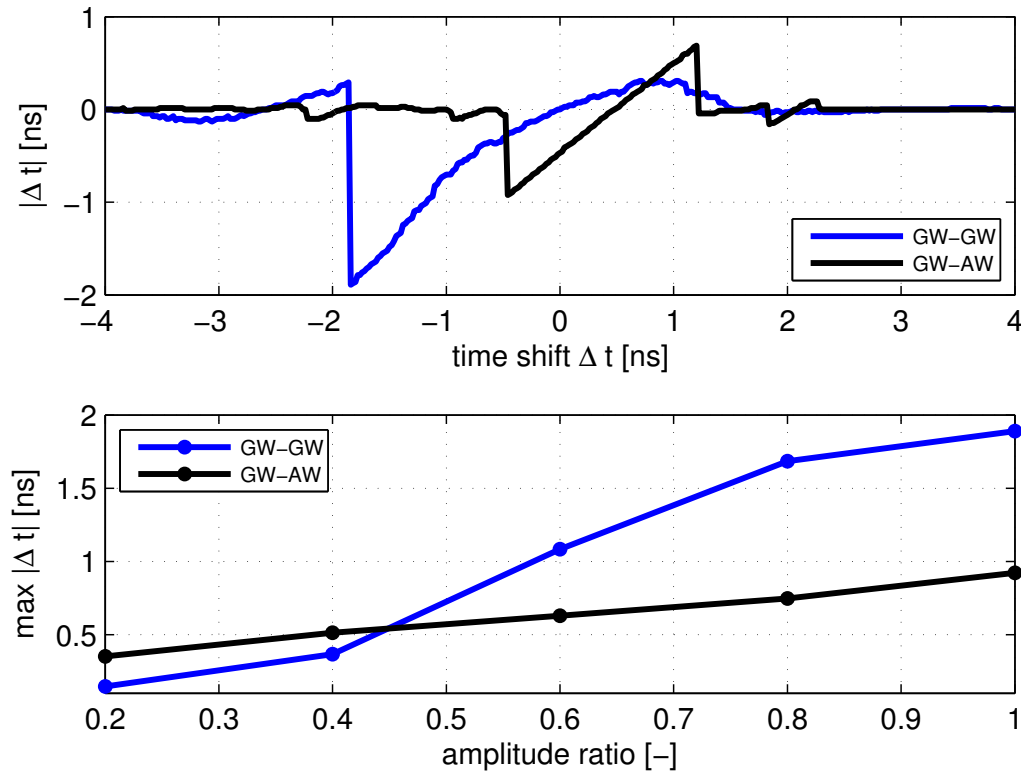
Figure 5.15: Influence of an interfering wavelet on the travel time of the central minimum feature of the ground wave. The upper part of the figure shows the induced travel time shift $|\Delta t|$ as a function of travel time difference to an air wavelet (black) or similar ground wavelet (blue), having the same maximum amplitude. The lower diagram shows the influence of the amplitude ratio of the two interfering wavelets on the maximum time shift.

which would guarantee absolute interference free results over the whole range of wetness conditions. Hence monitoring schemes based on CO measurements would possibly have to adapt the employed antenna separation accordingly. Similarly it can be expected that at some point within the range of antenna separations usually employed for evaluating the direct ground wave signal in a WARR radargram, the ground wave signal might not be interference free. Hence, great care has to be taken when interpreting the direct ground wave fit over a larger extent of antenna separations.

In the following section, the influence which can be expected of such an interfering wavelet on the retrieved travel time will be investigated more closely.

(a) time shift of $\Delta t = 0.5$ ns   **(b)** time shift of $\Delta t = 1$ ns
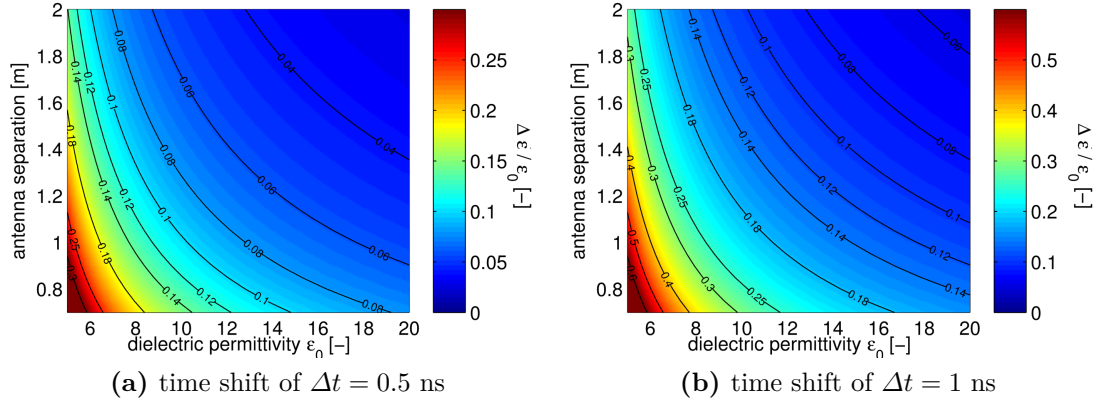
Figure 5.16: Relative uncertain imposed by a time shift of 0.5 ns (left) and 1 ns (right) on the retrieved dielectric permittivities ε_b as a function of prevalent wetness conditions of the soil as signified by permittivity ε_0 and the employed antenna separation.

5.6.2 Influence of interference effects on retrieved travel times

For assessing the impact of such an interfering wavelet on the retrieved travel time of the ground wave wavelet, we can calculate the shift of the central minimum feature of the ground wave wavelet as a function of the travel time difference to an interfering secondary wavelet. Since our focus is on interferences which might occur under certain situations in the field, we consider directly interferences between experimentally recorded wavelets. Two cases have been investigated here: Interference between the primary ground wave wavelet and a second wavelet of the same shape (which we for simplicity term GW-GW) and interference between the ground wave wavelet and an air wave wavelet (GW-AW). For these considerations, the experimentally recorded wavelets shown in Figure 5.1 have been employed. Also, different amplitude ratios between the primary and secondary wavelet have been considered.

The upper diagram of Figure 5.15 pictures the position of the central minimum of the primary wavelet, after superposition with the secondary wavelet which has been shifted by $|\Delta t|$. In this case, both wavelets have the same amplitude. As can be seen, the maximum deviation can be up to almost 2 ns, while the exact value for any given shift depends mainly on the exact shape of the interfering wavelet. As can be seen, this comparatively large time shift of the central minimum feature only occurs for travel time differences which are less than 2 ns: Within this range, the impact is significant and highly variable. However, for travel time differences larger than about 2 ns, the maximum impact is closer to 0.1 ns, which is only about twice the normal time resolution of our GPR measurements. The result remains similar if the interfering wavelet is flipped (not shown). As can be seen from the lower diagram of Figure 5.15, the maximum shift is mostly determined by the amplitude ratio. If the amplitude ratio is around 0.2, then the maximum possible

deviation remains below 0.5 ns. For larger amplitude ratios, the impact of a similar wavelet shape (GW-GW case) is significantly larger than for the GW-AW case. This corroborates the observation of a significant influence of the wavelet shape on the exact impact of the interference.

This result relaxes somewhat the strict constraints which were set in the previous section, at least for the cases considered here: If just a 3 ns separation is needed between interfering wavelets for reliable evaluation drastically improves the situation for the trust region argument made with Figure 5.14. Of course, other pathologic examples could be constructed with interfering distorted signals (e.g. stretched wavelets and the like), which could potentially lead to much larger time shifts of the wavelet feature in question. However, such distortions are not simply to be expected in the field under normal conditions. Hence, if such a case arose in reality, it should be clearly distinguishable in the field data and excluded from further evaluation.

5.6.3 Interference impact on the ground wave evaluation in CO data

For common offset measurements, the impact of such a time shift on the retrieved permittivities can be directly calculated. As an example, Figure 5.16 pictures the relative error of retrieved permittivity values as a function of wetness conditions of the soil and employed antenna separation for two different time shifts (note the different color scales). As expected, the influence of such a constant time shift will decrease with increasing antenna separation or under wetter soil conditions. However, especially for dry soil conditions the influence can be severe. For example for permittivities of $\varepsilon = 6 \ldots 8$ and antenna separations of $1 \ldots 1.5$ m, the relative error can be more than 10 % already for a time shift of 0.5 ns, limiting the attainable accuracy of the derived water contents. Obviously, these results are valid for any other effect leading to a similar time shift of several tenths of a nanosecond of the wavelet feature used for evaluation.

5.6.4 Interference impact on the ground wave evaluation in WARR data

The analysis of the influence of interference effects is more involved for WARR measurements, since the impact of an interfering wavelet will differ for each of the used antenna separations. Hence, we turn to numerical modeling. As a starting point, we use a 200 MHz center frequency dataset acquired at a field site in the vicinity of Enschede, The Netherlands. The soil profile consists of approximately 0.4 m of loamy sand overlying a sandy layer with a shallow groundwater table at about 1.5 m depth. Hence we can expect exactly the conditions discussed in the previous section: A shallow layer boundary which may generate a reflection potentially interfering with the measured ground wave wavelet. The topsoil was covered by grass and the overall topsoil conditions were fairly

(a) Measured SCBC WARR radargram   **(b)** Measured LCBC WARR radargram
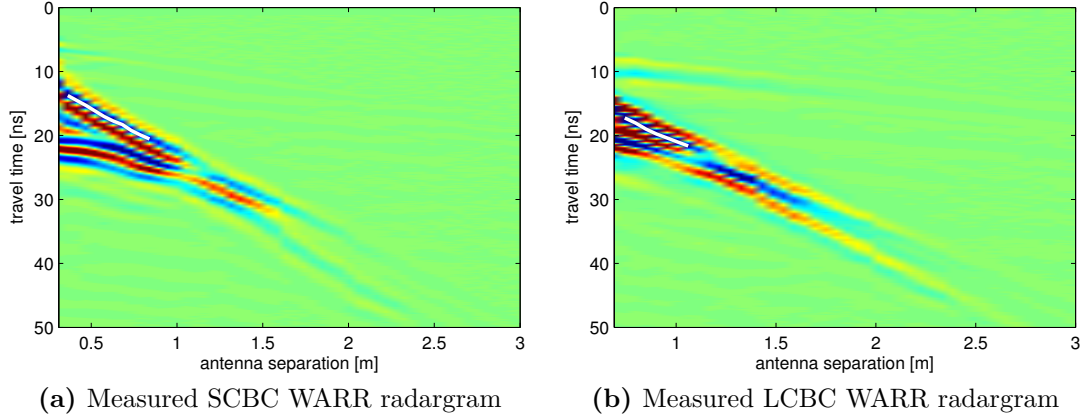
Figure 5.17: WARR data measured at the Enschede site, featuring a loamy sandy 0.4 m top soil layer with sandy soil beneath. The white picks are used for evaluation.

wet, 0.10 m TDR probes indicate topsoil water contents between 0.35...0.4. Using longer TDR rodlengths (0.2...0.4 m), the measured water content values vary between 0.28 and 0.32. Along a stretch of two meters, three consecutive WARR radargrams were recorded with a spacing of 1 m. The first SCBC WARR radargram is pictured in Figure 5.17a with the corresponding LCBC radargram shown in Figure 5.17b. As can be seen clearly, there is indeed a signal from the layer boundary present, which definitely interferes with the ground wave beyond antenna separations of about 1 m. Using only this short stretch of the ground wave yields a water content of 0.32 for the SCBC data and 0.29 for the LCBC radargram. The results for the other WARR measurements are in the same range. The GPR data seem to agree best with vertical TDR measurements based on 0.2 and 0.3 m rodlength, while the vertically measured 0.1 m TDR data show a decidedly higher water content, albeit with a considerable small scale variation. The question is how reliable the GPR derived water contents can be in the light of the presence of this shallow reflector, noting that the difference between the two crossbox channels does vary significantly with the choice of pick extent. The choices shown in Figure 5.17 essentially depend on expert judgment of the stretch of the signal which is deemed to be most trustworthy.

For a more systematic approach of determining the impact of this shallow reflection on the ground wave derived water contents, we can turn to synthetic datasets. In a first step, we use the GPRMax 2D numerical simulator (e.g. *Giannopoulos* [2005]) and use a Ricker-type source wavelet to calculate WARR radargrams for a two layered system with the layer boundary at varying depths. Taking the case just discussed, the upper-layer permittivity is set to $\varepsilon_1 = 22$ (corresponding to a water content of about 0.38), compatible with the range of 10 cm TDR values. Since we do not have any quantitative information about the lower layer, we just assume a drier value of $\varepsilon_1 = 12$ corresponding to a water content of

(a) Simulated WARR radargram with layer boundary at 0.4 m depth

(b) Permittivity values derived from all simulated WARR radargrams
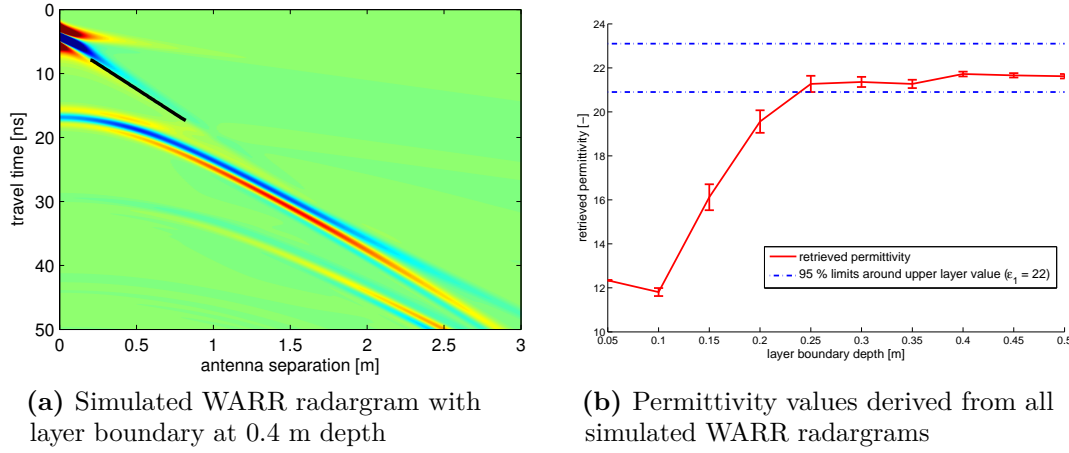
Figure 5.18: Modeling results for a two layer case with a wet ($\varepsilon_1 = 22$) top soil layer over a drier $\varepsilon_2 = 12$ soil. On the left, the radargram shows the result for the layer boundary at 0.4 m depth. The black pick has been used for permittivity evaluation. The diagram on the right pictures the retrieved permittivities for all considered reflector depths.

about 0.22) for producing a strong contrast. The modeling result for the case of the layer boundary at 0.4 m depth is shown in Figure 5.18a. Evaluating the slope of the ground wave pick (drawn in black) yields a permittivity value of 21.6 ± 0.5. Similarly, modeled radargrams with the layer boundary at different depths can be evaluated. The resulting permittivities are pictured in Figure 5.18b. From these permittivities, we can draw the conclusion that for the case investigated here, the true permittivity can be reasonably well retrieved if the layer boundary is deeper than about 0.25 m, keeping in mind that this represents a rather favorable case, since the top-layer was assumed to be rather wet.

From a broader perspective, these considerations could be transferred to different parameters sets. Eventually, rastering the permittivity - layer boundary depth parameter space depending on the site characteristics would yield a handle on reliably evaluable conditions. Such a quick modeling check for the influence of possible interferences could easily be included when investigating the reliability of a ground wave based monitoring scheme for a specific field site.

There are several further considerations possible which would lead to a even more realistic result. First, as we have seen in Section 5.6.2, the impact of the interference depends on the shape of the involved wavelets. Hence, the modeling procedure could be adapted to account for the experimental source wavelet. Furthermore, for ensuring a more realistic result, such a modeling scheme should be extended to include soil water content profiles instead of the simple two layer case. For example, we can use HYDRUS1D (*Simunek et al.* [2005]) to calculate a stationary water content profile, using a topsoil water content of $\theta_{\text{top}} = 0.4$, a water table at -1.5 m and the standard Mualem van Genuchten parameter

(a) Simulated soil water content profile

(b) Simulated WARR radargram
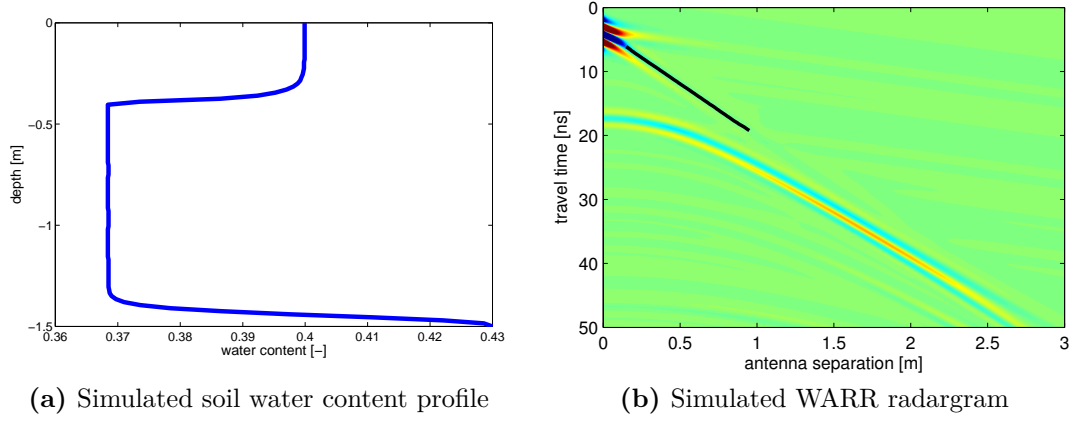
Figure 5.19: Modeled WARR radargram (right) for a simulated stationary soil water content profile as shown on the left.

sets provided with HYDRUS (based on *Carsel and Parrish* [1988]) for 0.4 m of loamy sand overlying a 1.1 m sand layer. The resulting soil water content profile is shown in Figure 5.19a. Converting this soil water content profile into permittivities, and discretizing into layers of 0.01 m, we can again calculate a corresponding WARR radargram with GPRMax2D, as shown in Figure 5.19b. Calculating the water content from the black pick in this figure yields for this case again a well compatible value of $\theta_{\text{top,retr}} = 0.405 \pm 0.005$.

5.7 Uncertainties Associated with the Petrophysical Relationship

In the previous sections, both instrument specific and measurement site dependent sources of uncertainty for deriving near-surface dielectric permittivities have been closely investigated. Assuming now well established and scrutinized permittivity values, the impact of the auxiliary data which are needed to convert these dielectric permittivity values into water contents as well as the choice for geometry factor α (setting $\alpha = 0.5$ in equation 2.19) will be discussed in this section.

As can be seen from equation 2.20, using the CRIM formula for linking the measured permittivities to water contents, there are three additionally needed parameters: The soil porosity ϕ, the dielectric permittivity of the soil matrix ε_s and the permittivity of water ε_w, which varies with soil temperature T_{soil}. For the near-surface, all three values are generally assumed to be constant along a given measurement line. As long as this assumption is valid, any uncertainty of these two parameters will only affect the accuracy and not the precision of the resulting water contents. Still, the impacts of uncertainties in the absolute values of these two parameters on the resulting water contents warrant closer attention.

5.7.1 Soil porosity ϕ

Porosity values are usually estimated from gravimetric samples of known volume. Sources of error include disturbances of the soil while the sample is taken, water loss before the first weight measurement and deformations of the probe cylinders. The latter two sources of uncertainty can be minimized by careful field operations and a separate determination of the probe volume after extracting the analyzed soil sample. A possible compaction can be harder to avoid however, depending on the specific soil conditions. Typical porosity values for the measurement sites considered in this thesis range between 0.3 and 0.5. For peat soils with high organic matter content, the values can be much larger. If there are no site specific values available, porosities between 0.4 and 0.45 are a good assumption for sandy soils (compare e.g. *Robinson and Friedman* [2003]). From field experience and the range of observed values, the associated uncertainty has to be assumed to be around 0.05. The influence of this uncertainty on the retrieved water content is illustrated in Figure 5.20a, where constant values of $\varepsilon_s = 5$ and $T_{\text{soil}} = 20°C$ have been assumed. As a rule of thumb, the error in water content is about 0.009 for every error in porosity of 0.05. Since the absolute uncertainty is constant for all permittivity values, the relative error will decrease with increasing water contents.

5.7.2 Soil temperature T_{soil}

Soil temperatures should be well determinable from onsite measurements, at least for the near-surface. The only issue which might arise could be a changing temperature over the course of a measurement day, which is especially the case for the semi-desert data sets subject to a high radiative forcing. In any case, the influence of temperature on the retrieved water content is rather small, since it impacts solely the permittivity of free water ε_w which varies only from about 88 to 73 for temperatures between 0 °C and 40 °C. Since only the square root of ε_w is relevant for equation 2.20, the impact of a varying soil temperature is small for dry soil conditions and only becomes relevant at high water contents. This is illustrated in Figure 5.20b.

5.7.3 Soil matrix permittivity ε_s

Lacking site specific laboratory measurements, the soil matrix permittivity is normally estimated from literature values. Various sources state values between 4...8 at 100 MHz for the dielectric permittivity of minerals commonly found in soils (e.g. *Daniels et al.* [2004], *Rubin and Hubbard* [2005], *Davis and Annan* [1989]). Values given for dry sands are usually a little smaller (e.g. 2...6 in *Daniels et al.* [2004] or 4...6 in *Cassidy* [2009]), with pure quartz being reported to reach about 4.5 (*Knight* [2001]). This last study also gives a comprehensive overview of a range of experimental investigations of the dielectric properties of geological materials.

The variation in water contents as derived with respect to different soil matrix permittivities is pictured in Figure 5.20c. For this figure, the porosity has been assumed as $\phi = 0.4$ and soil temperature as $T_{\text{soil}} = 20°C$. For a change of ε_s from 4 to 6, the calculated water contents will vary for approximately 0.04. Especially when the GPR derived ε_b values are in a similar range of $6 \ldots 10$, this may lead to relative uncertainties of around 30 %. Again, the relative error in calculated water contents will be much smaller for wet soil conditions.

5.7.4 Geometry parameter α

An additional source of uncertainty lies in the choice for the geometry factor α. For field applications, an isotropic medium is usually assumed, which allows to set $\alpha = 0.5$, leading to the petrophysical relationship employed for this work (equation 2.20). However, as has recently been pointed out in a theoretical analysis by *Brovelli and Cassiani* [2008], this assumption may not always be valid and α might for instance depend also on the dielectric contrast between different phases. With respect to TDR measurements, *Roth et al.* [1990] have found for a range of soils the optimal value to be $\alpha = 0.46$, while *Ponizovsky et al.* [1999] report α-values between 0.35 and 0.49 for different soil types. These results have prompted *Steelman and Endres* [2011] to use α as an additional fitting parameter. Based on the comparison of GPR-derived water contents to gravimetric samples, their study reports best-fit values for α ranging between 0.11 and 0.52, apparently depending on the soil texture and the employed antenna frequency. However, since the latter apparent dependency already indicates that such an approach may not account for the nature of all occuring effects, we here continue to use $\alpha = 0.5$ and keep in mind, that anisotropies of the medium might be another potential source of uncertainty.

5.7.5 Summary

From these considerations, it can be concluded that a potential variation of soil permittivity is currently the largest source of uncertainty of the three parameters discussed here, taking into account the large range of values reported in the literature. Soil porosity determination leads to an uncertainty in the water content determination of approximately 0.01; uncertainties from soil temperature can be neglected for dry soil conditions.

Hence the accuracy of GPR derived water contents using the CRIM formula could profit from more detailed knowledge about the variation of ε_s and robust laboratory measurements of soil samples taken in the field. Recent laboratory experiments with sand samples measured in a coaxial cell indicate permittivity values for sands of approximately 4.9 (P. Bohleber, personal communication). Without access to site specific values, we hence assume a value of $\varepsilon_s = 5$ for all evaluations in this thesis. For characterizing the uncertainty of this value with respect to our field sites one could possibly design a series of laboratory experiments with different soil samples. Alternatively, time-series measurements in the field could help disentangle the contributing factors, since material properties like porosity and soil matrix permittivity should not change.
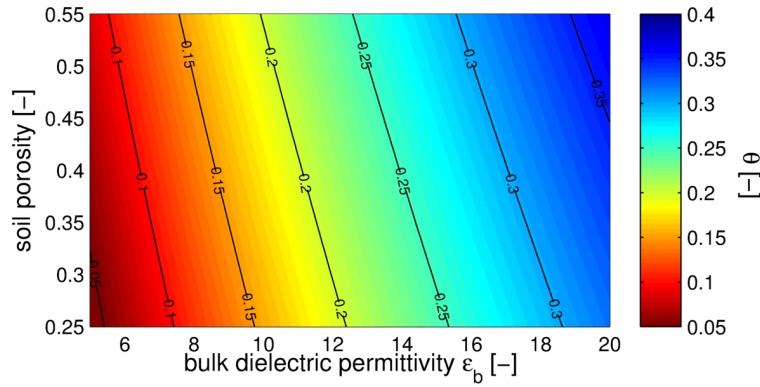
(a) Water content values calculated from ε_b as a function of different soil porosities ϕ
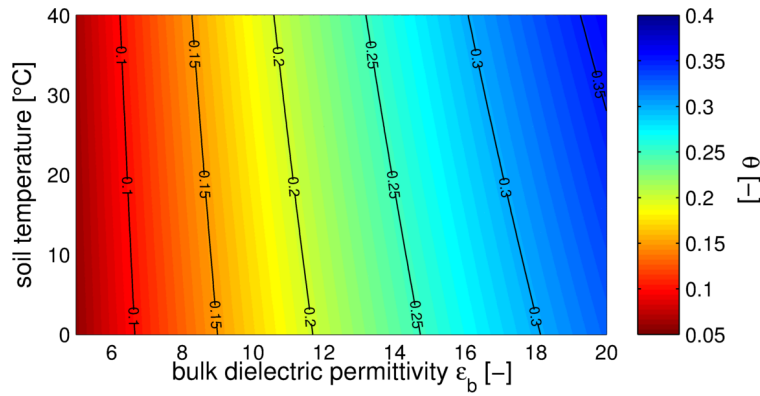
(b) Water content values calculated from ε_b as a function of different soil temperatures T_s
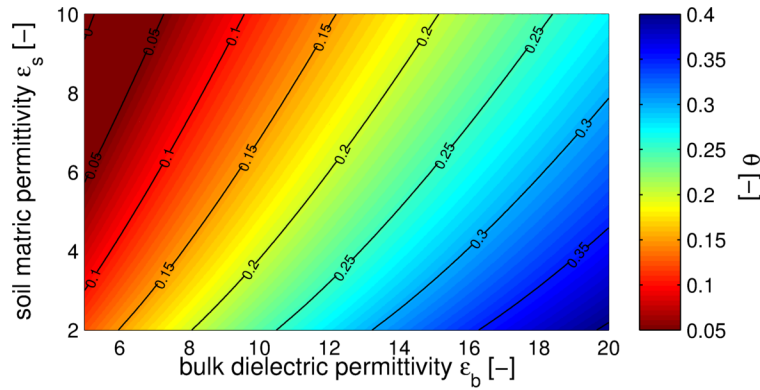
(c) Water content values calculated from ε_b as a function of different soil matrix permittivities ε_s

Figure 5.20: Influence of the different petrophysical parameters on water contents calculated from measured bulk dielectric permittivities ε_b.

5.8 Summary and Conclusions

This chapter has investigated some aspects of current GPR methods for estimating near-surface soil water content which impact the accuracy and precision of the result. The following conclusions should be drawn at this point before proceeding with applications:

- Commonly applied approaches for determining the time zero offset in common offset measurements (Section 5.2.1) cannot account for all occurring effects, even when the picking scheme is adapted to account for different wavelet shapes (Section 5.2.2). This is due to further ground coupling and near field effects, leading to additional contributions to the observed offset.

- For antenna separations between $1 \ldots 2$ m, a calibration procedure has been proposed and tested under several different soil conditions based on the two crossbox channels of our GPR system (Section 5.3). Based on four different datasets, a set of optimized calibration parameters has been found which is suitable for yielding results which are in good agreement with auxiliary data. After application of the calibration procedure, the averaged difference between permittivities derived from the different crossbox channels is less than 0.02. If needed, site specific calibration can further improve the result. For the cases reported in this chapter, the agreement between the channels after site specific calibration is better than 10^{-4} in permittivity.

- A second effect concerning the stability of the signal has been observed in AIRWARR measurements (5.4). The specific combination of antennas and connecting cables has a distinct impact on the shape of wavelets which are recorded at different antenna separations. This might have an impact on all data recorded at different absolute travel times and hence may for instance be responsible for the remaining variations which are still observed after the new common offset calibration procedure has been applied.

- In general a correction of this effect will not be possible, however, as has been shown in Section 5.5, the inversion result of dispersed GPR datasets can be significantly improved through a correction for the observed air wave velocity.

- Site specific characteristics which can lead to signal interference might be an issue for establishing monitoring schemes over a large range of different soil conditions (Section 5.6). Numerical modeling based on the specific site characteristics could aid in determining the reliability of WARR derived soil water contents (Section 5.6.4).

- The soil parameters which are needed for converting measured permittivities to soil water contents can be a major source of uncertainty, especially for dry soil conditions (Section 5.7). In dry soils, foremost the soil matrix permittivity ε_s can introduce a significant bias.

6 On the Reliability of the GPR Ground Wave for Measuring Near-Surface Soil Water Contents

In this chapter, the stability of the Ground-Penetrating Radar (GPR) ground wave signal and its applicability for measuring near-surface water contents is investigated at a semi-vegetated dune site close to the desert rim in Fukang, Xinjiang, P.R. China (a detailed site description is provided in section 4.2.2). Two separate measurement campaigns have visited this site in April 2010 and exactly one year later, both taking place just weeks after the annual snow melt, i.e. the most dynamic time in terms of soil water content change in this area.

First results from the 2010 data set have been presented by *Klenk et al.* [2011], concluding that the direct ground wave signal can be used as a stable proxy for measuring near-surface soil water content at this site. However, in the same study the absolute water content has been found to be difficult to establish without auxiliary information (e.g. through TDR point measurements), which has been attributed to the instrument limitations for time zero calibration. *Klenk et al.* [2012] has subsequently expanded on the previous study by comparing the data sets acquired in subsequent years. This chapter summarizes these results and additionally discusses the efficacy of employing the new calibration procedure for common offset ground wave datasets which has been developed in chapter 5.

6.1 Materials and Methods

All GPR measurements which will be considered in this chapter were acquired along a roughly 550 m long GPR profile perpendicularly crossing four north-south aligned dune chains, as can be seen in the snapshot taken from Google Earth™ shown in figure 6.1. GPR data were recorded with the IDS four channel setup as described in section 3.5. In 2010, measurements were executed at center frequencies of both 200 and 400 MHz. Traces were acquired every 0.3 m. For both center frequencies, the profile was consecutively measured with two different antenna-box separations (1 m and 1.5 m). These four profiles (P1...P4) were acquired within a time period of approximately two hours. Thus, evaluating both crossbox channels for each profile, we have a total of eight GPR data sets from 2010 to consider. In 2011, a further 400 MHz measurement has been acquired at an antenna box separation of 1.5 m, denoted as P5. The 2010, GPR data have been acquired at a trace spacing of $dx = 0.3$ m, while in 2011 traces have been acquired every 0.05 m. For clarity of terminology, a short overview of pertinent profile parameters is provided in table 6.1. Following the discussion in section 5.3, we will here first focus on the long crossbox

Figure 6.1: Google Earth™ snapshot of the 550 m GPR line measurement area. The satellite image was acquired two months after the measurement. The measurement line (red dots) as well as locations of soil profiles (blue squares) have been marked for clarity.

channel (LCBC, antenna separation is $a_{LCBC} = a_{box} + a_{int}$) derived water content values for considering the overall phenomenology of the observed soil water content field. These GPR data have been corrected with the site specific optimized calibration function as described in chapter 5. Here, the results for different measurement frequencies and antenna separations are compared for the first dune valley along the measurement line. Then, we discuss the specific impact of the calibration procedure by comparing both LCBC and SCBC derived water content values with and without correction to TDR measured water contents. Finally, the interannual variation between 2010 and 2011 is illustrated.

Table 6.1: Overview of the GPR datasets discussed in this chapter.

Profile name	f [MHz]	a_{box} [m]	a_{SCBC} [m]	a_{LCBC} [m]	dx [m]
P1 (2010)	400	1.00	0.86	1.14	0.3
P2 (2010)	400	1.50	1.36	1.64	0.3
P3 (2010)	200	1.00	0.81	1.19	0.3
P4 (2010)	200	1.50	1.31	1.69	0.3
P5 (2011)	400	1.50	1.36	1.64	0.05
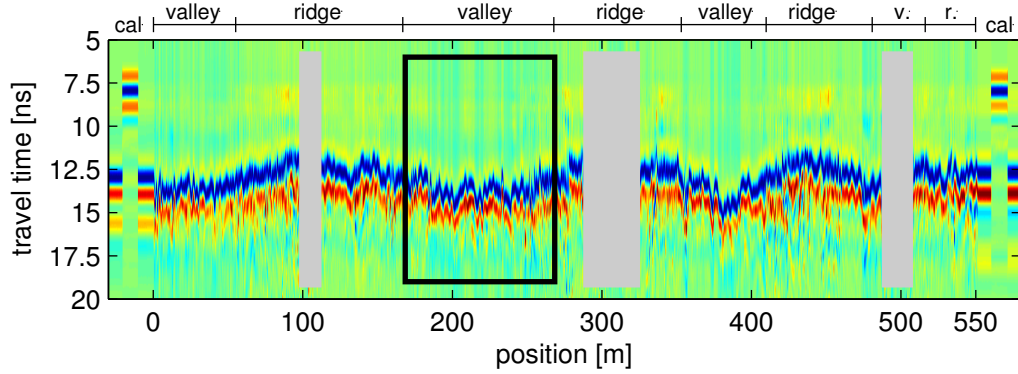
Figure 6.2: Exemplary radargram for the complete GPR line under investigation, show-ing the P1/LCBC measurement. Profile parts before 0 m and beyond 550 m are used for calibration purposes; profile parts where the ground wave signal is notably influenced by subsurface root systems are masked out. The black box indicates the first dune valley, which is more closely investigated in figure 6.4.
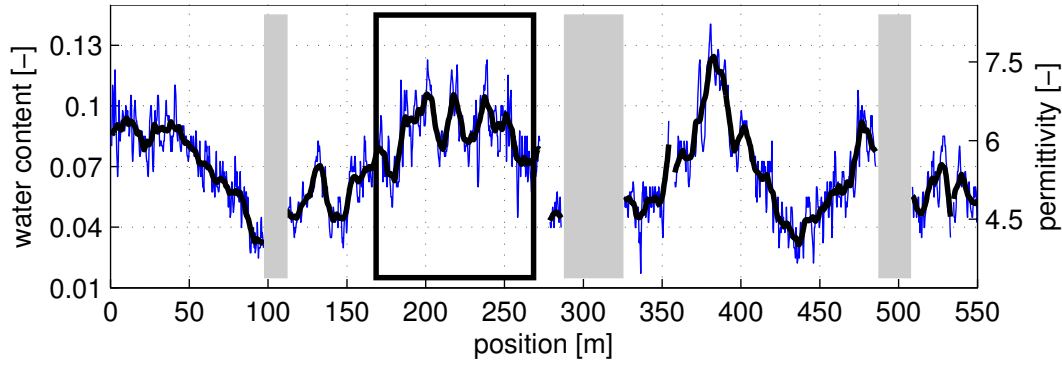
Figure 6.3: Soil water contents calculated from the LCBC ground wave signal shown in Figure 6.2. The blue line pictures the original data, with the thick black line indicating a 10 trace moving average. The black box denotes the first dune valley, which is more closely investigated in Figure 6.4.

6.2 Results and Discussion

One exemplary radargram of the overall GPR line is pictured in figure 6.2. The figure shows the P1/LCBC data (400 MHz, $a_{\text{box}} = 1$ m, evaluating the LCBC), crossing the four dune chains in eastward direction. The profile parts before the zero meter mark and beyond 550 m (marked as "cal") are used for calibration, profile parts where the ground wave signal is notably influenced by subsurface root systems are masked out by grey boxes. Differences between wet parts of the profile, located in between dunes (marked "valley"), and much drier parts on the upper slopes of the dunes (marked "ridge") cause
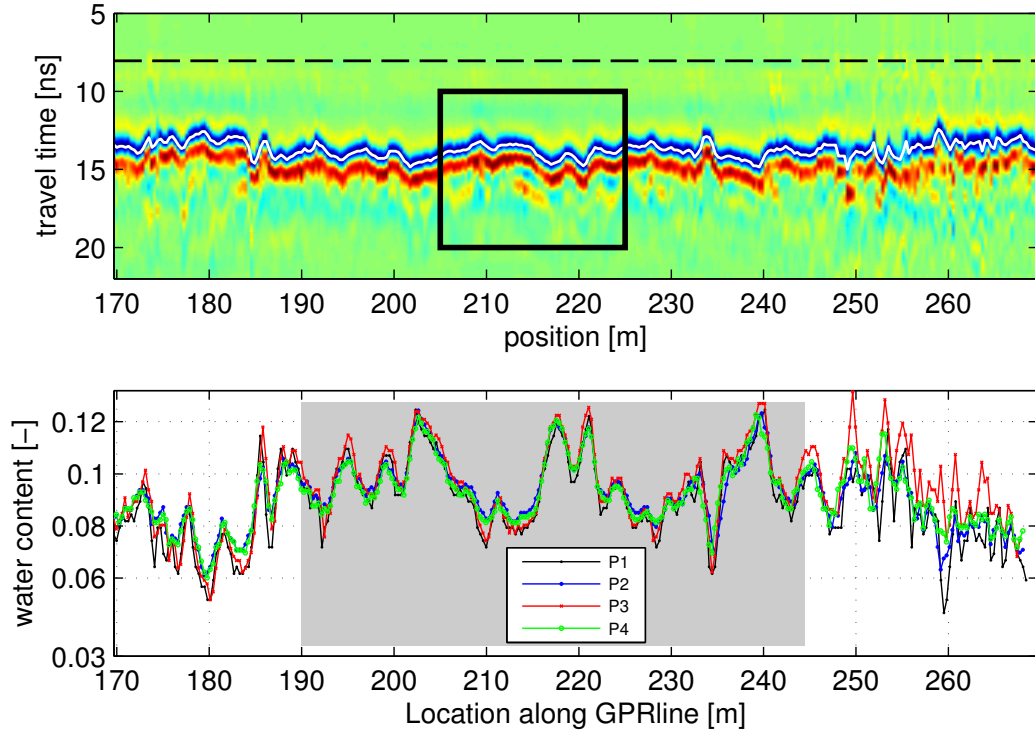
Figure 6.4: Exemplary data evaluation for the first dune valley. The upper part shows the corresponding part of the P1/LCBC radargram out of Figure 6.2. The ground wave pick is drawn in white, the uncorrected air wave travel time is indicated by the dashed black line. The black box denotes the stretch of the profile evaluated in more detail in Figure 6.5. In the lower part of the figure, the water content evaluation for all LCBC channel radargrams are compared. Note the excellent agreement of all data sets along the valley floor (roughly from 190 m to 245 m, as shaded in light grey).

periodic changes in recorded ground wave signal travel times, which gets reflected in the corresponding water content values shown in figure 6.3. This implies that the topography exerts the dominant control on the soil water content distribution at scales of several tens to hundreds of meters for the situation considered here.

The large-scale modulations are superimposed on quite significant small-scale soil water content changes, amounting to variations of up to 0.06 within a distance of a few traces. The question arises, if these fluctuations are just due to measurement noise or whether this can be truly associated with small scale soil water content differences. Thus we first establish the stability of the signal as a basis for all further considerations. To this end, we focus on the part of the profile measured in the dune valley between the first two dune chains, roughly extending between 170 m and 270 m (as indicated by the black boxes in figures 6.2 and 6.3). However, all conclusions drawn from this section are valid for other

dune-valley parts of the profile as well.

The radargram of the P1/LCBC profile for this section is shown in the upper part of
Figure 6.4, where the ground wave pick is drawn in white. The dashed black line indicates
the corresponding uncorrected air wave travel time which has been determined from the
calibration parts of the profile shown in figure 6.2. Water contents derived from this
radargram and all available LCBC (long channel) data of the consecutively acquired three
other profiles are shown in the lower part of figure 6.4.

We first note the good reproducibility of the measured data, most notably for the profile
parts along the valley floor, where almost every feature of the signal is reproduced in later
profiles. Significant deviations do not occur before the onsets of surrounding dune chains,
where an exact retracing of the previously measured profile becomes challenging. Secondly,
data evaluation from profiles acquired with different frequencies yield approximately the
same results. Measuring at longer antenna separations just averages out more of the
small scale variations, as would be expected due to the larger averaging volume. These
visual interpretations can be substantiated in terms of mean water content values $\bar{\theta}$ and
corresponding standard deviations σ which have been calculated for all datasets using the
whole extent of the dune valley floor (as marked by the shaded grey area in figure 6.4).
The results are reported in table 6.2, where the mean water content for the whole valley is
consistently calculated to just under 0.1 from all LCBC datasets, after having employed
the time zero calibration correction with the site specific optimized parameters. Profiles
P1 and P3, acquired at the shorter antenna separation of 1.14 and 1.16 m show a slightly
larger standard deviation, indicating a smaller averaging extent. Average water content
values calculated from the SCBC differ by about 0.01 for both antenna separations, which
is within the range of remaining variation after the calibration procedure as had been
illustrated in figure 5.3.

Table 6.2: Overview of mean water contents and corresponding standard deviations calcu-
lated for the first dune valley from all available datasets with site specific optimized time
zero correction.

Profile name	$\bar{\theta}_{\mathrm{SCBC}}$ [-]	σ_{SCBC} [-]	$\bar{\theta}_{\mathrm{LCBC}}$ [-]	σ_{LCBC}
P1 (2010)	0.096	0.017	0.094	0.013
P2 (2010)	0.108	0.012	0.097	0.011
P3 (2010)	0.093	0.018	0.097	0.014
P4 (2010)	0.108	0.013	0.095	0.011
P5 (2011)	0.073	0.011	0.078	0.011

(a) SCBC, no correction

(b) LCBC, no correction

(c) SCBC, site specific optimized correction

(d) LCBC, site specific optimized correction
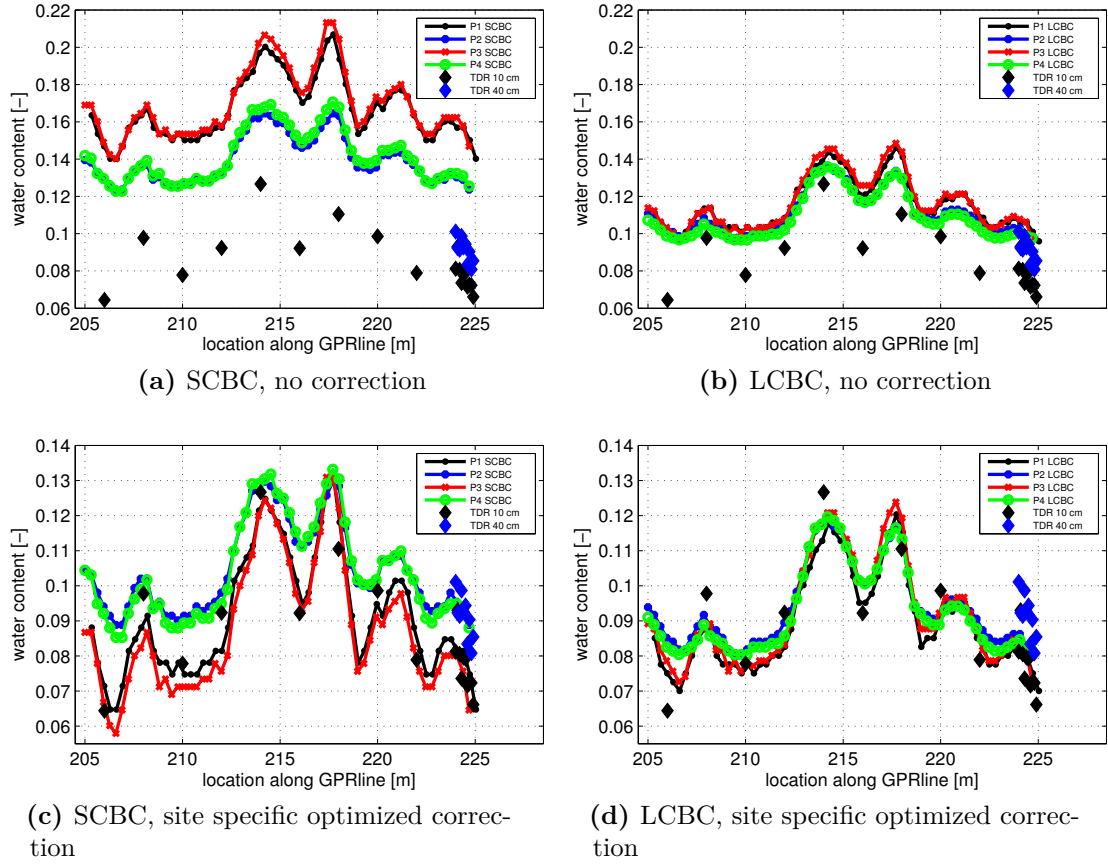
Figure 6.5: Comparison of water contents measured by GPR and TDR along the 20 m stretch indicated in Figure 6.4. Employed antenna separations and frequencies for P1...P4 are summarized in Table 6.1.

Hence, having established the stability of the measurement and, especially for the LCBC datasets, the consistency of retrieved water content values for both measurement frequencies and antenna separations, we turn again to the nature of the observed small scale variations. The GPR ground wave signal is not only very stable, but seems to be an

Table 6.3: Comparison of uncorrected (*org*) and corrected (*corr*) GPR water content values with TDR values as shown in figure 6.5.

	$\mathrm{SCBC_{org}}$	$\mathrm{LCBC_{org}}$	$\mathrm{SCBC_{corr}}$	$\mathrm{LCBC_{corr}}$	TDR (0.1 m)
$\bar{\theta}$ [-]	0.154	0.113	0.097	0.092	0.092
σ [-]	0.021	0.013	0.017	0.013	0.018
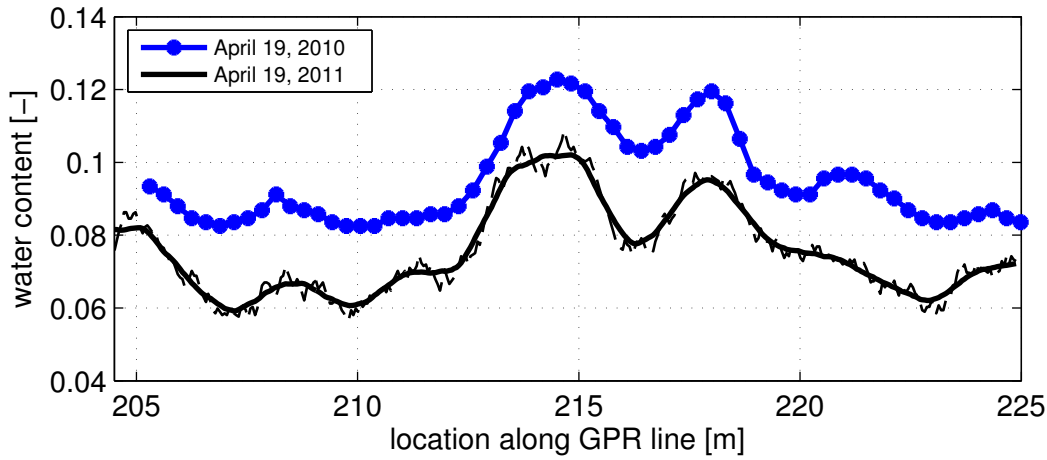
Figure 6.6: Comparison of water contents retrieved in 2010 (P2/LCBC, blue) and 2011 (P5/LCBC, black) along the same subsection of the GPR line shown in figure 6.5. The basic features remain mostly unchanged, only the total water content varies between the two years. Data from 2010 were acquired at a trace spacing of 0.3 m, data from 2011 at 0.05 m (dashed black line). The thick black line shows the data from 2011 when averaged to the same scale as the 2010 data.

excellent proxy for soil water content. This can be seen when comparing the GPR derived water contents to data acquired with TDR probes of 0.1 m rod length (figure 6.5). These TDR data have been measured by vertically inserting the probes at several points along a 20 m long stretch of the profile (its position is indicated by the black box in the radargram of Figure 6.4). Additionally, between 255 and 256 m, both 0.1 m and 0.4 m rodlengths have been used to measure water content at a 0.1 m spacing. At this location, the 0.4 m long TDR probes measure slightly higher water contents, which is compatible with a soil profile which has been excavated close to the 260 m point of the profile and indicated a slowly increasing moisture content with depth for the top 0.4 m of the soil.

The uncorrected GPR estimates for water content do not fit well to the absolute TDR derived values, although both TDR and GPR data follow the same trends along the profile (see figures 6.5a and 6.5b). LCBC estimated water content values are on average about 0.01 (1% vol.) higher than those derived from TDR. Meanwhile, the SCBC clearly overestimates the water contents significantly, as would have been expected from the considerations in chapter 5. Having applied the correction however, the LCBC data fit the absolute water contents as observed by TDR very well. The slightly larger range of the TDR values can be attributed to their much smaller averaging volume. The SCBC data exhibit the difference in water content estimates for the two antenna separations which had just been observed in table 6.2, but the absolute values are now compatible with both LCBC and TDR derived estimates. Still, since the LCBC data seem to give the better results in this case, all further considerations of ground wave data in Fukang both in this

chapter and also in section 8.1 will use LCBC data only.

Next, we can extent this analysis by considering the additional LCBC dataset P5, acquired one year later in April 2011. This second dataset has been evaluated in exactly the same way as the 2010 data. Comparing these two datasets, we can show that the observed small-scale water content variations largely persist in time. For example, figure 6.6 shows that the small scale structures observed in the previous year remain largely unchanged by taking a detailed look at 2011 data of the same stretch of the GPR line evaluated in figure 6.5. Since the 2011 data were acquired at a higher spatial resolution, even smaller variations might be resolved, judging from the dashed black line in figure 6.6. Only the overall mean water content of the 2011 measurement is approximately two volume percent lower than in 2010, hinting at slightly drier overall conditions during the second measurement.

So far we have shown that our GPR data exhibit detailed small-scale variation in observed water contents which is consistent for a series of different measurement setups. This variation exhibits very small interannual variability and can be similarly observed using 0.1 m TDR probes. Since these variations are only within a range of about 0.02 in water content, several different factors might be responsible, including e.g. an influence of topography, textural changes, differences in porosity or the vegetation cover. The topography for this stretch of the GPR line is largely flat. Also, a detailed soil texture analysis of three soil samples taken at 245, 247 and 249 m to cover potential differences of the most prominent peaks observed in soil water content variation in figure 6.6 did only show small textural differences, similarly for porosity. Hence, we currently attribute these persisting small scale variations to a soil-vegetation feedback mechanism through snow accumulation in winter at places with more vegetation. Since snow melt is the most important moisture input for vegetation growth in the semi-desert area in spring (snow represents more than 30% of total moisture input in this region, see e.g. *Zhou et al.* [2009]), this leads to enhanced growth of grasses and small shrubs during the vegetation period and hence will again more efficiently capture snow during the following winter. Since both our measurement campaigns took place shortly after the annual snow melt, this would mean that the small scale variations in our GPR datasets essentially trace local differences in the amount of snow melt infiltration.

In order to study this phenomenon more closely, a series of at least seasonal GPR monitoring measurements would be necessary to assess whether e.g. these variations diminish over the summer.
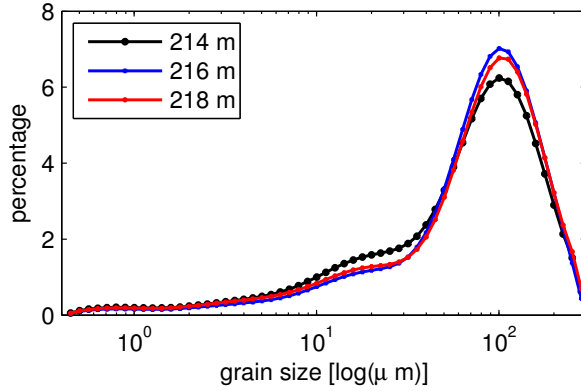
(a) Soil texture analysis

(b) GPR line in summer

Figure 6.7: The left side shows the soil texture analysis of the three samples taken at 245, 247 and 249 m. All three samples are classified as loamy fine sand according to the USDA soil texture classification. The picture on the right shows the stretch of the GPR line which has been evaluated in figure 6.5. The picture was taken in summer, about 3.5 months after the last measurement.

6.3 Summary and Conclusions

In conclusion, we have seen in this chapter, that detailed monitoring of the soil water content distribution with GPR is possible at this site. Using the time zero calibration procedure as outlined in chapter 5, consistently stable results can be achieved. For this type of environment, evaluating the GPR ground wave allows to get a stable handle on the multiscale generators of the soil water content field, observing distinct variations at scales between less than one meter and more than 100 meters. The large scale (on the order of 50...100 m) changes already apparent in figure 6.2 can be attributed to topographic variations. Smaller scale variations as observed in figure 6.5 largely persist in time (figure 6.6) and are most likely due to a soil-vegetation-snow feedback enhancing vegetation growth and in turn water content variations.

7 Towards Quantitative GPR at the Plot Scale

This chapter discusses the field experiments which have been carried out in Heidelberg. In these settings, the well-controlled nature of the experiments in combination with the availability of apt ancillary data show the most promise for achieving a quantitative monitoring of hydrological processes in the near surface with Ground-Penetrating Radar.

7.1 Imbibition and Drainage Experiments at ASSESS-GPR

Between September 2011 and July 2012, several field experiments have been conducted on the ASSESS-GPR site (for the site description, refer to section 4.1), during which the soil water dynamics while imposing a varying water table has been observed by GPR. The most interesting cases include experiments where water is first pumped in and subsequently pumped out again, potentially creating different hydraulic regimes during imbibition and drainage due to the strong non-linearities of the hydraulic conductivity function. The general aims of these experiments were to:

- take a detailed look at the GPR response with respect to different hydraulic states under such transient but well-controlled circumstances;

- assess the precision of measuring average relative water content changes in the subsurface structure with GPR;

- investigate the interactions of the moving capillary fringe with the subsurface structure;

- assess the accuracy to which we can retrieve hydraulic information from observing the movement of the capillary fringe through the subsurface with GPR.

From an experimental point of view, there are two main approaches for conducting GPR measurements during these experiments. The first is to put several antennas at distinct fixed positions on the measurement site and measure continuously at these fixed locations during the whole duration of the experiment. This allows for a high temporal resolution and ensures perfect comparability between the measurements due to a high instrument stability. However, interpretation of the different recorded signals might be difficult because of interactions of the signal with the background structure surrounding the point of the measurement. The second possibility is to use the normal four channel setup (see 3.5 for details) for continuously measuring CO profiles over the structure during the whole

experiment. The latter can obviously yield more information about the interaction of the moving water table with the different subsurface materials and structures, since we get a full $2 + 1$D (space/time) image of the subsurface. The trade-off however is a decreased temporal resolution with respect to measurements at the same location and potentially a higher instrument instability since the antennas are moved around.

A first experiment of this kind has been carried out on November 29, 2011 (in the following denoted as the "November Experiment"), a second experiment has been conducted on March 27, 2012 (in the following denoted as the "March Experiment") and a third on July 7, 2012 (denoted as the "July Experiment"). In the next sections, the results, interpretation and implications of these experiments will be thoroughly discussed. With respect to increasing complexity of the hydrological processes involved we will start with the July experiment where the antennas have been kept in fixed positions while only lowering the water table at a fixed rate. Subsequently, the other two experiments will be discussed with a focus on the most comprehensive March Experiment, both featuring imbibition and subsequent drainage.

7.2 Drainage Only: The July Experiment
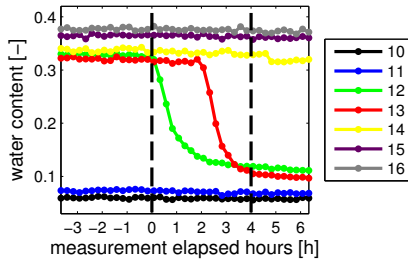
Figure 7.1: Water content change as observed by the profile P2 TDR probes #10 - #16 (see Figure 7.2) at the synclinal structure around meter eleven along the profile.

Due to strong precipitation events in previous weeks, the water table position was fairly high before the July experiment – judging from TDR saturation data, its approximate depth was at around 0.7 m. During the experiment, the water table was lowered by pumping out 10.4066 ± 0.0001 m^3 over the course of 4 h (which converts to a constant pumping rate of 3.255 cm/h) while monitoring the interaction of the water table with subsurface structures at several fixed locations over time with GPR. The corresponding drop in the water table as measured in the observation well is shown in Figure 7.6.

Before and after the pumping process, two CO profiles were run over the ASSESS-GPR site to map the initial water content distribution of the structure. During the pumping process, three IDS 400 MHz antennas were positioned at fixed locations along the middle stretch of the ASSESS-GPR structure, as indicated in the sketch in Figure 7.2. This sketch also indicates the changing water saturation as induced by the pumping in the ASSESS-GPR structure. The position of the top of the capillary fringe before (dashed blue line) and after (solid blue line) the pumping was estimated from the change in water saturation as observed by the different TDR sensors. Their positions are indicated in the
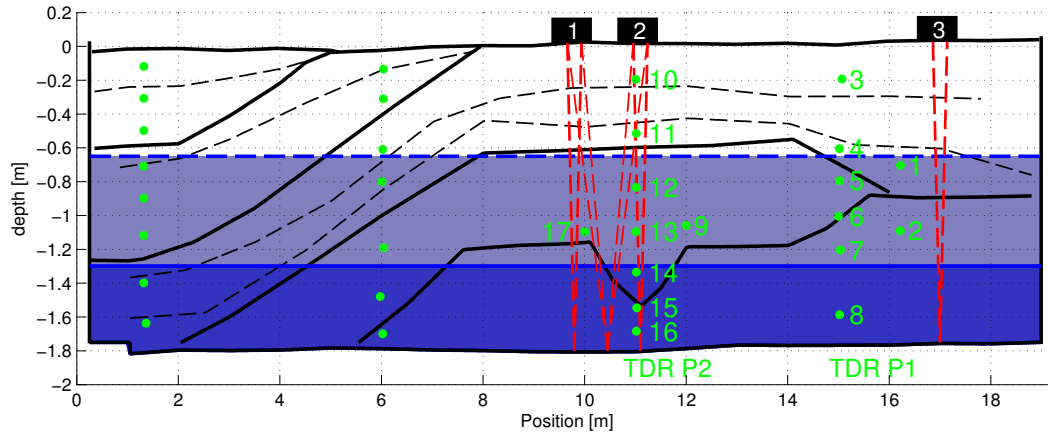
Figure 7.2: Experimental setup for the July Experiment. Approximate water table positions before (dashed) and after (solid) the experiment are indicated by the blue lines. Green dots indicate the locations of TDR probes.

sketch as green dots. Specifically labeled are sensors from TDR profiles P1 and P2, since they will be used for comparison with the GPR data.

With this setup, there are five GPR measurement channels recording data: The three internal channels yield information about the water table interacting with the two layered (antenna 3), the synclinal (antenna 2) and the three layered (antenna 1) parts of the structure. The antenna positions were chosen such that the measured water content changes can be compared to data from TDR profiles P1 and and especially P2 (see Figure 7.1), as indicated in Figure 7.2.

7.2.1 Hydraulic state before and after the experiment

For a general overview of the hydraulic state of the ASSESS-GPR site before and after the pumping experiment, we first take a look at the CO measurements evaluated in Figure 7.3. Both radargrams shown in this figure were acquired by the same internal channel; there is no filtering applied beyond a standard dewow filter removing the low frequency noise. In particular, no amplification was added, but the color scale has been clipped by the same fixed value for both radargrams. In the radargram taken before the pumping a horizontal reflection is clearly visible around a travel time of approximately 19 ns. It stretches almost evenly throughout the different materials, although its specific shape (i.e. the number and ordering of maxima and minima) seems to change. Also, beyond 15 m the reflection seems to move to slightly smaller traveltimes. From its relative position to the reflection signals of the subsurface structures, one would estimate its depth of origin to be around 0.7 m. This is roughly in the same region where TDR data indicate the position of the top of the capillary fringe. The nature of this reflection will be discussed more closely in Section 7.3.2.
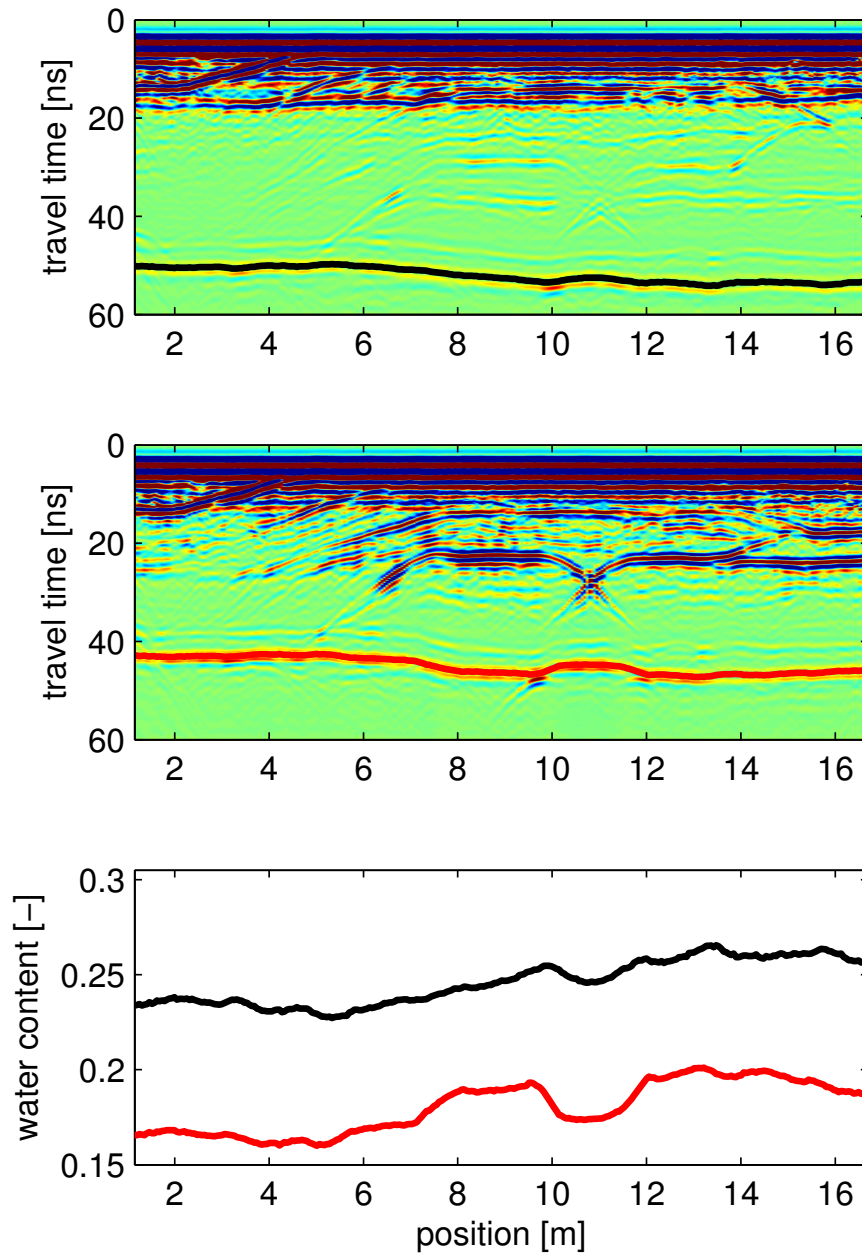
Figure 7.3: Internal channel measurement. The top figure shows the common offset radargram before and the middle figure the corresponding radargram after pumping. The bottom diagram pictures the average water content evaluated from the respective bottom reflections.

For now, we will simply term it the capillary fringe reflection (CFR), keeping in mind that the apparently different shapes recorded at different locations of the profile hint at a more complicated origin than a simple reflection from a well defined interface.

At the beginning of the experiment, the strength of the capillary fringe reflection masks most of the layer boundary features normally present below; the bottom reflection can however still be discerned very well around 50 ns, as indicated by the black pick. After the pumping, the subsurface structure is clearly visible again, with the bottom reflection (as picked in red) now appearing at travel times around 45 ns. A much fainter capillary fringe reflection can still be discerned, now located around 24 ns, most prominently in the part between $1 \ldots 6$ m, where there is no layer boundary at the same depth giving rise to interfering reflections. Subfigure (iii) shows the result of evaluating the bottom reflection before (black) and after (red) the pumping process. The mean change in average water contents is around 0.07 $\mathrm{m^3/m^3}$, with the largest variation to be found in the region of the synclinal structure between 10 and 12 meters, indicating that the material above the interface is to a certain extent drier at that location than below.

7.2.2 Timelapse data: Average water content change

We next turn to the timelapse measurements which were recorded at fixed locations throughout the pumping process, as indicated in Figure 7.2. The two crossbox channels between antennas one and two are expected to potentially yield quite complicated signals since they are sampling directly across the slanted interfaces enclosing the synclinal structure. Furthermore, the rather large angles may lead to different characteristics with respect to the capillary fringe reflection. Therefore, we resort to the three internal channels for quantitative discussions.

The timelapse radargrams for all three internal channels are shown in Figure 7.4. Before discussing the potentially complicated dynamics between the capillary fringe and the different subsurface structures, we first evaluate the signal of the bottom reflection, inferring the change in travel time from the indicated picks. This travel time change is indicative for the overall decrease in average water content at each of the three measurement locations, which is shown in the bottom right diagram in Figure 7.4. As can be seen in that diagram, the overall decrease in average water content as measured by GPR is between 0.075 and 0.082 $\mathrm{m^3/m^3}$, depending on the location. This result is in good agreement with the average water content decrease calculated from TDR measured permittivities, which also yields values between 0.07 and 0.08, depending on the assumption for the exact position of the water table depth. Furthermore, the average water content decrease exhibits an approximately constant slope for the location of antenna 2 (red line), measuring above the synclinal structure. Terminating the drainage after 4 h leads to almost instant leveling out of the curve, indicating a very fast response of the system. The water content change as observed by antenna 1 (blue) and foremost antenna 3 (black) distinctly deviates from this general trend whenever the water table at their respective locations approaches a layer boundary.
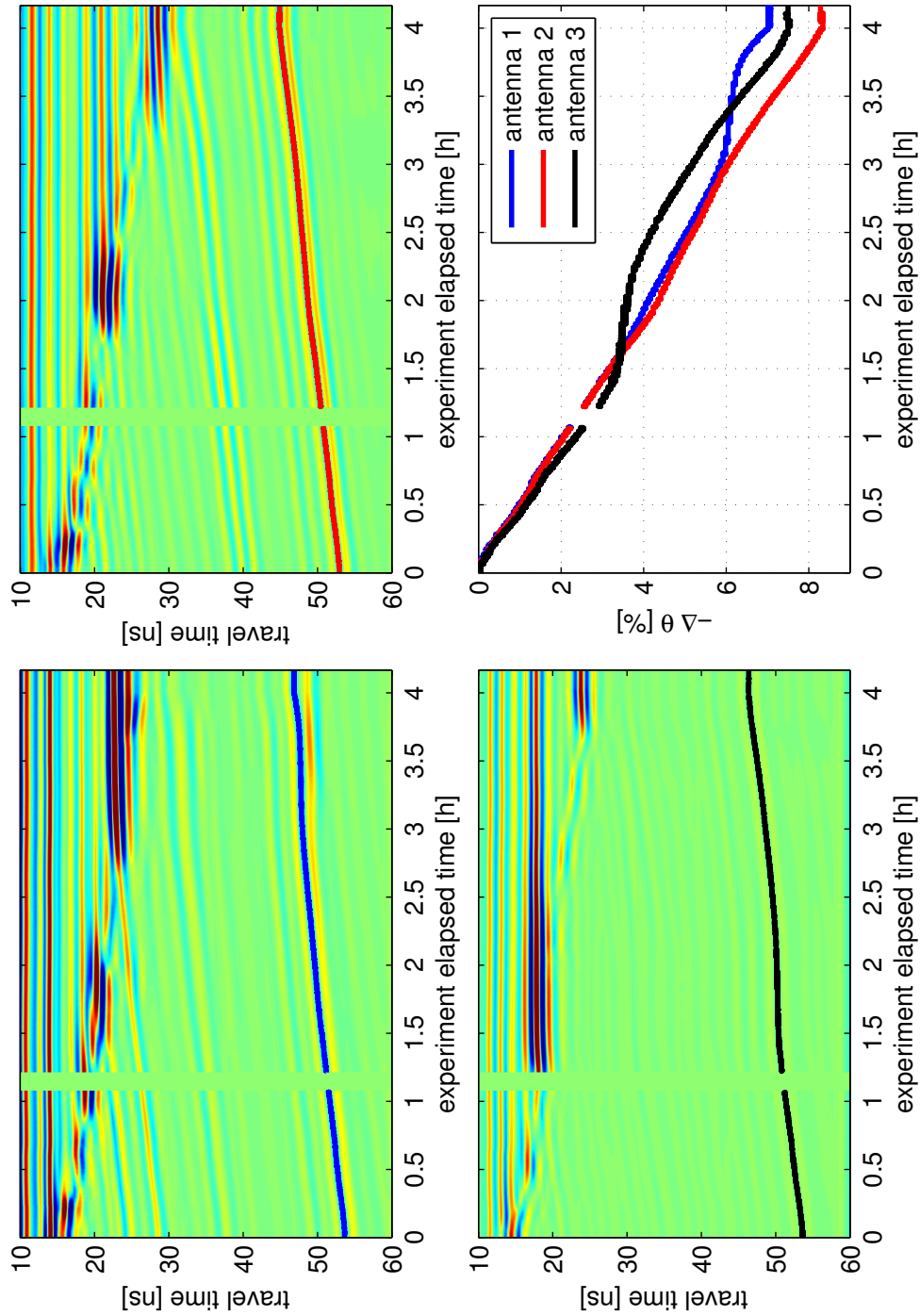
Figure 7.4: Timelapse Radargrams for the three internal channels. Top left shows the antenna 1 data, top right the radargram for antenna 2 and bottom left the data for antenna 3. Bottom right pictures the change in average water content as evaluated from the respective bottom reflection at the three locations.

Judging from the radargrams, this is the case for antenna 3 between 1.2...2.2 hours into the measurement, where the water table "crosses" the layer boundary at 0.9 m and for antenna 1 starting at about 3.1 h, where the water table at that location moves into the second layer boundary at 1.2 m depth. Furthermore, for the first part of the experiment before the water table reaches the layer boundary at the two layer part (antenna 3), the water content decrease seems to be slightly faster for the two layer part than for the other two curves.

This behavior can be understood in terms of the hydraulic parameters of the respective materials. These material properties determine the height of the capillary fringe as well as the shape of the transition zone between saturation and residual water content in static equilibrium. The vertical extent of this transition zone is mainly determined by the pore size distribution, while the dynamic range depends on the accessible pore volume, i.e. the difference between the saturated and residual water contents θ_s and θ_r. The saturated water content in turn is given by the porosity ϕ, possibly reduced by the presence of residual air. Given a very narrow pore size distribution, all pores will drain more or less simultaneously for a specific hydraulic potential, which leads to a small extent of the transition zone. Its extent will increase with a broadening of the pore size distribution as the pores will no longer drain for the same hydraulic potential.

Imposing a drainage flux at the lower boundary leads to a continuous decrease of the matric potential at any position in the profile. In turn, this induces the lowering of the capillary fringe and a correspondingly moving transition zone between saturation and residual water content through the subsurface for the different sands used at ASSESS-GPR. If the drainage flux was small enough for the system to pass through a series of quasi-equilibrium states, i.e. if the relaxation time was much smaller than the external time scale, the shape of this transition zone should stay constant while the transition zone moves entirely in the same layer. This would simply lead to a constant decrease in water content with time. However, under more general transient conditions, the exact shape of this dynamic transition zone additionally depends on the specific shape of the hydraulic conductivity function $K(\theta)$. Hence, even for a transition zone moving completely within a homogeneous medium, the slope of the observed water content decrease cannot be expected to be constant since the system will display different relaxation times for differing water contents. Furthermore, for any explicit change of these parameters, e.g. due to the crossing of a layer boundary, the shape of the transition zone will vary accordingly, which changes the speed of the water content decrease even more noticeably.

In our case, we observe a slower decrease in water content once the capillary fringe reaches the layer boundary, as discussed above. This should e.g. be the case for a transition crossing from a medium featuring a small air entry value $|h_0|$ (compare equation 2.36) to a medium with a large air entry value $|h_0|$. In this case, it may not be possible to extract water at this location for the present hydraulic potential once the transition zone moves into the second medium. Only after the hydraulic potential has fallen below the air entry value of the second medium, water can again be extracted at this position. This
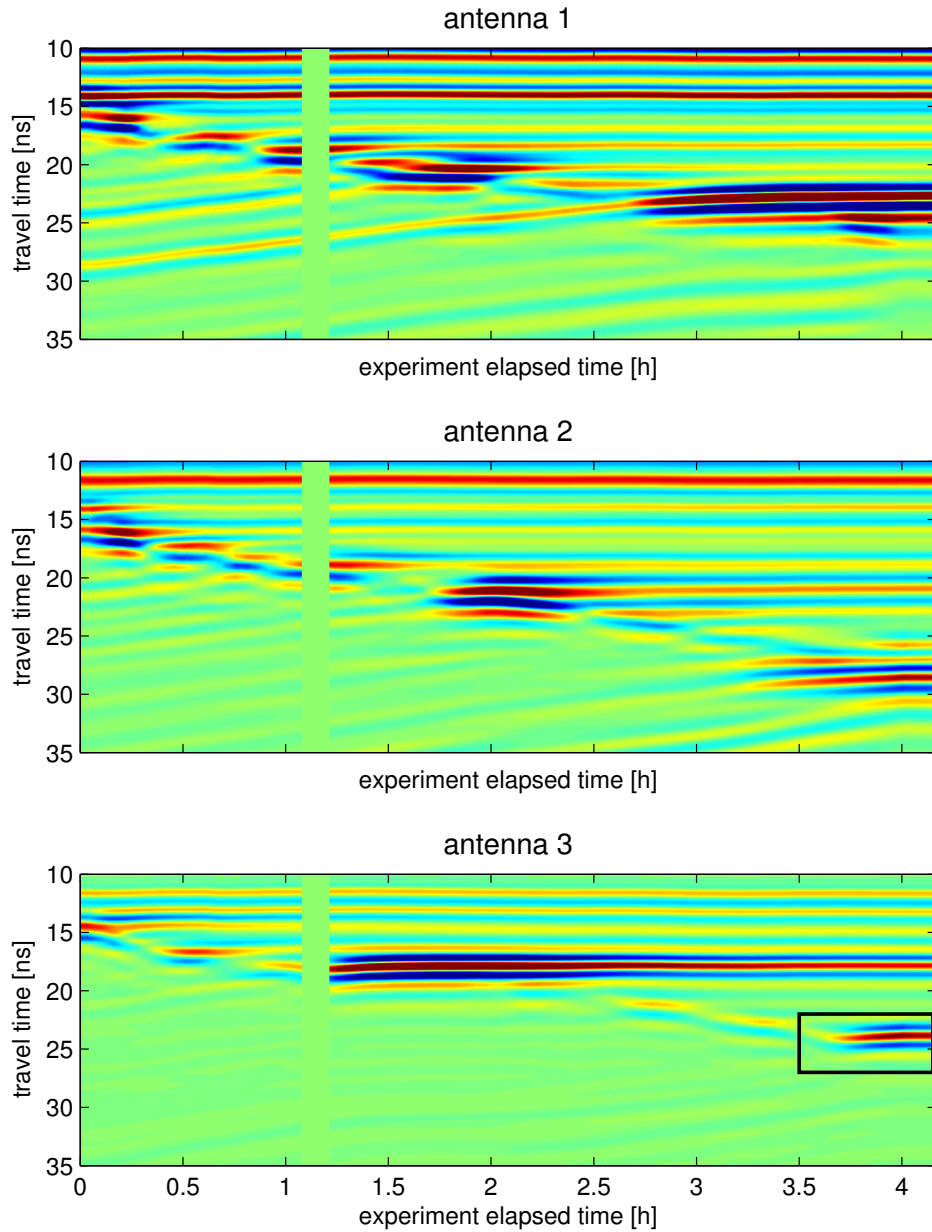
Figure 7.5: Detailed radar data excerpts from Figure 7.4 for illustrating the capillary fringe movement at the three antenna locations. From top to bottom, the diagrams picture the data from antennas one, two and three. The black box in the bottom radargram denotes an example of a compaction interface reflection which can only be observed under certain hydraulic conditions.

means that for this particular location the average water content decrease will slow down until the matric potential falls below the air entry value of the second medium. In the meantime, water is only extracted from other parts of the ASSESS-GPR structure where drainage can occur for the current hydraulic potential. Following this explanation, the GPR-derived average water content change data would suggest that, in our case the lowest material, sand A (compare Figure 4.1) should feature a larger air entry value than both sands B and C, since for both transitions, as observed by antennas 1 and 3, the water content decrease slows down considerably once the transition zone starts to enter sand A. This explanation is in accordance with the results from *Jaumann* [2012], who estimated effective hydraulic parameters for the ASSESS-GPR site based on the TDR data acquired during different pumping experiments. The current best estimate for effective parameters of the ASSESS-GPR sands based on that research are reported in Section 4.1.

Still, alternative explanations are possible. Another viable interpretation could for example include differences in hydraulic parameters specifically for the region around the layer boundary. After all, due to the building process of the ASSESS-GPR structure, the region around layer boundaries could be dominated by a mixture of the two enclosing materials with distinctly different properties. For example, the mixture of both materials would be likely to exhibit a broader grain size distribution.

In order to distinguish the different influencing factors, observations of the transition zone moving through effectively homogeneous materials for longer periods of time would be needed. This is however difficult to achieve, since, as we will see in the next section, even while moving within a single layer, there is quite substantial interaction of the capillary fringe reflection with background substructures.

7.2.3 Timelapse data: A detailed look at the dynamics

For taking a closer look at the detailed dynamics of the transition zone as observed by GPR, Figure 7.5 shows a smaller excerpt of the timelapse radargrams which were pictured in Figure 7.4. All three radargrams showcase the interferences between the reflection which is generated by the capillary fringe and the various reflections which originate from the subsurface structures at the respective locations. During the pumping process, static reflections move to smaller traveltimes, while the capillary fringe reflection is being recorded at ever longer travel times due to the falling water table. The result is a quite complicated picture of the interaction seen "through the eyes of GPR" with significantly enhanced amplitudes recorded whenever the capillary fringe reflection coincides with signals generated by static subsurface structures. Some features can still be discerned with certainty.

Most prominently, interface reflections become clearly visible once they start interacting with the capillary fringe reflection and still give rise to comparatively strong signals after it has moved past. For example, for antenna three, measuring over the two layered part, the capillary fringe reflection is recorded at about 15 ns at the start of the experiment. At about 1 h into the pumping, the capillary fringe signal coincides with

the reflection originating from the layer boundary between sands A and C, which leads to a strong signal arriving at travel times around 19 ns. After about 2.5 hours into the pumping, the two reflections are clearly distinguishable again. While the arrival time of the layer boundary reflection now stays constant, the capillary fringe reflection moves to even longer traveltimes. Similarly, antenna one starts measuring a distinctive increase in signal amplitudes around 24 ns after 2.5 h, which is the coincidence of the capillary fringe and the layer boundary between sands B and C at 1.2 m depth at that location.

Besides these clearly distinguishable features which were already noticed while evaluating the bottom layer reflection, there are other strong signals observed which cannot be associated with the location of layer boundaries. For example, beyond 3.5 hours, antenna three seems to measure another quite distinct interaction of the capillary fringe reflection with a background structure signal which again leads to a significant increase in the recorded reflection amplitude. This has been marked by the black box in the corresponding radargram. There is no layer boundary present at this particular location. Furthermore, a comparison with the CO data recorded before and after the pumping pictured in Figure 7.3 shows that this signal is part of a quite distinctive reflection which for profile positions beyond 14 m is detectable around 23 ns only after the pumping. While the water table is located a safe distance above, there is no reflection generated at all. The same is true for the strong signal antenna one and even more prominently antenna two measure starting from 1.5 h after the experiment start around travel times of 23 ns. Hence these are reflections which only arise for specific hydraulic states of the ASSESS-GPR site.

In this case these reflections are generated by interfaces which are basically an artifact of the building process. As has been mentioned in Section 4.1, the sand layers had to be compacted at regular intervals during the building process. The position of some major compaction interfaces has been specifically measured and are e.g. drawn into Figures 7.2 and 4.1 as dashed lines. Further compaction interfaces exist at depths of 0.9 m at the locations of antennas one and two and at 1.2 meters depth at the location of antenna three, coinciding well with the observed signals. Across such a compaction interface the material stays the same, but porosity will vary. In the saturated case, this does not lead to a significant change in permittivities over the interface. However, in the unsaturated case, this porosity change leads to a distinct variation in water content across the interface which translates to a permittivity change giving rise to the observed reflections.

This proves that strong GPR reflections cannot only be generated at distinct material boundaries, where the basic material properties change. Depending on the specific hydraulic state of a field site, secondary structures such as local porosity changes can also lead to a large enough permittivity contrast generating GPR reflections. This should sound a note of caution for interpreting single-instance-in-time field datasets and calls for measurements acquired over different hydraulic states of the field site under investigation for ensuring a correct interpretation of subsurface features.

Last but not least, even beyond these strong variations in recorded reflection amplitude, there seems to be significant interaction of the capillary fringe reflection with further

minor signals generated from the background structure. This leads to a repeated variation in reflected amplitude, basically resembling a step-like structure along the path of the capillary fringe reflection. However, the origin of these reflections is hard to determine without additional information. Also, the properties of the capillary fringe reflection have not yet been appropriately studied. To do so, we will in the following section turn to experiments featuring both imbibition and drainage paired with continuous multichannel GPR measurements to gain the additional advantage of 2D information.

7.3 Experiments Featuring Both Imbibition and Drainage

During both the November and March experiments, the water table was adjusted by pumping water in and out of the measurement well located at the far end of the site. An overview of the water table position as measured in the observation well during the different stages of the experiments can be found in Figure 7.6. The abrupt jumps which can be observed in the water table positions are due to the change in the hydraulic potential imposed when operating the water pump. Imbibition and drainage speeds were limited by the capabilities of the groundwater supply and the employed water pump.

Preliminary results of the November experiment have recently been presented by *Seegers* [2012]. Based on the experiences gained, the March experiment featured a much larger dynamic range in terms of water table variation and the highest temporal resolution of multichannel GPR measurements, hence its results are the foundation of the discussion in this section. At the start of the experiment, the water table position was between 1.2 and 1.3 m, again judged from the saturation as seen by the TDR sensors. During the experiment, 10.0810 ± 0.0001 m^3 of water were infiltrated through the pumping well over the course of 5.3 h, which yields a constant imbibition rate of 2.38 $^{cm}/_h$ imposed at the lower boundary if referenced to the area of the whole ASSESS-GPR structure. Afterwards, one hour was allowed for equilibration during which the measurements were continued. Then, 9.5630 ± 0.0001 m^3 of water were pumped out again over the course of 3.5 h, equaling a drainage rate of 3.42 $^{cm}/_h$.

Over the whole experiment duration of about twelve hours, four-channel GPR data have been acquired along a 7 m-stretch up and down the middle axis of the site at a rate of approximately one radargram per minute. We here evaluate one of the resulting 400 MHz datasets, which consists of 220 radargrams acquired moving from 6 to 18 m along the profile. Thus the resulting temporal resolution with which we observe every point along the measurement line is approximately one trace every three minutes. This is obviously much less than the timelapse radargrams discussed in the previous section, but the availability of the whole 2D information will greatly enhance the ability to interpret the interaction of dynamic and static structures in the GPR radargrams.
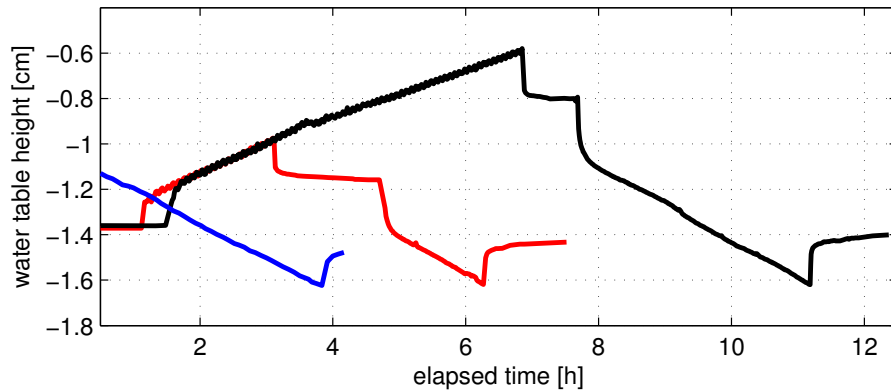
Figure 7.6: Variation of the water table over the course of the November (red), March (black) and July (blue) Experiments as measured in the pumping well.

7.3.1 Water content dynamics as seen by GPR

A timelapse movie showcasing all radargrams recorded by the INT2 channel along the 7 m stretch starting at 6 m can be found in the digital supplementary materials, as described in Appendix B. Due to the combination of the 2D information and the high time resolution, this movie truly gives an impression of the possibilities for observing hydraulic dynamics through the eyes of GPR.

In order to get an impression of the different hydraulic states which were observed throughout the experiment, Figure 7.7 pictures eight common offset radargrams measured by the INT2 channel across the entire ASSESS-GPR site at different characteristic times of the experiment.

Before the start of the experiment, the capillary fringe gives rise to a two-feature reflection (one maximum, one minimum peak) which is fairly faint and arrives at travel times around 25 ns. The reflections generated by structural features located above the capillary fringe are clearly visible.

Fifteen minutes after starting the pumping the CFR has already started to move to smaller travel times, which is especially visible in the synclinal structure around 11 m.

Two hours later the overall reflection amplitude of the CFR has intensified significantly. Depending on the location the antenna mostly seems to record a three-feature wavelet. This might be due to the interaction with the compaction layer interface respectively the layer boundary beyond 14 m present at 0.9 m depth, giving rise to a distinct increase in recorded reflection amplitudes as discussed in the previous section. Also, the arrival time of the CFR seems to depend slightly on the respective materials.

Having moved past this interface, at 4 h, the reflection amplitude is still greatly enhanced compared to the start of the experiment. We also note that the capillary fringe position now is in the same range in which the drainage for the July experiment was started.
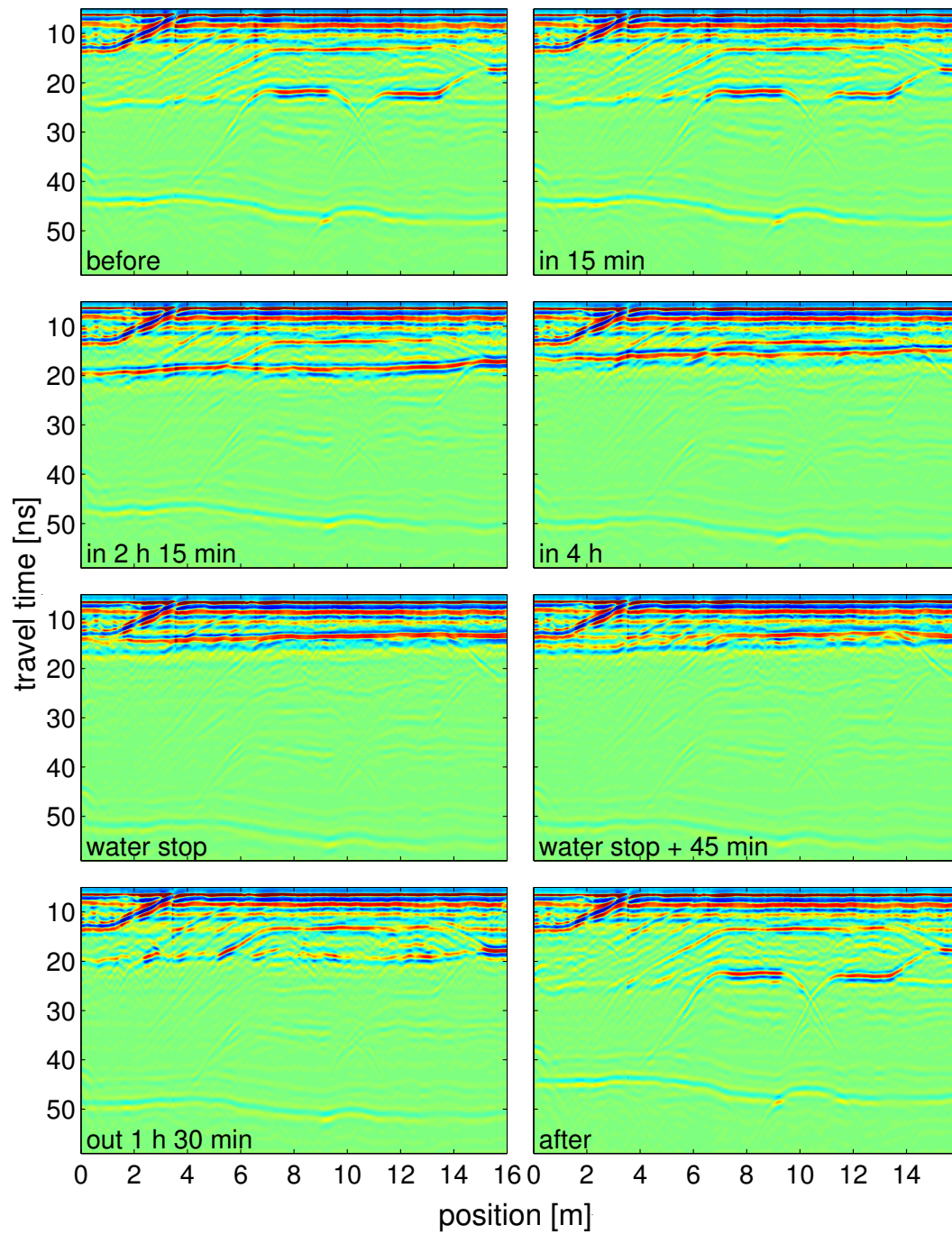
Figure 7.7: Eight radargrams acquired by internal channel CH 2, illustrating the hydraulic state of the March-experiment at several distinct times.

Comparing the dynamic case of the March experiment 4 h radargram to the stationary common offset radargram before the start of the July experiment (see Figure 7.3), the data look quite similar with suppressed reflection intensities of all structural features located below the CF. However, in the dynamic case the recorded CF wavelet seems to be flipped. At the stop of the imbibition after 5.3 h, the capillary fringe has reached a depth of around 0.6 m where the first layer boundary between sands C and B is located between 6...14 m. The main CFR wavelet is now recorded at travel times of approximately 14 ns, consisting of a minimum and a maximum feature. However, there seems to be an additional minimum "trailing" the main part of the reflection which arrives around 18 ns. This curious feature is even more discernible in the timelapse movie.

45 minutes after stopping the imbibition, this apparent splitting of the capillary fringe reflection becomes even more evident. Most prominently for the profile part between 2...6 m, there seem to be two separate wavelets, one minimum-maximum feature wavelet at 14 ns and immediately afterwards another maximum-minimum feature wavelet recorded at about 17 ns. Hence, both during imbibition but even more prominently during the relaxation time, the reflection generated by the capillary fringe seems to undergo quite significant changes.

During drainage (compare the out 1.5 h radargram), the reflection generated by the capillary fringe is much fainter, with the resulting signal having a spotty appearance due to largely variable reflection amplitudes. Most probably, the recorded amplitudes are now dominated by interactions of the CFR with signals generated from the background structure, which already hampered the interpretation of timelapse data acquired at a single points for the July experiment.

After stopping the drainage, the signal of the CFR reflection arrives slightly later than before the start of the experiment at travel times of about 26 ns. At least in the first part of the profile (0...6 m), the recorded wavelet has again a maximum-minimum, two feature appearance.

In summary, despite the considerable interference with the background structure, the following characteristics of the CFR can be observed through this experiment:

- In equilibrium, the CFR displays two distinct features, a maximum-minimum shape;

- during the imbibition process, the reflection intensity increases significantly while the shape of the reflected wavelet changes substantially;

- towards the end of the imbibition process and more prominently during the equilibration phase, the recorded CFR wavelet splits;

- during drainage, the CFR is much fainter, and can at times hardly be discerned from background signals.
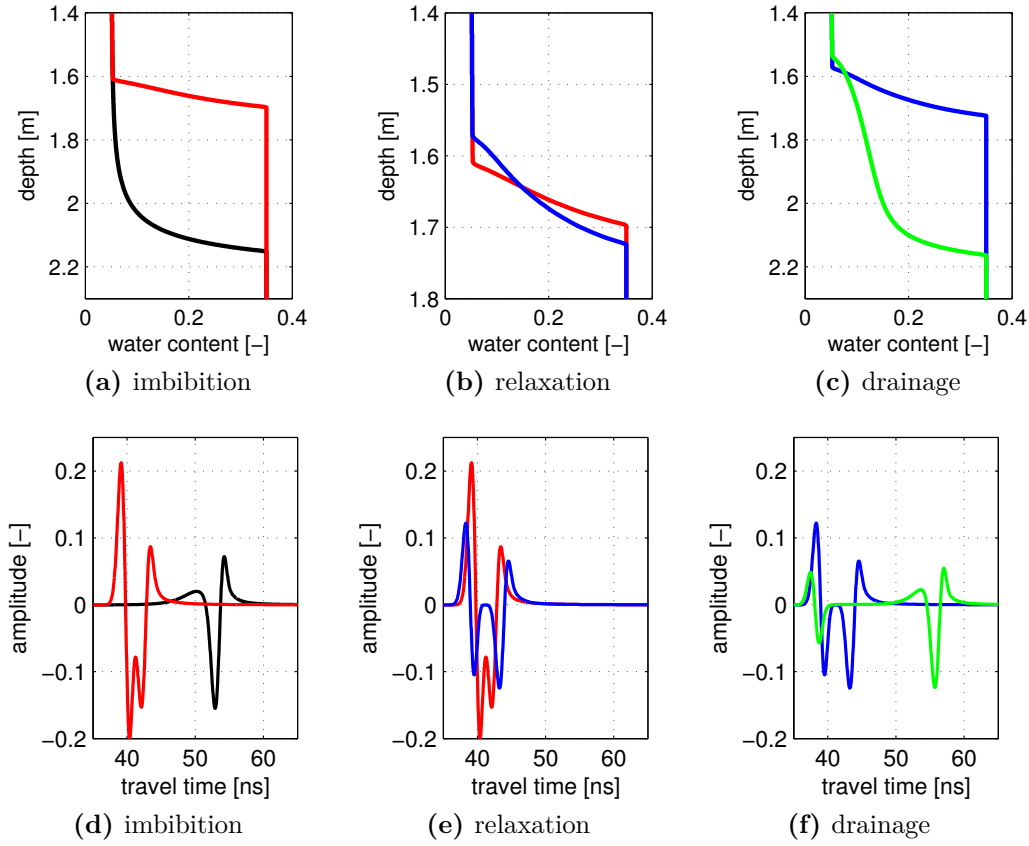
Figure 7.8: Capillary fringe shapes (upper row) and corresponding GPR signals (second row) for different hydraulic states in a homogeneous sand with the same forcing as applied during the experiment: Black lines denote the state and corresponding GPR signal before starting the imbibition, red at the end of the imbibition, blue after relaxation and green at the end of the drainage *(based on the results of Dagenbach [2012])*.

7.3.2 Dynamics of the Capillary Fringe Reflection

Despite the constant interaction of the capillary fringe signal with the different subsurface structures, the observations from the previous section can be explained quite well, building on the numerical simulations which were presented by *Dagenbach* [2012]. That work has shown that what we observe as the capillary fringe reflection is essentially the integral sum of all infinitesimal contributions of reflections generated by the whole transition zone. In equilibrium, the most prominent contribution of the observed signal originates from the top of the capillary fringe. Using 2D calculations based on the FDTD electromagnetic simulation code MEEP (e.g. *Oskooi et al.* [2010]) and a Ricker source current excitation for the simulation, the resulting shape is a two-featured wavelet. Under transient conditions

however, the shape of the transition zone above the capillary fringe changes, giving rise to other significant signal contributions. For illustrating these phenomena, the forcing as applied during the March experiment and the soil hydraulic parameters as noted in table 7.1 have been used to simulate transient conditions in a homogeneous sand similar to what can be expected for the ASSESS-GPR site. Following the approach put forward in *Dagenbach* [2012], the correspondingly expected GPR reflection signal shapes can be calculated. Both the resulting dynamic change of the transition zone and the corresponding expected signal shapes are pictured in Figure 7.8. Corresponding hydraulic conditions and wavelet shapes have been drawn in the same color. Despite the differences between simulation and real measurement (e.g. source wavelet, 2D simulation), a characteristic behavior very similar to the experimental results can be observed for the simulated GPR response of the dynamic transition zone:

- Before the experiment, the equilibrium transition zone gives rise to a mainly two featured wavelet (Figure 7.8d), dominated by the contribution of the kink at the top of the capillary fringe.

- Due to the highly non-linear hydraulic conductivity function, the transition zone sharpens during the imbibition, resulting in a second kink at the dry end of the transition zone (red line in Figure 7.8a). Basically, the hydraulic conductivity is too low in the dry region to ensure a constant shape of the transition zone. This kink gives rise to another significant signal contribution which in the case considered here even dominates the response. The resulting wavelet (red line in Figure 7.8d) seems to have three dominant features, although the kink at about 40 ns already hints at its nature of consisting of two separate significant contributions. Also, the sharpening of the transition zone leads to an increase in the overall reflection coefficient. Hence, the recorded CFR amplitudes increases.

- After stopping the imbibition, the transition zone relaxes. Again, due to the non-linearities of the hydraulic conductivity function, the two dominating kinks separate somewhat in depth (blue line in Figure 7.8b), leading to the observed splitting in the observed GPR signal (blue line in Figure 7.8e). Overall amplitudes decrease.

- During drainage, the transition zone becomes elongated (green line in Figure 7.8c). While the top of capillary fringe kink follows the drainage, the kink at the dry end moves only very little due to the low hydraulic conductivity in the dry range.

Table 7.1: Soil hydraulic Brooks-Corey parameters used for the simulation of the transient soil conditions shown in Figure 7.8.

h_0 $[\mathrm{m}^{-1}]$	λ [-]	θ_s [-]	θ_r [-]	K_s $[\mathrm{cm}\ \mathrm{h}^{-1}]$	τ [-]
0.15	3.0	0.35	0.05	20	0.5

Hence, while the dominating reflection is again recorded as a mainly two-featured wavelet around 58 ns, the contribution from the dry end kink stays put, just slowly decreasing in amplitude.

A timelapse movie showing the continuous change of the transition zone shape and the corresponding wavelet shapes with more detail can be found in the digital supplementary materials as described in Appendix B.

Obviously, the exact shape of the transition zone depends strongly on the respective hydraulic parameters. Especially the form of the hydraulic conductivity function governs the evolution of the kink at the dry end. This explains the differences observed in the CFR signal for the different parts of the profile during the experiment. Furthermore, this also implies, that the form of the recorded CFR signal in principle comprises detailed information about the specific governing hydraulic parameter set. This has been discussed for synthetic data in *Dagenbach* [2012]. However, trying to directly invert the experimental data for material properties would be greatly impaired by the strong interactions of the CFR with the structural heterogeneities, most importantly the compaction interfaces. It essentially seems impossible to acquire undisturbed observations of the capillary fringe reflection over a sufficiently long pumping period in the ASSESS-GPR structure for separating the different effects.

However, other considerations are feasible. For example, one can use these datasets to decide on the appropriate form of the parameterizing function of the soil hydraulic characteristics. As has been shown by *Dagenbach et al.* [2012], using the simplified van Genuchten parametrization cannot reproduce the observed CFR signals sufficiently well. A sharp air entry value as e.g. provided by a Brooks-Corey type parameterization is crucial for explaining the observations. This is also why Figure 7.8 is directly focused on transition zone shapes calculated with a Brooks-Corey type parameterization.

7.3.3 Quantitative evaluation of the bottom reflection time-lapse data

Keeping in mind the rich dynamics which have just been described in the previous sections, we will now again turn to the bottom reflection, discussing the integral behavior of the water dynamics for different profile parts over the course of the experiment. As a starting point, we use the bottom layer pick in all the acquired common offset radargrams to evaluate the travel time and the travel time change at every point in the profile over the course of the experiment. Figure 7.9 shows this result for radargrams as recorded by the INT1 channel. The upper part of the figure shows the time-zero corrected absolute travel times of the bottom reflection and the middle figure the travel time change over time for each measurement location. The white horizontal lines in both figures denote the start of the imbibition and the end of the drainage process. For calculating the travel time change, the bottom reflection travel times were averaged over the first five profiles which had
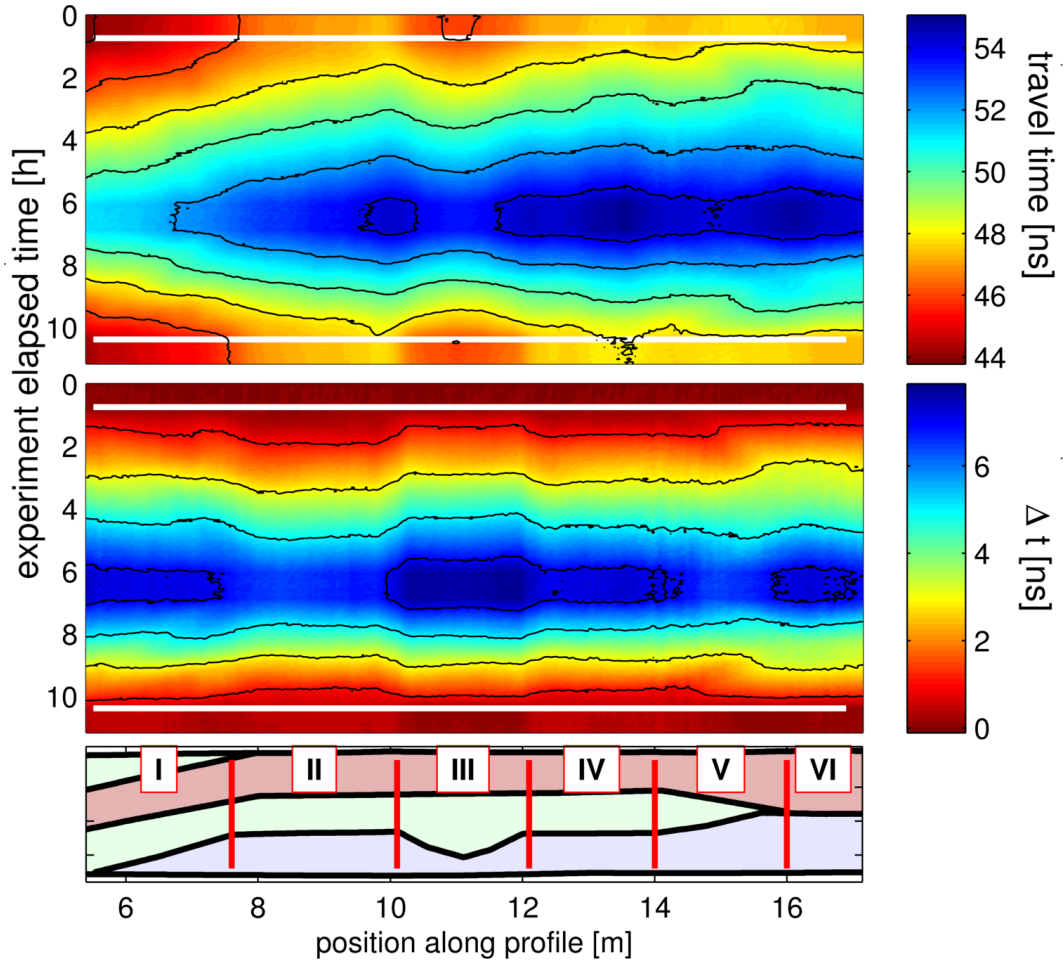
Figure 7.9: 2D representation of the travel time (top) and the travel time change (middle) referenced to the start of the experiment as measured by the INT1 channel. The horizontal white lines indicate the start of the imbibition and the end of the drainage respectively. For comparison, the ASSESS-GPR structure is pictured again at the bottom. Structurally different regions are specifically marked by Roman numbering.

been measured before starting the imbibition and were subtracted from all subsequently acquired datasets. At the bottom, the ASSESS-GPR structure is pictured for reference with the structurally different profile parts marked by Roman numbers.

As expected, we see a substantial variation in travel times over the ASSESS-GPR profile. As can be seen from Figure 7.9, the resulting diagram of travel time changes over the course of the experiment can be divided into characteristic areas according to the structurally different profile parts. Region III exhibits the largest dynamic range. Here, the travel time increases by over 8 ns due to the infiltrating water. The two three layered parts, regions

(a) Two layered part
(b) Synclinal structure
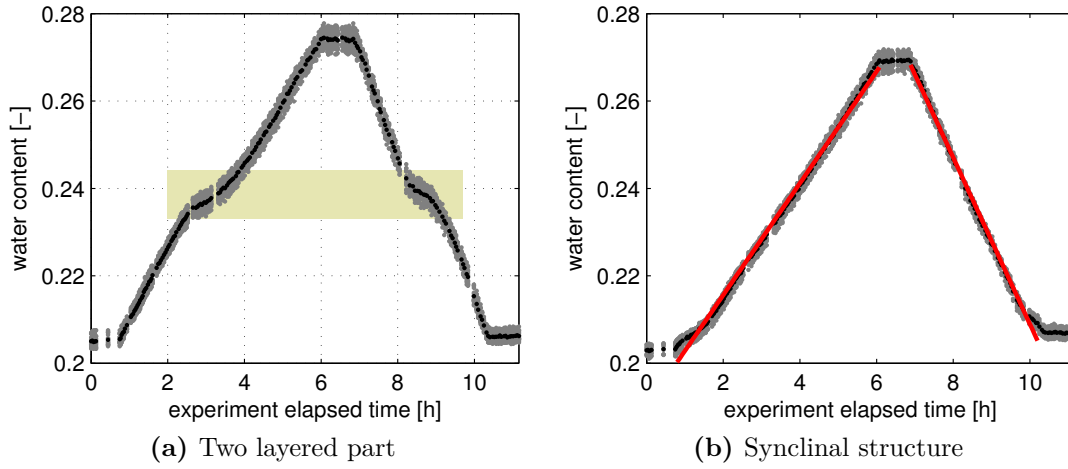
Figure 7.10: Average water contents calculated from the INT1 channel bottom reflection data. The left side shows all values from the two layered part of the ASSESS-GPR site shaded in gray; averages of the whole part are drawn in black; the light yellow box shades the region where the capillary fringe passes the layer boundary. The right side shows the same for the profile part with the synclinal structure, with the red lines indicating the regression fit for calculating the ratio of the water content change.

II & IV, exhibit a quite similar behavior. Last but not least, after the end of the drainage, the observed travel times seem to be slightly longer for regions I, II, IV and V than before the start of the experiment, which might indicate that the 0.5 m^3 of water which are not extracted again remain foremost in these sections.

For a more detailed look at the water content dynamics, we next calculate the water content from these travel time changes and evaluate the results for the different regions. Figure 7.10 shows a comparison for regions III and VI, the synclinal structure and the two layer part, respectively. Keeping in mind that each data point represents a value taken from a different common offset measurement, the precision for measuring the water content change seems to be quite remarkable. In fact, these figures show that we achieve a sensitivity better than 0.001 m^3/m^3 for measuring water content changes.

Looking first at region VI (Figure 7.10a), we see both during imbibition and drainage that the water content change slows down considerably when the capillary fringe crosses the layer boundary. This happens for the imbibition between 1.8...3.5 hours and during the drainage between 7.5 and 8.5 hours, a behavior which has been observed and explained for the drainage in the July experiment in Section 7.2.2. For the imbibition, a possible explanation follows a similar argumentation. In our experiment, imbibition results from a continuous increase of the hydraulic potential, causing a corresponding rise of the water table and the associated capillary fringe above. The width of this capillary fringe is

essentially determined by the air entry value of the medium $|h_0|$ (compare the sketch in Figure 2.2 and equation 2.36). Hence, the top of the capillary fringe will reach the layer boundary for a certain potential. Now, assuming a smaller air entry value $|h_0|$ in the upper medium (i.e. a larger maximum pore size), the high water content cannot yet be sustained in the upper medium for this hydraulic potential. Hence the amount of water which can be infiltrated at this point by a continued increase of the hydraulic potential will be less until the capillary fringe can be sustained, slowing down the observed increase in average water content.

Turning to the diagram showing the water contents as derived over region III, we see that there both the increasing and decreasing branch of the average water contents basically follow straight lines. This is to be expected, since the capillary fringe here does not cross any layer boundaries. Only at the very beginning and the very end there are slight deviations from this straight line, here the capillary fringe reaches the bottom of the synclinal structure. Fitting straight lines to both branches (indicated as red lines in Figure 7.10b), we can calculate the ratio of the their slopes as $|^{\mathrm{incr}}/_{\mathrm{decr}}| = 0.69$. This is in very good agreement with the ratio of the pumping rates of 0.695.

7.3.4 Cumulative change of the hydraulic state

Having discussed the time-lapse data we can take another detailed look at the averaged water contents observed along the whole profile, contrasting the results before and after the experiment with the situation after imbibition. As has just been mentioned, the 2D diagram of travel time changes in Figure 7.9 suggests that there are certain regions where the water content stays higher after the experiment. For getting a better picture, Figure 7.11 shows the water content changes as observed by the two internal channels. More precisely, Figure 7.11a pictures the average water content increase which is due to the imbibition process and Figure 7.11a the analogous water content change when comparing the measurement before and after the entire experiment. On average, the GPR data would indicate an average increase in water content by about 0.07 $\mathrm{m^3/m^3}$ due to the infiltrating water. After the drainage process average water contents are evaluated to remain approximately 0.003 $\mathrm{m^3/m^3}$ higher than before. However, comparing the results for the two internal channels with respect to Figure 7.11a, there seems to be an offset between the two internal channels: The water content change as observed by INT2 is about 0.3% larger than for INT1. Since both channels should in principle yield the same result, this does raise the question whether such minute variations can be reliably interpreted, although the results for 7.11b match very well.

7.3.5 Uncertainty discussion

As we have seen in the previous section, minute changes have been observed during the experiment, both in terms of travel time and water content changes. For example, an extremely high precision for measuring average water content changes over the course of

(a) Water content difference after imbibition

(b) Water content difference at the end of the experiment
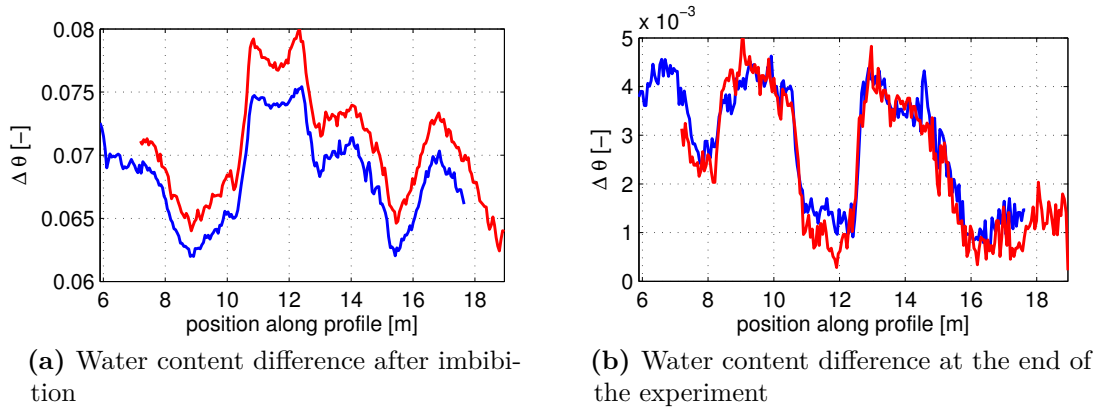
Figure 7.11: Water content change as calculated from the INT1 (blue) and INT2 (red) channels as a function of position along the intensively monitored part of the ASSESS-GPR profile. The water content increase due to the imbibition process is shown on the left. The right pictures the remaining water content differences after the end of the drainage.

the experiment has been achieved. Comparing the hydraulic state before and after the experiment, variations seem to be observable amounting to less than 0.5% in water content. These results seem to fit the auxiliary data well (TDR data, total amount of water), but the question of the uncertainty of these results warrants some additional attention.

Channel Crosscheck

As has been practiced in chapter 5, we can again resort to a comparison of the different channels which are available due to our measurement setup for crosschecking the results. At least, the evaluation of the two internal channels should in principle yield the same result. Interpreting potential differences observed for the two crossbox channels is more difficult, as in this case any deviation can have several reasons due to the increase in the measurement angle. This could e.g. include potentially different ray paths, or a different spectral impact of the transition zone. Now, Figure 7.12 shows the water content variation for all four available channels, averaged over a representative part of approximately ten traces for each of the six regions marked in Figure 7.9. The blue dots in Diagrams 7.12c and 7.12f denote INT1 channel data, and have already been part of Figures 7.10b and 7.10a, respectively. As can be seen clearly after having referenced all water contents to the same start value at the beginning of the experiment, the observed variation in water content seem to differ by up to 0.01 m³/m³. Furthermore, this is not only true for the crossbox channels – which might be explainable e.g. by the just mentioned potential impact of the differences in the measurement angle – but also for the two internal channels, pictured by the blue and red dots, which do not show exactly the same variation.

For explaining the observed differences, we take a closer look at the shape of the respective
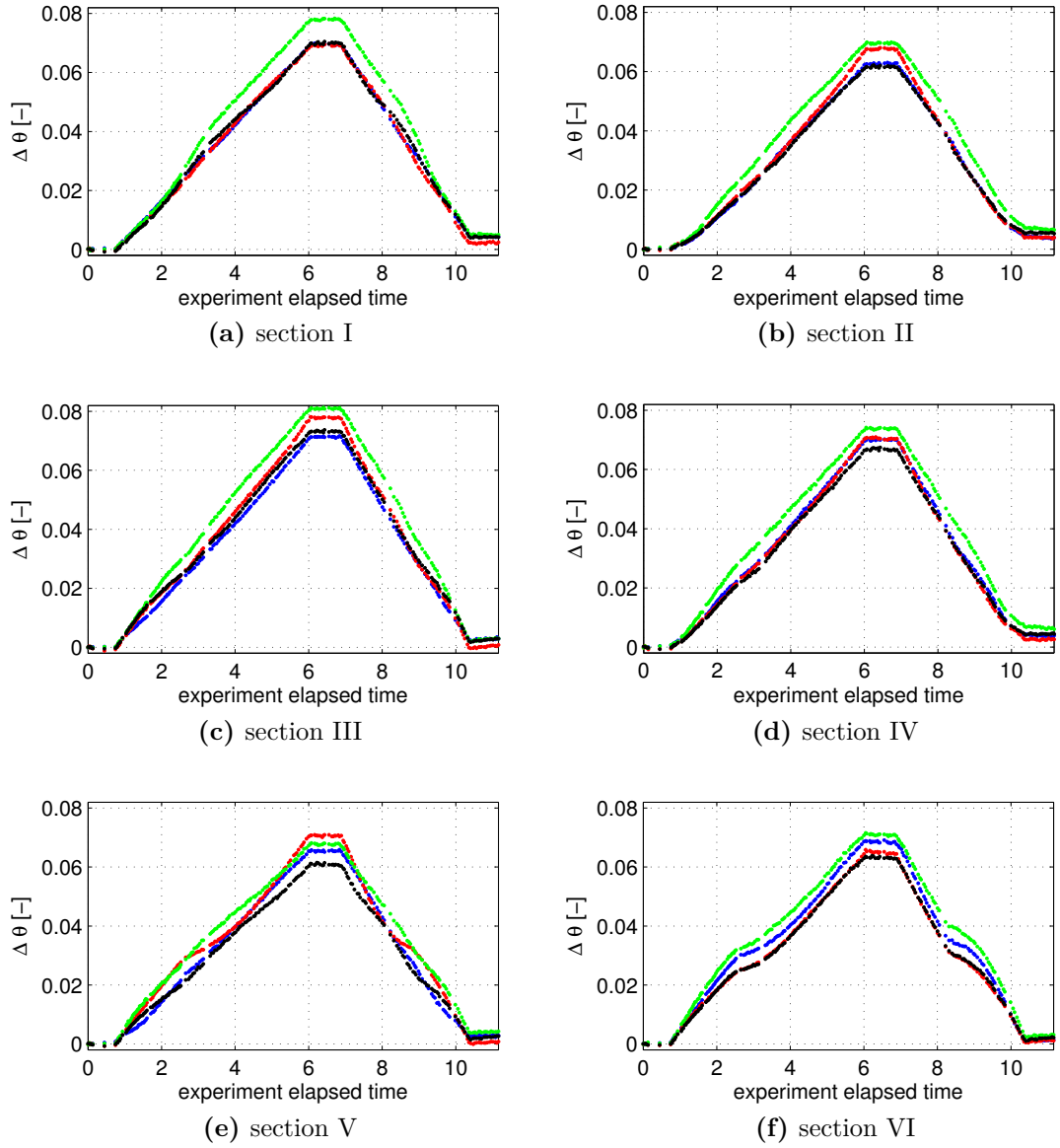
Figure 7.12: Water content changes as calculated from all available channels, representative for the different sections indicated in Figure 7.9. Channel INT1 data are plotted in blue, INT2 in red, SCBC in black and LCBC in green.

wavelets. Figure 7.13 illustrates the changing shape of the bottom reflection wavelet for both internal channels over the course of the experiment. A corresponding time-lapse movie showcasing the changing wavelet shape for each time step can be found in the digital
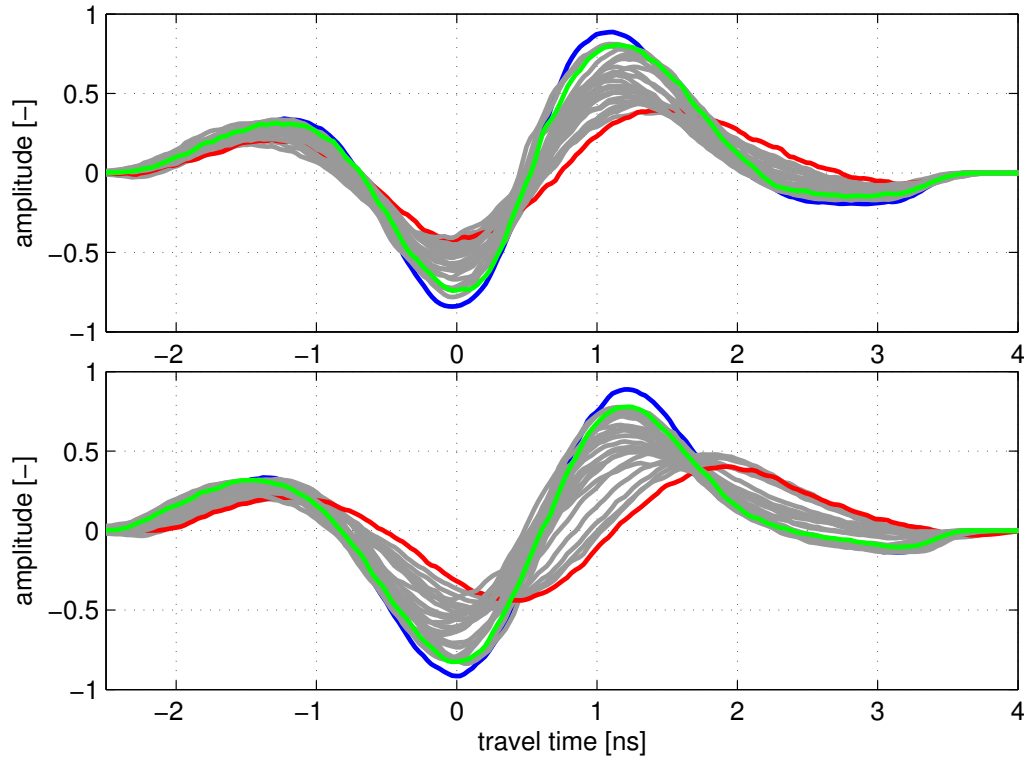
Figure 7.13: Changing shape of the bottom reflection wavelet over the course of the experiment. The upper diagram shows the INT1 channel data, the lower diagram the corresponding INT2 channel data. Specifically marked are the recorded wavelet (i) before the start of the imbibition (blue), (ii) after the end of the imbibition (red) and (iii) after the end of the drainage process. Both INT1 and INT2 wavelets have been referenced to the first minimum of the respective INT1 channel wavelet to highlight the travel time differences observed between the two internal channels at high water levels. A corresponding movie can be found in the digital supplementary materials in Appendix B.

supplementary materials, as described in Appendix B. All wavelets shown in Figure 7.13 were averaged over a 1 m stretch of the two layered part (region VI) for noise reduction and and shifted with respect to the first minimum feature of the corresponding INT1 channel wavelet as zero reference. This allows to directly compare the variation of the wavelet shape and position between both channels. As can be seen, the wavelet shape is quite similar for both channels before (blue lines) and after (green lines) the experiment. In particular, the first minima of the wavelets are recorded at the same travel time, leading to the same observed water content, as expected. However, there is a significant change to be observed in the shape of the recorded wavelets over the course the experiment. To illustrate this changing shape, the red lines denote the wavelet shapes after the end of the

imbibition. The overall amplitude values decrease due to the higher average water content leading to an increase in attenuation. At the same time, the wavelet gets significantly broader, which is also reflected in a decrease in its center frequency by about 100 MHz. In this particular case, the INT2 wavelets show more variation: The wavelets recorded by the INT2 channel around the time of the highest water table position are broader and the first minimum feature (which is used for travel time evaluation) is recorded at longer travel times as compared to the INT1 channel data. Hence, although both channels record the first minimum at approximately the same time before and after the experiment, calculating travel times from the INT2 channel will lead to a variation which is about 0.5 ns larger than for the INT1 channel due to the more significant changing of the shape of the recorded bottom reflection wavelet. This in turn leads to the variations we observe in the water content changes calculated from the different channels as shown in Figures 7.12.

One source of this effect could lie in the changing hydraulic state over the course of the experiment. In principle, the interaction of the dynamic and stationary features in the profile above the bottom reflection act as a dynamic filter which may affect different spectral ranges of the signal, depending on the specific contribution of certain reflections. The capillary fringe itself acts as a filter as well, however, numerical simulations have shown that the relative magnitude of a pure capillary fringe reflection is too small to have a significant impact on the frequency content of the transmitted signal. Still, especially for the differences observed between internal and crossbox channels the interaction between the capillary fringe reflection and stationary reflections which may or may not reflect significant parts of the signal depending on the hydraulic state could play a major role.

Secondly, interference effects cannot be completely ruled out, e.g. with multiples of structures located above the capillary fringe (and as such not changing over time). If such a multiple arrives later than the bottom reflection at a certain position at the start of the experiment, it will lead to a continuously changing interference with the arrival time of the bottom reflection changing over the course of the experiment. This argumentation is basically similar to the modeling exercise which lead to Figure 5.15.

However, both approaches cannot per se explain the differences observed between the two internal channels. In this case, the specific antenna characteristics must play a significant role. Towards the end of the imbibition process, the capillary fringe reflection occurs at a distance of approximately 0.6 m from the respective antennas. According to the definition of *Balanis* [1982], this might already be close to the region of the radiative near-field of our GPR antennas. In this region "radiation fields dominate and the angular field distribution is dependent upon the distance from the antenna", i.e. the target response may depend significantly on the radiation pattern of the specific antenna. First, this might in part explain the significantly differing shape of the bottom reflection towards high water levels. Secondly, assuming that the radiation pattern of both antennas is significantly different for these regions, this could also yield a possible explanation for the different impacts on

both internal channels.

Finally, the signal stability issues discussed in Section 5.4 could also be a source for these observed inconsistencies. In the case discussed there, a channel specific variation of the wavelet shape was observed as a function of antenna separation in WARR radargrams. As described, this can be translated to a variation of the wavelet shape as a function of the time of recording. In our case this could lead to a variation of the recorded signal shape with the in- and decrease of the average water content, since over the course of the experiment, the absolute time of recording of the bottom reflection varies continuously. Such a variation could then also differ with respect to the specific range of travel times at a location, explaining the different effects on the separate regions shown in Figure 7.12.

Independent of the specific cause, this result currently limits the quantifiability of the observed GPR response as well as the interpretability of minor variations observed in the water content changes in Figure 7.12. The remaining irrefutable feature is the strong impact of the layer boundary for the two layered part, since this effect is consistently observed by all four channels.

7.3.6 Summary and Conclusions

This chapter has described recent experiments with a fluctuating water table at the ASSESS-GPR site in Heidelberg, Germany, which were aimed at quantifying observed GPR response to the imposed water content dynamics. At this point, the following conclusions can be drawn:

- High-resolution multichannel GPR measurements provide a unique view on the inter- actions between stationary structures and dynamic processes during the experiments discussed here.

- Dielectric contrasts vary significantly depending on the hydraulic state. Certain secondary structural features like compaction layers within the same layer may be observable only under certain situations. This raises a note of caution for the interpretation of single-instance-in-time field measurements.

- The capillary fringe dynamics is well observable during the experiments. The general behavior can be explained using numerical simulations of the changing hydraulic state and the resulting GPR response. A quantitative evaluation of the capillary fringe dynamics is however difficult for the ASSESS-GPR site due to the strong interactions with subsurface structures and small-scale heterogeneities.

- Evaluating the bottom reflection allows for high-resolution monitoring of the overall average water content change during imbibition and drainage processes. A decrease in the observed speed of average water content change can be observed when the

capillary fringe crosses certain material boundaries. This can be explained in terms of the different hydraulic properties of the respective materials.

- The high precision of the measurement is limited by variations in the shape of the observed wavelets for different hydraulic states. Although the specific hydraulic conditions may play a role, the variation is most likely due to instrument limitations, since the two internal channels show a distinctly different behavior.

- Despite all challenges, the current results can already be used for consistency checks with simulation and inversion results describing the effective hydraulic properties of the ASSESS-GPR structure, like put forward by *Jaumann* [2012]. If the apparent instrument issues can be resolved, potentially different water content changes in the respective regions along the GPR profile could become interpretable as well, which might allow for further constraining distinct model descriptions.

8 GPR Applications in a Highly Structured Watershed

The aim of this chapter is to further our understanding of GPR methods applied in a highly structured regional watershed. In particular for exploring the moisture state of a watershed at regional scales through local field measurements, it is neccessary to assess the applicability of GPR methods for determining near-surface water contents at characteristically distinct sites. Hence, in comparison to previous chapters, a broader view is taken here: Applications of GPR are reviewed in the larger context of investigating the hydrologic processes of a highly structured regional watershed in Northwestern China. These data were acquired over two field campaigns in spring 2010 and 2011, executed jointly with colleagues from the Xinjiang Institute of Ecology and Geography, CAS. This chapter expands the discussion put forward in *Klenk et al.* [2012], where the datasets shown in sections 8.2, 8.3 and partly 8.4 have been presented recently.

A detailed site description for Fukang, Shirengou and Houxia is provided in chapter 4. Here, we will first extend the considerations in chapter 6 by discussing a second dataset acquired in the semi-desert area close to Fukang (section 8.1). Secondly, two datasets acquired in 2011 at a hillslope area in the foothills of the Tianshan mountains (section 8.2) and at a high mountain grassland site (section 8.3) will be discussed. After the presentation of measurements at agricultural sites in the region (section 8.4) and on Urumqi's glacier No.1 (section 8.5), the chapter concludes with some general remarks about the achieved results and potentials for future research.

8.1 Semidesert 2D-Plot Measurement

As we have seen in the previous chapter 6, the direct ground wave signal could be successfully employed for measuring temporally stable patterns in soil moisture content in the semi-desert region at the rim of the Gurbantüngüt desert. Approximately 500 m to the south of that measurement site, a second site has been established, focusing on mapping soil water content patterns within a 50 m × 50 m sized area. As can be seen from Figure 8.1a, the site is lodged roughly in the middle between two neighboring dune chains. Figure 8.1a also introduces the reference coordinate system for the discussion in this section, which has its origin at the (approximate) eastern corner of the plot area. Reported X/Y coordinates are always to be understood in meters, with the first coordinate describing the location along the axis running roughly north-south and the second coordinate similarly

(a) Site overview

(b) Central part of the measurement site
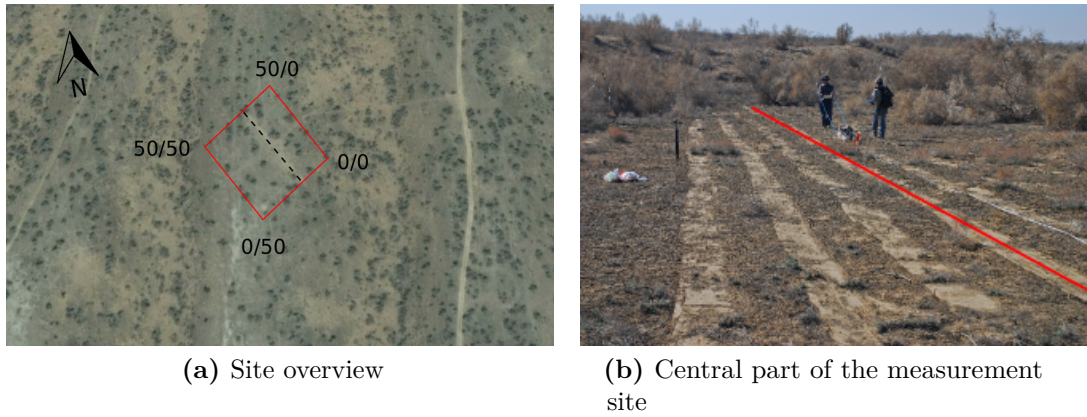
Figure 8.1: The left shows a Google Earth™snapshot of the 50 m × 50 m 2D-measurement area, which has been marked with the red rectangle. The satellite image was acquired two months after the measurement. The right side pictures the central part of the measurement plot, viewed to the north. The location of the exemplary radargram shown in Figure 8.2 is marked by the dashed black line in the satellite image on the left and correspondingly by the red line in the picture on the right.

denoting the location along the approximately east-west oriented axis.

To support the interpretation of the observed water content distribution, a comprehensive survey of the vegetation cover has been part of the 2010 measurement campaign, estimating the ground vegetation cover as well as the location, width and height of brushes within 5 m × 5 m sized subpixels. The site has been visited by both measurement campaigns in 2010 and 2011.

The overall measurement setup was the same as for the GPR line evaluated in chapter 6. All GPR data which will be presented here were acquired at 400 MHz center frequency and an antenna separation of 1.14 m. During the first campaign, the whole plot has been covered by a perpendicular grid of GPR lines with a line spacing of 5 m in order to establish the suitability of this site for GPR monitoring. A part in the central area of the plot has been investigated more closely by adding further north-south running GPR lines with a 1 m linespacing. This central part has been the special focus of the second campaign in 2011. During the second campaign, the whole part between the points 10/15 and 35/40 have been investigated by a perpendicular grid with a 1 m line spacing.

An exemplary radargram, which has been acquired between the 0/20 and 50/20 points (as marked by the black dashed line in Figure 8.1a) during the 2011 campaign, is pictured in Figure 8.2. The radar measurement features a well-evaluable groundwave signal along the whole profile except for the region between 35 and 45 m, which is marked by the black rectangle in Figure 8.2. For this 10 m stretch, TDR measurements revealed increased near-surface conductivity values, as shown by the grey shaded box in Figure 8.3b. Comparing
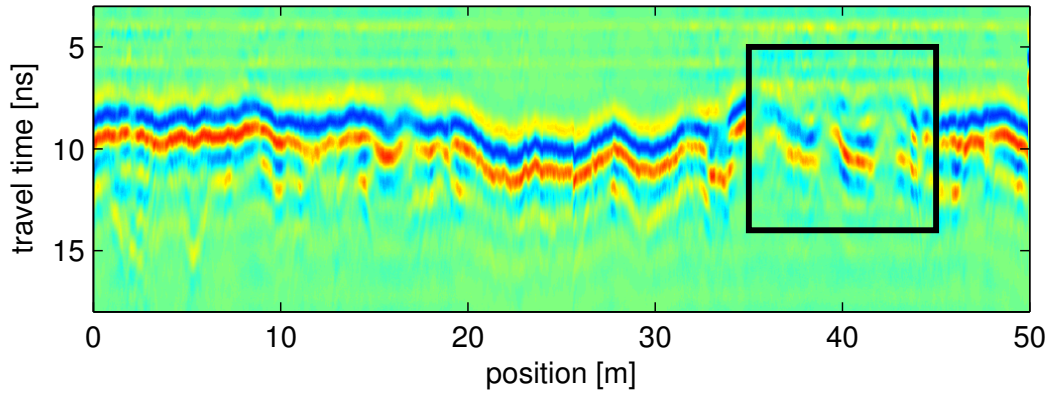
Figure 8.2: Exemplary radargram from the 50 m × 50 m measurement site established in the Fukang semi-desert area. This measurement shows 400 MHz LCBC data acquired in 2011 at an antenna separation of 1.14 m. Note the poor signal quality between 35 m 45 m, which is due to comparatively high conductivities at this part.

(a) water content

(b) electric conductivity
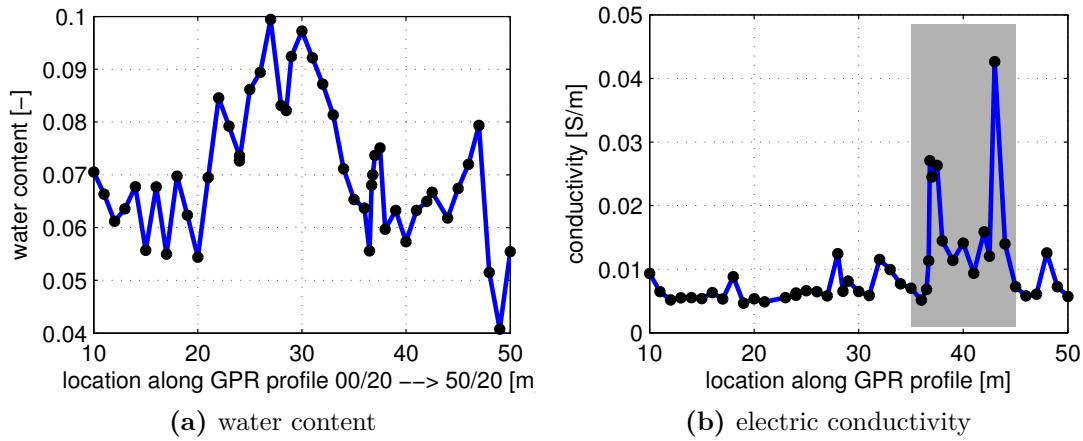
Figure 8.3: Water contents (left) and electric conductivity (right) values derived from 0.3 m rodlength vertical TDR measurements along the exemplary GPR profile shown in Figure 8.2.

the GPR signal attenuation to corresponding TDR derived conductivities, evaluation for the antenna separation employed here is possible up to conductivities of around 0.01 S/m. Since areas of higher conductivity values do not allow for reliable evaluation of GPR data, they have been excluded from further processing.

In this semi-desert environment, such spots of high conductivity are most likely due to an increase in near-surface salt contents, which severely increase the attenuation of the GPR

(a) Data from soil profile P1 *(good GPR signal)*

(b) Data from soil profile P1

(c) Data from soil profile P2 *(unusable GPR signal)*
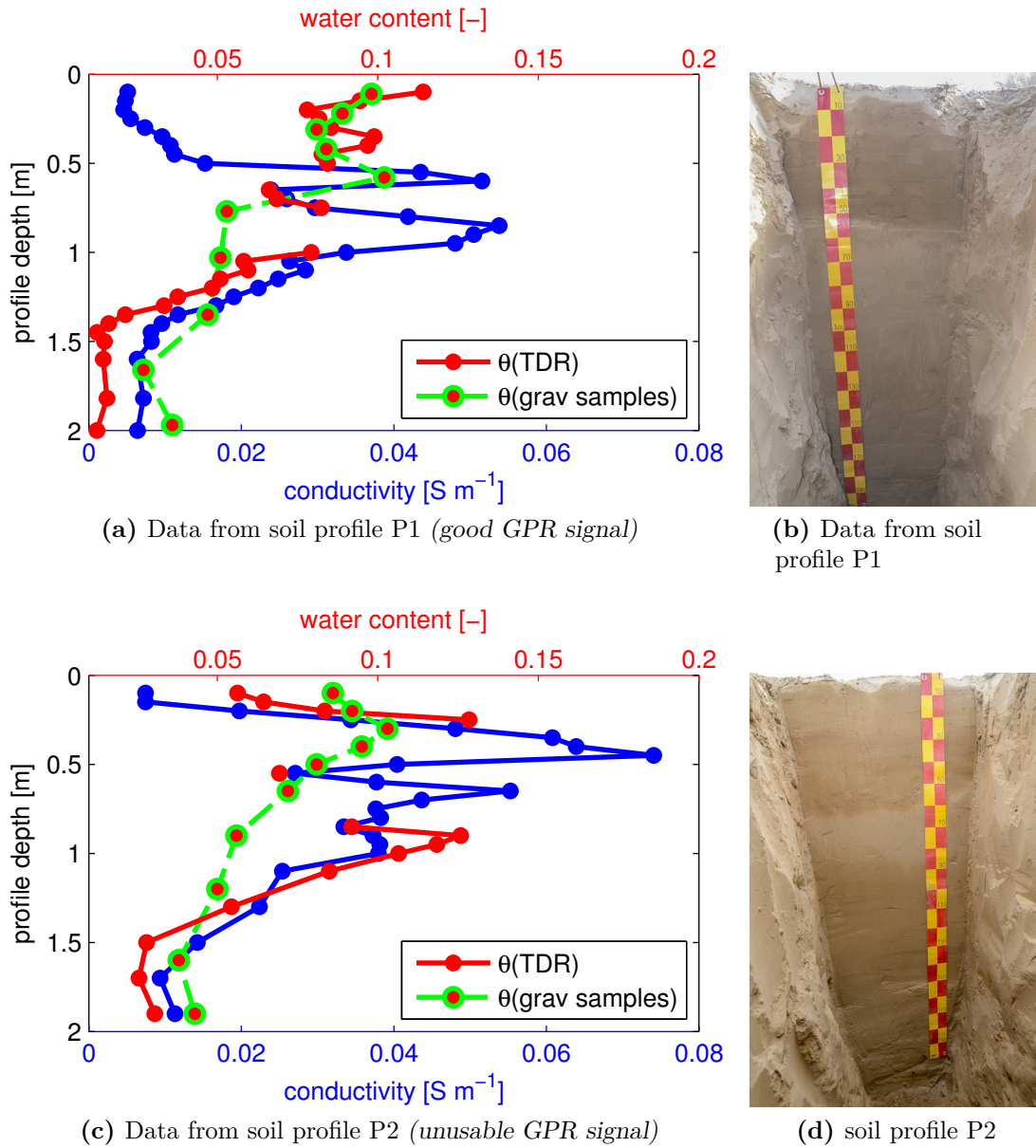
(d) soil profile P2

Figure 8.4: Comparison of the two soil profiles excavated at the Fukang 2D-plot site in spring 2011. The top row shows the profile data and a picture from the 27 m point, the bottom row the corresponding data and picture from the 40 m point.

signal. In order to corroborate this interpretation, two soil profiles have been excavated during the 2011 campaign. The locations were chosen adjacent to the GPR line shown in 8.2, roughly at positions 27/19 (in the following termed P1) and 40/19 (in the following

termed P2). The aim was to closely investigate the two areas with the most distinct signal differences. The evaluation of both soil profiles is presented in Figure 8.4. The upper two plots show the data evaluation and a profile picture of the P1 profile, which has been dug in the region with the most stable GPR signal. The bottom plots show the corresponding data evaluation and a profile picture of the P2 profile, where the GPR signal cannot be evaluated reliably. A TDR probe with 0.2 m rodlength has been used for measuring both water contents (drawn in red) and electrical conductivity values (drawn in blue) for the two profiles. Due to partly high conductivity values, the recorded TDR traces were not evaluable for water content at some positions of the profile; in general, this was the case whenever the conductivity was larger than about 0.04 to 0.05 S/m. Hence, several soil samples have been taken in order to use gravimetrically determined water content values (green-edged red dots) as additional ground truth.

Although both profiles exhibit a similar, distinct transition from comparatively wet to dry sand between 0.5 and 0.6 m, the differences between the two profiles close to the surface become apparent from the data evaluation. At P1, conductivity values remain around 0.01 S/m for the top 0.5 m of the profile, while both TDR and gravimetric samples indicate water contents around 0.1 m^3/m^3. In contrast, conductivity values at P2 quickly increase to over 0.07 S/m at a depth of 0.5 m. In general, TDR derived water contents and conductivities seem to be highly correlated in these profiles, except for the top 0.5 m of P1. This is to be expected if the observed conductivities can be traced to high salt content, since the presence of water will significantly enhance the ionic conductivity under these conditions.

Another notable difference between the two profiles is the near-surface gradient in water content, as observed by both the gravimetric samples and TDR. While the water content seems to decrease slightly for the top 0.3 m at P1, the opposite is true for P2. This might be associated with differences in vegetation at the two locations. While P1 was covered by grass patches, the location of P2 was almost completely bare of vegetation. In such a case, the observed gradients would be consistent with the grass roots drawing the water from depths to around 0.3 m, while at the barren soil, the top centimeters dry out quickly, effectively prohibiting further evaporation from lower parts of the profile.

In any case, the observed differences in conductivity for the top 0.5 m of the profile can explain the high attenuation of the GPR signals around P2 as viewed in Figure 8.2.

We next turn to the interpretation of the observed spatial patterns of the water content distribution at this site. Figure 8.5 displays the main results of the 2010 campaign, showing (i) a picture of the central part of the plot, (ii) the fractional vegetation cover map and (iii) a spatial interpolation of the retrieved GPR data. At the time of the measurement, the first 2-3 cm of the soil were basically completely dry. Hence, as our measurement shows, this virtually dry surface conceils a quite heterogeneous distribution of soil water content below, with water contents ranging between 0.03 and 0.16 m^3/m^3. It can be remarked that this information might not be directly accessible to current remote sensing methods. Comparing the water content distribution to the vegetation map, the general soil water

(a) fractional vegetation cover

(b) 2010 water content distribution as measured by GPR
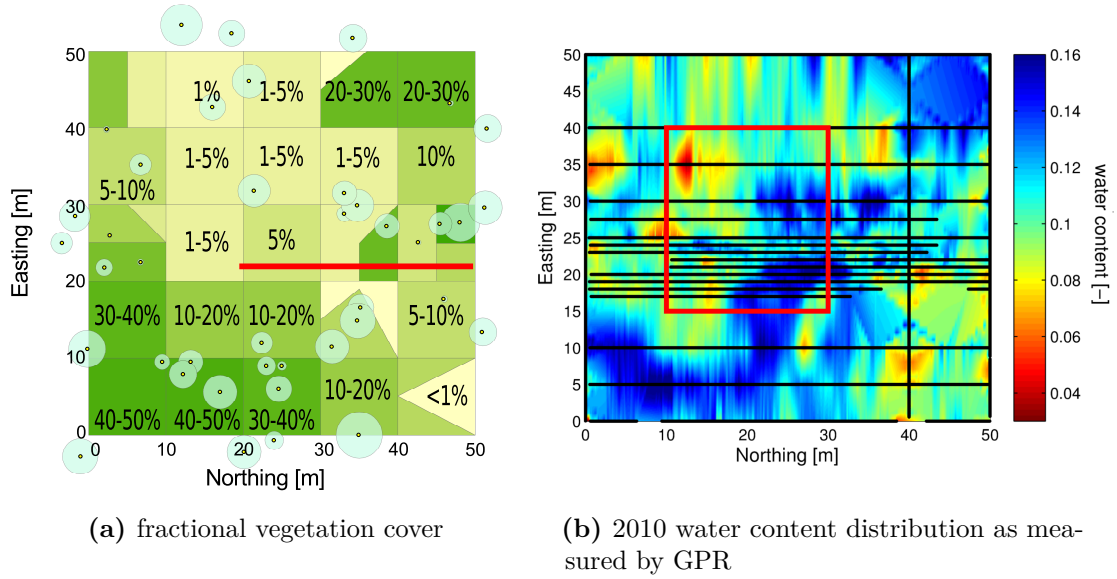
Figure 8.5: Overview of the results of the 2010 measurement campaign at the 50 m × 50 m measurement site in the Fukang semi-desert area. The left figure pictures the fractional vegetation cover within the plot as well as the location of brushes and small trees, where the width of the trees is indicated by the corresponding circle size. The red line marks the location of the radar profile shown in Figure 8.2. The diagram on the right shows an interpolated view of the 2010 GPR data measured along the black lines. The red rectangle marks the central part of the area which is compared to the results acquired in 2011 in Figure 8.6.

content pattern seems to be associated with the fractional vegetation cover. The highest water contents are oberseved in areas with a comparatively large fractional vegetation cover, for example around the south-eastern corner of the plot. Likewise, areas with less vegetation tend to exhibit lower water contents, e.g. towards the south-western corner of the plot. The location of the trees does not seem to have a large impact on the near-surface water content distribution.

For a detailed interpretation of the spatial patterns, the GPR sampling over the whole plot area was probably not dense enough. Hence, we turn to the central part of the area, which has been marked by the red rectangle in Figure 8.5 (iii), featuring the most dense sampling in 2010. Figure 8.6 compares the observed water contents in this center part of the plot in subsequent years. The upper part of the figure shows a more detailed view of the 2010 data plotted in Figure 8.5 (iii), while the lower diagram pictures the situation in 2011. Due to the irregularity of the measurement grid in 2010, the location of the 2010 GPR measurement lines are specifically indicated in the upper plot. Since the data have been sampled on a dense regular grid with an 1 m line spacing in 2011, those GPR lines are not explicitly plotted in the lower diagram. As has been observed in chapter 6 (specifically in

Figure 6.6), the overall conditions were somewhat drier in 2011: Average water contents for the two datasets shown in Figure 8.6 drop from approximately 0.10 $\mathrm{m^3/m^3}$ in 2010 to 0.07 $\mathrm{m^3/m^3}$ in 2011. These mean water contents are consistent with the results observed for the dune valley parts of the measurement line discussed in chapter 6.

Due to the less dense sampling grid, the 2010 data cannot resolve as much detail as the 2011 measurement. Nevertheless, the general patterns can be observed to remain largely similar. This temporal stability of the general patterns in the soil water content distribution is consistent with the findings discussed in chapter 6.

In summary, we reiterate that we can observe detailed soil water content distributions on such a 50 m × 50 m site in the semi-desert area around Fukang. The small scale patterns observed in this plot remain similar between the years and seem to be associated with the vegetation cover, which is consistent with the hypothesis of a snow-vegetation feedback put forward in chapter 6. A more extensive time series would help in assessing the extent to which these patterns change over the seasons. We also note that high electrical conductivities, which are due to high near-surface salt contents, do hamper the evaluation of GPR data at several points at this site. Since high electrical conductivities lead to an increase in the imaginary part of the dielectric permittivity, our assumptions of negligible losses may no longer be valid. This is definitely the case for profile parts, where the GPR signal quality could be directly observed to deteriorate ($\sigma_{\mathrm{dc}} > 0.02$ $\mathrm{S/m}$).
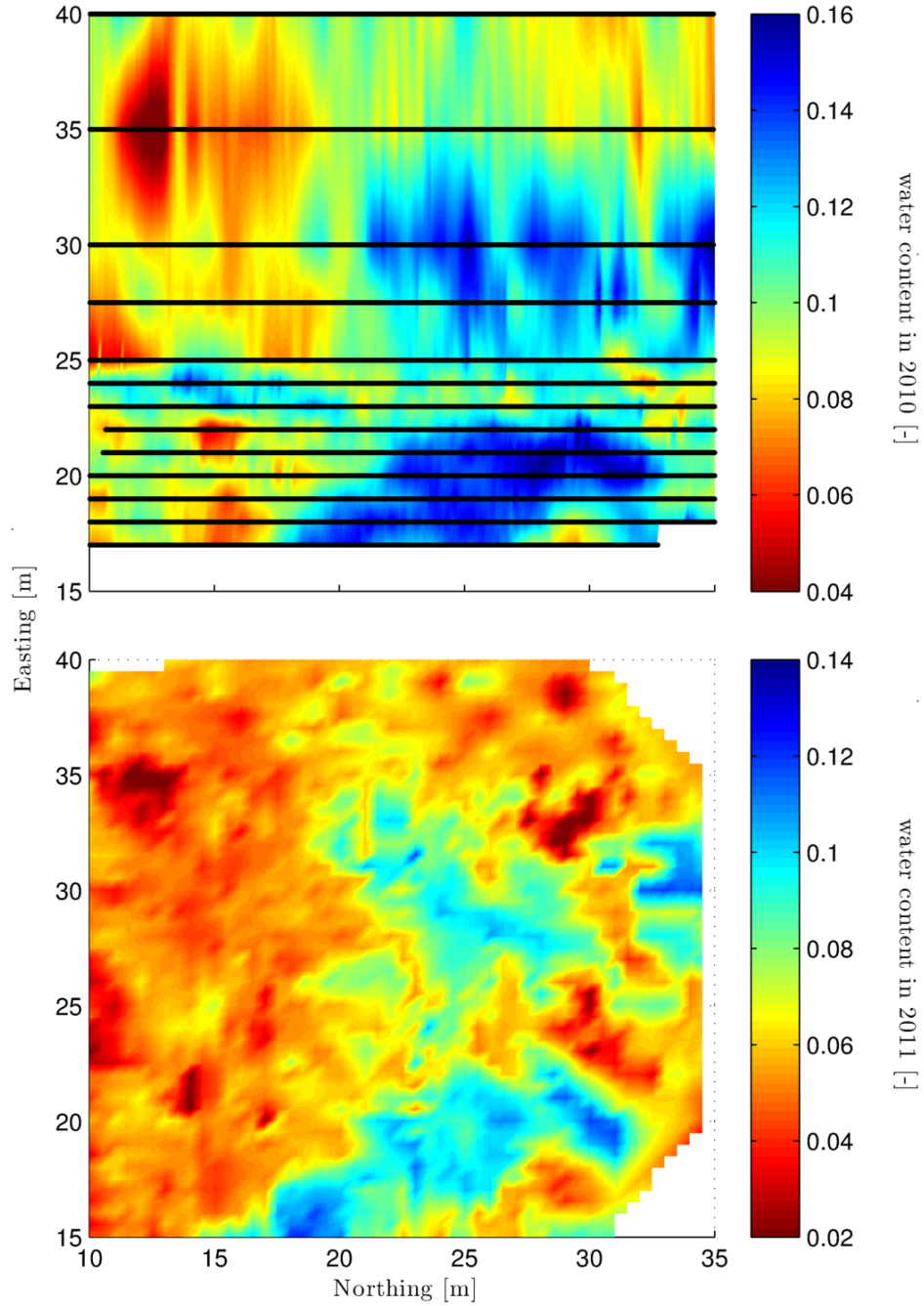
Figure 8.6: Comparison of the 2010 (upper diagram) vs. 2011 (lower diagram) LCBC derived water contents for the central part of the 2D-plot. The color scale for 2010 is deliberately shifted by 2% towards higher water contents to highlight the similarity of the spatial distribution patterns despite the slightly wetter conditions which were already observed in Figure 6.6. The 2010 data is based on the GPR measurement lines shown in black, whereas the 2011 dataset comprises a regular measurement grid with 1 m line spacing in both directions.

8.2 Shirengou Dataset

The second measurement site is situated in the foothills of the Tian Shan mountains, characterized by undulating slopes. These hillslope areas are characteristic for about 23 % of the region of interest. The soil is covered by grass and the area is used for grazing between spring and fall. GPR measurements in the hillslope areas took place along a 1000 m long GPR line in May 2011, moving upslope while covering a total elevation difference of approximately 140 m. Figure 8.7 shows the corresponding radargram, where time zero has been adjusted according to the elevation difference.

We observe a relatively high near-surface water content from evaluating the direct ground wave signal, with a slightly increasing trend towards the higher regions of the profile (Figure 8.8). The soil water content distribution is quite narrow with an overall high mean water content of 0.3 m³/m³, which is due to a large precipitation event on the day before our measurement. Similar to the desert measurements, we can again observe considerable small scale structures. We attribute these variations here to a combination of microtopography effects (e.g. diverging and converging flows due to curvature) and vegetation differences. This hypothesis could be more closely examined by evaluating high-resolution remote sensing data of the area, mapping the vegetation patterns along the whole GPR line.

Furthermore, we have to note that the measurement shown here is most probably representing a quite unusual situation. According to locals, such strong precipitation events rarely occur more than once or twice a year in this area. Hence, for attributing the observed patterns to specific properties or processes, more detailed timeseries data would be needed. If the signal quality stayed similarly well also during dry conditions, this hillslope site would be a good candidate for implementing GPR-based monitoring of soil water content, representative for a large part of our region of interest around the city of Urumqi. However, the site is located fairly close to the city and this specific area might be converted to a golf course in the not-too-distant future, according to local peasants.
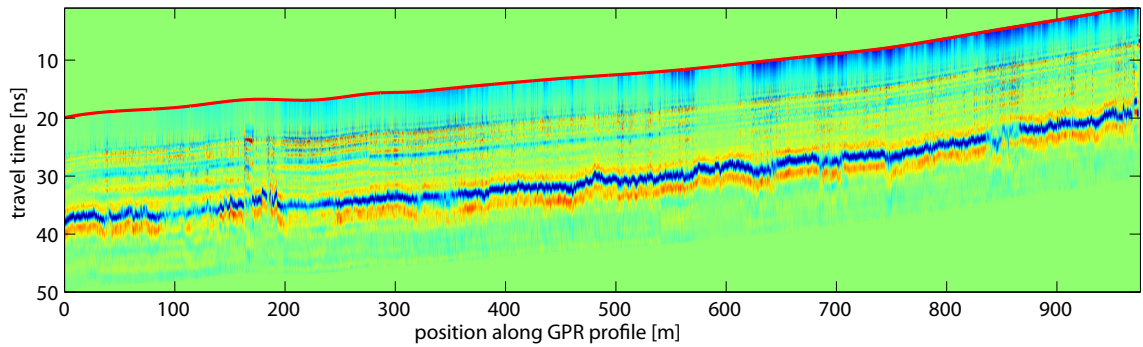
Figure 8.7: GPR radargram from the hillslope site ("B"), running upslope for approximately 1 km. The overall elevation difference is approximately 140 m. Time zero has been adjusted accordingly, as indicated by the red line (1 m corresponds to 0.7 ns). Here, antenna separation was 1.0 m. *Modified from: Klenk et al. [2012].*
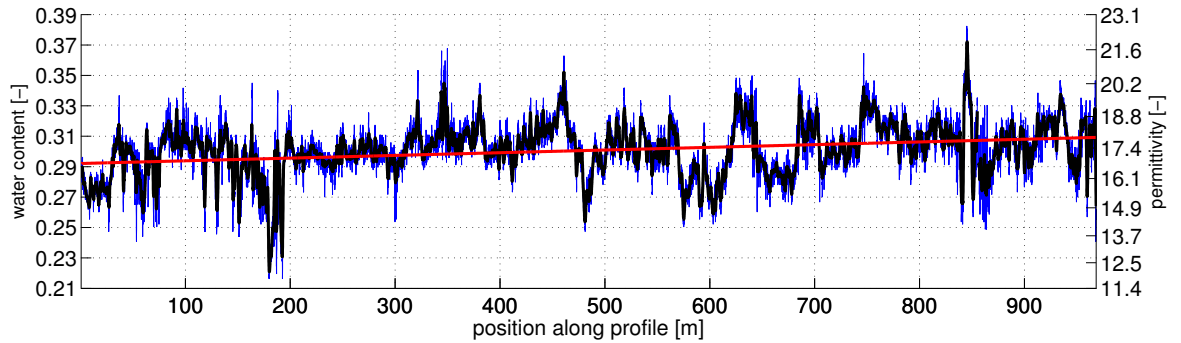
Figure 8.8: Water contents derived from the ground wave signal along the hillslope measurement (radargram in Figure 8.7). The black line shows a moving average of 0.5 m. The overall average water content increases slightly when moving upslope, as indicated by the linear fit in read. *Modified from: Klenk et al. [2012].*

8.3 Houxia Dataset

A third characteristic site was chosen in the high mountain grasslands in the upper reaches of the Urumqi river. This area is located at an elevation of about 3000 m. In such high mountain areas, which comprise about 17 % of the region of interest, the vegetation is already limited by comparatively short vegetation periods. Still, the ground is covered by tundra grass and the area is used for grazing in summer, mostly by goats and even some cattle. The GPR measurement discussed here was acquired within a 50 m × 50 m 2D-measurement plot in late April 2011. The measurement day saw some light snow, while the soil was still frozen below a depth of approximately 0.4 to 0.5 m. This frost table was directly observed when excavating a shallow soil profile at the origin of the measurement plot (i.e. the southwest corner), as illustrated in Figure 8.9. The rough position beneath

(a) Soil profile data **(b)** soil profile picture
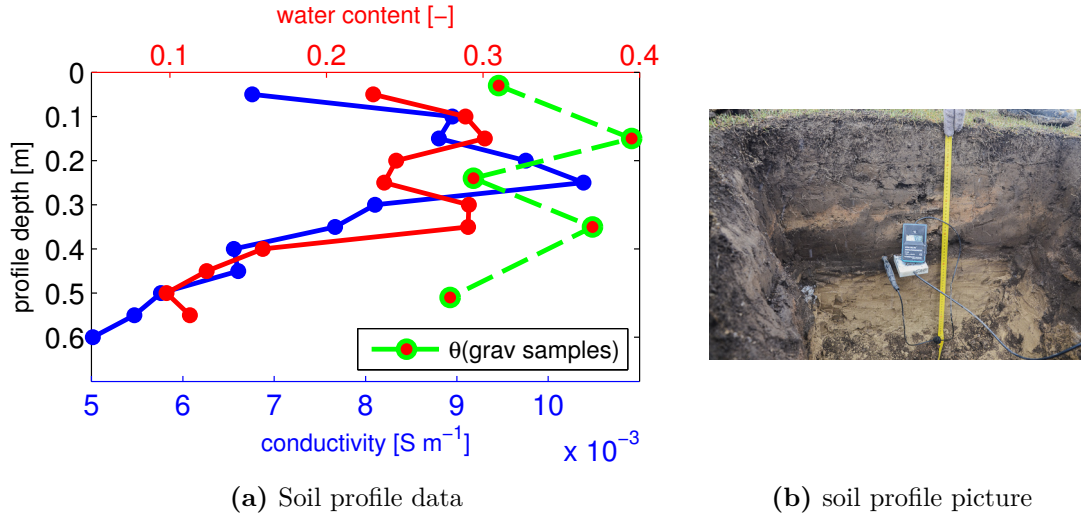
Figure 8.9: Soil profile excavated at the Houxia high mountain grassland site. The thermometer in the picture marks the top of the frost table.

which temperatures fell below 0 °C is marked by the location of the TDR probe in the soil profile picture shown in Figure 8.9b. The top 10 to 15 cm of the soil profile revealed high soil organic matter content, which unfortunately could not be quantified in the framework of this measurement campaign. The soil profile beneath showed a complicated structure of silty material. Electric conductivities for the whole soil profile are considerably smaller than for the semidesert area. For the GPR measurement, the standard four-channel setup was used, as indicated by the inset in Figure 8.10. GPR data were acquired along a rectangular grid, with GPR lines running both in north-south and east-west direction with a line spacing of 5 m. The radargram in Figure 8.10 shows the LCBC data from the measurement along the northern edge of the plot. Based on this dataset of four channels with three distinct antenna separations, multichannel evaluation could retrieve both the average water content above the seasonal frost table as well as the frost table position itself. A spatially interpolated 3D-representation of the measurement result is shown in Figure 8.11, with the z-axis denoting the reflector depth and the color scale picturing the average water content above. We can observe the frost table at depths of 0.41±0.02 m, which fits well to the information obtained from the soil profile. We also find a quite heterogeneous soil water content pattern above the frost table with a mean water content of 0.30±0.02 m³/m³. The water content distribution shows almost bimodal characteristics, with areas of higher water contents located in the southwestern part of the plot and lower water contents in its northeastern part. Due to the local topography, a possible explanation for this characteristic varation is an exposition-induced differing energy input, leading to enhanced thawing of the ground where the soil receives more radiation input. However, a detailed interpretation is difficult, since there might be a significant bias on
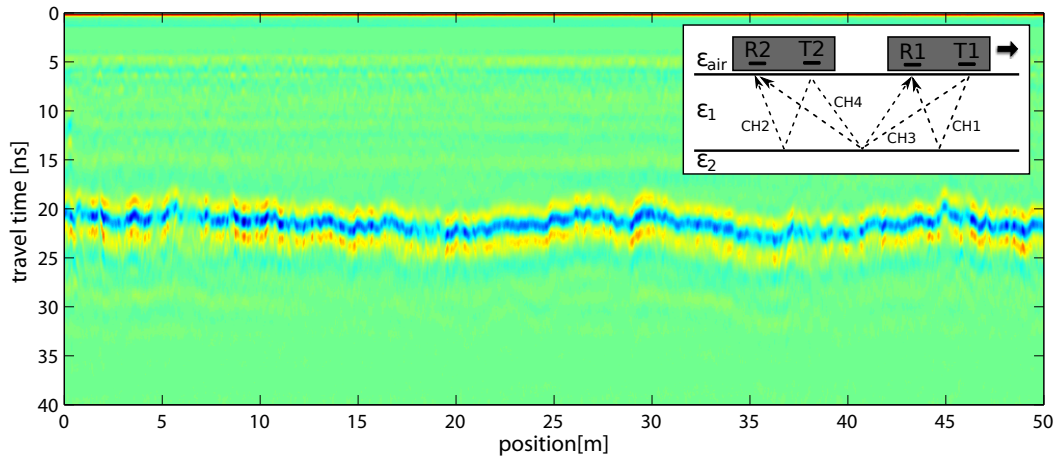
Figure 8.10: Exemplary LCBC radargram, measured at the high mountain grassland site with an antenna box separation of 1.2 m. The reflection from the freezing table around 20 ns is clearly visible. The inset in the upper right shows the four channel setup which was used for the evaluation shown in Figure 8.11. *Modified from: Klenk et al. [2012].*

the retrieved water content data, as seen by comparing the TDR measured water contents from the soil profile with corresponding gravimetric samples. Both datasets seem to follow the same general trend, but TDR values comparatively underestimate water contents by about 0.08-0.10 $\mathrm{m^3/m^3}$, also in the unfrozen part of the profile. This might be an impact of the high organic matter content. Hence, resolving these inconsistencies would probably warrant both a detailed study on the amount and impact of the organic matter content as well as acquiring a time series over the extent of the thawing season. Still, judging from the dataset presented here this site should be suitable for a detailed monitoring of seasonal freeze-thaw processes.
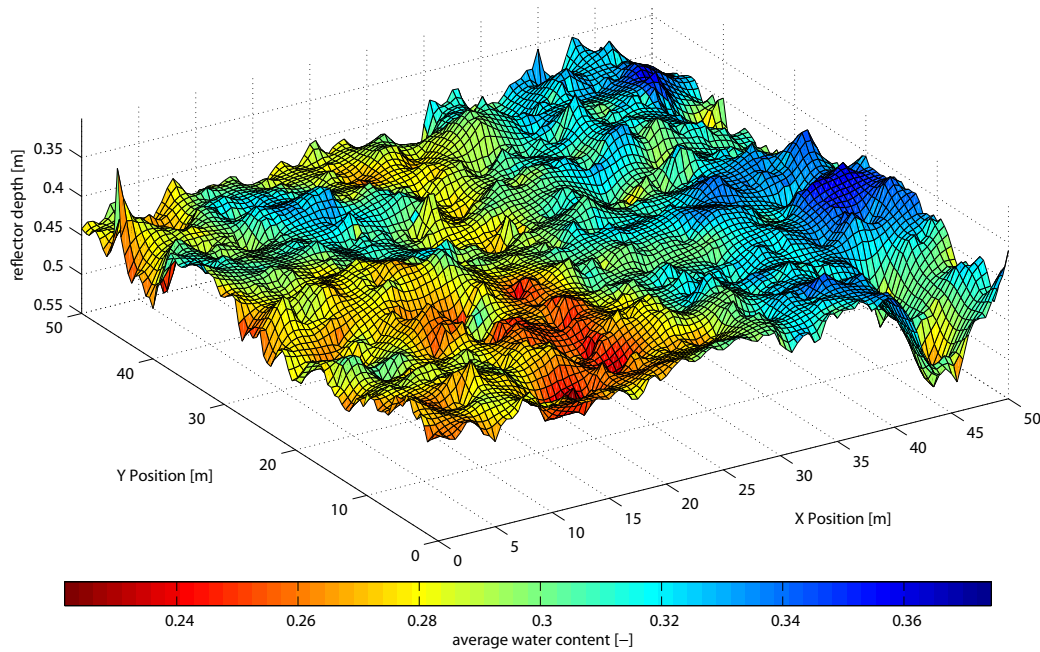
Figure 8.11: Spatially interpolated 3D-representation of the multichannel evalution of the seasonal frost table reflection at Houxia. The x and y axes show the horizontal extent of the measurement, the z axis denotes reflector depth and the coloring the average water content in the thawed region of the ground. The origin marks the southwest corner of the measurement plot *Modified from: Klenk et al. [2012].*

8.4 Agricultural Fields

Several field site under agricultural use were explored with GPR as well. However, the application of GPR methods in agricultural areas is predominantly challenging in the Urumqi region, with the situation worsening towards the desert rim. This is mostly due to intensive irrigation which leads to severe salinization of the fields. Also, most agricultural fields are located in the oasis belt around the desert rim, where the groundwater table is quite shallow. This exacerbates the problem through a strong ascending movement of soil water under the high radiative forcing. Both effects result in generally very high electrical conductivities on agricultural fields. TDR-derived near-surface electrical conductivities reached about 1-3 $^S/_m$ on some fields, which is up to an order of magnitude above what has already been seen to cause problems in the Fukang semi-desert data sets in section 8.1. The associated high losses of any electromagnetic signal lead to significant deterioration of the GPR signal quality, hampering any quantitative interpretations in these areas. This problem can be illustrated from a measurement taken directly across the desert rim, covering both an area of semi-vegetated dunes (positions $0 \ldots 22$ m) and a fallow agricultural field (positions $22 \ldots 40$ m, see Figure 8.12). As can be seen, in this case the
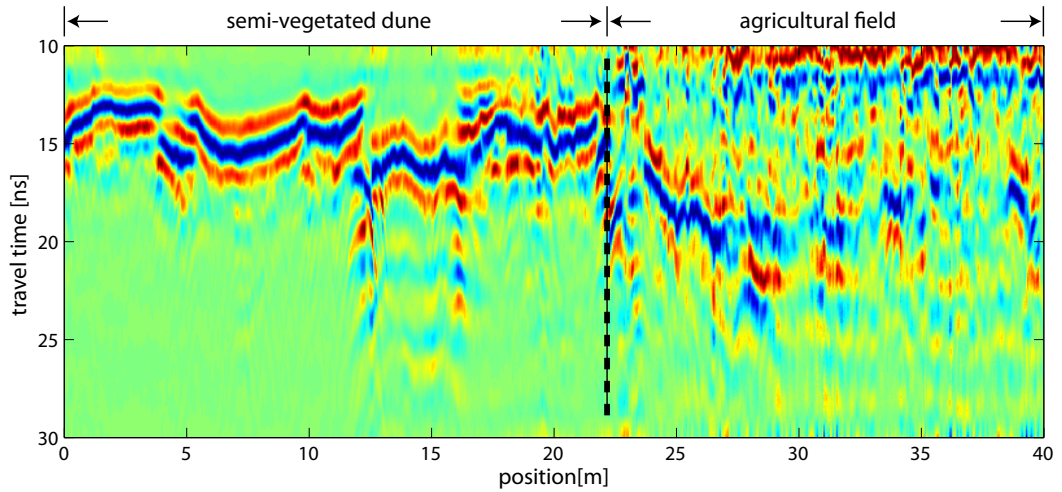
Figure 8.12: Examplary radargram showing the signal quality deterioration when comparing sections measured across the desert rim, moving from a semi-vegetated dune area to an agricultural field. Between 13 m and 16 m, the measurement line crosses a dirt track. *Modified from: Klenk et al. [2012].*

ground wave signal which could be observed between 12...18 ns in the dune part can just barely be discerned around 20 ns on the fallow field.

The situation gets better the further we move away from the desert rim and follow the Urumqi river towards the mountain regions. In fact, a successful measurement could be conducted on an agricultural field site in Lucaogou, which is a valley just some kilometers north of the Shirengou site (section 8.2). Here, the main crops are wheat and corn. The soil texture at this site could be classified as silt loam according to the USDA classification. Several fields were exploratively investigated with GPR. One example is evaluated in Figure 8.13, yielding water contents of 0.19±0.01 m³/m³ along the 250 m long northern edge of the field (see the picture in Figure 4.8d, where north is to the right). The signal is quite noisy, which is due to the nature of the ground – the field had recently been ploughed and subsequently just coarsly harrowed, leaving the surface covered with dry soil clods. This led to a significantly varying air gap unterneath the antennas which in turn caused the observed large noise. In general, the site was characterized by quite wet conditions covered by a thick dried crust on top.

Still, despite this successful dataset, GPR measurements on agricultural sites are rarely possible in the region. And even if there are no physical restrictions, there are still practical issues which will hamper the development of a measurement site, e.g. potentially conflicting interests with local peasants.

(a) Lucaogou field site radargram

(b) Lucaogou field site water contents
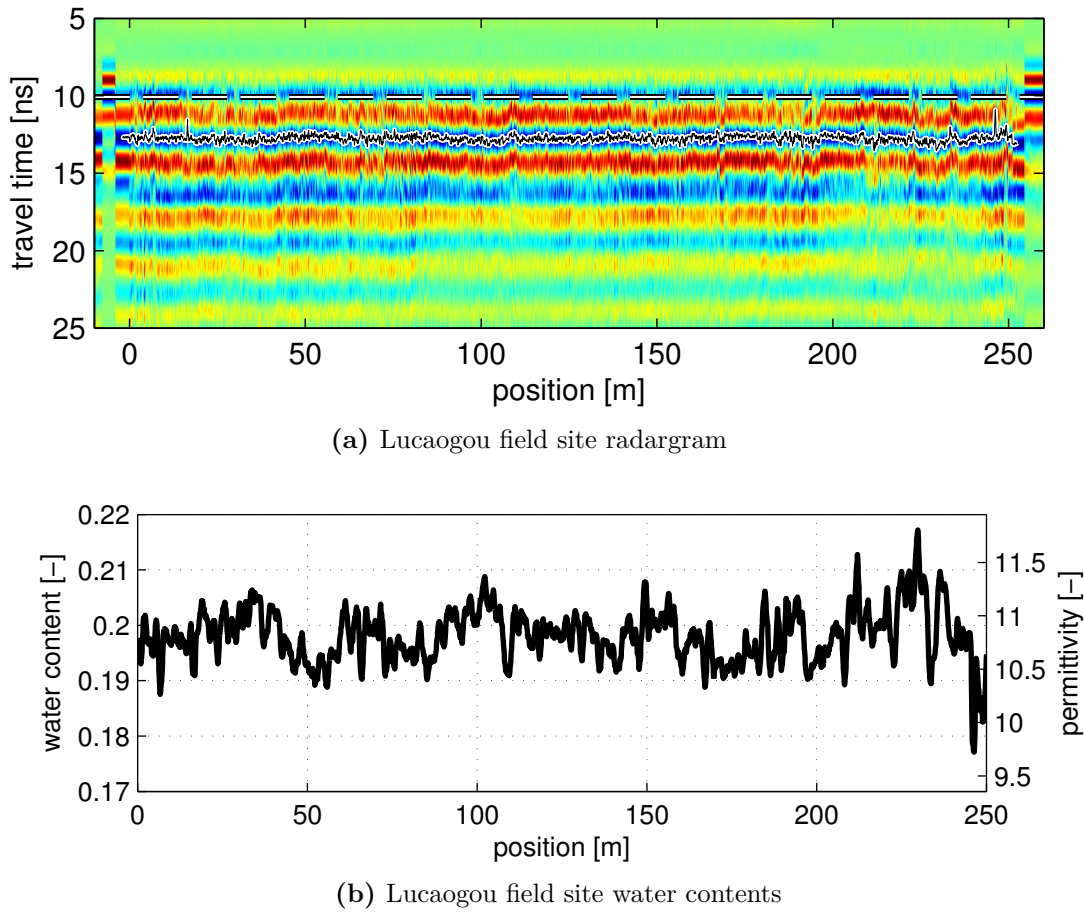
Figure 8.13: Exemplary LCBC Radargram (top) measured with a center frequency of 200 MHz at an antenna separation of 1.19 m across a recently plowed field site in Lucaogou and the correspondingly derived water contents (bottom), using the all-set optimized calibration parameters (compare section 5.3 for details).

8.5 Urumqi Glacier No.1

Last but not least, one measurement could also be executed on Urumqi's Glacier No.1. The glacier is situated at an altitude between 3700 and 4500 m and had a surface area of approximately 1.7 km^2 in 2009 (*Zemp et al.* [2011]). It has been under scientific scrunity of the glacier research station of the Chinese Academy of Science's CAREERI since the early 1960's. The glacier's melt water is the main source of baseflow for the Urumqi river. In recent decades, the glacier has continuously receded, separating into two branches in the mid-1990's, as shown in Figure 8.14a. A picture taken in 2011 is provided in Figure 8.15c. The melt water runoff has been continuously increasing since 1960 as has for example

(a) Variation of glacial surface area

(b) Temporal change of glacial runoff
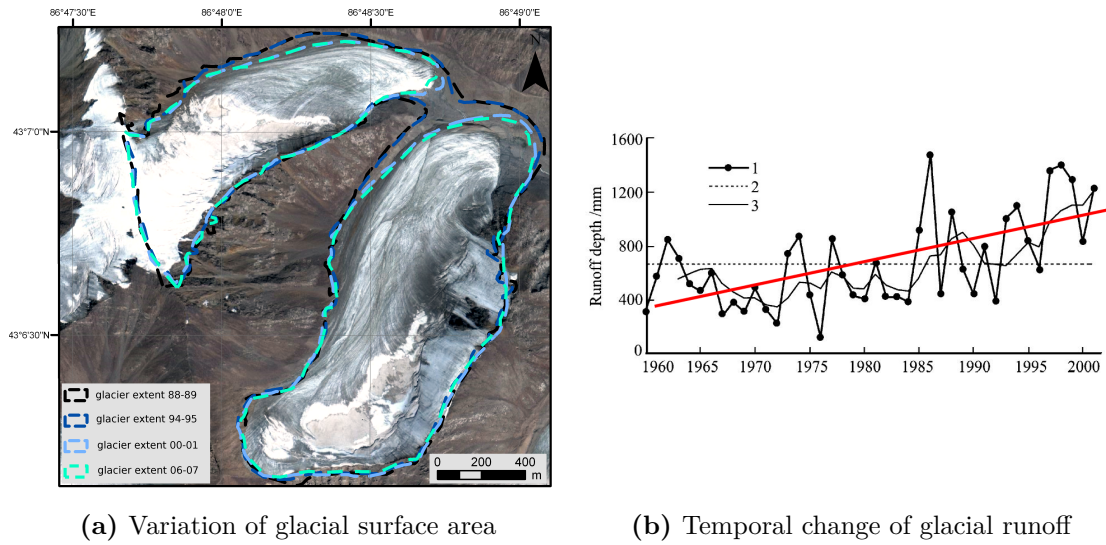
Figure 8.14: The figure on the left shows the change in the surface area of Urumqi Glacier No.1 *(modified from: Fuchs [2012])*. The right diagram shows the variation of glacial melt water runoff from Urumqi Glacier No.1 between 1960 and 2001. (1. depth of runoff; 2. mean annual runoff depth; 3. 5-year moving average. The red line indicates the increasing trend in runoff over the decades *(adapted from: Shi et al. [2007])*.

been shown by *Shi et al.* [2007], pictured in Figure 8.14b. At the same time, local field studies have observed a relative decrease in glacier thickness of 12 m. More details about the changes of the surface area of this and further glaciers in the Eastern Tian Shan can be found in *Fuchs* [2012].

To our knowledge no comprehensive study on the thickness of Urumqi Glacier No.1 has been executed to date. In principle, estimating the thickness of a glacier is possible from the travel time of the bedrock reflection in GPR data. Additionally, internal reflections can give information e.g. about the accumulation and ablation history or the existence of internal moraines (see e.g. *Navarro and Eisen* [2010]).
Figure 8.15a shows a radargram which has been measured with an 80 MHz single channel setup perpendicularly to the ice flow on the East Branch approximately halfway up the glacier. The comparatively low center frequency was chosen to maximize the penetration depth in order to map the depth to the bedrock across the glacier. To emphasize the reflected signals, the direct wave which was recorded at approximately 100 ns has been cut. The location of this measurement line is indicated by the red line in Figure 8.15d. Unfortunately, due to the weather conditions, the top of the glacier showed a high content of melt water, seriously limiting the penetration depth of the radar signal. As a consequence, the reflection of the bedrock could only be observed to absolute two-way travel times of approximately 900 ns, as indicated by the black dashed lines in Figure 8.15a. Assuming a

(a) Radargram on the East Branch

(b) Glacier radargram detail

(c) Urumqi Glacier No. 1, showing both the east (left) and the west branch

(d) East branch of the glacier with the measurement line indicated in red
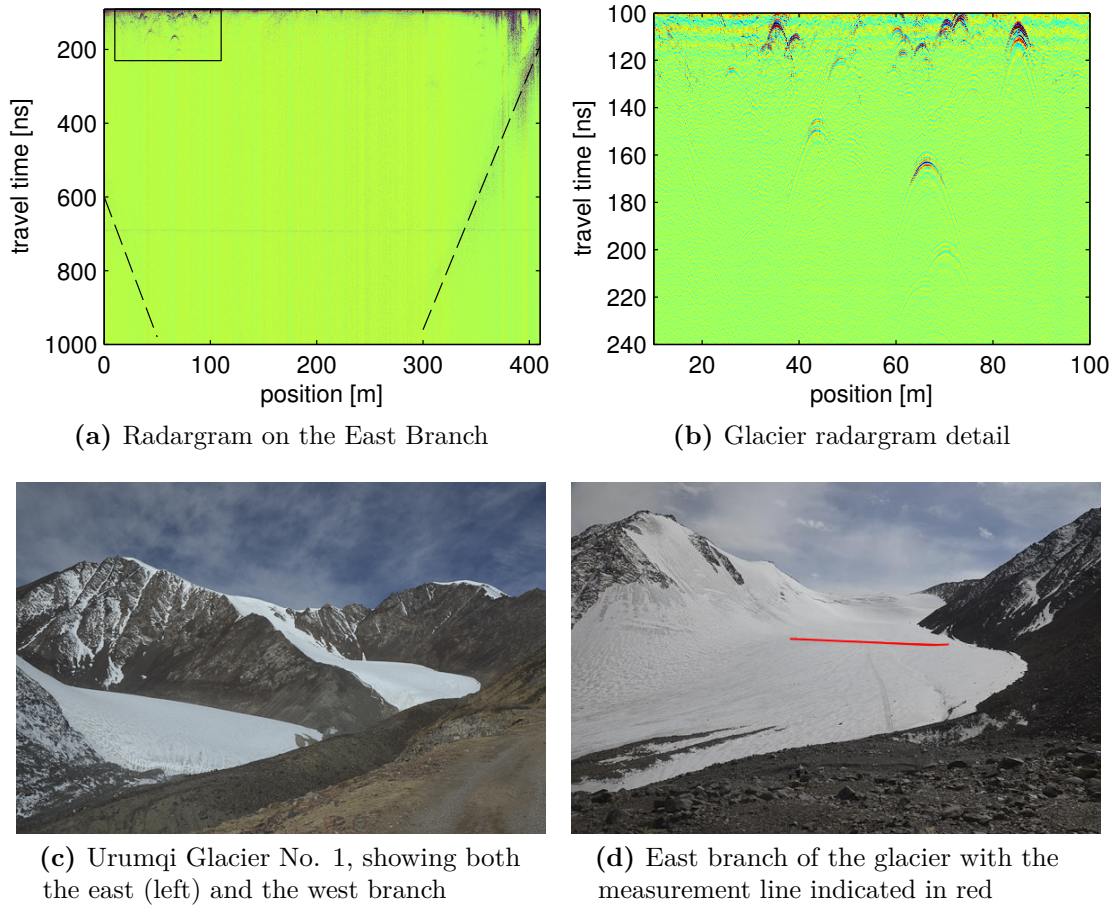
Figure 8.15: Urumqi Glacier No.1 measurement. Top left shows a radargram measured at 80 MHz perpendicular to the flow direction of Glacier No.1, approximately halfway up the glacier. The reflections from the bedrock have been marked by the dashed black line, the excerpt marked by the black box is shown more detailed on the top right, picturing multiple near-surface diffraction hyperbolas. Due to the moist conditions of the top of the glacier, the radar signal was attenuated too strongly for revealing the bedrock in the middle of the glacier

mean ice permittivity of $\varepsilon_{ice} = 3.2$, this would indicate a thickness of the glacier ice of more than 250 m at this position. For more precise data, the measurement would need to be repeated under colder conditions. At both sides of the glacier, some rock debris is carried internally, which can be deduced from the presence of diffraction hyperbolas at travel times between 100 and 200 ns as shown in the detail excerpt of the radargram in Figure 8.15b. The rest of the radargram does not show any reflected signals, hence the glacier does not seem to carry large amounts of concealed debris.

8.6 Discussion

In contrast to the data discussed in previous chapters, site access and the availability of auxiliary data is increasingly limited for a large part of the region, which is mostly due to current political circumstances. This poses a challenge for the comprehensive interpretation of observed soil water content features in terms of respective site properties and relevant processes.

Clearly, additional information would be needed for more detailed interpretation of the datasets presented in this chapter. In particular, *multi-temporal measurements* could help to pin down the generating processes of the small scale water content variations observed. For example, if the small scale variations which have been shown in Figure 6.3 or 8.5 diminished over the summer, this would corroborate our current hypothesis of the vegetation-snow-feedback. Conversely, if similar variations were still observed during the summer, this would indicate an influence of small-scale variations of the material properties. More information about the *external forcing* in the time between measurements (e.g. precipitation, air temperatures, snow heights) could also help distinguish between the different influencing factors.

Similarly, time-lapse measurements would be able to monitor the freeze-thaw processes in the high-mountain grasslands. For further quantifying the results currently observed at Houxia, a more *detailed investigation of top soil properties* would be crucial. Especially the influence of the apparently high organic matter content in the top soil on the GPR response should be studied more closely.

Additional information could also be acquired from *remote sensing data*. For example, as has already been shown in chapter 6, the large scale variations in the soil water content distribution are generated by the topographic variations. Hence, mapping the distribution of dune ridges and dune valleys, e.g. from high resolution optical remote sensing data, would give a direct handle on the soil water content distribution of the whole semi-vegetated dune area. Similarly, mapping vegetation differences in the hillslope area could substantiate the hypothesis for our observed water content variations at Shirengou and then potentially be used as well for extending the analysis to other similar areas. A closer investigation of the potential influence of microtopography would need a high resolution *digital elevation model*.

8.7 Conclusions

This chapter has discussed several examples for GPR measurements acquired in the large context of a highly structured watershed in Northwestern China. For political reasons, site access was severely limited in this region. Hence, a detailed assessment of the accuracy

of the results reported in this chapter was not possible in the framework of this thesis. Nevertheless, at this point the following conclusions can be drawn:

- GPR methods are suitable for efficient high-resolution mapping of a large variety of distinct soil water content characteristics in this highly structured watershed. Further potential observables include the seasonal frost table and possibly the ice sheet thickness of Urumqi's Glacier No.1.

- The temporal stability of the measurement as e.g. shown for the semi-vegetated dune area opens the door for interpreting observed water content changes in terms of different generating processes.

- There is no universally applicable measurement scheme. Due to the different site characteristics, any measurement scheme will have to be adapted accordingly.

- Measurements on agricultural fields in the region are difficult due to the large degree of salinization. Especially close to the desert rim this renders the use of both TDR and GPR methods impossible.

- Nevertheless, measurements could be successfully executed at characteristically different sites which are representative for about 70 % of the region of interest (*Fricke* [2012]). In principle, this paves the way for implementing GPR based monitoring schemes of near-surface hydrological processes in a large part of the region.

9 Conclusions and Outlook

> It is a great thing for us to carry on the tradition
> of holding nature up to examination,
> of asking again and again why it is the way it is.
> *Steven Weinberg*

As defined in the introduction to this thesis, quantifying the observed GPR response in hydrogeophysical studies requires advancements on three levels of process understanding: (i) the physical interaction of the GPR signal with distinct subsurface characteristics, (ii) the connection between concepts of soil physics and the subsurface water dynamics as seen through the eyes of GPR and (iii) the characteristics of the employed instruments. In this sense, this thesis has put forward several important contributions.

After the introduction of the pertinent theories and experimental sites, major results start with Chapter 5, which has assessed the precision and accuracy of current GPR methods for studying near-surface soil water contents. For fast and efficient mapping of larger areas with GPR, common offset measurements are currently the only option. As a result of instrument limitations, a time-zero calibration is crucial for all such common offset measurements which has hampered their quantitative evaluation in the past. The reason is that due to a strong influence of the specific instrument properties, interface and coupling effects, consistently correcting for all occurring offsets is not difficult. Hence, in this thesis, a novel approach for finding a feasible time-zero calibration has been developed, which is based on analyzing the signal recorded by two separate channels of our multichannel setup (section 5.3). Previously, additional ground truth data were needed (e.g. through TDR measurements or via gravimetric sampling) to determine absolute water contents.
In a thorough analysis of a corresponding field dataset, Chapter 6 has shown that employing this calibration approach allows to use GPR ground wave data measured at antenna separations between 1 m and 2 m for calculating absolute near-surface water contents to a similar precision as TDR derived values without relying on additional auxiliary information. Furthermore, the parameters of the calibration function vary little with respect to different site characteristics (e.g. Table 5.2). This opens the door for comparative measurements without the need for a site specific calibration.
Furthermore, Chapter 5 has described a second effect, which is most likely connected to a non-linearity in the time base of the GPR instruments. The specific impact is connected to the physical setup of antennas and connecting cables and leads to a small variation in the recorded wavelet shape. This variation depends on the time of signal recording (section 5.4).

For evaluating dispersed GPR datasets, a correction based on the direct air wave signal has been shown to yield considerable improvement for the resulting parameter sets (section 5.5).

Chapter 7 has demonstrated the potential for quantitative observations of near-surface soil water dynamics with ground-coupled Ground-Penetrating Radar. In order to connect the observed GPR response to soil physical process understanding, GPR measurements were acquired during imbibition and drainage experiments into and from a complicated but known subsurface structure. These measurements achieved an unprecedented temporal and spatial resolution, basically imaging the continuously changing hydraulic state of the subsurface throughout these experiments (this is best illustrated by the corresponding movie provided in the digital supplementary materials). In particular, this allows for a direct observation of the interference of the capillary fringe reflection with signals generated by static structural features (Sections 7.2.3 and 7.3.1). The observed behavior can be consistently explained by comparison with numerical simulations of a changing transition zone shape with the imbibition and drainage processes (Section 7.3.2). Hence, in principle, there is detailed hydraulic information which can be gained from observing the movement of the capillary fringe reflection with GPR. However, a quantitative evaluation of the capillary fringe dynamics might be impaired at this site by the multitude of different interactions with subsurface structures and small-scale heterogeneities.

Furthermore, the evaluation of the bottom reflection of the structure allowed for monitoring the average soil water content change over the whole structure. Consistent changes in water content of less than 0.001 $^\mathrm{m^3}/\mathrm{m^3}$ could be observed in the GPR data (e.g. Figure 7.10). Major differences observed along the GPR profile could be associated with the structural differences of the soil profile at the respective locations (Figure 7.9). The characteristics of the water content change as influenced by layer boundaries has been discussed with respect to the differing hydraulic properties of the bordering materials. The observed behavior can be explained with a differing air entry value (e.g. section 7.2.2). These GPR derived results are consistent with current inversions of effective hydraulic parameter sets based on TDR data from the same experiment (Table 4.1). The lesser features observed in the water content change data cannot be quantitatively evaluated at this point, since the available channels show a slightly differing behavior. This is most likely due to instrument limitations. First, the water table after imbibition is close to the radiative near-field of our antennas, where the specific antenna characteristics increasingly dominate the response. Second, an influence of the time-base nonlinearity effect cannot be excluded at this point (section 7.3.5).

Besides the reflections from the bottom, from known layer boundaries and the moving capillary fringe reflection, reflected signals were also generated from secondary structural features, depending on the specific hydraulic state. In particular, compaction interfaces, which are essentially an artifact of the building process and mainly manifest as porosity variations may or may not lead to significant reflected signal amplitudes (e.g. section 7.2.3). This raises a note of caution that single-instance in time field measurements may be prone to misinterpretation, depending on the specific hydraulic state of the investigated site.

Finally, Chapter 8 has broadened the perspective and discussed the applicability of GPR based methods for monitoring hydrological processes in the framework of a highly structured regional watershed in Northwestern China. Over the course of two field campaigns, several monitoring sites could be successfully tested which are representative for approximately 70 % of the region of interest. In particular, the soil water distribution characteristics were described at a field site located in a semidesert area (section 8.1), a hillslope in the mountain foothills (section 8.2), and a high-mountain grassland site (section 8.3). For example, the semidesert dataset exhibits water content variations at least at two distinct scales; large-scale variations (on the order of 50...100 m) are connected to topography differences while the small-scale variations on the order of centimeters to meters are consistent with a snow-vegetation feedback. Unexpectedly, as has been shown in both Chapters 6 and 8, the small-scale variations largely persist in time between two subsequent years. This testifies to an impressive stability of the measurement setup and opens the door for interpreting observed small changes in terms of the generating processes. However, for a detailed interpretation of the observed phenomena, most importantly more dense multi-temporal measurements would be needed. So far this has not been possible for political reasons, which is also why a detailed assessment of the accuracy of the results reported in Chapter 8 was not possible in the framework of this thesis.

9.1 Considerations On The Road Ahead

Summarizing all the results discussed above, the here employed GPR system is now operational for quantifying near-surface soil water contents measured in a multi-common offset setup under a variety of different site characteristics and hydraulic states, to a similar precision as accessible with TDR. Furthermore, an extremely high precision is attainable in well-controlled field experiments, enabling a direct observation of water content dynamics.

Still, in both cases, instrument characteristics seem to play a far more important role than previously anticipated. The results achieved within this thesis are likely pushing the edge of what is achievable with current commercially available antennas without detailed knowledge about the functioning of the instruments. A detailed description of the remaining inconsistencies and a further reduction of the observed uncertainties will most probably need a much deeper understanding of the characteristics of the employed instruments. A first step could be an explicit treatment of the specific antenna characteristics along the lines recently presented for single shielded antennas by *Diamanti et al.* [2012] and *Warren and Giannopoulos* [2012]. Extending such an analysis to include several antenna boxes could for example give a handle on finding a detailed explanation for the setup-dependent contribution to the observed time-zero offset.

Meanwhile, great care should be taken to ensure that datasets which are supposed to be

comparable are always recorded with exactly the same measurement setup. This thesis has shown that not only each antenna is unique but that at the level of accuracy presented here, the specific combination of antennas and different connecting cables does in fact notably influence the recorded signal.

Still, as far as the impact of these instrument issues on the observed water content dynamics is concerned, the remaining uncertainties are now at least on the same order as the uncertainties introduced by the auxiliary parameters employed by the petrophysical relationship. Some of these auxiliary parameter uncertainties could be reduced by sophisticated laboratory measurements, e.g. a detailed determination of the soil matrix permittivity. However, following the paradigm of measuring directly at the scale of interest, it might be preferable to conduct a series of multi-temporal measurements instead. This could for example decide on the nature of the small-scale variations observed in the semi-desert datasets. If forcing data were additionally available (e.g. precipitation, temperatures), one could aim at driving a Richards solver with these datasets and possibly invert for the necessary parameters.

The integration of GPR methods with soil physical process understanding should be pursued further. In particular, the combination of conducting high-precision GPR experiments, carrying out numerical simulations of the expected GPR response and deriving an effective hydraulic description of water content dynamics based on TDR observations which has been started by this thesis and the works of *Dagenbach* [2012] and *Jaumann* [2012] has built a solid foundation for future research. A direct comparison between measured GPR data and radargrams modeled based on the inverted effective hydraulic parameters will probably remain challenging unless the implications of the antenna characteristics can be fully understood. Nevertheless, information about water content dynamics as seen through the eyes of the GPR instruments is already a valuable consistency check for the results of hydraulic inversions at ASSESS-GPR. As the currently remaining inconsistencies get resolved, smaller observed variations could become interpretable as well. Such information could then be incorporated as additional orthogonal information for constraining future inversions.

When considering further experiments, additional information could possibly be gained by varying the imbibition and drainage fluxes. One could even think of implementing a form of a large scale multistep outflow experiment by adding several relaxation phases during both imbibition and drainage. Furthermore, the experiments presented here featured comparatively high pumping rates, limiting the dynamic range of the experiment. Using a slower drainage speed could for instance extend the dynamic range to the lower parts of the profile. However, it has to be kept in mind that the most comprehensive experiment considered in this thesis already took more than twelve hours. Extending these experiments over several days would warrant a certain degree of automation of the GPR measurements. This would also further increase the stability and comparability of the obtained measurements. Then, other information contained in the observed GPR response

(e.g. frequency content, amplitude variation) could become reliably interpretable as well.

With respect to the large scale applications of GPR as discussed for the Urumqi region, apt ancillary data from remote sensing could give a handle on extrapolating the features characterized at the specific field sites to their entire area of representativity. This could for example include mapping topographic or vegetation features which define the locally observed water content distribution over larger areas from high-resolution remotely sensed optical data. Hence this could form the foundation for a simple approach of upscaling locally observed measurements on a process basis, avoiding the plentiful pitfalls associated with directly calculating locally calibrated large scale soil water content distributions, e.g. from coarse resolution radar data.

In any case, there seems to be an ample amount of possible research ahead for – quoting Steven Weinberg – carrying on the tradition of holding nature up to examination and asking again and again why it is the way it is.

Bibliography

Albergel, C., E. Zakharova, J. Calvet, M. Zribi, M. Pardé, J. Wigneron, N. Novello, Y. Kerr, A. Mialon, and N. Fritz (2011), A first assessment of the SMOS data in southwestern France using in situ and airborne soil moisture estimates: The CAROLS airborne campaign, *Remote Sensing of Environment*, *115*(10), 2718–2728, doi: 10.1016/j.rse.2011.06.012. Cited on page 4.

Allan, J. A. (2002), Hydro-Peace in the Middle East: Why no Water Wars? A Case Study of the Jordan River Basin, *SAIS Review*, *22*(2), 255–272, doi: 10.1353/sais.2002.0027. Cited on page 3.

Annan, A. P. (1973), Radio Interferometry Depth Sounding: Part I – Theoretical Discussion, *Geophysics*, *38*(3), 557–580, doi: 10.1190/1.1440360. Cited on page 29.

Annan, A. P. (2005), GPR Methods for Hydrogeological Studies, in *Hydrogeophysics*, *Water Science and Technology Library*, vol. 50, edited by Y. Rubin, S. S. Hubbard, and V. Singh, pp. 185–213, Springer Netherlands, doi: 10.1007/1-4020-3102-5. Cited on page 10.

Antz, B. (2010), Entwicklung und Modellierung der Hydraulik eines Testfeldes für geophysikalische Messungen, Diploma thesis, Heidelberg University. Cited on pages 39, 40, and 41.

Balanis, C. A. (1982), *Antenna theory: analysis and design*, John Wiley & Sons, Inc., New York, USA. Cited on page 120.

Bano, M. (2006), Effects of the transition zone above a water table on the reflection of GPR waves, *Geophysical Research Letters*, *33*, L13309, doi: 10.1029/2006GL026158. Cited on page 32.

Bartalis, Z., W. Wagner, V. Naeimi, S. Hasenauer, K. Scipal, H. Bonekamp, J. Figa, and C. Anderson (2007), Initial soil moisture retrievals from the METOP-A Advanced Scatterometer (ASCAT), *Geophysical Research Letters*, *34*(20), L20401, doi: 10.1029/2007GL031088. Cited on page 4.

Beaulieu, J. P., D. M. Kipping, V. Batista, G. Tinetti, I. Ribas, S. Carey, J. A. Noriega-Crespo, C. A. Griffith, G. Campanella, S. Dong, J. Tennyson, R. J. Barber, P. Deroo, S. J. Fossey, D. Liang, M. R. Swain, Y. Yung, and N. Allard (2010), Water in the atmosphere of HD 209458b from 3.6–8 μm IRAC photometric observations in primary

transit, *Monthly Notices of the Royal Astronomical Society*, *409*(3), 963–974, doi: 10.1111/j.1365-2966.2010.16516.x. Cited on page 2.

Bevan, M. J., A. L. Endres, D. L. Rudolph, and G. Parkin (2003), The non-invasive characterization of pumping-induced dewatering using ground penetrating radar, *Journal of Hydrology*, *281*(1–2), 55 – 69, doi: 10.1016/S0022-1694(03)00200-2. Cited on page 32.

Bikowski, J., J. A. Huisman, J. A. Vrugt, H. Vereecken, and J. van der Kruk (2012), Integrated analysis of waveguide dispersed GPR pulses using deterministic and Bayesian inversion methods, *Near Surface Geophysics, in press*, doi: 10.3997/1873-0604.2012041. Cited on pages 32 and 72.

Binley, A., G. Cassiani, R. Middleton, and P. Winship (2002), Vadose zone flow model parameterisation using cross-borehole radar and resistivity imaging, *Journal of Hydrology*, *267*(3-4), 147–159, doi: 10.1016/S0022-1694(02)00146-4. Cited on pages 5 and 25.

Birchak, J. R., C. G. Gardner, J. E. Hipp, and J. M. Victor (1974), High dielectric constant microwave probes for sensing soil moisture, *Proceedings of the IEEE*, *62*(1), 93–98, doi: 10.1109/PROC.1974.9388. Cited on page 15.

Blindow, N., C. Salat, V. Gundelach, U. Buschmann, and U. Kahnt (2011), Performance and calibration of the helicopter GPR system BGR-P30, in *Advanced Ground Penetrating Radar (IWAGPR), 2011 6th International Workshop on*, pp. 1–5, IEEE, doi: 10.1109/IWAGPR.2011.5963896. Cited on page 25.

Bogda, F. (2011), Untersuchung der Bodenwasserdynamik mit Mehrkanal-GPR, Staatsexamensarbeit, Heidelberg University. Cited on page 41.

Bogena, H. R., M. Herbst, J. A. Huisman, U. Rosenbaum, A. Weuthen, and H. Vereecken (2010), Potential of Wireless Sensor Networks for Measuring Soil Water Content Variability, *Vadose Zone Journal*, *9*(4), 1002–1013, doi: 10.2136/vzj2009.0173. Cited on page 5.

Brooks, R. H. (1966), Properties of porous media affecting fluid flow, in *Journal of the Irrigation and Drainage Division, Proceedings of the American Society of Civil Engineers*, vol. 92, pp. 61–88. Cited on page 20.

Brovelli, A., and G. Cassiani (2008), Effective permittivity of porous media: a critical analysis of the complex refractive index model, *Geophysical Prospecting*, *56*(5), 715–727, doi: 10.1111/j.1365-2478.2008.00724.x. Cited on page 84.

Buchner, J. S., U. Wollschläger, and K. Roth (2012), Inverting surface GPR data using FDTD simulation and automatic detection of reflections to estimate subsurface water content and geometry, *Geophysics*, *77*(4), H45–H55, doi: 10.1190/geo2011-0467.1. Cited on pages 31 and 41.

Buchner, R., J. Barthel, and J. Stauber (1999), The dielectric relaxation of water between 0°C and 35°C, *Chemical Physics Letters*, *306*(1-2), 57–63, doi: 10.1016/S0009-2614(99)00455-8. Cited on page 13.

Cardell-Oliver, R., M. Kranz, K. Smettem, and K. Mayer (2005), A Reactive Soil Moisture Sensor Network: Design and Field Evaluation, *International Journal of Distributed Sensor Networks*, *1*(2), 149–162, doi: 10.1080/15501320590966422. Cited on page 5.

Carsel, R. F., and R. S. Parrish (1988), Developing joint probability distributions of soil water retention characteristics, *Water Resources Research*, *24*(5), 755–769, doi: 10.1029/WR024i005p00755. Cited on page 82.

Cassidy, N. J. (2009), Electrical and Magnetic Properties of Rocks, Soils and Fluids, in *Ground Penetrating Radar: Theory and Applications*, edited by H. Jol, chap. 2, pp. 41–72, Elsevier, Amsterdam. Cited on page 83.

Christensen, N. S., and D. P. Lettenmaier (2007), A multimodel ensemble approach to assessment of climate change impacts on the hydrology and water resources of the Colorado River Basin, *Hydrology and Earth System Sciences*, *11*(4), 1417–1434, doi: 10.5194/hess-11-1417-2007. Cited on page 3.

Crutzen, P. J. (2002), Geology of mankind, *Nature*, *415*(6867), 23–23, doi: 10.1038/415023a. Cited on page 1.

Crutzen, P. J. (2006), Albedo Enhancement by Stratospheric Sulfur Injections: A Contribution to Resolve a Policy Dilemma?, *Climatic change*, *77*(3), 211–220, doi: 10.1007/s10584-006-9101-y. Cited on page 1.

Dagenbach, A. (2012), Untersuchung der hydraulischen Bodeneigenschaften durch GPR: Analyse der Kapillarsaumreflexion durch numerische Simulationen, Diploma thesis, Universität Heidelberg. Cited on pages 20, 21, 32, 42, 111, 112, 113, and 146.

Dagenbach, A., J. S. Buchner, P. Klenk, and K. Roth (2012), Identifying a soil hydraulic parameterisation from on-ground GPR time lapse measurements of a pumping experiment, *Hydrol. Earth Syst. Sci. Discuss.*, *9*, 9095–9117, doi: 10.5194/hessd-9-9095-2012. Cited on pages 21, 42, and 113.

Dai, R., and C. T. Young (1997), Transient fields of a horizontal electric dipole on a multilayered dielectric medium, *Antennas and Propagation, IEEE Transactions on*, *45*(6), 1023–1031, doi: 10.1109/8.585751. Cited on pages 29 and 55.

Daniels, D. J., et al. (2004), *Ground Penetrating Radar*, The Institution of Electrical Engineers, London, UK, doi: 10.1049/PBRA015E. Cited on pages 9 and 83.

Dansgaard, W., S. J. Johnsen, H. B. Clausen, D. Dahl-Jensen, N. S. Gundestrup, C. U. Hammer, C. S. Hvidberg, J. P. Steffensen, A. E. Sveinbjörnsdottir, J. Jouzel, et al.

(1993), Evidence for general instability of past climate from a 250-kyr ice-core record, *Nature*, *364*(6434), 218–220, doi: 10.1038/364218a0. Cited on page 1.

Davis, J. L., and A. P. Annan (1989), Ground-Penetrating Radar for High-Resolution Mapping of Soil and Rock Stratigraphy, *Geophysical Prospecting*, *37*(5), 531–551, doi: 10.1111/j.1365-2478.1989.tb02221.x. Cited on pages 14 and 83.

Deiana, R., G. Cassiani, A. Villa, A. Bagliani, and V. Bruno (2008), Calibration of a Vadose Zone Model Using Water Injection Monitored by GPR and Electrical Resistance Tomography, *Vadose Zone Journal*, *7*(1), 215–226, doi: 10.2136/vzj2006.0137. Cited on page 5.

Diamanti, N., P. Annan, and D. Redman (2012), Quantifying GPR responses, in *Ground Penetrating Radar (GPR), 2012 14th International Conference on*, pp. 237–242, IEEE, doi: 10.1109/ICGPR.2012.6254867. Cited on page 145.

Doetsch, J., N. Linde, and A. Binley (2010), Structural joint inversion of time-lapse crosshole ERT and GPR traveltime data, *Geophysical Research Letters*, *37*(24), L24404, doi: 10.1029/2010GL045482. Cited on page 5.

Doolittle, J. A., B. Jenkinson, D. Hopkins, M. Ulmer, and W. Tuttle (2006), Hydropedological investigations with ground-penetrating radar (GPR): Estimating water-table depths and local ground-water flow pattern in areas of coarse-textured soils, *Geoderma*, *131*(3-4), 317–329, doi: 10.1016/j.geoderma.2005.03.027. Cited on page 32.

Endres, A. L., W. P. Clement, and D. L. Rudolph (2000), Ground Penetrating Radar Imaging of an Aquifer During a Pumping Test, *Ground Water*, *38*(4), 566–576, doi: 10.1111/j.1745-6584.2000.tb00249.x. Cited on page 32.

Entekhabi, D., E. G. Njoku, P. E. O'Neill, K. H. Kellogg, W. T. Crow, W. N. Edelstein, J. K. Entin, S. D. Goodman, T. J. Jackson, J. Johnson, J. Kimball, J. R. Piepmeier, R. D. Koster, N. Martin, K. C. McDonald, M. Moghaddam, S. Moran, R. Reichle, J. C. Shi, M. Spencer, S. W. Thurman, L. Tsang, and J. Van Zyl (2010), The Soil Moisture Active Passive (SMAP) Mission, *Proceedings of the IEEE*, *98*(5), 704–716, doi: 10.1109/JPROC.2010.2043918. Cited on page 4.

Falkenmark, M., and J. Rockström (2006), The New Blue and Green Water Paradigm: Breaking New Ground for Water Resources Planning and Management, *Journal of Water Resources Planning and Management*, *132*(3), 129–132, doi: 10.1061/(ASCE)0733-9496(2006)132:3(129). Cited on page 3.

Fegley Jr., B. (2003), Venus, in *Treatise on Geochemistry*, vol. 1: Meteorites, Comets, and Planets, edited by H. D. Holland and K. K. Turekian, pp. 487–507, Pergamon,Oxford, UK, doi: 10.1016/B0-08-043751-6/01150-6. Cited on page 1.

Fricke, K. (2012), Analysis and modelling of water supply and demand under climate change, land use transformation and socio-economic development – The water resource challenge and adaptation measures for Urumqi Region, Northwest China, Ph.D. thesis, Heidelberg University. Cited on pages 45, 46, and 141.

Fuchs, J. (2012), Multi-temporal detection of glacier changes in the Eastern Tian Shan with regard to climate change (AR Xinjiang, China), *in German*, Bachelor thesis, Heidelberg University. Cited on pages 45 and 138.

Galagedara, L. W., G. W. Parkin, and J. D. Redman (2003), An analysis of the ground-penetrating radar direct ground wave method for soil water content measurement, *Hydrological Processes*, *17*(18), 3615–3628, doi: 10.1002/hyp.1351. Cited on page 54.

Gerhards, H. (2008), Ground Penetrating Radar as a Quantitative Tool with Applications in Soil Hydrology, Ph.D. thesis, Heidelberg University. Cited on page 32.

Gerhards, H., U. Wollschläger, Q. Yu, P. Schiwek, X. Pan, and K. Roth (2008), Continuous and simultaneous measurement of reflector depth and average soil-water content with multichannel ground-penetrating radar, *Geophysics*, *73*(4), J15–J23, doi: 10.1190/1.2943669. Cited on pages 5, 27, 31, 33, and 34.

Giannopoulos, A. (2005), Modelling ground penetrating radar by GprMax, *Construction and Building Materials*, *19*(10), 755–762, doi: 10.1016/j.conbuildmat.2005.06.007. Cited on pages 34 and 80.

Glassmeier, K. H., H. Boehnhardt, D. Koschny, E. Kührt, and I. Richter (2007), The Rosetta Mission: Flying Towards the Origin of the Solar System, *Space Science Reviews*, *128*(1), 1–21, doi: 10.1007/s11214-006-9140-8. Cited on page 2.

Gross, M. (2012), The search for life on Earth and other planets, *Current Biology*, *22*(7), R207–R211, doi: 10.1016/j.cub.2012.03.040. Cited on page 2.

Grote, K., S. Hubbard, and Y. Rubin (2003), Field-scale estimation of volumetric water content using ground-penetrating radar ground wave techniques, *Water Resources Research*, *39*(11), 1321, doi: 10.1029/2003WR002045. Cited on page 29.

Grotzinger, J., J. Crisp, A. Vasavada, R. Anderson, C. Baker, R. Barry, D. Blake, P. Conrad, K. Edgett, B. Ferdowski, R. Gellert, J. Gilbert, M. Golombek, J. Gómez-Elvira, D. Hassler, L. Jandura, M. Litvak, P. Mahaffy, J. Maki, M. Meyer, M. Malin, I. Mitrofanov, J. Simmonds, D. Vaniman, R. Welch, and R. Wiens (2012), Mars Science Laboratory Mission and Science Investigation, *Space Science Reviews*, *170*(1-4), 5–56, doi: 10.1007/s11214-012-9892-2, 10.1007/s11214-012-9892-2. Cited on page 2.

Hajnsek, I., T. Jagdhuber, H. Schön, and K. P. Papathanassiou (2009), Potential of Estimating Soil Moisture Under Vegetation Cover by Means of PolSAR, *Geoscience and Remote*

Sensing, IEEE Transactions on, *47*(2), 442–454, doi: 10.1109/TGRS.2008.2009642. Cited on page 4.

Heimovaara, T. J., A. G. Focke, W. Bouten, and J. M. Verstraten (1995), Assessing Temporal Variations in Soil Water Composition with Time Domain Reflectometry, *Soil Science Society of America Journal*, *59*, 689–698, doi: 10.2136/sssaj1995.03615995005900030009x. Cited on page 37.

Henderson, P., and G. Henderson (2009), *The Cambridge Handbook of Earth Science Data*, Cambridge University Press, Cambridge, UK. Cited on page 2.

Hoekstra, A. Y. (Ed.) (2003a), *Virtual Water Trade – Proceedings of the International Expert Meeting on Virtual Water Trade*, IHE Delft, The Netherlands. Cited on page 3.

Hoekstra, A. Y. (2003b), Virtual water: An introduction, in *Virtual water trade. Proceedings of the international expert meeting on virtual water trade*, edited by A. Hoekstra, pp. 13–23. Cited on page 3.

Hoekstra, A. Y., and A. K. Chapagain (2007), Water footprints of nations: water use by people as a function of their consumption pattern, *Water Resources Management*, *21*(1), 35–48, doi: 10.1007/s11269-006-9039-x. Cited on page 3.

Huisman, J. A., and W. Bouten (2003), Accuracy and Reproducibility of Measuring Soil Water Content with the Ground Wave of Ground-Penetrating Radar, *Journal of Environmental and Engineering Geophysics*, *8*(2), 67–75, doi: 10.4133/JEEG8.2.67. Cited on page 56.

Huisman, J. A., J. J. J. C. Snepvangers, W. Bouten, and G. B. M. Heuvelink (2003a), Monitoring Temporal Development of Spatial Soil Water Content Variation: Comparison of Ground Penetrating Radar and Time Domain Reflectometry, *Vadose Zone Journal*, *2*(4), 519–529. Cited on page 5.

Huisman, J. A., S. S. Hubbard, J. D. Redman, and A. P. Annan (2003b), Measuring Soil Water Content with Ground Penetrating Radar: A Review, *Vadose Zone Journal*, *2*(4), 476–491. Cited on pages 5 and 29.

Ippisch, O., H. Vogel, and P. Bastian (2006), Validity limits for the van Genuchten-Mualem Model and implications for parameter estimation and numerical simulation, *Advances in Water Resources*, *29*(12), 1780–1789, doi: 10.1016/j.advwatres.2005.12.011. Cited on page 34.

Jackson, J. D. (1999), *Classical Electrodynamics*, 3 ed., John Wiley & Sons, Inc., New York, USA. Cited on page 11.

Jacob, R. W., and J. F. Hermance (2004), Assessing the Precision of GPR Velocity and Vertical Two-way Travel Time Estimates, *Journal of Environmental and Engineering Geophysics*, *9*(3), 143–153, doi: 10.4133/JEEG9.3.143. Cited on page 5.

Jacob, R. W., and J. F. Hermance (2005), Random and Non-Random Uncertainties in Precision GPR Measurements: Identifying and Compensating for Instrument Drift, *Subsurface Sensing Technologies and Applications*, *6*(1), 59–71, doi: 10.1007/s11220-005-4226-z. Cited on page 66.

Jaumann, S. (2012), Estimation of effective hydraulic parameters and reconstruction of the natural evaporative boundary forcing on the basis of TDR measurements, Master thesis, Heidelberg University. Cited on pages 41, 105, 122, 146, and 167.

Jol, H. M. (2009), *Ground Penetrating Radar: Theory and Applications*, Elsevier Science Ltd, Amsterdam, The Netherlands. Cited on page 9.

Keith, D. W. (2000), Geoengineering the Climate: History and Prospect, *Annual Review of Energy and the Environment*, *25*(1), 245–284, doi: 10.1146/annurev.energy.25.1.245. Cited on page 1.

Kerr, Y. H., P. Waldteufel, J. P. Wigneron, J. Martinuzzi, J. Font, and M. Berger (2001), Soil moisture retrieval from space: The Soil Moisture and Ocean Salinity (SMOS) mission, *Geoscience and Remote Sensing, IEEE Transactions on*, *39*(8), 1729–1735, doi: 10.1109/36.942551. Cited on page 4.

Kitzes, J., M. Wackernagel, J. Loh, A. Peller, S. Goldfinger, D. Cheng, and K. Tea (2008), Shrink and share: humanity's present and future Ecological Footprint, *Philosophical Transactions of the Royal Society B: Biological Sciences*, *363*(1491), 467–475, doi: 10.1098/rstb.2007.2164. Cited on page 1.

Klenk, P. (2009), Determining Spatial Structures of Soil Water Content Obtained from Multichannel Ground-Penetrating Radar Measurements, Diploma thesis, Heidelberg University. Cited on pages 9, 15, 53, 54, 57, and 58.

Klenk, P., J. S. Buchner, K. Roth, U. Wollschlager, Y. Qin, and K. Zhou (2011), On the reliability of current GPR ground wave methods for determining near-surface water contents, in *Advanced Ground Penetrating Radar (IWAGPR), 2011 6th International Workshop on*, pp. 1–5, IEEE, doi: 10.1109/IWAGPR.2011.5963881. Cited on pages 27, 57, and 87.

Klenk, P., Y. Qin, K. Zhou, and K. Roth (2012), Exploring Spatial Patterns of Soil Water Content in the Urumqi Region with Ground-Penetrating Radar, in *Ground Penetrating Radar (GPR), 2012 14th International Conference on*, pp. 713–717, IEEE, doi: 10.1109/ICGPR.2012.6254954. Cited on pages 87, 123, 132, 134, 135, and 136.

Knight, R. (2001), Ground Penetrating Radar for Environmental Applications, *Annual Review of Earth and Planetary Sciences*, *29*(1), 229–255, doi: 10.1146/annurev.earth.29.1.229. Cited on pages 14 and 83.

Kühne, A. (2010), Experimentelle Untersuchung der zeitlichen Variabilität des Bodenwassergehalts mit GPR, Staatsexamensarbeit, Heidelberg University. Cited on page 41.

Lambot, S., E. C. Slob, M. Vanclooster, and H. Vereecken (2006), Closed loop GPR data inversion for soil hydraulic and electric property determination, *Geophysical Research Letters*, *33*(21), L21405, doi: 10.1029/2006GL027906. Cited on pages 5 and 25.

Lenton, T. M., H. Held, E. Kriegler, J. W. Hall, W. Lucht, S. Rahmstorf, and H. J. Schellnhuber (2008), Tipping elements in the Earth's climate system, *Proceedings of the National Academy of Sciences*, *105*(6), 1786–1793, doi: 10.1073/pnas.0705414105. Cited on page 1.

Lodde, A. (2009), Determining soil moisture contents through time-series groundwave GPR measurements, Diploma thesis, Heidelberg University. Cited on pages 57 and 58.

Loew, A., R. Ludwig, and W. Mauser (2006), Derivation of surface soil moisture from ENVISAT ASAR wide swath and image mode data in agricultural areas, *Geoscience and Remote Sensing, IEEE Transactions on*, *44*(4), 889–899, doi: 10.1109/TGRS.2005.863858. Cited on page 4.

Maxwell, J. C. (1873), *A treatise on electricity and magnetism*, Clarendon Press, Oxford, UK. Cited on page 9.

Minet, J., S. Lambot, E. C. Slob, and M. Vanclooster (2010), Soil Surface Water Content Estimation by Full-Waveform GPR Signal Inversion in the Presence of Thin Layers, *Geoscience and Remote Sensing, IEEE Transactions on*, *48*(3), 1138–1150, doi: 10.1109/TGRS.2009.2031907. Cited on page 5.

Mualem, Y. (1976), A new model for predicting the hydraulic conductivity of unsaturated porous media, *Water Resources Research*, *12*(3), 513–522, doi: 10.1029/WR012i003p00513. Cited on page 21.

Navarro, F. J., and O. Eisen (2010), Ground-Penetrating Radar in glaciological applications, in *Remote sensing of glaciers: techniques for topographic, spatial and thematic mapping of glaciers*, edited by P. Pellikka and W. Rees, chap. 11, pp. 195–229, CRC Press, Taylor & Francis Group, London, UK. Cited on page 138.

Oliva, R., E. Daganzo, Y. H. Kerr, S. Mecklenburg, S. Nieto, P. Richaume, and C. Gruhier (2012), SMOS Radio Frequency Interference Scenario: Status and Actions Taken to Improve the RFI Environment in the 1400–1427-MHz Passive Band, *Geoscience and Remote Sensing, IEEE Transactions on*, *50*(5), 1427–1439, doi: 10.1109/TGRS.2012.2182775. Cited on page 4.

Oskooi, A. F., D. Roundy, M. Ibanescu, P. Bermel, J. D. Joannopoulos, and S. G. Johnson (2010), MEEP: A flexible free-software package for electromagnetic simulations by the FDTD method, *Computer Physics Communications*, *181*(3), 687–702, doi: 10.1016/j.cpc.2009.11.008. Cited on pages 34 and 111.

Pan, X., U. Wollschläger, H. Gerhards, and K. Roth (2012), Optimization of multi-channel ground-penetrating radar for quantifying field-scale soil water dynamics, *Journal of Applied Geophysics*, *82*, 101–109, doi: 10.1016/j.jappgeo.2012.02.007. Cited on page 27.

Pathe, C., W. Wagner, D. Sabel, M. Doubkova, and J. B. Basara (2009), Using ENVISAT ASAR Global Mode Data for Surface Soil Moisture Retrieval Over Oklahoma, USA, *Geoscience and Remote Sensing, IEEE Transactions on*, *47*(2), 468–480, doi: 10.1109/TGRS.2008.2004711. Cited on page 4.

Ponizovsky, A. A., S. M. Chudinova, and Y. A. Pachepsky (1999), Performance of TDR calibration models as affected by soil texture, *Journal of Hydrology*, *218*(1–2), 35–43, doi: 10.1016/S0022-1694(99)00017-7. Cited on page 84.

Reynolds, J. M. (1997), *An Introduction to Applied and Environmental Geophysics*, John Wiley & Sons, Inc., New York, USA. Cited on page 14.

Richards, L. A. (1931), Capillary conduction of liquids through porous mediums, *Physics*, *1*(5), 318–333, doi: 10.1063/1.1745010. Cited on page 18.

Robinson, D. A., and S. P. Friedman (2003), A method for measuring the solid particle permittivity or electrical conductivity of rocks, sediments, and granular materials, *Journal of Geophysical Research*, *108*(B2), 2076, doi: 10.1029/2001JB000691. Cited on page 83.

Robinson, D. A., S. B. Jones, J. M. Wraith, D. Or, and S. P. Friedman (2003), A Review of Advances in Dielectric and Electrical Conductivity Measurement in Soils Using Time Domain Reflectometry, *Vadose Zone Journal*, *2*(4), 444–475. Cited on pages 4 and 37.

Robinson, D. A., C. S. Campbell, J. W. Hopmans, B. K. Hornbuckle, S. B. Jones, R. Knight, F. Ogden, J. Selker, and O. Wendroth (2008), Soil Moisture Measurement for Ecological and Hydrological Watershed-Scale Observatories: A Review, *Vadose Zone Journal*, *7*(1), 358–389, doi: 10.2136/vzj2007.0143. Cited on pages 4 and 5.

Rockström, J., W. Steffen, K. Noone, Å. Persson, F. S. Chapin, E. F. Lambin, T. M. Lenton, M. Scheffer, C. Folke, H. J. Schellnhuber, et al. (2009), A safe operating space for humanity, *Nature*, *461*(7263), 472–475, doi: 10.1038/461472a. Cited on page 2.

Roth, K. (2012), *Soil Physics Lecture Notes*, Heidelberg University, Germany. Cited on pages 16, 21, and 22.

Roth, K., R. Schulin, H. Flühler, and W. Attinger (1990), Calibration of time domain reflectometry for water content measurement using a composite dielectric approach, *Water Resources Research*, *26*(10), 2267–2273, doi: 10.1029/WR026i010p02267. Cited on pages 15, 37, and 84.

Roth, K., U. Wollschläger, Z. H. Cheng, and J. B. Zhang (2004), Exploring soil layers and water tables with ground-penetrating radar, *Pedosphere*, *14*(3), 273–282. Cited on page 32.

Rubin, Y., and S. S. Hubbard (2005), *Hydrogeophysics*, *Water Science and Technology Library*, vol. 50, Springer Netherlands, The Netherlands, doi: 10.1007/1-4020-3102-5. Cited on page 83.

Sagan, C., and A. Druyan (1997), *Pale blue dot*, Ballantine Books, New York, USA. Cited on page 2.

Schrag, D. P., R. A. Berner, P. F. Hoffman, and G. P. Halverson (2002), On the initiation of a snowball Earth, *Geochemistry Geophysics Geosystems*, *3*(6), 1036, doi: 10.1029/2001GC000219. Cited on page 1.

Seegers, C. (2012), Experimentelle Untersuchung der Bodenwasserdynamik mittels Georadar, *in German*, Diploma thesis, Heidelberg University. Cited on pages 42 and 107.

Sharma, P. V. (1997), *Environmental and Engineering Geophysics*, Cambridge University Press, Cambridge, UK. Cited on pages 10 and 14.

Shi, Y., Y. Shen, E. Kang, D. Li, Y. Ding, G. Zhang, and R. Hu (2007), Recent and Future Climate Change in Northwest China, *Climatic Change*, *80*, 379–393, doi: 10.1007/s10584-006-9121-7, 10.1007/s10584-006-9121-7. Cited on pages 45 and 138.

Sihvola, A. (1999), *Electromagnetic Mixing Formulas and Applications*, The Institute of Electrical Engineers, London, UK. Cited on page 13.

Simunek, J., M. T. van Genuchten, and M. Sejna (2005), *The HYDRUS-1D Software Package for Simulating the Movement of Water, Heat, and Multiple Solutes in Variably-Saturated Media, Version 3.0, HYDRUS Software Series 1*, Department of Environmental Sciences, University of California Riverside, Riverside, USA. Cited on pages 34 and 81.

Solomon, S., D. Qin, M. Manning, Z. Chen, M. Marquis, K. B. Averyt, M. Tignor, and H. L. Miller (2007), IPCC, 2007: Summary for policymakers, *Climate change*, *IV*, 93–129. Cited on page 1.

Sperl, C. (1999), Erfassung der raum-zeitlichen Variation des Bodenwassergehalts in einem Agrarökosystem mit dem Ground-Penetrating Radar, Ph.D. thesis, Technical University Munich, Germany. Cited on page 29.

Steelman, C. M., and A. L. Endres (2011), Comparison of Petrophysical Relationships for Soil Moisture Estimation using GPR Ground Waves, *Vadose Zone Journal*, *10*(1), 270–285, doi: 10.2136/vzj2010.0040. Cited on pages 15 and 84.

Strobbia, C., and G. Cassiani (2007), Multilayer ground-penetrating radar guided waves in shallow soil layers for estimating soil water content, *Geophysics*, *72*(4), J17–J29, doi: 10.1190/1.2716374. Cited on page 31.

Tapley, B., S. Bettadpur, J. Ries, P. Thompson, and M. Watkins (2004), GRACE Measurements of Mass Variability in the Earth System, *Science*, *305*(5683), 503–505, doi: 10.1126/science.1099192. Cited on page 4.

Topp, G., and A. Davis, J.L .and Annan (1980), Electromagnetic determination of soil water content: Measurements in coaxial transmission lines, *Water Resources Research*, *16*(3), 574–582, doi: 10.1029/WR016i003p00574. Cited on page 15.

van der Kruk, J. (2006), Properties of surface waveguides derived from inversion of fundamental and higher mode dispersive GPR data, *Geoscience and Remote Sensing, IEEE Transactions on*, *44*(10), 2908 –2915, doi: 10.1109/TGRS.2006.877286. Cited on page 31.

van der Kruk, J., R. Streich, and A. G. Green (2006), Properties of surface waveguides derived from separate and joint inversion of dispersive TE and TM GPR data, *Geophysics*, *71*(1), K19–K29, doi: 10.1190/1.2168011. Cited on page 32.

van der Kruk, J., S. A. Arcone, and L. Liu (2007), Fundamental and Higher Mode Inversion of Dispersed GPR Waves Propagating in an Ice Layer, *Geoscience and Remote Sensing, IEEE Transactions on*, *45*(8), 2483–2491, doi: 10.1109/TGRS.2007.900685. Cited on pages 5, 31, 34, and 69.

van der Kruk, J., C. M. Steelman, A. L. Endres, and H. Vereecken (2009), Dispersion inversion of electromagnetic pulse propagation within freezing and thawing soil waveguides, *Geophysical Research Letters*, *36*(18), L18503, doi: 10.1029/2009GL039581. Cited on page 5.

van der Kruk, J., R. W. Jacob, and H. Vereecken (2010), Properties of precipitation-induced multilayer surface waveguides derived from inversion of dispersive TE and TM GPR data, *Geophysics*, *75*(4), WA263–WA273, doi: 10.1190/1.3467444. Cited on pages 5 and 31.

Van der Velde, R., Z. Su, and Y. Ma (2008), Impact of Soil Moisture Dynamics on ASAR $\sigma°$ Signatures and Its Spatial Variability Observed over the Tibetan Plateau, *Sensors*, *8*(9), 5479–5491, doi: 10.3390/s8095479. Cited on page 4.

Van Dishoeck, E., L. Kristensen, A. Benz, E. Bergin, P. Caselli, J. Cernicharo, F. Herpin, M. Hogerheijde, D. Johnstone, R. Liseau, et al. (2011), Water in Star-forming Regions with the *Herschel Space Observatory* (WISH). I. Overview of Key Program and First Results, *Publications of the Astronomical Society of the Pacific*, *123*(900), 138–170, doi: 10.1086/658676. Cited on page 2.

Van Genuchten, M. (1980), A Closed-form Equation for Predicting the Hydraulic Conductivity of Unsaturated Soils, *Soil Science Society of America Journal*, *44*(5), 892–898, doi: 10.2136/sssaj1980.03615995004400050002x. Cited on page 20.

Vereecken, H., J. A. Huisman, H. Bogena, J. Vanderborght, J. A. Vrugt, and H. J. W. (2008), On the value of soil moisture measurements in vadose zone hydrology: A review, *Water Resources Research*, *44*, W00D06, doi: 10.1029/2008WR006829. Cited on page 5.

Villarreyes Rivera, C., G. Baroni, and S. Oswald (2011), Integral quantification of seasonal soil moisture changes in farmland by cosmic-ray neutrons, *Hydrology and Earth System Sciences*, *15*(12), 3843–3859, doi: 10.5194/hess-15-3843-2011. Cited on page 5.

Wagner, W., C. Pathe, M. Doubkova, D. Sabel, A. Bartsch, S. Hasenauer, G. Blöschl, K. Scipal, J. Martínez-Fernández, and A. Löw (2008), Temporal Stability of Soil Moisture and Radar Backscatter Observed by the Advanced Synthetic Aperture Radar (ASAR), *Sensors*, *8*(2), 1174–1197, doi: 10.3390/s8021174. Cited on page 4.

Waite Jr, J., W. Lewis, B. Magee, J. Lunine, W. McKinnon, C. Glein, O. Mousis, D. Young, T. Brockwell, J. Westlake, et al. (2009), Liquid water on Enceladus from observations of ammonia and ^{40}Ar in the plume, *Nature*, *460*(7254), 487–490, doi: 10.1038/nature08153. Cited on page 2.

Walker, J., P. Houser, and G. Willgoose (2004), Active microwave remote sensing for soil moisture measurement: a field evaluation using ERS-2, *Hydrological Processes*, *18*(11), 1975–1997, doi: 10.1002/hyp.1343. Cited on page 4.

Warren, C., and A. Giannopoulos (2012), Investigation of the directivity of a commercial Ground-Penetrating Radar antenna using a Finite-Difference Time-Domain antenna model, in *Ground Penetrating Radar (GPR), 2012 14th International Conference on*, pp. 226–231, IEEE, doi: 10.1109/ICGPR.2012.6254865. Cited on page 145.

Weast, R. C., et al. (1986), *CRC handbook of chemistry and physics*, CRC Press, Boca Raton, USA. Cited on page 14.

Weihermüller, L., J. Huisman, S. Lambot, M. Herbst, and H. Vereecken (2007), Mapping the spatial variation of soil water content at the field scale with different ground penetrating radar techniques, *Journal of Hydrology*, *340*(3-4), 205–216, doi: 10.1016/j.jhydrol.2007.04.013. Cited on page 5.

Westermann, S., U. Wollschläger, and J. Boike (2010), Monitoring of active layer dynamics at a permafrost site on Svalbard using multi-channel ground-penetrating radar, *The Cryosphere*, *4*(4), 475–487, doi: 10.5194/tc-4-475-2010. Cited on pages 27 and 54.

Western, A., R. Grayson, and G. Blöschl (2002), Scaling of soil moisture: a hydrologic perspective, *Annual Review of Earth and Planetary Sciences*, *30*(1), 149–180, doi: 10.1146/annurev.earth.30.091201.140434. Cited on page 4.

Wigneron, J. P., J. C. Calvet, T. Pellarin, A. A. V. de Griend, M. Berger, and P. Ferrazzoli (2003), Retrieving near-surface soil moisture from microwave radiometric observations:

current status and future plans, *Remote Sensing of Environment*, *85*(4), 489–506, doi: 10.1016/S0034-4257(03)00051-8. Cited on page 4.

Winship, P., A. Binley, and D. Gomez (2006), Flow and transport in the unsaturated Sherwood sandstone: Characterization using cross-borehole geophysical methods, *Geological Society, London, Special Publications*, *263*(1), 219–231, doi: 10.1144/GSL.SP.2006.263.01.12. Cited on pages 5 and 25.

Wollschläger, U., T. Pfaff, K. Roth, et al. (2009), Field-scale apparent hydraulic parameterisation obtained from TDR time series and inverse modelling, *Hydrology and Earth System Sciences*, *13*(10), 1953–1966, doi: 10.5194/hess-13-1953-2009. Cited on pages 3 and 54.

Wollschläger, U., H. Gerhards, Q. Yu, and K. Roth (2010), Multi-channel ground-penetrating radar to explore spatial variations in thaw depth and moisture content in the active layer of a permafrost site, *The Cryosphere*, *4*(3), 269–283, doi: 10.5194/tc-4-269-2010. Cited on pages 5 and 27.

WPP (2011), *World Population Prospects: The 2010 Revision, Highlights and Advance Tables*, United Nations, Department of Economic and Social Affairs, Population Division. Cited on page 1.

Zemp, M., S. U. Nussbaumer, I. Gärtner-Roer, M. Hoelzle, F. Paul, and W. Haeberli (2011), Glacier Mass Balance Bulletin No.11, ICSU(WDS)/ IUGG(IACS)/ UNEP/ UNESCO/ WMO, World Glacier Monitoring Service, Zurich, Switzerland. Cited on page 137.

Zhou, H. F., Y. Li, Y. Tang, B. J. Zhou, and H. W. Xu (2009), The characteristics of the snow cover and snowmelt water strorage in the Gurbantüngüt desert, *in Chinese*, *Arid Zone Research*, *26*, 312–317. Cited on page 94.

Zreda, M., D. Desilets, T. Ferré, and R. Scott (2008), Measuring soil moisture content non-invasively at intermediate spatial scale using cosmic-ray neutrons, *Geophysical Research Letters*, *35*(L21402), L21402, 5 PP., doi: 10.1029/2008GL035655. Cited on page 5.

List of Figures

List of Tables

A List of Acronyms

ASAR Advanced Synthetic Aperture Radar, active radar instrument on ENVISAT satellite

ASL above sea level

BMBF German Federal Ministery of Education and Reasearch

CAREERI Cold and Arid Regions Environmental and Engineering Research Institute

CMP Common Mid-Point

CRIM Complex Refractive Index Model

dc direct current

ESA European Space Agency

GRACE Gravity Recovery and Climate Experiment

INT1 Internal Channel of the Front Antenna

INT2 Internal Channel of the Back Antenna

NASA National Aeronautics and Space Administration

FDTD Finite-Difference Time-Domain

LCBC long cross box channel

MEEP MIT Electromagnetic Equation Propagation

REV Representative Elementary Volume

SCBC short cross box channel

SMAP Soil Moisture Active Passive

SMOS Soil Moisture and Ocean Salinity

TDR Time Domain Reflectometry

TE transverse-electric

TM transverse-magnetic

USDA United States Department of Agriculture

WARR Wide Angle Reflection and Refraction

XIEG Xinjiang Institute of Ecology and Geography, CAS

B List of Digital Supplementary Materials

Several results which were obtained in this work can be illustrated more precisely in terms of short movies. This is a list of all videos which can be found in the digital supplementary materials. When opening the pdf version of this thesis under a unix-type system within the provided folder structure, the links to the video should work directly.

Chapter 4

- Video showing an overview of the measurement campaigns executed in the framework of the project RECAST Urumqi: Video1.mp4.

Chapter 5

- Video illustrating modal wave propagation within a leaky waveguide. The numerical calculation was carried out with MEEP and assumed a 0.17 m ice layer with ε_{ice} overlying a pure water half-space $\varepsilon_{\text{w,T}=0} = 88.15$: Video2.mp4.

- A timelapse movie illustrating the changing shape of the air wave wavelet as a function of antenna separation during an AIRWARR measurement: Video3.mp4.

Chapter 7

- A timelapse movie showcasing all radargrams recorded by the INT2 channel along the 7 m stretch starting from the 6 m position along the profile: Video4.avi.

- A timelapse movie showing the continuous change of the transition zone shape in a homogeneous sand and the corresponding shape of the GPR response assuming the forcing from the March experiment: Video5.mp4.

- A timelapse movie illustrating the changing shape of the bottom reflection wavelet for both internal channels over the course of the March experiment: Video6.mp4.

- "Life of a geophysicist" – a timelapse movie of still photos which were taken at regular intervals during the March experiment, showing the measurement procedure over the course of the whole day.

C Acknowledgements - Danksagungen

True Enthusiasm

True Enthusiasm